

Title	Evaporation maps for ternary non-ideal liquid mixtures
Authors	Dillon, Paul
Publication date	2016
Original Citation	Dillon, P. 2016. Evaporation maps for ternary non-ideal liquid mixtures. PhD Thesis, University College Cork.
Type of publication	Doctoral thesis
Rights	© 2016, Paul Dillon. - http://creativecommons.org/licenses/by-nc-nd/3.0/
Download date	2025-07-03 04:02:59
Item downloaded from	https://hdl.handle.net/10468/2239

Evaporation Maps for Ternary Non-Ideal Liquid Mixtures

Paul Dillon

BE, MSc

97111660

**Thesis submitted for the degree of
Doctor of Philosophy**



NATIONAL UNIVERSITY OF IRELAND, CORK

SCHOOL OF ENGINEERING

DEPARTMENT OF PROCESS AND CHEMICAL ENGINEERING

February 2016

Supervisors: Dr Kevin Cronin
Dr. Edmond Byrne

Contents

List of Figures	v
List of Tables	vii
Nomenclature	ix
Acknowledgements	xv
Abstract	xvii
1 Introduction	1
1.1 Aims and Objectives	3
1.2 Novel Contributions	4
1.3 Thesis Outline	5
1.4 Publications	7
2 Background and Literature Review	9
2.1 Multicomponent Mass Transfer	10
2.1.1 Multicomponent Effects and Limitations of Fick's law	10
2.1.2 Maxwell-Stefan Equations and Generalized Fick's Law	12
2.2 Residue Curve Maps	15
2.2.1 Construction of Residue Curve maps	15
2.2.2 Computation of Azeotropes	21
2.2.3 Residue Curve Maps under non-equilibrium conditions	21
2.3 Evaporation and Drying of Multicomponent Mixtures	24
2.3.1 Evaporation of Multicomponent Liquids	25
2.3.2 Drying of Solids Containing Multicomponent Liquids	29
2.4 Chapter Summary and Conclusions	33
3 Evaporation Maps for Gas Phase Limited Conditions	35
3.1 Theory	37
3.1.1 Analytic Solution to Maxwell-Stefan Equations	37
3.1.2 Application of Analytic Solution to Fluxes in Gas Phase	41
3.1.3 Conservation Equations for Liquid Phase	42
3.1.4 Multicomponent Wet-bulb Temperature	46
3.1.5 Pseudoazeotrope Compositions	48
3.2 Numerical Methods	49
3.2.1 Evaporation Trajectories	49
3.2.2 Multicomponent Wet-bulb Temperature	51
3.2.3 Computation of Pseudo-Azeotrope Compositions	52
3.2.4 Construction of Evaporation Maps	53
3.3 Simulation Results and Discussion	56
3.3.1 Validation of Evaporation Model	56
3.3.2 Binary and Ternary Pseudo-Azeotropes	57
3.3.3 Multicomponent Wet-Bulb Temperature	60
3.3.4 Evaporation Trajectories - IPA/Ethanol/Water Example	65
3.3.5 Ternary Evaporation Maps	70
3.4 Reduction of Multicomponent Wet-Bulb Model to Single Component Case	77
3.5 Chapter Summary and Conclusions	79
4 Bifurcations in Evaporation Maps	81
4.1 Introduction	81

4.2	Azeotropes and Pseudo-Azeotropes via Homotopy	82
4.2.1	Computation of Azeotropes By Newton's Method	83
4.2.2	Overview of Homotopy Methods	84
4.2.3	Computation of Azeotropes by Homotopy Method	87
4.2.4	Computation of Pseudo-Azeotropes by Homotopy Method	90
4.3	Bifurcations in Evaporation Maps	93
4.3.1	Overview of Bifurcations and Numerical Continuation	93
4.3.2	Bifurcation Analysis of Evaporation Maps	98
4.3.3	Effect of Gas Pre-Loading on Evaporation Maps	105
4.4	Interaction Effects	107
4.5	Chapter Summary and Conclusions	113
5	Stability Analysis	115
5.1	Stability of Fixed Points in Residue Curve Maps	115
5.2	Stability of Fixed Points in Evaporation Maps	120
5.3	Chapter Summary and Conclusions	125
6	Separation Boundaries	129
6.1	Separation boundaries from linearized analysis	131
6.2	Separation boundaries by optimization	132
6.2.1	Optimization of integral trajectory length	135
6.2.2	Optimization of integral area	138
6.2.3	Computed Separation Boundaries	140
6.3	Flexure of the wet-bulb temperature surface	141
6.3.1	Location of ridges and valleys in wet-bulb surface by optimization	143
6.3.2	Location of ridges and valleys by finite difference method	144
6.4	Chapter Summary and Conclusions	145
7	Evaporation maps including diffusion effects in liquid	151
7.1	Governing Equations	152
7.1.1	Mass and Heat Transfer in Gas Phase	152
7.1.2	Mass Transfer in Liquid Phase	152
7.1.3	Boundary Conditions for Mass Transfer	157
7.1.4	Heat Transfer in Liquid Phase	158
7.1.5	Vapour-Liquid Equilibria and Physical Properties	158
7.1.6	Liquid Diffusion Coefficients	159
7.1.7	Initial Conditions	159
7.2	Numerical Methods	159
7.2.1	Finite Volume Formulation for Mass Transport in Liquid Phase	160
7.2.2	Component Material Balances	160
7.2.3	Spatial Discretization	161
7.2.4	Treatment of Boundary Conditions	166
7.2.5	Time Discretization	168
7.3	Simulation Results and Discussion	169
7.3.1	Comparison with Experimental Data	170
7.3.2	Evaporation Paths for Selected Ternary Mixtures	176
7.4	Chapter Summary and Conclusions	180
8	Conclusions and Further Work	185
8.1	Summary and Outcomes	185

8.2	Suggestions for Further Work	189
A	Governing Equations	209
A.1	Multicomponent Fluxes	209
A.2	Conservation Equations	211
A.3	Maxwell-Stefan Equations	215
A.3.1	Maxwell-Stefan Equations from Momentum Balance	216
A.3.2	Generalized Maxwell-Stefan Equations from IRT	219
B	Physical Property Modelling	227
B.1	Vapour-Liquid Equilibria	227
B.2	Composition Derivatives of NRTL model	230
B.3	Vapour Pressure	230
B.4	Diffusivity	232
B.4.1	Gas/Vapour Diffusivity	232
B.4.2	Liquid Diffusivity	234

List of Figures

1.1	Schematic of tray dryer	2
2.1	Experiment of Duncan & Toor (1962)	12
2.2	Residue curve maps for example ternary mixtures	18
3.1	Evaporation from surface of ternary liquid mixture.	38
3.2	Schematic of evaporation from planar surface	44
3.3	Construction of evaporation map	56
3.4	IPA-water droplet evaporation comparison	58
3.5	Evaporation of ethanol-MEK-toluene mixture ($x_1 = 0.33, x_2 = 0.33, x_3 = 0.34$)	58
3.6	Evaporation of ethanol-MEK-toluene mixture ($x_1 = 0.6, x_2 = 0.1, x_3 = 0.3$)	59
3.7	Evaporation of ethanol-MEK-toluene mixture ($x_1 = 0.8, x_2 = 0.05, x_3 = 0.15$)	59
3.8	Figures 3.5-3.7 on ternary co-ordinates	60
3.9	Wet-bulb temperature and selectivities	61
3.10	Magnified portion of figure 3.9a	63
3.11	Ethanol/water multicomponent wet-bulb lines	64
3.12	Wet-bulb temperature surface for ethyl acetate/DCM/methanol	65
3.13	Wet-bulb temperature surface for ethanol/MEK/toluene	66
3.14	Wet-bulb temperature surface for acetone/chloroform/methanol	67
3.15	Example evaporation trajectory for IPA/ethanol/water	68
3.16	Example film concentration profiles for IPA/ethanol/water	69
3.17	Component fluxes for IPA/ethanol/water	70
3.18	Evaporation map for IPA-ethanol-methanol	74
3.19	Evaporation map for water-ethanol-methanol	74
3.20	Evaporation map for IPA-water-ethanol	75
3.21	Evaporation map for ethanol-MEK-toluene	75
3.22	Evaporation map for dichloromethane/methanol/ethyl acetate	76
3.23	Evaporation map for acetone/chloroform/methanol	76
3.24	Multicomponent wet-bulb for single component case	78
4.1	Hypothetical composition and bubble-points at various values of homotopy parameter for binary mixtures	89
4.2	Location of azeotropes in acetone-chloroform-methanol mixture by homotopy method	91
4.3	Hypothetical selectivity and wet-bulb temperature at various values of homotopy parameter for binary mixtures	94
4.4	Location of pseudo-azeotropes in acetone-chloroform-methanol mixture by homotopy method	95
4.5	Saddle-node bifurcation	96
4.6	Bifurcation diagrams for acetone-chloroform-methanol; $T^G = 40^\circ C$, $u^G = 0.5m/s$, $d = 0.03m$	102
4.7	Normalized evaporative fluxes for acetone-chloroform-methanol; $T^G = 40^\circ C$, $u^G = 0.5m/s$, $d = 0.03m$	103

4.8	Bifurcation diagrams for ternary acetone-chloroform-methanol pseudo-azeotrope	104
4.9	Evaporation maps for gas phase pre-loaded with acetone	108
4.10	Evaporation maps for gas phase pre-loaded with chloroform	109
4.11	Evaporation maps for gas phase pre-loaded with methanol	110
4.12	Tracking of ternary pseudo-azeotrope bifurcation	111
4.13	Off-diagonal contributions to diffusive fluxes	112
5.1	Eigen-values for residue curve map of benzene-acetone-chloroform . .	121
5.2	Eigen-values for residue curve map of example mixtures	122
5.3	Surface plots of fluxes (normalized) in acetone/chloroform/methanol mixture	126
5.4	Eigen-values for evaporation map of example mixtures	127
6.1	Schematic for determination of separation boundaries	131
6.2	Trajectory-lengths and separation boundaries for example residue curve maps	134
6.3	Trajectory-lengths and separation boundaries for example evaporation maps	136
6.4	Trajectory-lengths and areas for acetone-methanol-chloroform mixture	139
6.5	Area and residue curve length for acetone-chloroform-methanol mixture	142
6.6	Valleys and ridges in wet-bulb temperature surfaces	150
7.1	Schematic of heat and mass transfer from liquid film surface, and finite-volume discretization within film	154
7.2	Control volumes for general 2-D finite-volume method	162
7.3	Control volumes for 1-D finite-volume method	163
7.4	Composition profiles for ethanol-MEK-toluene mixture; $x_1 = 0.33, x_2 = 0.33, x_3 = 0.34$	173
7.5	Composition profiles for ethanol-MEK-toluene mixture; $x_1 = 0.6, x_2 = 0.1, x_3 = 0.3$	173
7.6	Composition profiles for ethanol-MEK-toluene mixture; $x_1 = 0.8, x_2 = 0.05, x_3 = 0.1$	174
7.7	Diffusivity values	174
7.8	Composition profiles for ethanol-MEK-toluene mixture	175
7.9	Evaporation paths of IPA-ethanol-methanol	178
7.10	Composition profiles and Biot numbers	179
7.11	Evaporation paths of ethanol-MEK-toluene	181
7.12	Comparison of lumped and distribute model trajectories	182
A.1	Control volume for derivation of conservation equations	211
A.2	Species Interaction for binary and ternary mixtures	219
B.1	Txy and activity coefficients for IPA-water-ethanol	231
B.2	Txy and activity coefficients for water-ethanol-methanol	232
B.3	Txy and activity coefficients for acetone-chloroform-methanol	233

List of Tables

2.1	Example ternary mixtures used in this work	17
3.1	Calculation of multicomponent fluxes using Newton method	51
3.2	Algorithm for computation of wet-bulb temperature	52
3.3	Algorithm for computation of pseudo-azeotrope composition	52
3.4	Jacobian for pseudo-azeotrope calculation	54
3.5	Algorithm for generation of evaporation maps	55
3.6	Results of pseudo-azeotrope calculations	62
4.1	Calculation of azeotropes using Newton's method	85
4.2	Azeotrope computation by Newton's method	86
4.3	Homotopy method for azeotrope determination	90
4.4	Homotopy method for azeotrope determination	93
5.1	Procedure for calculation of eigenvalues and eigenvectors (with analytic Jacobian)	118
5.2	Computed eigenvalues for benzene-acetone-chloform mixture	120
5.3	Algorithm for calculation of eigenvalues and eigenvectors of evaporation maps	124
6.1	Algorithm for generation of separation boundaries in residue curve maps using eigenvector calculated at saddle node	132
6.2	Algorithm for generation of separation boundaries in evaporation maps using eigenvector calculated at saddle node	133
6.3	Optimum angle, line integral and area integrals for residue curve map of acetone-chloform-methanol mixture	140
6.4	Optimum angle, line integral and area integrals for evaporation map of acetone-chloform-methanol mixture	141
6.5	Algorithm for generation of separation boundaries in residue curve map	147
6.6	Algorithm for generation of separation boundaries in evaporation map	148
6.7	Optimization algorithm for location of valleys and ridges in wet-bulb temperature surface	149
6.8	Gradient algorithm for location of valleys and ridges in wet-bulb temperature surface	149
7.1	Summary of gas-phase heat and mass transfer	153
8.1	Comparison of some key features of residue curve maps and evaporation maps	188
A.1	Contributions to entropy production rate	224
A.2	Forces and fluxes in entropy production	224
A.3	Possible dependencies from third postulate of IRT	225
B.1	NRTL parameters for IPA-ethanol-methanol	228
B.2	NRTL parameters for water-ethanol-methanol	228
B.3	NRTL parameters for IPA-water-ethanol	228
B.4	NRTL parameters for ethanol-MEK-toluene	229
B.5	NRTL parameters for DCM-methanol-ethyl acetate	229

B.6	NRTL parameters for benzene-acetone-chloroform	229
B.7	NRTL parameters for acetone-chloroform-methanol	230
B.8	Parameters for Antoine vapour pressure correlation	234
B.9	Lennard Jones potentials	234

Nomenclature

\bar{H}_i^G	Vapour enthalpy of component i [$J \text{ mol}^{-1}$]
\bar{H}_i^L	Liquid enthalpy of component i [$J \text{ mol}^{-1}$]
ΔH_i^{vap}	Enthalpy of vaporization of component i [$J \text{ mol}^{-1}$]
\dot{m}_v	Mass evaporation rate [$kg \text{ s}^{-1}$]
\mathfrak{D}_{ij}	Maxwell-Stefan diffusivity for pair ij [$m^2 \text{ s}^{-1}$]
\mathfrak{D}_{ij}	Maxwell-Stefan diffusivity [$m^2 \text{ s}^{-1}$]
\mathbf{D}	Generalized Fick diffusivity matrix
\mathbf{f}	Body force [N]
A	Area for heat/mass transfer [m^2]
Bi_M	Biot number for mass transfer
c_i	Vapour phase concentration of component i (ideal gas) [mol m^{-3}]
c_T	Vapour phase total concentration (ideal gas) [mol m^{-3}]
Cp_i	Specific heat capacity of component i [$J \text{ kg}^{-1} \text{ K}^{-1}$]
d	Characteristic length or droplet diameter [m]
D_{ij}	Binary diffusivity of ij pair [$m^2 \text{ s}^{-1}$]
F_i	Discrepancy or residual function
h_G	Low-flux heat transfer coefficient [$W \text{ m}^{-2} \text{ K}^{-1}$]
h_i	Molar hold-up of component i [mol]
h_T	Molar hold-up of component i [mol]
J_i	Diffusive molar flux [$\text{mol m}^{-2} \text{ s}$]
j_i	Diffusive mass flux [$\text{kg m}^{-2} \text{ s}$]
k	Thermal conductivity [$W \text{ m}^{-1} \text{ K}^{-1}$]
K_i	$\gamma_i p_i / P$
K_L	Characteristic number for mass transfer
k_{ij}	Low-flux multicomponent mass transfer coefficient for pair ij [m s^{-1}]
k_{ij}^\bullet	Multicomponent mass transfer coefficient corrected for non-zero mass flux, for pair ij [m s^{-1}]
M_i	Molecular weight of component i [g mol^{-1}]
M_t	Total mass hold-up [kg]
n	Number of components
N_i	Molar flux of component i [$\text{mol m}^{-2} \text{ s}$]
n_i	Mass flux of component i [$\text{kg m}^{-2} \text{ s}$]

Nu	Nusselt number
P	Ambient pressure [Pa]
p_i	Vapour pressure of component i [Pa]
Pr	Prandtl number (gas phase)
q	Heat flux [$W\ m^{-2}$]
Re	Reynolds number
RH	Relative humidity
s	Entropy [$J\ mol^{-1}\ K$]
S_i	Selectivity of component i
Sc_{ij}	Schmidt number for pair ij
Sh_{ij}	Sherwood number for pair ij
T	Temperature [$^{\circ}C$]
t	Time [s]
u^G	Gas velocity [$m\ s^{-1}$]
x_i	Mole fraction of component i (liquid phase)
y_i	Mole fraction of component i (gas phase)
z	distance (film thickness) [m]

Greek

δ	Kronecker delta function
ϵ	Increment of molefraction
η	Relative depth of film
γ_i	Activity coefficient of component i
κ_{ij}	Binary mass transfer coefficient for pair ij [$m\ s^{-1}$]
λ	Homotopy parameter
μ	Viscosity [$Pa\ s$]
ω	Mass fraction
Φ	Mass transfer factor
ϕ	Fugacity coefficient
Φ_H^G	Heat transfer factor
ρ	Density [$kg\ m^{-3}$]
τ	Relative time
Ξ	Correction factor for mass transfer
ξ	Relative number of moles

Ξ_H Correction factor for heat transfer

Subscripts

e Effective

t Total

Superscripts

G Gas

I Interface

L Liquid

I, Paul Dillon, certify that this thesis is my own work and has not been submitted for another degree at University College Cork or elsewhere.

Paul Dillon

To Sarah and James

Acknowledgements

I would like to thank my supervisors, Dr. Kevin Cronin and Dr. Ed Byrne for their guidance and support throughout this project. I would also like to thank Dr. John Fitzpatrick and Dr. Nima Shokri for acting as internal and external examiners respectively.

Abstract

This thesis deals with the evaporation of non-ideal liquid mixtures using a multicomponent mass transfer approach. It develops the concept of *evaporation maps* as a convenient way of representing the dynamic composition changes of ternary mixtures during an evaporation process. Evaporation maps represent the residual composition of evaporating ternary non-ideal mixtures over the full range of composition, and are analogous to the commonly-used residue curve maps of *simple* distillation processes.

The evaporation process initially considered in this work involves gas-phase limited evaporation from a liquid or wetted-solid surface, over which a gas flows at known conditions. Evaporation may occur into a pure inert gas, or into one pre-loaded with a known fraction of one of the ternary components. To explore multicomponent mass-transfer effects, a model is developed that uses an exact solution to the Maxwell-Stefan equations for mass transfer in the gas film, with a lumped approach applied to the liquid phase. Solutions to the evaporation model take the form of trajectories in temperature-composition space, which are then projected onto a ternary diagram to form the map.

Novel algorithms are developed for computation of “pseudo”-azeotropes in the evaporating mixture, and for calculation of the multicomponent wet-bulb temperature at a given liquid composition. A numerical continuation method is used to track the bifurcations which occur in the evaporation maps, where the composition of one component of the pre-loaded gas is the bifurcation parameter. The bifurcation diagrams can in principle be used to determine the required gas composition to produce a specific terminal composition in the liquid.

A simple homotopy method is developed to track the locations of the various possible pseudo-azeotropes in the mixture. The stability of pseudo-azeotropes in the gas-phase limited case is examined using a linearized analysis of the governing equations.

Algorithms for the calculation of separation boundaries in the evaporation maps are developed using an optimization-based method, as well as a method employing eigenvectors derived from the linearized analysis. The flexure of the wet-bulb temperature surface is explored, and it is shown how evaporation trajectories cross ridges and valleys, so that ridges and valleys of the surface do not coincide with separation boundaries.

Finally, the assumption of gas-phase limited mass transfer is relaxed, by employing a model that includes diffusion in the liquid phase. A finite-volume method is used to solve the system of partial differential equations that results. The evaporation trajectories for the distributed model reduce to those of the lumped (gas-phase limited) model as the diffusivity in the liquid increases; under the same gas-phase conditions the permissible terminal compositions of the distributed and lumped models are the same.

Chapter 1

Introduction

The evaporation of organic solvent mixtures, and the drying of solids containing such solvents are common operations in the process industries, spanning technologies from spray-drying of pharmaceutical products to fuel combustion. In many manufacturing processes, the use of solvent mixtures may offer desirable features. In the pharmaceutical industry for example, some 90% of all compounds in modern pharmaceutical drug delivery pipelines are reported to be poorly soluble in water (Reintjes 2011); the use of solvent mixtures enhances the solubility of many active pharmaceutical ingredients (APIs), allowing reaction steps to occur in liquid phase, and allowing the final active ingredient to be spray-dried to a solid, and ultimately processed to the required final dosage form. As a motivational example, figure 1.1 shows a practical case of a tray dryer used to dry pharmaceutical solids; the wetted solids, often from a preceding granulation step using a solvent mixture, are loaded into trays and stacked on mobile trolleys. When placed within the tray dryer, the flow of heated air across the tray surface causes heat transfer from the gas phase to the wetted solid and mass transfer from the wetted solid into the gas. A portion of the solvent-laden air may be recirculated, and the balance is discharged for further treatment. After a pre-defined time period, the trays are removed from the dryer and move to the next step such as encapsulation or tableting (Parikh 1997). Various solvent mixtures, together with examples of poorly water-soluble APIs and polymeric carriers commonly used to manufacture solid dispersions suitable for spray drying have been compiled (Paudel et al. 2013). Since the drying process rarely runs to completion, there is inevitably some residual solvent in the final product, the identity and quantity of which may be critical to product quality. In the case of spray dried powders, physiochemical properties like permeability and crystallinity, as well as glass transition temperature are affected by residual solvents (Witschi & Doelder 1997). In addition, residual organic solvent represent a potential risk to human health due to the toxicity and undesirable side effects. Indeed, limits for residual solvent content are set by various national bodies such as US and European Pharmacopoeia, as well as ICH guidelines ICH (2011).

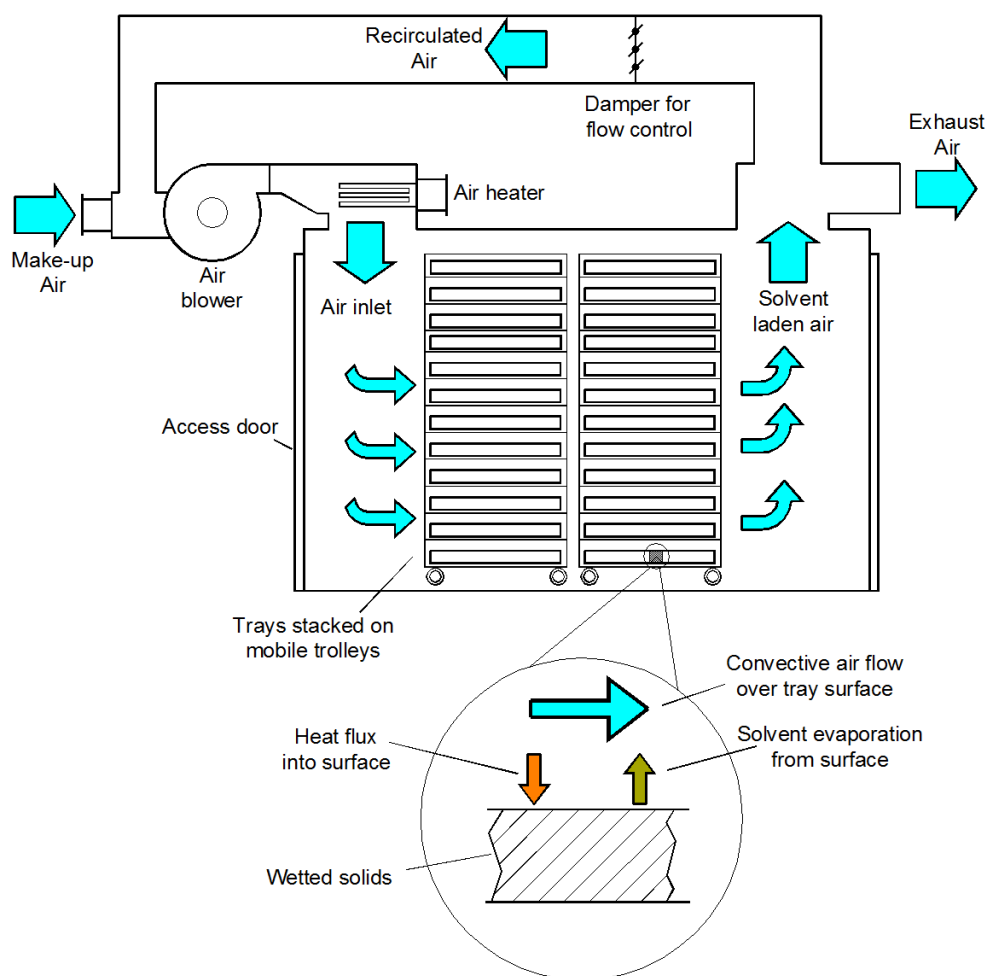


Figure 1.1: Schematic of tray dryer used for production of pharmaceutical granulates; magnified portion shows heat and mass transfer at surface on an individual tray

Industrially significant examples involving evaporation and drying of solvent mixtures include the preparation of thin polymer coatings during production of adhesives and varnishes, and the casting of asymmetric membranes for reverse osmosis applications. A further example is the prediction of evaporation rates from liquid spills which is relevant for hazard analysis and emergency response systems (van den Bosch 1997, Khajehnajafi & Pourdarvish 2011, Galeev et al. 2015).

In some industrial applications, *selective drying* is desirable, where one component is removed preferentially. In drying of foodstuffs for example, water should be removed but the aroma retained. In some cases, the solvents removed are flammable and certain concentrations in the dryer circulation or exhaust air must not be exceeded (Turner & Schlunder 1986). For drying or evaporation of single component systems e.g. water, the final liquid content after drying is determined by the operating conditions and the

process kinetics. However, when the moisture content of a process consists of a *mixture* (specifically, a *non-ideal* mixture in this thesis), the final state of the evaporation or drying process depends also on the initial composition. For non-ideal, multicomponent mixtures the number of possible final compositions increases as the number of components in the mixture; the ability to predict process paths and terminal compositions of multicomponent mixtures is therefore of practical importance. The problem is not straightforward due to the complex interactions of external (gas-phase) heat and mass transfer, mass and heat transfer within the liquid (and solid, in case of drying) and phase equilibria. This thesis attempts to shed some additional light on this area of chemical engineering.

1.1 Aims and Objectives

This work is focused on the modeling of the dynamic heat and mass transfer processes that occur during evaporation of non-ideal liquid mixtures. The specific objectives of this thesis are:

- Develop a multicomponent heat and mass transfer model for evaporating non-ideal ternary liquid mixtures. These models should not be limited to conventional Fickian diffusion, but should be capable of describing multicomponent mass transfer effects, and of quantifying the multicomponent interactions that occur.
- Develop numerical methods to depict the composition dynamics of ternary liquid mixtures on ternary diagrams in the form of *evaporation maps*, and demonstrate key features of the maps for various common ternary mixtures of varying complexity. In the first instance, consider heat and mass transfer in the gas phase, assuming a lumped character for the liquid phase. Use the analogy with the well-understood *residue-curve maps* concept as a guide.
- As part of the evaporation map concept, develop numerical models and solution methods to calculate *pseudo-azeotropes* for binary and ternary mixtures undergoing evaporation. Develop a related model and numerical method to allow *multicomponent wet-bulb temperatures* to be computed.
- Develop a numerical method for determination of *separation boundaries* that occur for some mixtures, and show how this approach also applies to residue-curve maps. Explore the relationship between separation boundaries and minima in the wet-bulb surface for ternary mixtures.
- Extend the gas-phase limited model to also include diffusion within the liquid phase, using a multicomponent description of the fluxes in the liquid. Develop

a mathematical model of multicomponent diffusive mass fluxes within the notional liquid film. Couple this with the evaporation fluxes from the gas-phase limited model to provide a comprehensive model for evaporation of multicomponent mixtures.

1.2 Novel Contributions

The contributions of this work can be summarized as follows:

1. The novel concept of a ternary *evaporation map* is presented and developed. Evaporation maps show the residual composition of a ternary liquid undergoing evaporation into a gas phase of specified composition, temperature and velocity relative to the liquid surface; a planar geometry is assumed for the bulk of this work. These maps are shown to be analogous to the *residue curve maps* commonly used in the analysis of equilibrium-based separations. A multicomponent mass transfer model is employed for the gas phase, using an analytic solution to the Maxwell-Stefan equations. The maps apply to liquids and to wetted solids, where the assumption of gas-phase limited mass transfer applies.
2. A novel application of a numerical *continuation* method is employed to analyze the *bifurcations* that occur in ternary evaporation maps as the composition of the bulk gas phase is varied. Simply homotopy methods are used to track solution branches of the governing equations for pseudo-azeotropes; these are motivated by previously published work on conventional azeotropes, and demonstrate how the pseudo-azeotropes originate from pure component branches as the degree of non-ideality of a mixture is increased via the homotopy parameter.
3. Multicomponent mass-transfer models are developed for calculation of composition binary and ternary pseudo-azeotropes, and for the calculation of multicomponent wet-bulb temperature of ternary mixtures. Algorithms are developed for the computation of pseudo-azeotropes and wet-bulb temperature, using a Newton-method approach with analytic forms of the Jacobian in each case.
4. A stability analysis of the fixed points of evaporation maps is presented. A numerical finite-difference method to analyse the mathematical stability in terms of the eigenvalues at the fixed points, from which the stability characteristics are determined. The method is demonstrated for various ternary mixtures.
5. Two approaches are presented for the location of separation boundaries in evaporation maps; for consistency and for pedagogical reasons, these are developed in parallel with analogous approaches for residue curve maps. The first approach involves a maximum-area method which avoids a limitation of previous maximum-arclength methods that are not globally optimal. A second approach uses the

eigenvectors from the preceding stability analysis to approximately compute the separation boundaries in both residue curve maps and evaporation maps.

6. A multicomponent model of diffusion in the liquid phase is developed, involving partial differential equations for the component balances, coupled with the analytic solution of the Maxwell-Stefan equations for the gas phase. The model is solved numerically using a modified *finite volume* technique. The effect of liquid-phase diffusion on the evaporation maps is examined for a number of ternary mixtures.

1.3 Thesis Outline

The work in this thesis is organised into eight chapters. In chapter 2, the background theory of multicomponent mass transfer is developed, including a derivation of the Maxwell-Stefan equations from first-principles. The literature on evaporation of multicomponent mixtures is reviewed. The theory behind *residue curve maps* is presented as they are a motivating factor for the development of the evaporation maps in subsequent chapters.

In chapter 3 the theory and implementation of evaporation maps under gas-phase limited conditions is presented. The calculation of multicomponent fluxes in the vapour phase at the interface using an exact solution to the Maxwell-Stefan equations is outlined, and applied to evaporation of multicomponent droplets and stationary planar films. Algorithms for computation of binary and ternary pseudo-azeotropes are given using efficient Newton-based solution methods. An optimization-based technique for computing evaporation trajectories is presented, leading to the construction of evaporation maps for a number of example non-ideal mixtures.

Chapter 4 deals with the bifurcations that may occur in evaporation maps as the composition of the gas-phase changes. As a prelude, homotopy methods for calculation of azeotropes and pseudo-azeotropes are developed. A numerical continuation method is used to conduct the bifurcation analysis, in which the composition of the surrounding gas as a continuation parameter.

In chapter 5, a linearized stability approach is used to analyse the stability of the fixed points for both residue curve and evaporation maps. A method for computing the eigen-directions of the fixed points based on analytical derivatives is demonstrated.

In chapter 6 a simple maximum-area optimization method is presented which facilitates computation of the separation boundaries for residue curve maps, and for evaporation maps (gas-phase limited). The concept of a "most-difficult" separation, drawn from the theory of residue curve maps, is extended to evaporation maps.

1. INTRODUCTION

In chapter 7 the restriction of gas-phase limited heat and mass transfer is relaxed, and the effect of diffusion in the liquid phase is examined. The governing equations for mass transfer in the liquid phase are presented as partial differential equations, requiring a numerical solution. A finite-volume method solution method is derived, where the off-diagonal terms in the diffusion fluxes are explicitly included in the spatial discretization. A *method-of-lines* approach is used to integrate the equations forward in time.

Chapter 8 summarizes the work and the conclusions that can be drawn. It also outlines directions for further work than can be used to extend this research.

1.4 Publications

The following peer-reviewed papers have been produced as part of this work to date:

1. Dillon P., Cronin K., Byrne E.P., Evaporation maps for non-ideal ternary mixtures, *Chemical Engineering Science* 126 (2015) 641-659

The above paper consists of material from chapter 3, as well as sections 4.3 and 4.4 of chapter 4.

Chapter 2

Background and Literature Review

In this chapter relevant background material is presented and the existing literature is surveyed. An outline of some relevant aspects of the theory of multicomponent mass transfer is given in section 2.1, including limitations of the conventional Fick's-law description of mass transfer in section 2.1.1, and an outline of the alternative Maxwell-Stefan approach in section 2.1.2 (with more detailed derivations given in appendix A.3). These form the basis for the multicomponent mass transfer model used in subsequent chapters.

The theory and application of residue curve maps is reviewed in section 2.2; the analogy between evaporation maps and residue curve maps is used in chapter 3 where the topology of residue curve maps (where equilibrium applies) motivates the development of evaporation maps (which are non-equilibrium or *rate-based*). Previous attempts to adapt the theory of residue curve maps for non-equilibrium processes are also discussed.

A review of literature related to evaporation and drying of multicomponent non-ideal liquid mixtures is given in section 2.3.1. This is primarily relevant to chapters 3-6 of this work which focuses on gas-phase limited evaporation/drying. Chapter 7 relaxes the gas-phase limited restriction by considering diffusion effects in the liquid phase; under certain conditions, drying of wetted solids may behave as though limited by gas-phase conditions, such as where diffusion in liquid phase (e.g. in capillaries of the wetted-solid) is rapid relative to mass transfer in the gas phase. Consequently, a review of relevant literature for evaporation from solids wetted with multicomponent non-ideal liquids is given in section 2.3.2.

2.1 Multicomponent Mass Transfer

Mass transfer may occur by diffusion and convection, and mass transfer fluxes are defined relative to various averaged velocities. In this section the fluxes in multicomponent mixtures are first outlined, before an outline of the governing equations for momentum, energy and mass is presented. The governing equations are then used in the derivation of the Maxwell-Stefan equations which follow. An understanding of the conventions for total and diffusive fluxes is relevant to the gas-phase limited model of evaporation employed in chapter 3 and to the distributed model of multicomponent mass transfer in chapter 7.

2.1.1 Multicomponent Effects and Limitations of Fick's law

Traditional procedures for design and analysis of mass transfer processes have used Fick's constitutive diffusion equation (or Fick's "law") which postulates a linear dependence of the diffusive flux J_i (for component i) on its composition gradient ∇x_i and diffusion coefficient D_i :

$$J_i = -c_i D_i \nabla x_i \quad (2.1)$$

Fick's law works satisfactorily for binary mixtures, for diffusion of a dilute species in a multicomponent mixture, and when external forces (electrostatic, centrifugal) are not present. When applied to multicomponent mixtures, the form of the diffusion coefficient in the Fickian relation often shows complex, unpredictable behaviour (Krishna & Wesselingh 1997). Phenomena such as *osmotic diffusion* (diffusion of a component in the absence of a concentration driving force), *reverse diffusion* (diffusion of a component in the direction opposite to its concentration driving force), and *diffusion barrier* (zero flux of a component despite a concentration driving force), identified by Toor (1957), have all been experimentally demonstrated (Duncan & Toor 1962), but are not well represented by a Fickian approach. The classical experiment by Duncan & Toor (1962) examined diffusion in an ideal ternary gas mixture of hydrogen(1)-nitrogen(2) and carbon dioxide(3) (depicted in figure 2.1), is used as a motivational example of the need for a multicomponent mass transfer model. The experiment involved two bulbs, one with an equimolar nitrogen/carbon-dioxide mixture and one with an equimolar nitrogen/hydrogen mixture, that were initially isolated by a stopcock. When the stopcock was opened the three species diffused, resulting in the measured concentration-time profiles shown in figure 2.1b.

The profiles for hydrogen and for carbon-dioxide follow expected Fick-like behaviour; hydrogen diffuses from bulb 2 to bulb 1 and the two concentrations equalise. Similarly, carbon dioxide diffuses from bulb 1 to bulb 2. Nitrogen however shows unusual behaviour; despite the fact that the initial concentrations of nitrogen in the two bulbs

are near identical (allowing for experimental measuring error), nitrogen diffuses from bulb 1 to bulb 2. This seems counter-intuitive as it occurs despite there being no concentration gradient for nitrogen. Diffusion of nitrogen against a concentration gradient (reverse diffusion) continues until a peak is reached at t_1 . As nitrogen diffuses to the right prior to t_1 , a non-zero concentration gradient between the bulbs is established; at t_1 , this gradient is sufficiently large to counter the reverse diffusion effect. At t_1 therefore, there is zero flux of nitrogen, despite a finite concentration gradient (diffusion barrier). At zero time, diffusion in the absence of a driving force occurs (osmotic diffusion).

Fick's law cannot adequately describe the multicomponent phenomena described by the experiments of Duncan & Toor. To do so on the basis of equation 2.1 would require the following of the diffusion coefficient for nitrogen (Krishna & Wesselingh 1997):

1. $D_{N_2} \rightarrow \infty$ at the initial osmotic diffusion point
2. $D_{N_2} < 0$ where reverse diffusion occurs ($t < t_1$), and
3. $D_{N_2} = 0$ at the diffusion barrier ($t = t_1$)

The phenomena described above can however be explained using the Maxwell-Stefan approach, with fluxes described by a generalized (multicomponent) version of Fick's law

$$(\mathbf{J}) = -c[\mathbf{D}](\nabla \mathbf{x})$$

(see equation 2.15) the basis for which is given section A.3 below. In this case $[\mathbf{D}]$ is a matrix of diffusion coefficients; for the ternary system of Duncan & Toor (1962), the generalized form expands to

$$\begin{pmatrix} J_1 \\ J_2 \end{pmatrix} = -c \begin{pmatrix} D_{11} & D_{12} \\ D_{21} & D_{22} \end{pmatrix} \begin{pmatrix} \nabla x_1 \\ \nabla x_2 \end{pmatrix}$$

where $J_3 = -(J_1 + J_2)$ by conservation of mass (i.e. the diffusive fluxes are not all independent). The diagonal terms D_{11} and D_{22} represent conventional Fick-like diffusion; the off-diagonal terms D_{12} and D_{21} represent non-Fickian *interaction* terms where a concentration gradient of x_1 affects the diffusive flux J_2 , and a gradient of x_2 similarly affects the diffusive flux J_1 . The solid and dashe lines in figure 2.1b were obtained using an analytic solution to the two-bulb problem using the generalized Fick's law form (Taylor & Krishna 1993). The basis for the generalized form is detailed in section A.3. The generalized form is used in the development of the gas-phase limited evaporation maps in chapter 3, and in the treatment of diffusion effect in the liquid in chapter 7.

The review article by Wesselingh & Krishna (2000) discusses the shortcomings of the traditional Fickian description of mass transfer, and outlines the basis for the Maxwell-Stefan approach in more detail. The theory of multicomponent diffusion in fluids (gas,

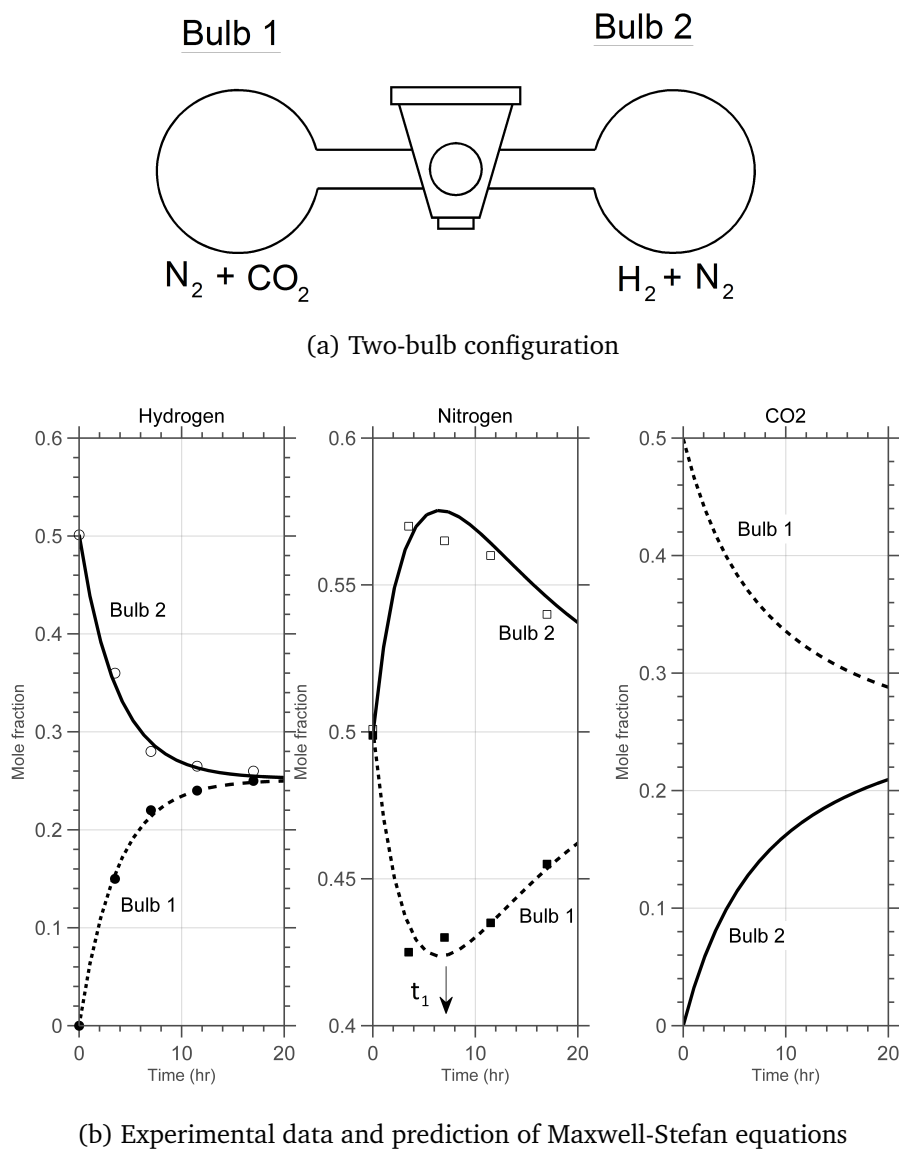


Figure 2.1: Experimental configuration of Duncan & Toor (1962)

liquid, electrolyte, polymer etc.) is described in the books by Taylor & Krishna (1993), Cussler (2009) and Bird et al. (2002). The texts of Hirschfelder et al. (1964) and Jakobsen (2008) give rather detailed treatments of the kinetic theory of gases including its extension to multicomponent gas mixtures. while the book by Lightfoot (1974) gives interesting applications of multicomponent mass transfer to biological systems.

2.1.2 Maxwell-Stefan Equations and Generalized Fick's Law

A derivation of the Maxwell-Stefan equations based on principles of irreversible thermodynamics is given in Appendix A.3. For ideal gas mixtures in the absence of pressure gradients and external forces, the Maxwell-Stefan equation of (see equation A.80) can

expressed in terms of molar fluxes N_i and J_i as

$$d_i = - \sum_{\substack{i=1 \\ i \neq j}}^n \frac{x_i N_i - x_j N_j}{c \mathfrak{D}_{ij}} = - \sum_{\substack{i=1 \\ i \neq j}}^n \frac{x_i J_i - x_j J_j}{c \mathfrak{D}_{ij}} \quad (2.2)$$

where N_i and N_i are the total and diffusive fluxes of component i respectively, c is the concentration, and \mathfrak{D}_{ij} are binary Maxwell-Stefan diffusion coefficients. This is the form of the Maxwell-Stefan equations that is used as a basis for the calculation of vapour phase molar fluxes in the generation of evaporation maps in chapter 3.

The generalized driving force equation A.72 has $n(n-1)/2$ transport parameters \mathfrak{D}_{ij} , since the diffusivities are symmetric so that $\mathfrak{D}_{ij} = \mathfrak{D}_{ji}$, and \mathfrak{D}_{ii} is not defined (Curtiss & Bird 1999). Where pressure and external forces can be ignored, the driving force given by equation A.72 reduces to

$$d_i \equiv \frac{x_i}{RT} \nabla_{T,P} \mu_i \quad (2.3)$$

The gradient of chemical potential can be expanded using the chain rule, noting that $\mu_i = \mu_i(T, P, x_j)$:

$$\nabla_{T,P} \mu_i = \sum_{j=1}^{n-1} \frac{\partial \mu_i}{\partial x_j} x_j \nabla x_j \quad (2.4)$$

The chemical potential μ_i can be expressed in terms of the activity of species i by

$$\mu_i = \mu_i^o + RT \ln a_i = \mu_i^o + RT \ln \gamma_i x_i$$

where μ_i^o is the chemical potential at a standard state, a_i is the activity of species i , and γ_i is the activity coefficient, so that equation 2.3 becomes (Taylor & Krishna 1993)

$$d_i \equiv \frac{x_i}{RT} \nabla_{T,P} \mu_i = \frac{x_i}{RT} \sum_{j=1}^{n-1} \frac{\partial \mu_i}{\partial x_j} x_j \nabla x_j \quad (2.5)$$

$$= \frac{x_i}{RT} \sum_{j=1}^{n-1} RT \frac{\partial \ln \gamma_i x_i}{\partial x_j} \bigg|_{T,P,\Sigma} \nabla x_j \quad (2.6)$$

$$= x_i \sum_{j=1}^{n-1} \left(\frac{\partial \ln x_i}{\partial x_j} + \frac{\partial \ln \gamma_i}{\partial x_j} \bigg|_{T,P,\Sigma} \right) \nabla x_j \quad (2.7)$$

$$= \sum_{j=1}^{n-1} \left(\delta_{ij} + \frac{\partial \ln \gamma_i}{\partial x_j} \bigg|_{T,P,\Sigma} \right) \nabla x_j \quad (2.8)$$

$$= \sum_{j=1}^{n-1} \Gamma_{ij} \nabla x_j \quad (2.9)$$

where

$$\Gamma_{ij} = \delta_{ij} + \frac{\partial \ln \gamma_i}{\partial x_j} \bigg|_{T,P,\Sigma} \quad (2.10)$$

In this way, equation 2.9 allows the driving force d_i to be expressed in terms of the more accessible mole-fraction gradients. The subscripts on the evaluation of the derivative in equation 2.10 imply that temperature and pressure are constant, while the differentiation of $\ln \gamma_i$ is carried out while keeping constant the mole fractions of each species apart from the n th. For liquids, the activity coefficient may be represented by a suitable model such as the NRTL or UNIQUAC models (Poling et al. 2001). See appendix B.1 for details of the NRTL model used in this work. The Maxwell-Stefan equations can be cast in a Fick-like form suitable for use in matrix calculations. Equation 2.2 can be written as

$$-c(\mathbf{d}) = [\mathbf{B}](\mathbf{J}) \quad (2.11)$$

where the column matrices \mathbf{d} and \mathbf{J} have elements

$$\mathbf{d} = \begin{pmatrix} d_1 \\ d_2 \\ \vdots \\ d_{n-1} \end{pmatrix} \quad \mathbf{J} = \begin{pmatrix} J_1 \\ J_2 \\ \vdots \\ J_{n-1} \end{pmatrix}$$

and where the $[\mathbf{B}]$ matrix has elements given by

$$B_{ii} = \frac{x_i}{\mathfrak{D}_{in}} + \sum_{\substack{k=1 \\ k \neq i}}^n \frac{x_k}{\mathfrak{D}_{ik}} \quad (2.12a)$$

$$B_{ij} = x_i \left(\frac{1}{\mathfrak{D}_{ij}} - \frac{1}{\mathfrak{D}_{in}} \right) \quad (2.12b)$$

Writing equation 2.9 in $n - 1$ dimensional matrix form gives

$$(\mathbf{d}) = [\Gamma](\nabla \mathbf{x}) \quad (2.13)$$

which, when combined with equation 2.11 gives an expression for the matrix of diffusive fluxes

$$(\mathbf{J}) = -c[\mathbf{B}]^{-1}[\Gamma](\nabla \mathbf{x}) \quad (2.14)$$

This can be written as a generalized Ficks' law:

$$(\mathbf{J}) = -c[\mathbf{D}](\nabla \mathbf{x}) \quad (2.15)$$

where

$$[\mathbf{D}] \equiv [\mathbf{B}]^{-1}[\Gamma] \quad (2.16)$$

where $[\mathbf{D}]$ is the Fick matrix, $[\mathbf{B}]$ has terms given by equation 2.12, and Γ has terms given by equation 2.10. Equation 2.16 shows how the Maxwell-Stefan approach allows the thermodynamic and "drag" effects of diffusion to be essentially decoupled.

Equations 2.15 with 2.16 are the form of the driving forces that are used in chapter 7 for diffusion in the liquid phase, using the NRTL model (see appendix B.2, following Poling et al. (2001)) to compute values of Γ_{ij} .

2.2 Residue Curve Maps

Many processes in the chemical industries rely on evaporation and condensation steps, the basis for which are that the vapour phase is richer in the more volatile compounds than the liquid. Mixtures with components that are nearly ideal are relatively straightforward to rank in order of volatility, or equivalently, in order of their normal boiling points (Kiva et al. 2003). A distillation sequence, for example, can then in principle be designed to separate each component. In industrial practice however, many mixtures display azeotropic behaviour, where the composition space is divided into regions where the order of volatility varies from region to region. At an *azeotrope*, the vapour and liquid compositions of a mixture are equal for a given pressure. Mixtures at azeotropic compositions cannot be separated by conventional distillation, as no enrichment of the vapour phase is possible at that composition; alternative means of separation such as *azeotropic-distillation* (where an additional component or *entrainer* is added to the mixture), or *pressure-swing* distillation are often used. To aid in the qualitative analysis of such mixtures, and the feasibility of their separation, a graphical tool known as the *residue curve map* is used. This thesis develops the Evaporation Map concept which applies to mixtures governed by rate-based processes (such as evaporation and drying), and therefore are not at equilibrium (except at a vapour-liquid interface); evaporation maps can therefore be considered as non-equilibrium analogues to residue curve maps. The background theory of residue curve maps is considered in the following sections.

2.2.1 Construction of Residue Curve maps

Residue curve maps (RCMs) are one of number of types of phase equilibrium diagram which represent the composition of liquid mixtures undergoing evaporation or condensation processes. The review article by Kiva et al. (2003) details the historical origins of azeotrope phase equilibrium diagrams, including residue curve maps. Schreinemakers (1901b,a) established the idea of *residue curves* relating the concentrations of vapour and liquid in an isobaric open evaporation process. In that conceptual process, the vapour formed is continuously removed (no reflux) so that the vapour at any instant is in equilibrium with the liquid residue (also known as *simple distillation*, or *Rayleigh distillation*). Tracing the change in residual liquid composition over time until the last drop is evaporated, and plotting composition on a Gibbs (ternary) diagram gives the

residue curve (Fien & Liu 1994, Doherty & Malone 2001). The edges of the RCM represent binary mixtures, while the vertices represent pure components.

In general, the vapour-liquid equilibrium of a homogeneous mixture at a specified pressure are characterized by relationships between the liquid and vapour compositions $\mathbf{x} = \{x_1, x_2, \dots, x_n\}$ and $\mathbf{y} = \{y_1, y_2, \dots, y_n\}$, together with a temperature representing the *bubble point* of liquid \mathbf{x} , and *dew point* of vapour \mathbf{y} (Rev 1992). The evolution of liquid molefraction in the mixture during evaporation can be determined by integrating a set of ordinary differential equations:

$$-\frac{d\mathbf{x}}{d\tau} = \mathbf{y}(\mathbf{x}) - \mathbf{x} \quad (2.17)$$

where τ is a dimensionless *warped time* that incorporates molar liquid holdup (Doherty & Malone 2001):

$$\tau = \ln \left(\frac{H}{H^o} \right) \quad (2.18)$$

where H^o and H are the initial molar hold-up, and molar hold-up at a subsequent time respectively. The liquid and vapour mole-fractions are subject to the condition that

$$\sum_{i=1}^n x_i = 1.0 \quad \sum_{i=1}^n y_i = 1.0 \quad (i = 1, 2 \dots n-1) \quad (2.19)$$

In practice, the residue curves can be found by integrating equation 2.17 forwards and/or backwards from a given initial composition in the warped time variable, using a vapour-liquid relationship between \mathbf{x} and \mathbf{y} . For mixtures that are relatively ideal in the liquid phase, a simple phase equilibrium relationship such as

$$y_i = Kx_i \quad i = 1, 2 \dots n \quad (2.20)$$

suffices, where K represents the so-called *K-value* or equilibrium ratio. Where there is non-ideality in the liquid phase, an expression involving an activity coefficient is generally more accurate:

$$y_i = \frac{x_i \gamma_i P_i}{P} \quad i = 1, 2 \dots n \quad (2.21)$$

p_i is the vapour pressure of component i , P is the total pressure, and where γ_i is the activity coefficient. A wide variety of activity coefficient models are available, including Wilson, NRTL, UNIQUAC and UNIFAC (Prausnitz et al. 1986). Non-ideality in the vapour phase can be incorporated in principle through use of a suitable vapour phase fugacity expression such as a Poynting correction factor (Poling et al. 2001). The total pressure P is a constant for a given residue curve map. Some mixtures exhibit strong sensitivity to operating pressure, a fact which is exploited in pressure-swing distillation processes.

In principle there is no limit to the number of components in the integration of equation

Table 2.1: Example ternary mixtures used in this work

Components				Azeotropes
1	IPA	Ethanol	Methanol	0
2	Water	Ethanol	Methanol	1
3	IPA	Water	Ethanol	2
4	Ethanol	MEK	Toluene	2
5	Dichloromethane	Methanol	Ethyl Acetate	2
6	Acetone	Chloroform	Methanol	4

2.17; however, for graphical presentation the practical limit is that of a ternary mixture. More complicated visualization techniques for higher-dimensional systems have only limited application (Wibowo & Ng 2002, Harjo et al. 2004). Other approaches such as lumping of components (Jaksland et al. 1995) or simplification of the boundary geometry (Rooks et al. 1998) have also been developed, but apply in rather specific conditions (Bruggemann & Marquardt 2011).

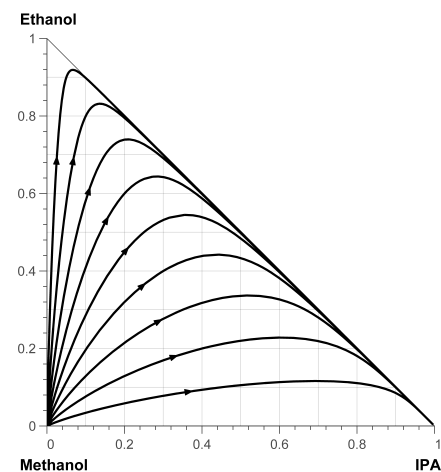
A number of residue curve maps for examples of homogeneous¹ ternary azeotropic and non-azeotropic mixtures are shown in figure 2.2. The mixtures are listed in table 2.1, and represent commonly used solvents in industrial practice. The degree of non-ideality increases as one moves down the table, indicated by the increasing number of azeotropes (binary and ternary). Taken as a group, these mixtures therefore represent the key features of non-ideality (azeotropic behaviour) present in a ternary mixture; the same group of mixtures will be used in the development and analysis of evaporation maps in subsequent chapters, where the similarities to residue curve maps will also be highlighted.

The residue curve maps in figure 2.2 were obtained by numerical integration of equation 2.17 together with equation 2.21 with NRTL parameters obtained from AspenProperties (AspenTech 2014); details of the NRTL model and binary interaction parameters are shown in appendix B.1. Figure 2.2a shows a non-azeotropic mixture where the residue curves run from the methanol unstable node to the IPA stable node, passing the pure ethanol node. The water-ethanol-methanol mixture in figure 2.2b has a single binary azeotrope (a *saddle* azeotrope) on the water-ethanol axis. Figures 2.2c, 2.2d and 2.2e each have two binary azeotropes, one being an unstable node, the other a saddle. The acetone-chloroform-methanol mixture (figure 2.2f) shows the most complex behaviour, with 3 binary azeotropes (one stable, two unstable) and a ternary saddle azeotrope.

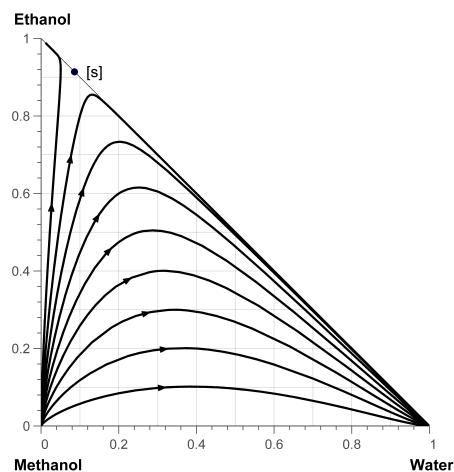
RCMs are used extensively in the qualitative analysis of equilibrium separation processes for ternary mixtures as they provide an intuitive graphical means of visualizing separation possibilities, and the constraints imposed by binary or ternary azeotropes (Villiers et al. 2002). The dynamics of simple distillation processes have been exten-

¹Containing only a single liquid phase

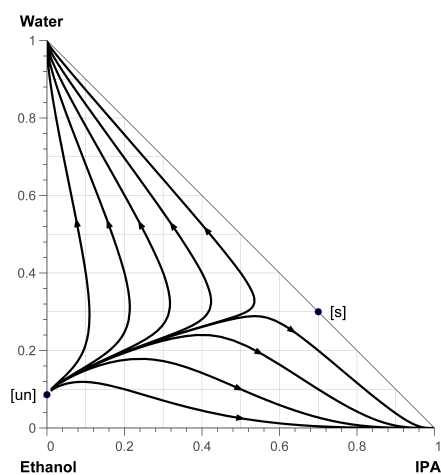
2. BACKGROUND AND LITERATURE REVIEW



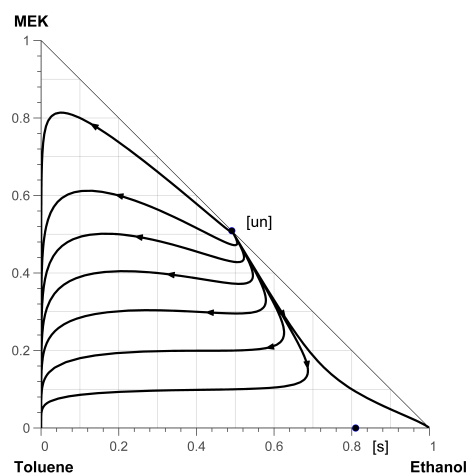
(a) IPA-ethanol-methanol



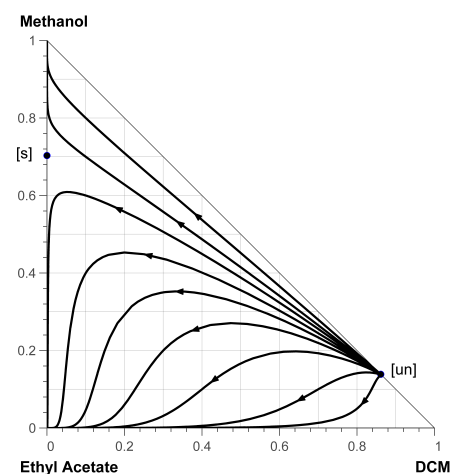
(b) Water-ethanol-methanol



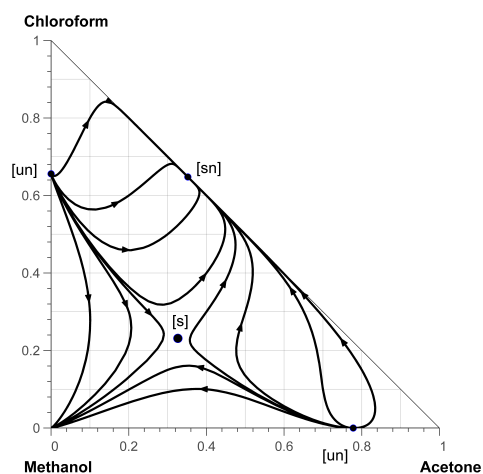
(c) IPA-water-ethanol



(d) Ethanol-MEK-toluene



(e) DCM-methanol-ethyl acetate



(f) Acetone-chloroform-methanol

Figure 2.2: Residue curve maps for ternary mixtures; solid circles denote azeotropes; arrows show increasing temperature; [s] = saddle; [sn] = stable node; [un] = unstable node

sively studied (Doherty & Perkins 1978a,b), and have been applied in the design and analysis of packed and staged distillation columns, where residue curves approximate the composition profiles of packed distillation columns at infinite reflux (van Dongen & Doherty 1985). Wahnschafft et al. (1992) extended the application of RCMs to columns at finite reflux. They developed a *pinch-point* curve for a column, consisting of the locus of points on residue curves at which the tangent passes through a product composition. A similar approach was used by Fidkowski et al. (1993b) who use the term *distillation limit* to refer to the pinch-point curve.

Residue curve maps also have been constructed for heterogeneous mixtures by Matsuyama (1978) and Pham & Doherty (1990a), who demonstrated that equation 2.17 applies also to heterogenous systems. In that case, the liquid mole fractions are replaced by the overall liquid mole-fractions x_i^o , and additional equilibrium expressions between the liquid phases also apply:

$$x_i^o = \alpha x_i^I + (1 - \alpha)x_i^{II} \quad i = 1, 2 \dots n \quad (2.22)$$

$$x_i^{II} = K^{LL} x_i^I \quad i = 1, 2 \dots n \quad (2.23)$$

$$\sum_{i=1}^n x_i^I = 1.0 \quad \sum_{i=1}^n x_i^{II} = 1.0 \quad (2.24)$$

where α is the fraction of liquid phase I in the total liquid, and K^{LL} is an equilibrium ratio between liquid phases. The superscripts I and II denote the two liquid phases. A further restriction applies to heterogenous azeotropes in that they cannot be stable nodes i.e. they cannot be maximum-boiling. Also, the compositions of the two liquid phases (at either end of a liquid-liquid tie-line) lie in different distillation regions; this feature is used in the operation of azeotropic distillation systems for separation of ethanol and water using a cyclohexane entrainer, where the presence of cyclohexane induces a phase split in the column decanter (Doherty & Malone 2001).

Studies of the use of residue curve maps in the design and optimization of distillation columns and separation sequences include those of Ryan & Doherty (1989) and Pham & Doherty (1990a,b). The details of the topology of a residue curve map allows development of flow-sheets for proposed separations, including the placement of recycle streams (Bruggemann & Marquardt 2011). Stichlmair & Herguieula (1992) consider standardized column configurations for some prototypical RCM topologies, and show application to several industrial mixtures. Doherty & Perkins (1978a,b, 1979) presented a thorough study of the topology of residue curve maps, including methods for checking the topological consistency. Refer also to Doherty & Cardorola (1985), Foucher et al. (1991), Laroche et al. (1992) and Wahnschafft et al. (1992) for further discussion of the features of residue curve maps. The residue curves described above find application in the design of continuous (packed) distillation columns. An analogous development for staged (trayed) distillation columns is that of *distillation lines*.

These are essentially iterated maps of the vapour-liquid relationship, repeated over the number of theoretical stages of a trayed column (Castillo & Towler 1998). The article by Widagdo & Seider (1996) reviews developments in residue curve maps as applied to azeotropic distillation processes. The textbooks by Stichlmair & Fair (1998) and Doherty & Malone (2001) (and the references therein) offer detailed examples of the use of topological information from residue curve maps in the design of distillation sequences.

The RCM defining equation (2.17) represents a dynamical system, the *fixed points* (or *singular points* or *stationary points*) of which are the pure components and azeotropes of the residue curve map (Fien & Liu 1994). Thus, the right-hand side of equation 2.17 equals zero at pure components and azeotropes only, and the system has no other fixed points. Also, using the stability theory of non-linear ordinary differential equations, the signs of the eigenvalues of equation 2.17 in the vicinity of the fixed points dictate the type of the fixed points (Varma & Morbidelli 1997). Recalling that the mixture is at its bubble point throughout, the temperature derivatives in the vicinity of the fixed point can also be used to infer the signs of the eigen-values; if $\partial T / \partial x_i$ is negative (positive), the liquid bubble point decreases (increases) as we progress in the eigen-direction away from the fixed point (Kiva et al. 2003). Note that for a ternary mixture, equation 2.17 has two eigenvalues at each fixed point. Three types of fixed points can be distinguished (Blagov & Hasse 2002):

- If all eigenvalues are negative, the fixed point is a stable node [sn], so that temperature decreases in all directions
- Conversely, if all eigenvalues are positive, the fixed point is an unstable node [un], so that temperature increases in all directions
- If eigenvalues have different signs, the fixed point is a saddle [s], so that temperature increases in some directions, and decreases in others

Note that residue curves also lie along the edges of the ternary composition space. In addition, two features of residue curves are relevant:

- Residue curves cannot intersect
- Residue curves always move along the bubble point surface in the direction of increasing temperature

Thus, the behaviour of the residue curves in the neighbourhood of a fixed point therefore depends on the shape of the bubble point surface near the point. The stable and unstable nodes are known in a mathematical setting as *attractor* and *repellor* respectively.

2.2.2 Computation of Azeotropes

Locating *all* the azeotropes of a given mixture is a fundamental but surprisingly difficult step (Fidkowski et al. 1993a). One approach is to simply plot residue curve maps as in figure 2.2. The existence of an azeotrope can be implied from the flow of the residue curves such as figure 2.2d where existence of an ethanol-MEK minimum-boiling azeotrope is implied from the fact that residue curves move away from it, towards either the pure ethanol or pure toluene nodes. Similarly, the existence of a maximum-boiling acetone-chloroform azeotrope is implied in figure 2.2f by the fact that residue curves track towards it.

The definition of the condition for an azeotrope to exist is given by:

$$f(\mathbf{x}) \equiv \mathbf{y}^*(\mathbf{x}) - \mathbf{x} = \mathbf{0} \quad (2.25)$$

where $\mathbf{y}^*(\mathbf{x})$ represents the vapour molefraction in thermodynamic equilibrium with liquid molefraction \mathbf{x} . The vector notation in equation 2.25 implies that the azeotrope condition applies to each component. An accurate phase equilibrium model is required to allow the azeotropes to be computed. This becomes more difficult for heterogeneous systems where both vapour-liquid and liquid-liquid equilibria are involved as it is difficult to find a model capable of representing both types of equilibria accurately (Gmehling et al. 2012). Fidkowski et al. (1993a) developed a homotopy-based method that efficiently locates all of the azeotropic compositions of a mixture. Tolsma & Barton (2000a) extended this approach to include heterogeneous mixtures. Alsam & Sunol (2006) further extended the homotopy approach to include non-ideal behaviour in both liquid and vapour, and analysed sensitivity of azeotropic composition to parameters of the NRTL activity coefficient model. A Newton method-based homotopy approach for calculation of azeotropes, using analytic form of Jacobian is presented in chapter 4. A method for computation of *pseudo-azeotropes* is also discussed in chapters 3 and 4.

2.2.3 Residue Curve Maps under non-equilibrium conditions

Implicit in the definition of residue curves in equations 2.17-2.21 is that thermodynamic equilibrium is assumed to apply to the vapour-liquid mixture. This reflects the common practice of assuming that vapour and liquid phases are in equilibrium when designing distillation and related processes, combined with a *tray efficiency* for trays, or a *Height Equivalent to a Theoretical Plate* (HETP) for packing. However, real separation processes normally operate at conditions *other than equilibrium*, so that the separation achieved depends on the rate of mass transfer between phases (Taylor & Krishna 1993), or the degree to which phases are *not* at equilibrium. *Non-equilibrium* or *rate-based* models have been developed in recent decades that employ correlations of heat and

mass-transfer coefficients to describe mass transfer processes in specific apparatus such as distillation packings and trays (Taylor et al. 2003). Of course, the conventional residue curve analysis does not apply when the assumption of equilibrium between phases does not hold. To address this a number of workers have developed approaches to account for non-equilibrium effects, while maintaining the general framework of residue curves. Taylor et al. (2004) developed the notion of a *Composition Trajectory Map* (CTM) that includes multicomponent mass transfer effects (via Maxwell-Stefan equations) for both packed and trayed columns at total reflux. Using vapour-phase component mass balances expressed in a matrix form (see section 12.3.1 and 13.3.1 of Taylor & Krishna (1993)), they expressed the differential liquid composition changes over a dimensionless height in terms of the matrix of overall number of transfer units for mass transfer, for both packed and trayed distillation columns. By integrating the differential composition over the dimensionless height, individual composition trajectories and the overall CTM for a given mixture can be computed. A unified model was presented that accounted for both trays and packing, as well as for residue curves in the limiting case that the binary mass transfer coefficients are all equal (equal facility for mass transfer), and assuming no resistance to mass transfer in the liquid phase. The vapour and liquid remain at their dew and bubble points respectively with this approach; the impact of mass transfer resistance due to non-condensibles (which would alter the vapour-liquid interface temperature) is not included. Latent heats for the various components are assumed to be equal, implying constant molar flows in the column. Sensible heating contributions to the energy balance are also excluded. A key feature of the model of Taylor et al. (2004) is that the fixed points of the CTM are the same as those of the corresponding RCM i.e. pure components and azeotropes; however the boundaries computed using the non-equilibrium CTM approach are not in general the same as those of an RCM. Experimental verification of non-equilibrium trajectories in distillation has been provided by a number of workers (Springer, Baur & Krishna 2002, Springer, Buttinger, Baur & Krishna 2002, Springer et al. 2003).

Baur et al. (2005) studied mass transfer effects in column design, showing that while pinch-point curves and pitchfork distillation boundaries in RCMs are unchanged by mass transfer effects, composition trajectories may cross the pinch-point curves. Further, minimum reflux is affected for less than very sharp separations. Baur et al. (2005) recommended that mass transfer effects be accounted for when trace components are a concern in a distillation process.

The model of Taylor et al. (2004) described above distinguishes specifically between RCMs (where phase equilibrium applies) and CTMs (where phase equilibrium does not apply). Conversely, a number of workers have attempted to include non-equilibrium mass transfer effects directly into the calculation of RCMs themselves. Sidhar et al. (2002) used a form of the component material balance for the vapour phase that is inconsistent in that it implies all $\Delta y_i = 0$ when the binary mass transfer coefficients

are equal (an unlikely but not infeasible situation), which implies that the total molar flux, and the individual molar fluxes are zero in that situation (Taylor et al. 2004). The model of Sidhar et al. (2002) also implies that $\sum N_i \Delta H_i^V = 0$, which implies that the molar fluxes have mixed signs, given that the heats of vapourization are all of the same sign. This would imply that some components would be condensing while some are evaporating; what is unclear is from where the components would condense, since the basis assumption of residue curve analysis is that the liquid which evaporates is immediately removed (Doherty & Malone 2001). Consequently, as outlined in the critique by Taylor et al. (2004), the model proposed by Sidhar et al. (2002) is fundamentally flawed.

Silva et al. (2003) presented a model which gives the molar flux in the vapour film in terms of a difference in partial pressures at the vapour-liquid interface and in the bulk vapour. The partial pressures were expressed in terms of vapour molefractions at interface and in bulk, and the total pressures at interface and bulk, resulting in a single parameter for each component that encapsulates the mass transfer rate. In this model the interface partial pressure is computed from a conventional bubble-point calculation; the partial pressure is determined from an expression involving mass transfer coefficients and total pressures at interface and in bulk. However, having a different total pressures at vapour-liquid interface and in bulk is not a realistic situation except in cases where bulk flow of material occurs; this is not applicable to cases involving mass transfer due to diffusion only. This model was also used by Teixeira et al. (2009), in an analysis of boundaries in non-equilibrium batch distillation, who justified the use of different pressures by stating that the vapour removal rate in an residue curve map analysis occurs at infinite velocity, thereby requiring a very high pressure drop across the film at the vapour-liquid interface. However, standard practice in mass transfer models (and in this thesis) is to assume that pressure is constant in the film adjacent to the phase boundary (Taylor et al. 2004). Further, the procedure of Silva et al. (2003) requires numerical values for mass transfer coefficients for all n species, when in fact only $n - 1$ mass transfer rate expressions can be used in a consistent mass transfer model, since the fluxes must sum to zero (Taylor & Krishna 1993). Given these shortcomings, the example calculations for ternary mixtures presented by Silva et al. (2003) and Teixeira et al. (2009) and are therefore likely to be inaccurate.

Castillo & Towler (1998) developed non-equilibrium versions of both residue curves and distillation lines, by employing a Murphree type efficiency to describe the modified equilibrium between liquid and vapour on a distillation tray, using the following expression:

$$y_i = \left(1 + E_i^{MV} K_i - E_i^{MV}\right) x_i$$

where $K_i = y_i/x_i$, and E_i^{MV} is the Murphree efficiency for component i . While this approach is perfectly valid for distillation lines (which apply to staged separations),

it is not appropriate for the open evaporation process upon which residue curves are based (Taylor et al. 2004). The Murphree efficiency was developed for continuous staged distillation processes, not the unsteady evaporation process which is the basis for residue curves. Consequently, in the context of residue curves, the use of a Murphree efficiency can be considered as a kind of non-equilibrium parameter, rather than a true efficiency relationship.

Residue curve maps have also been applied to reactive distillation systems (Barbosa & Doherty 1988, Doherty & Malone 2001, Huang et al. 2004). It is known that reactions in the liquid phase can lead to both the appearance and disappearance of azeotropes, and that reactive azeotropes may exist in mixtures that are otherwise thermodynamically ideal (Taylor et al. 2006). Residue curve maps have been extended to consider melt crystallisation by replacing vapour-liquid equilibria with solid-liquid equilibria (Slaughter & Doherty 1995). The analysis of membrane and hybrid membrane-distillation systems is another area where residue curve maps have been applied (Aiouache & Goto 2003, Peters et al. 2008, 2011).

The analogy between residue curve maps and the evaporation maps of this work is developed in chapter 3. The bubble point temperature of the residue curve maps described above is analogous to the mixture wet-bulb temperature in the case of evaporation maps.

2.3 Evaporation and Drying of Multicomponent Mixtures

The drying of mixtures containing multicomponent solvents has numerous industrial applications including manufacture of pharmaceuticals, juice concentrates, coated laminates, magnetic storage media, and removal of solvent from varnish layers. In this work drying is distinguished from evaporation in that the drying application leaves behind a solid component. Evaporation of multicomponent liquids occurs in fuel combustion applications. In the following sections, relevant research is reviewed firstly in the area of evaporation, and secondly for drying involving multicomponent mixtures. The development of evaporation maps in chapter 3 uses an assumption of gas-phase limited heat and mass transfer; consequently, section 2.3.1 is relevant to studies of evaporation of liquid mixtures in that regime. This assumption is relaxed in the model developed in chapter 7 where diffusion effects are considered. The initial drying phase of wetted solids can behave as though gas-phase limited; consequently, section 2.3.2 focuses on studies of multi-component drying that examine transitions between gas-phase limited, and diffusion-limited processes. The literature on solids drying is not the focus of this work; rather, the emphasis in section 2.3.2 is on studies of multicomponent drying that examine conditions where the gas-phase limited assumption applies (in which case the evaporation maps of chapter 3 would apply to solids drying), and where that

assumption does not apply.

2.3.1 Evaporation of Multicomponent Liquids

Studies of evaporation of multicomponent mixtures have been conducted for various geometries including films and droplets. For clarity of presentation, previous work published is grouped into the type of application involved in the papers reviewed. In chapter 3 a single multicomponent mass transfer model is developed that may be applied to different geometries by use of appropriate forms for heat and mass transfer coefficients; consequently, the model of chapter 3 is general in nature, and not limited to a specific geometry.

Evaporation of mixtures from planar surface: In gas-phase limited drying, the drying rate is controlled by external conditions only; this is often the case in low-intensity drying (Luna & Martinez 1998), so that the gas-phase controlled approach may be applied there also. Martinez & Setterwall (1991) studied isothermal, convective drying of a number of non-ideal mixtures under conditions of gas-phase-limited heat and mass transfer. Evaporation fluxes were calculated using a generalized Fick's law and the linearized theory of Toor (1964) and Stewart & Prober (1954). An evaporation process may be considered gas-phase controlled if the resistance to mass transfer lies in the gas phase only. Experiments included a Teflon-substrate wetted with ethanol-MEK-water (see also chapter 3 for comparison of their data with model produced in this work). Calculations by Martinez & Setterwall showed that liquid composition, liquid temperature, gas composition and diffusional interactions had a significant impact on selectivity, while the effect of gas temperature and flow-rate was less significant. They also concluded that any desired selectivity may be achieved by appropriate manipulation of the gas composition (gas pre-loading). Martinez & Setterwall also analyzed data of Riede & Schlunder (1988) who examined evaporation of IPA(isopropyl-alcohol)/water mixtures and found that IPA selectivity was enhanced by higher humidity (water content) in the gase phase; they (Martinez & Setterwall) showed by calculation that the higher IPA selectivity was likely to be due to a negative cross-coefficient in the generalized Fick matrix, which is an insightful example of multicomponent mass transfer effects.

Riede & Schlunder (1988, 1990) studied the selectivity of a simple evaporation process containing a ternary mixture of IPA (isopropyl alcohol)-water-glycerol, where the glycerol is effectively a non-volatile component. A theoretical analysis of the problem suggested that the selectivity of the evaporation depended on three mechanisms: vapour-liquid equilibrium, mass transfer in the gas-phase, and mass-transfer in the liquid phase. The selectivity was also affected by air flow rate and composition, and by the temperature of the liquid. Experiments indicated that the selectivity could be adjusted

in any direction by an appropriate selection of evaporation conditions, in particular the humidity (water content) of the air stream. They found for example that by increasing the humidity, the selectivity was shifted to a preferential evaporation of IPA.

The evaporation of binary and ternary liquid mixtures containing azeotropes was examined by Pakowski (1992). For binary mixtures, selectivity curves for evaporation under different conditions of gas pre-loading were developed; these were obtained by solving a condition for existence of a pseudo-azeotrope (or dynamic azeotrope or *arheotrope* (Sundmacher et al. 2005)) under gas-phase limited conditions. For a number of ternary mixtures, a multicomponent mass-transfer model was used to generate concentration paths on ternary diagrams; these paths do not cover the entire composition space (a topic covered in detail in chapter 3). Pakowski identified the problem of finding the particular composition that yields a specific terminal composition in the liquid as a complex matter; in chapter 4 of this work, a bifurcation analysis is used to identify just these gas compositions (for case of pre-loading with a single gas).

Pakowski (1992) also suggested that minima in the normalised total flux, or in the entropy generation rate could be used to identify stable pseudo-azeotropes, and that minima of each correspond to *separatrices* on the composition ternary map. Location of minima in evaporation maps is the subject of chapter 6 of this thesis.

The evaporation of ternary mixtures in batch and continuous modes has been investigated by Luna & Martinez (1998, 1999). Using a gas-phase limited model for evaporation of multicomponent liquid films, they analysed the governing system of ordinary differential equations to determine their mathematical stability in terms of the eigenvalues of the Jacobian matrices evaluated at the fixed points of the mixture (pure components and pseudo-azeotropes). They demonstrated bifurcations in the batch mode as the concentration of the gas phase with one of the ternary components increased (a topic which is expanded upon in chapter 4 of this work). They found that binary pseudo-azeotropes are stable when the combination of selectivities of the binary components is negative, and that ternary pseudo-azeotropes were either unstable or saddle points. For the continuous case, fixed points represent dynamic equilibria dependent on the inlet gas/liquid ratio; as the ratio approaches infinity, the behaviour approached that of a batch process.

Evaporation of polymer/solvent films: The drying of polymeric films has been an active area of research; many lacquer, paint and varnish coatings are obtained by a process of solvent evaporation from an initially dilute solution (Vrentas & Vrentas 1994). These films are often considered as either binary mixtures of solvent and polymer, or ternary mixtures consisting of solvent, non-solvent and polymer components. Choice of a particular mixture is based on various goals including the solubilization of one or more polymeric components, control of the rate of drying and development of desired

surface tension versus relative volatility required for defect minimization (Dabral et al. 2002).

Guerrier et al. (1998) studied the drying kinetics of polymer films cast from a polymer-solvent solution, including diffusion of solvent through the varnish layer, moving interface, and coupled heat and mass transfer between the interface and the drying air. Drying operations of this type are characterised by two regimes: a "fast" regime where evaporation flux from the surface is similar to that of the evaporation of pure solvent, followed by a "slow" regime where both diffusion with the film and evaporation rate decline significantly.

Dabral et al. (2002) considered the composition paths of ternary polymer solutions. An isothermal model was used, in which a solvent and non-solvent evaporated from the surface, but the polymer component was non-evaporating. The phase separation of solvent/polymer solutions (or "blush") was explained in terms of the drying process-paths and the two-phase immiscible region. Non-Fickian transport occurs during the drying of some polymers which can develop stress during drying and have high shear modulus; non-Fickian drying was analyzed by Vinjamur & Cairncross (2002, 2003) who developed a model to include solvent transport due to stress gradients. Numerical modeling of non-isothermal drying of film coatings has been carried out by Arya (2013) and Arya & Bhargava (2015) using a finite-element method. The model developed in chapter 7 of this work employs a finite volume technique to solve a related system of equations.

Luna et al. (2005) and Gamero et al. (2006) developed an analytic solution to the problem of isothermal drying of a liquid film assuming constant physical properties; variation in liquid diffusion coefficients along the process path was accounted for by a piecewise application of the solution using averaged coefficients from preceding time steps.

Evaporation of droplet mixtures: There have been numerous studies on evaporation of droplets, both droplets of pure liquid, and of multicomponent mixtures. Marchese & Dryer (1996) studied the effect of liquid mass transport on the combustion and extinction of bicomponent droplets of methanol and water. Abramson & Sirignano (1989) developed an extended film theory of heat and mass transfer for droplets that is widely used in other studies of droplet vapourisation. This model includes effect of variable thermophysical properties, the effect of Stefan flow on heat and mass transfer between droplet and gas, and the effect of droplet internal circulation and transient liquid heating; a simplified effective thermal conductivity is used to account for transient heating of the droplet, as an alternative to the classical *Hill's vortex* model (Clift et al. 1978). Daif et al. (1998) conducted an experimental study of multicomponent fuel vaporisation for heptane-decane mixtures and modelled the vaporisation rate suc-

cessfully using the model of Abramson & Sirignano (1989) for both natural and forced convection. In that work, the droplets were suspended on filaments in the flowing gas stream. In contrast, Maqua et al. (2008) used a laser-induced fluorescence technique to measure internal temperatures of evaporating binary droplets (acetone/ethanol) in falling droplets at high gas temperature. Bader et al. (2013) investigated ideal and non-ideal behaviour of ethanol/iso-octane droplets via a parametric study over a range of ambient pressures and temperatures. They employed binary and ternary diagrams to analyse the transient droplet behaviour and used a separation factor as a quantitative means to measure the effective relative volatility of each component.

Other work on droplets includes that of Pakowski (1990, 1992, 1994) who studied evaporation of droplets of binary (IPA/water, methanol/water) and ternary (ethanol/chloroform/hexane, acetone/chloroform/methanol) mixtures using a Maxwell-Stefan model, and plotted computed droplet composition profiles on a ternary diagram. In that work, droplets were suspended on a glass fibre and exposed to a gas flow of known velocity, temperature and humidity. A lumped model was used to model the evaporation process (ignoring diffusion effects within the liquid). Pakowski (1990) found that by modification of the concentration of the drying air, the location of stable pseudo-azeotropes could be affected. This work in particular has motivated the calculation and presentation of composition profiles on ternary diagrams that is the focus of chapter 3 of this thesis.

The vapourisation of fuels during combustion processes is an example of a common application of multicomponent evaporation. Typically the liquid fuel is sprayed under pressure into a combustion chamber. The rate of vapourisation is critical as the vapourisation is generally the rate-determining step in the overall burning rate (Sirignano 2010). The overall combustion process involves heat- and mass-transport as well as fluid-dynamics (within an engine cylinder for example) and chemical kinetics (describing the combustion reaction). Turbulence in the vapour-phase, as described by the Reynolds number is an important indicator of the flow-regime; this is in turn based on droplet diameter, droplet-gas relative velocity and gas phase properties such as viscosity and density. In addition to the vapour-phase, there may be internal circulation within the droplet itself driven by shear forces at the interface (Sirignano 2010).

Extensive effort has been invested in the development of computational fluid dynamics (CFD) codes for the simulation of fuel droplet heating, vapourisation and combustion in internal combustion engines. In addition to the solution of the momentum (Navier-Stokes) equations during combustion cycles, a model of droplet vapourisation is required. Simplified models for radiative heating are generally employed. For combustion of real (multicomponent) fuels, Sazhin (2006) concludes that the distillation curve model is a reasonable compromise between accuracy and CPU efficiency. Commercial codes (FLUENT, VECTIS, STAR-CD, PHOENICS) and public domain (KIVA) codes are

available for modelling or droplet vapourisation and combustion. Sazhin (2006) provides a comprehensive review of advanced models of fuel droplet heating evaporation and combustion characteristics.

Real fuels contain a large number of hydrocarbon components, so that models based on distillation curves or pseudo-components are often used. Burger et al. (2003) modeled fuel droplet evaporation using physical properties derived from a ASTM D-86 distillation curve model of the fuel.

Kneer et al. (1993) studied the effect of variable liquid properties on diffusion-controlled evaporation of multicomponent droplet. Bader et al. (2013) performed a parametric study of the influence of non-ideal VLE on the evaporation of droplets containing a range of ethanol/iso-octane mixtures, using a lumped model for the droplet and adopting the approach of Abramson & Sirignano (1989) for evaporation rate. Randolph et al. (1986) examined the importance of liquid phase diffusional resistance in multicomponent droplet gasification using theory and falling-drop experiments. They found the gasification mechanism to be intermediate to those of a batch distillation (i.e. a residue-curve) and a liquid-phase diffusion limited steady state. Kim et al. (1990) studied the gasification of non-azeotropic and azeotropic (1-propanol/tetrachloroethene) droplets finding that the "gasification azeotropic" composition was different from the azeotropic point and was determined by the specific combustion parameters (similar to a pseudo-azeotrope). By adding a third component (n-hexadecane) they also found that the azeotropic character could be broken (similar to an extractive distillation process). The books by Sirignano (2010) and Kuo (2005) discuss the fluid dynamics of droplets for combustion processes in detail.

Evaporation of solvent spills: The evaporation characteristics of pools of multicomponent liquid are also relevant for models of the combustion of fuel spills. Accurate predictions of the amount of vapour released and estimates of vapour concentration resulting from spills are also important for hazardous-area rating of industrial plant (Lee 2002). Okamoto et al. (2010) measured evaporation rates by loss-in-weight from pools of a number of hydrocarbons (n-pentane, n-hexane, n-heptane, toluene, p-xylene) under stagnant conditions. Results were compared against a simple model incorporating vapour pressure and activity coefficients for the fuels. The same workers also developed a model to predicted flash-point of the mixtures during evaporation.

2.3.2 Drying of Solids Containing Multicomponent Liquids

The drying of materials wetted with water has been the subject of innumerable theoretical and experimental studies which have yielded qualitative understanding of the mechanisms involved. The development of mathematical predictive models is compli-

cated by the hysteretic and difficult-to-quantify transport phenomena in porous materials (Keey 1972). Thus, in spite of the extensive work on the topic, it is not generally possible to reliably predict drying curves for all but the most simple applications (Pakowski & Mujumdar 2006). Many industrial processes involve drying of products which contain not only water, but also solvents or other volatiles; drying of foodstuffs and pharmaceutical products are but two examples. In many cases the quality of a product can be altered by the drying conditions; in particular, drying conditions may dictate that the *selectivity* of a volatile component is affected, so that a component may be removed preferentially to a greater or lesser extent. For aroma-retention in foodstuffs, steep drying conditions may lead to greater retention of aromatics, even though they may be more volatile (have higher vapour pressure) than other components present. This effect is due to selective diffusive effect in the liquid which retards the diffusion of the aromatic compounds (Coumans et al. 1993). By contrast, the drying of pharmaceutical compounds may target the removal of toxic organic solvents while retaining moisture to aid subsequent tableting steps. Paudel et al. (2013) considered effects of solvent type and concentration on the formation of amorphous solid suspensions of API (active pharmaceutical ingredients) for spray-drying. For API formulations, the selection criteria selection for a suitable solvent mixture include:

- high solubility of the API and other additives
- generation of a solution with acceptably low viscosity
- low toxicity; see also ICH guidelines on residual solvent (ICH 2011)
- high volatility for ease of evaporation during drying
- non-combustibility (e.g. in a spray-drying environment) (Miller 2012)

The drying of solids wetted with multicomponent mixtures has characteristics that are common to those of conventional single-component drying. At high moisture content, a period of constant-rate drying occurs (*constant rate period*); the temperature is also constant during this period. The porous solid reaches the wet-bulb temperature of the mixture during this time. In this period, mass transport from within the solid to the surface is equivalent to evaporation rate of a free-liquid surface of the same geometry and drying conditions (Steinbeck 1999), so that capillaries transport as much material to the surface as can be evaporated. If material cannot be transported to the surface at a sufficient rate, the wet core in the porous material shrinks and the drying rate declines; this is the *falling rate period*.

While the research into drying of water-wet materials is extensive, the work done on drying of solvent-laden (solvents other than water) is less complete. Thijssen & Rulkens (1968) and Thijssen (1971) studied aroma retention during the drying of foodstuffs, by spray-drying solutions of water, ethanol and sugar. As the drying progressed the sugar formed a membrane-like coating on the droplet surface. The smaller, less volatile water molecules were apparently able to diffuse more rapidly through the coating than the

larger, more volatile ethanol species; put another way, the water had a higher effective diffusion coefficient in the coating than the ethanol, and the process was consequently selective in favour of water.

Thurner & Schlunder (1986) and Heimann et al. (1986) studied the evaporation of binary IPA-water mixtures from both a free-surface, and from porous materials wetted with IPA-water. At low drying rates they found the selectivity to be governed by the relative volatility of the components in the mixture. At high drying rates they found drying to be non-selective due to diffusion effects in the liquid side (mass transfer resistance). Non-selective drying also occurred when a pseudo-azeotrope formed in the liquid; in that situation, the less volatile compound can be preferentially removed provided the solvent/water composition is above the pseudo-azeotrope, a situation analogous with conventional azeotropes in distillation processes.

Schwarzbach & Schlunder (1993) studied evaporation of IPA-water mixture through sintered materials of various porosity floating on the liquid surface. At concentrations above the azeotropic composition they found non-selective evaporation at all pore sizes tested. Below the azeotrope point however, they found selective behaviour that reduced in effect as the pore size reduced. They attributed this phenomenon to differences in the bulk density and surface tension leading to both Bénard and Marangoni convection, and a very large enhancement of mass transfer through the plate which was no-longer diffusion-controlled.

Schwarzbach (1986) and Schwarzbach & Schlunder (1993) examined porous particles wetted with a binary mixture and dried in a fluidized bed. They found that there was a transition from an initial state of equilibrium to a phase of diffusion-controlled mass transfer during the drying process. With increasing particle Biot number (ratio of external to internal mass-transfer resistance) the transition to a diffusion-controlled regime occurred earlier in the process. For small Biot numbers the drying remained in an equilibrium-controlled state throughout. The models of Schwarzbach (1986) and Schwarzbach & Schlunder (1993) employ a modified version of the shrinking-core approach for drying of spherical particles wetted with one component (i.e. water); the solid particle is divided into a partially saturated core and a dry outer shell, and a sharp evaporation front is assumed. An effective diffusivity was employed to account for the combined effects of gas and liquid diffusion. The model was successfully used to describe fluidized bed drying of alumina particles wetted with an IPA-water mixture. Application of a shrinking core model to fluidized bed drying Schwarzbach & Schlunder (1993) suggests that in the early stages, when the air at the surface is close to saturated, the evaporation flux from the wet core is controlled by equilibrium, and composition changes are limited by azeotropic conditions. In the later stages, as the process becomes gas-phase controlled the composition changes become limited by a pseudo-azeotrope (Pakowski 1994).

Viduarre & Martinez (1997) examined the continuous, non-isothermal drying of solids wetted with ternary mixtures, and studied the influence of process variables using a gas-phase-limited model. They found that gas composition had the most pronounced effect on the computed composition trajectories; the extent of these effects depended on the gas/liquid flow rate ratio (both liquid and solid move continuously through the notional dryer as it operates in a continuous mode). Viduarre & Martinez also found that the temperature of the solid material affected the location of positive/negative selectivity areas on a ternary composition space. They analysed the effect of addition by conduction during the process, a practice that occurs by contact heating in some manufacturing processes; for the acetone-ethanol-water ternary mixture they found that additional heat addition was unfavourable for the evaporation of the more volatile components (acetone, ethanol) as the higher temperature increases the selectivity for water.

Pakowski (1994) gave an overview of research on drying of solids containing multicomponent mixtures, include impact of liquid-side controlled evaporation, and evaporation from porous solids. Pakowski (1990) identified two cases for liquid-side diffusion control: evaporation from a stationary liquid surface supplied by bulk flow from a reservoir of constant composition, and evaporation from a receding liquid surface. For the first case, the liquid side separation factor K_L (Thurner & Schlunder 1986) can be used to distinguish situations where liquid side resistance will dominate:

$$K_L = \exp\left(-\frac{\dot{m}_v}{k_L \rho_L}\right)$$

where k_L is a liquid-side mass transfer coefficient, and \dot{m}_v is evaporation rate. When $K_L \rightarrow 0$, gas-phase control applies, no concentration gradients exist in the liquid phase, the evaporating flux has constant composition, and the process is non-selective. For the other limiting case (receding liquid with diffusion through capillary to surface, capillary sealed at one end), Pakowski (1990) showed by simulation for an IPA-water mixture that selectivity for the more volatile component initially falls before rising again at the end of the process due to diffusion effects in the capillary.

Steinbeck & Schlunder (1997) and Steinbeck (1999) tested the drying of mixtures of IPA/water/1-butanol in a bed of glass beads. This mixture forms a two-phase region at lower IPA concentrations. Composition trajectories that passed through the two-phase region were tested experimentally but no significant alteration in the drying rate was observed. Steinbeck experimentally detected the presence of a pseudo-azeotrope by virtue of composition trajectories that tended to pure water or pure 1-butanol depending on the initial composition, and on the drying conditions. The pore size of the solid had a noticeable impact on selectivity within the two-phase region, but that effect was not present for composition paths in the single-phase region. This was attributed to differences in density and wettability of the two-phase mixture.

Gamero & Martinez (2005) conducted an experimental and theoretical study of drying of a porous solid (sand) wetted with ternary mixtures (water/methanol/ethanol and 2-propanol/methanol/ethanol). A mathematical model involving isothermal capillary movement of the liquid and diffusion in gas and liquid phases was developed. Beyhaghi et al. (2011) conducted experiments on the transport of multicomponent hydrocarbons (decane, dodecane and hexadecane) in synthetic wicks made of sintered polymer beads. These wicks are representative of consumer products such as air-fresheners. They used a volume-averaged form of the transport equations to describe the limiting process of capillary-pressure-driven transport in the wick, and found the evaporation rate to be a strong function of the tortuosity of the wick itself, and of the gas-phase film thickness at the wick-air interface. Berggren & Alderborn (2001a,b) investigated effect of ratio of ethanol/water content on the porosity and tableting behaviour of cellulose pellets, finding higher drying rates at higher ethanol content and that higher ethanol content increased the porosity of the solid product.

2.4 Chapter Summary and Conclusions

This chapter summarises the status of a number of areas that form the basis for the work of this thesis. The governing equations of mass and heat, and the theory of the Maxwell-Stefan equations of multicomponent mass transfer described above are used to develop the models for evaporation maps in the next chapter. The background material on properties of residue curve maps (RCMs) sets the scene for the development of evaporation maps which can be viewed as an analogy of RCMs for non-equilibrium, gas-phase mass transfer-limited conditions. The review of evaporation and drying of multicomponent mixtures serves as background to the intended purpose of evaporation maps and helps to place them in a proper context.

Chapter 3

Evaporation Maps for Gas Phase Limited Conditions

In this chapter, the idea of *evaporation maps* is developed. Evaporation maps are seen to be a convenient way of representing the dynamic composition of evaporating liquid mixtures. Specifically, these maps represent the residual composition of evaporating ternary non-ideal mixtures over the full range of composition. The maps consist of evaporation trajectories that are selected to portray graphically the "flow" of residual composition over the entire composition space (i.e. the ternary diagram). The map then gives a straightforward representation of the direction of composition changes in the mixture as the evaporation progresses. A number of ternary mixtures of varying levels of non-ideality are used as examples, including a number of common solvents of industrial importance (e.g. ethanol, methanol, water, MEK, toluene, acetone). A planar geometry, as shown in figure 3.1, is used as a basis for the development. Evaporation maps for the various mixtures show how the residual liquid composition is in many cases sensitive to the initial composition, so that an appropriate selection of the initial composition can be made if there is a particular undesirable solvent to be avoided in the final product. The liquid mixture is at its wet-bulb temperature throughout the evaporation/drying process.

Evaporation may occur into a pure inert gas, or into one pre-loaded with a known fraction of one or more of the ternary components. The model developed here uses an exact solution to the Maxwell-Stefan equations for mass transfer in the gas film, with a lumped approach applied to the liquid phase. Solutions to the evaporation model take the form of trajectories in temperature-composition space, which are then projected onto a ternary diagram to form the map. The evaporation process considered here involves gas-phase limited heat & mass transfer from a liquid or wetted-solid surface, over which a gas flows at known conditions.

The evaporation maps are analogous to residue curve maps (RCMs) which are used ex-

tensively in the analysis of equilibrium separation processes for ternary mixtures. The similarities between RCMs and the residual composition of evaporating liquid mixtures, under conditions of gas-phase controlled mass transfer, was highlighted by Luna & Martinez (1999). As noted in section 2.2, the *singular points* or *fixed points* of the RCMs are the pure components and azeotropes of the mixture (Fien & Liu 1994). In the case of evaporation maps developed here, the pure components are also fixed points of the maps, as are the binary and ternary *pseudo-azeotropes* of the mixture (where they exist). To compute the evaporation maps, these pseudo-azeotropes under the given evaporation conditions must first be located. As with RCMs, the fixed points may be stable or unstable nodes, or saddles. For evaporation into a pure inert gas, trajectories originate from a neighbourhood of each unstable node, terminating at a stable node. In addition to the component mass balances and phase equilibrium relationships, an overall energy balance for the liquid phase is required for computation of the evaporation maps; the energy and component mass balances are coupled through the multicomponent fluxes.

The topics covered in this chapter are as follows:

- The theory section 3.1 deals with the calculation of multicomponent fluxes using an analytic solution to the Maxwell-Stefan equations, the development of heat and material balance for an evaporating mixture, a model for calculation of multicomponent wet-bulb temperature, and a model for calculation of binary and ternary pseudo-azeotropes
- The numerical methods section 3.2 covers a Newton-method approaches for calculation of the multicomponent fluxes. The Newton-method is combined with the heat and material balances and integrated to form the evaporation trajectories. Newton-based methods are also developed for the multicomponent wet-bulb temperature and pseudo-azeotropes using analytic forms of the Jacobian matrix in each case. An optimization method for location of evaporation trajectories to cover the ternary composition space is also developed. The pseudo-azeotrope method is seen to be an augmented form of the wet-bulb method. The forms for the analytic derivative terms used in Jacobian for the Newton-method calculation are also discussed.
- Section 3.3 covers model validation (for droplets and planar geometry), some numerical results on wet-bulb temperature and ultimately, generation of the evaporation maps for specified gas-phase conditions (air temperature and velocity).
- Finally, in section 3.4 the multicomponent wet-bulb temperature model is shown to reduce to a simpler, well-known form for single component fluids, where multicomponent effects can be neglected.

3.1 Theory

The development of the theory required to compute the evaporation maps is outlined in the following sections. The computation of multicomponent mass transfer coefficient matrix using an analytic solution to the Maxwell-Stefan equations is first presented; this matrix is then combined with mass transfer coefficients for the planar geometry. It is then shown how the fluxes are used in the calculation of *evaporation trajectories*. The computation of multicomponent wet-bulb temperature at given liquid composition is then presented. This is then further extended to the calculation of binary and ternary pseudo-azeotropes. Each of these steps is required to compute the evaporation maps.

To set the scene, figure 3.1a shows the configuration used to develop the theory for this work; this would be representative of a horizontal liquid film (in case of drying of polymer sheets), or a solid saturated with liquid (e.g. tray dryer for pharmaceutical production), or perhaps an evaporating pool of spilled solvent mixture. A cross-sectional view of the evaporation process is shown in figure 3.1b. A steady stream of gas of known temperature T^G and composition y_i^G flows over the planar surface. A notional film of thickness ℓ is assumed to exist at the vapour liquid interface; temperature and composition gradients exist within this film only, reaching the values of the flowing gas stream at the outer edge of the film. Using an IPA/ethanol/methanol liquid mixture as an example, the individual diffusive fluxes of the evaporating components are denoted by J_{IPA} , J_{EtOH} and J_{MeOH} . A corresponding diffusive flux of air occurs in the opposite direction. For evaporation of liquid mixtures, a heat flux q_G occurs from the liquid to the vapour phase due to evaporative cooling. The liquid composition is x_i for each component i , while the corresponding gas-phase composition at the interface is y_i^S .

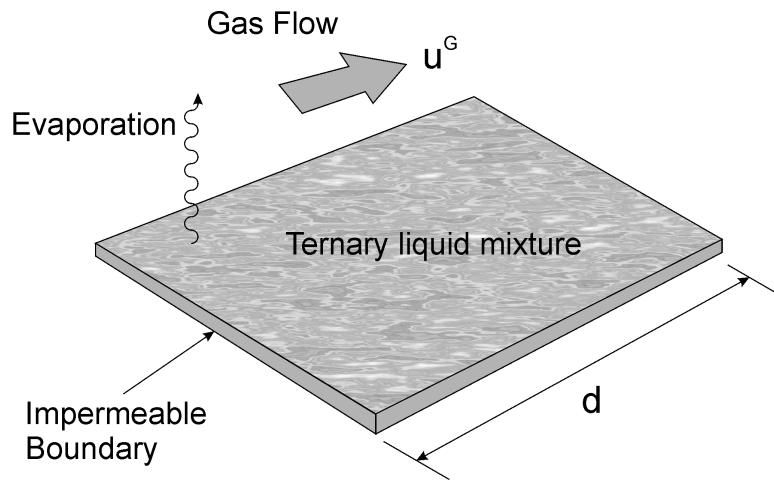
3.1.1 Analytic Solution to Maxwell-Stefan Equations

The theory leading to the Maxwell-Stefan equations was given in section A.3. Driving forces for mass transfer other than concentration differences have been ignored in this work. From equation 2.2, the Maxwell-Stefan equations for an n -component isothermal, isobaric, ideal gas system are given by:

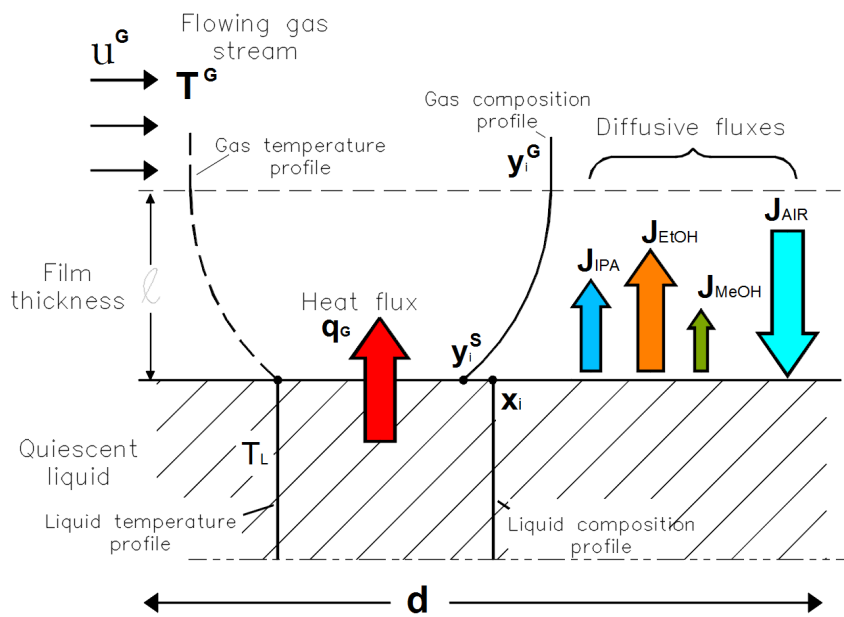
$$\frac{dy_i}{dz} = \sum_{j=1}^n \frac{y_i N_j - y_j N_i}{c \mathfrak{D}_{ij}} \quad (3.1)$$

for gas phase molefractions y_i and molar fluxes N_i . The driving force on the left hand side is the gradient of composition from equation A.74. The \mathfrak{D}_{ij} are the Maxwell-Stefan diffusivities. An evaluation of various film models for multicomponent mass transfer is given by Smith & Taylor (1983); in this chapter we employ the analytic solution due to Krishna & Standart (1976) to model mass transfer in the vapour film at the vapour-liquid interface. For mass transfer through a notional film thickness ℓ , we use a

3. EVAPORATION MAPS FOR GAS PHASE LIMITED CONDITIONS



(a) Characteristic length d is the length of the exposed surface in direction of gas flow at velocity u^G .



(b) Cross-section of liquid surface with heat flux q_G into liquid phase, and molar fluxes N_i into vapour phase; δ is notional film thickness at vapour-liquid interface; diffusive fluxes J_{IPA} etc. are shown for an example IPA/ethanol/methanol liquid mixture

Figure 3.1: Evaporation from surface of ternary liquid mixture.

normalised dimension $\eta = z/\ell$, so that

$$\frac{1}{\ell} \frac{dy_i}{d\eta} = \sum_{\substack{j=1 \\ i \neq j}}^n \frac{y_i N_j - y_j N_i}{c \mathfrak{D}_{ij}} \quad (3.2)$$

$$= y_i \sum_{\substack{j=1 \\ i \neq j}}^n \frac{N_j}{c \mathfrak{D}_{ij}} - \frac{y_n N_i}{c \mathfrak{D}_{in}} - \sum_{\substack{j=1 \\ i \neq j}}^{n-1} \frac{y_j N_i}{c \mathfrak{D}_{ij}} \quad (3.3)$$

where, in order to eliminate y_n from equation 3.2 we write y_n as

$$y_n = 1 - \sum_{j=1}^{n-1} y_j = 1 - y_i - \sum_{\substack{j=1 \\ i \neq j}}^{n-1} y_j \quad (3.4)$$

Equation 3.2 then becomes:

$$\frac{1}{\ell} \frac{dy_i}{d\eta} = x_i \sum_{\substack{j=1 \\ i \neq j}}^n \frac{N_j}{c \mathfrak{D}_{ij}} - \frac{N_i}{c \mathfrak{D}_{in}} \left(1 - x_i - \sum_{\substack{j=1 \\ i \neq j}}^n x_j \right) - \sum_{\substack{j=1 \\ i \neq j}}^{n-1} \frac{y_j N_i}{c \mathfrak{D}_{ij}} \quad (3.5)$$

$$= y_i \left(\frac{N_i}{c \mathfrak{D}_{ij}} + \sum_{\substack{j=1 \\ i \neq j}}^n \frac{N_j}{c \mathfrak{D}_{ij}} \right) - \frac{N_i}{c \mathfrak{D}_{ij}} + \sum_{\substack{j=1 \\ i \neq j}}^{n-1} \left(\frac{N_i}{c \mathfrak{D}_{in}} - \frac{N_i}{c \mathfrak{D}_{ij}} \right) x_j \quad (3.6)$$

so that (moving ℓ to right hand side):

$$\frac{dy_i}{d\eta} = \underbrace{\left(\frac{N_i}{c \mathfrak{D}_{in}/\ell} + \sum_{\substack{j=1 \\ i \neq j}}^n \frac{N_j}{c \mathfrak{D}_{ij}/\ell} \right)}_{\Phi_{ii}} x_i + \sum_{\substack{j=1 \\ i \neq j}}^n \underbrace{\left(\frac{N_i}{c \mathfrak{D}_{in}/\ell} - \frac{N_i}{c \mathfrak{D}_{ij}/\ell} \right)}_{\Phi_{ij}} x_j - \underbrace{\frac{N_i}{c \mathfrak{D}_{in}/\ell}}_{\phi_i} \quad (3.7)$$

We can therefore re-cast equation 3.7 as:

$$\frac{dy_i}{d\eta} = \Phi_{ii} x_i + \sum_{j=1, j \neq i}^{n-1} \Phi_{ij} x_j + \phi_i \quad (3.8)$$

or, in matrix form

$$\frac{d(y)}{d\eta} = [\Phi](x) + (\phi) \quad (3.9)$$

The analytic solution to equation 3.9 is given by Krishna & Standart (1976):

$$(y - y_o) = [\exp([\phi]\eta) - [I]][\exp[\Phi] - [I]]^{-1}(y_\ell - y_o) \quad (3.10)$$

where $\exp[\Phi]$ represents the matrix exponential. Thus, given the total fluxes N_i , the composition profile can be obtained analytically. Using Δy for the concentration differ-

ence across the film, the generalized form of Fick's law can be written in matrix form as:

$$(J) = -\frac{c}{\ell}[D]\frac{d(y)}{d\eta} = c[k^\bullet](\Delta y) \quad (3.11)$$

where $[D]$ is the matrix of multicomponent diffusion coefficients. The matrix of mass-transfer coefficients $[k^\bullet]$ is introduced as an alternative approach to calculating the diffusive fluxes, given that the value of ℓ is not accessible. At $\eta = 0$ (corresponding to vapour-liquid interface for this work), inserting equation 3.10 into 3.11 and differentiating gives an expression for the diffusive fluxes at the interface:

$$(J_0) = -\frac{c}{\ell}[D_0][\Phi][\exp[\Phi] - [I]]^{-1}(\Delta y) \quad (3.12)$$

With the definition of $[k^\bullet]$ from equation 3.11, we have:

$$[k_0^\bullet] = \frac{D_0}{\ell}[\Phi][\exp[\Phi] - [I]]^{-1} = \frac{D_0}{\ell}[\Xi_0] \quad (3.13)$$

where $[\Xi_0]$ is a correction factor. The exponential matrix term involving $\exp[\Phi]$ can be evaluated using Sylvester's theorem (Greenberg 1978). In the limit as $N_i \rightarrow 0$ this gives the zero-flux mass transfer coefficients as $[k_0] = [D_0]/\ell$. To formulate in terms of low-flux binary mass transfer coefficients κ_{ij} (which can be evaluated using correlations for specific geometries), we replace the \mathfrak{D}_{ij}/ℓ terms in the rate factor matrices Φ and ϕ above with the κ_{ij} . The matrix $[R_0]$ is defined with terms:

$$\begin{aligned} R_{0ii} &= \frac{y_i^I}{\kappa_{in}} + \sum_{k=1}^n \frac{y_k^I}{\kappa_{ik}} \\ R_{0ij} &= -y_i^I \left(\frac{1}{\kappa_{ij}} - \frac{1}{\kappa_{in}} \right) \end{aligned} \quad (3.14)$$

where the y_i^I are calculated at the interface ($\eta = 0$). The matrix of low-flux multicomponent mass transfer coefficients is then:

$$[k_0] = [R_0]^{-1} \quad (3.15)$$

so that the matrix of corrected mass transfer coefficients used in the calculation of the diffusive fluxes at the interface J_0 is finally given by:

$$[k_0^\bullet] = [k_0][\Xi_0] \quad (3.16)$$

The subscript 0 is dropped in subsequent use.

3.1.2 Application of Analytic Solution to Fluxes in Gas Phase

Section 2.1.1 presented a motivational example of multicomponent diffusion effect from the classic experiments of Toor (1957, 1964). Evaporation and drying of multicomponent solvent mixtures can entail diffusive interactions not present in drying of single solvents. Consequently, in this work the Maxwell-Stefan approach is used to model mass transfer in the gas phase. A lumped description applies to the liquid phase. For evaporation of a ternary liquid mixture into an inert gas (air), the presence of non-condensable air implies a quaternary system ($n = 4$) in the "film". There are 3 flux expressions ($F_1 - F_3$) in 3 of the 4 unknown total fluxes $N_1 - N_3$. The total flux of air (N_4) is zero, as air is assumed to be insoluble in the liquid (*Stefan diffusion*). Following Taylor & Krishna (1993), *discrepancy* or *residual* functions for the total fluxes are defined as:

$$F_i \equiv J_i + y_i^G \sum_{j=1}^3 N_j - N_i = 0 \quad \text{for} \quad i = 1, 2, 3 \quad (3.17)$$

where J_i are the diffusive fluxes. Using a pseudo steady-state approach for the notional film at the gas-liquid interface, the mole-fractions at either side of the film are specified at each moment in time using known liquid composition, and known composition of the surrounding gas phase. The fluxes defined at the interface are selected to solve the system of equations. The $n - 1$ diffusive fluxes J_i are given by

$$J_i = c \sum_{j=1}^3 k_{ij}^{\bullet} \Delta y_i \quad \text{for} \quad i = 1, 2, 3 \quad (3.18)$$

where $\Delta y_i = y_i^I - y_i^G$, and k_{ij}^{\bullet} is the mass transfer coefficient corrected for non-zero mass flux from equation 3.16. The diffusive flux of air is given by the summation $J_4 = -\sum_{i=1}^3 J_i$. The gas-phase molefraction at the vapour-liquid interface is y_i^I while that in the bulk gas is y_i^G . To calculate the k_{ij}^{\bullet} , we firstly calculate the zero-flux binary mass transfer coefficients κ_{ij} using correlations. For evaporation from a flat geometry and from a droplet (the geometries of interest), the relevant correlations are (Bird et al. 2002):

$$Sh_{ij} = \frac{d\kappa_{ij}}{D_{ij}} = \left(0.65 Re^{1/2} Sc_{ij}^{1/3}\right) \quad (3.19)$$

for mass transfer to/from a planar surface, and

$$Sh_{ij} = \left(2.0 + 0.6 Re^{1/2} Sc_{ij}^{1/3}\right) \quad (3.20)$$

for mass transfer to a droplet. $Sc_{ij} = \frac{\mu}{\rho D_{ij}}$, and $Sh_{ij} = \frac{\kappa_{ij} d}{D_{ij}}$ are the Schmidt and Sherwood numbers for pair ij , and d is the characteristic length scale. The correlation for the flat geometry is valid for $Re < 3 \times 10^5$ and Schmidt numbers in range $0.6 < Sc < 2500$ (Bird et al. 2002). Physical properties are calculated at the average

film temperature (average of liquid and bulk-gas temperatures). In the dynamic analysis that follows (section 3.1.3), a quasi-steady state approach is used, with properties evaluated at the average conditions applying at each time interval.

For given gas-phase concentrations at the interface and in the bulk, the total fluxes N_i can be found by using a Newton's-method solution to the discrepancy functions $F_1 - F_3$, as described in section 3.2.1. The N_i are coupled with a dynamic heat- and mass balance to calculate specific liquid trajectories as outlined next.

3.1.3 Conservation Equations for Liquid Phase

The evaporation of a quantity of liquid (total molar holdup h_T^L) is shown schematically in figure 3.2, in a planar geometry. This is a "batch" process in the sense that the liquid hold-up and composition change over time. The following assumptions apply:

1. Gas temperature (T^G) and composition (y_i^G) in the bulk do not change as it passes over the exposed surface
2. Liquid is well mixed so can be treated in a "lumped" manner, with no diffusional limitations in the liquid phase
3. All resistance to heat and mass transfer is in the gas film at the interface
4. Equilibrium applies at the gas-liquid interface with non-ideality in the liquid phase captured by an activity coefficient model. The liquid is also assumed to be non-ionic.
5. The gas phase behaves ideally, and air is insoluble in the liquid so there is no net flow of air towards the interface (Stefan flow)
6. Apart from the area exposed to the gas flow, the evaporating liquid is assumed to be isolated from its surroundings, so that heat transfer to liquid is via convective flow only (not radiation or conduction)
7. The effect of the regression of the vapour-liquid interface is neglected

Assumption (1) reflects the situation that commonly occurs in experimental situations, where a large excess of gas flow relative to the flow of evaporating vapours is used, and where the sample size is small (Martinez & Setterwall 1991). The assumption is that the rate of evaporation and the characteristic dimension (length in direction of gas flow) of the sample are small so that the bulk gas composition and temperature do not change along the sample length due to effects of evaporating liquid. Where those assumptions do not hold, such as with a long characteristic length typical of an industrial dryer, then bulk gas composition and temperature would be functions of length. This variation would be addressed by discretizing overall heat and material

balances over the exposed length, using a lumped parameter model for liquid/solid mixture and for gas phase in each increment (Pakowski & Mujumdar 2006).

Assumption (2) states that no diffusive effects are accounted for in the liquid phase; in practice this may be due to mixing effects within the liquid that occur due to flow of gas phase over the gas-liquid interface, or due to natural convection effects within the liquid. In general, the analysis would also apply to a liquid containing a solid phase provided the solids present do not affect the assumption of a well-mixed liquid phase - see also assumption (6).

Assumption (3) implies that the evaporation rate is governed by conditions in the gas phase. The controlling steps for evaporation of a binary liquid mixtures, and drying of porous materials containing binary mixtures were investigated by Thurner & Schlunder (1986) and by Steinbeck (1999). The controlling steps were found to be determined by drying intensity, so that at moderate conditions of gas temperature and velocity the process is controlled by gas-side heat and mass transfer or thermodynamic equilibrium. Under intensive conditions, heat and mass transfer in the liquid (or wetted-solid) phase becomes significant. A characteristic number for liquid-side mass transfer is given by (Thurner & Schlunder 1986)

$$K_L = \exp\left(-\frac{\dot{m}_v}{k_L \rho_L}\right) \quad (3.21)$$

where k_L is a liquid-side mass transfer coefficient, and \dot{m}_v can be found from equation 3.30. At low gas velocities, and when $K_L \rightarrow 1$, no concentration profiles exist in the liquid phase, and the selectivity depends on gas-side mass transfer and thermodynamic equilibrium. At high evaporation rates and/or low liquid-side mass transfer coefficients, $K_L \rightarrow 0$, and liquid-side resistance is the limiting step. For the simulations in this work the evaporation rates are such that $K_L \rightarrow 1$ (using typical values of k_L for free gas-liquid interface from (Thurner & Schlunder 1986) so the assumption of gas-side controlling resistance is applicable.

Assumption (6) indicates that the thermal mass of any solids is ignored. In a practical dryer, solids would of course be present, however it is assumed here that solids do not exert a vapour pressure or otherwise interact with the liquid and therefore do not affect the residual composition during the process.

The final assumption (7) says that the rate of movement of the vapour-liquid interface is negligible with respect to the flux of material away from the surface. The rate of interface regression is however included in the distributed model of chapter 7.

A differential mass balance for the hold-up h_i^L of component i yields

$$\frac{dh_i^L}{dt} = -AN_i \quad (3.22)$$

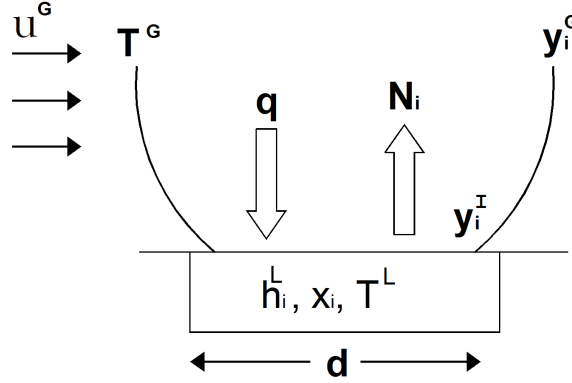


Figure 3.2: Schematic of evaporation of liquid at temperature T^L , and composition x_i into gas at temperature T^G and composition y_i^G , with heat flux q into liquid.

where N_i is the molar evaporation flux of component i . The multicomponent fluxes at required time intervals are found using the approach discussed in the previous section.

The equilibrium which is assumed to exist at the vapour-liquid interface (assumption 4) is expressed mathematically by equations for equality of the chemical potentials of each component in the vapour and liquid phases:

$$\mu_i^V = \mu_i^L \quad i = 1 \dots n \quad (3.23)$$

where the chemical potential (or partial molar Gibbs energy) is given by

$$\mu_i = \bar{g}_i = \left(\frac{\partial G}{\partial n_i} \right)_{T, P, n_i} \quad (3.24)$$

This is equivalent to an expression of equal fugacities in each phase:

$$f_i^V = f_i^L \quad i = 1 \dots n \quad (3.25)$$

For practical computations, the fugacities are given by (DeNevers 2012)

$$f_i^V = \hat{\phi}_i y_i P \quad \text{and} \quad f_i^L = \gamma_i x_i p_i \quad (3.26)$$

so that

$$y_i = \frac{x_i \gamma_i p_i}{P \hat{\phi}_i} \quad (3.27)$$

where γ_i are the (NRTL) activity coefficients representing non-ideality in the liquid phase, p_i is the vapour pressure of component i and P is the total pressure. $\hat{\phi}$ is the vapour fugacity coefficient. Refer to appendix B.1 for details of the NRTL model used in this work. It is assumed in equation 3.27 that the gas phase is ideal, so that $\hat{\phi} = 1.0$. This is a standard assumption for gas mixtures at low pressure in the absence of such effects as dimerization in the vapour phase; if a pressure-explicit equation of state is

known to describe the vapour phase, $\hat{\phi}$ can be conveniently calculated (Poling et al. 2001, p. 145).

Thus, by coupling the mass fluxes with an overall heat- and material-balance, the composition and temperature of the residual liquid over time may be found. The area for heat and mass transfer A is defined appropriately for the geometry in question (droplet, film etc.) To track the composition changes in the liquid, $n - 1$ component balances are required - the summation of mole-fractions in the liquid phase $\sum_{i=1}^3 x_i = 1$ gives the remaining n th mole fraction. Expressing the component material balance in terms of mole fraction gives

$$\frac{dx_i}{dt} = -\frac{A}{h_T^L} (N_i - x_i N_t) \quad (3.28)$$

where

$$h_T^L = \sum_{i=1}^n h_i^L \quad (3.29)$$

An overall balance gives the rate of evaporation as

$$\frac{dM_T^L}{dt} = -\dot{m}_v \quad (3.30)$$

where M_T^L is the total liquid mass, \dot{m}_v is the instantaneous mass rate of evaporation. The energy balance for the system may be written in terms of liquid temperature T^L as the independent variable (liquid is at interface temperature throughout). Using equation A.33:

$$\frac{dT^L}{dt} = \frac{A \left[q_G - \sum_{i=1}^3 N_i (\bar{H}_i^G - \bar{H}_i^L) \right]}{\sum_{i=1}^3 h_i M_i C_{p_i}^L} \quad (3.31)$$

where \bar{H}_i^G and \bar{H}_i^L are the partial molar vapour and liquid molar enthalpies respectively of component i . The convective heat flux term is given by

$$q_G = h_G^\bullet (T^G - T^L) \quad (3.32)$$

h_G^\bullet is the heat-transfer coefficient corrected for finite mass transfer. Expanding the enthalpy terms \bar{H}_i^G and \bar{H}_i^L , and the heat flux term gives

$$\frac{dT^L}{dt} = \frac{\left[h_V^\bullet (T^G - T^L) - \sum_{i=1}^3 N_i \Delta H_i^{vap} - \sum_{i=1}^3 N_i M_i C_{p_i}^G (T^G - T^L) \right]}{\sum_{i=1}^3 h_i^L M_i C_{p_i}^L} \quad (3.33)$$

where M_i is the molecular weight of component i . The fluxes are summed from $i = 1-3$ only, as the flux of the inert gas (air) is zero. The heat-transfer coefficient corrected for finite mass transfer is in turn given by

$$h_G^\bullet = h_G \Xi_H = h_G \left[\frac{\Phi_H^G}{\exp(\Phi_H^G) - 1} \right] \quad (3.34)$$

where Ξ_H is known as the Ackermann correction (Taylor & Krishna 1993), and Φ_H^G is the heat transfer rate factor, given by

$$\Phi_H^G = \frac{\sum_{i=1}^3 n_i C p_i^G}{h_G} \quad (3.35)$$

for mass transfer flux n_i . The zero-flux heat transfer coefficient h_G for film and droplet and geometries can be found from heat-transfer analogies to equations 3.19 and 3.20:

$$Nu = \frac{h_G d}{k} = 0.65 Re^{1/2} Pr^{1/3} \quad (3.36)$$

$$Nu = 2.0 + 0.6 Re^{1/2} Pr^{1/3} \quad (3.37)$$

The term within the square brackets in equation 3.33 can be recognised as equation 3.44 derived below for the multicomponent wet-bulb temperature. Thus, in the limit as temperature changes tend to zero, the square-bracket term becomes zero, and the liquid temperature becomes that of its wet-bulb temperature at that composition.

3.1.4 Multicomponent Wet-bulb Temperature

The wet-bulb temperature is the equilibrium temperature reached by a liquid evaporating from a surface when a small amount of liquid is taken up by a large amount of gas partially saturated with the vapour (Thurner & Schlunder 1985). In the case of mixture with more than one component, a steady temperature will strictly only be reached in the limit when remaining liquid contains a single component, or when a pseudo-azeotrope has been reached (refer to section 3.1.5). Nevertheless, an "equilibrium" or wet-bulb temperature for a notional evaporating multicomponent mixture of given (steady) composition can be calculated as discussed below. This equilibrium or multicomponent wet-bulb temperature is the temperature which an evaporating liquid approaches over time. In certain cases, this temperature is approached rather rapidly, as comparison with experimental data for droplet evaporation in section 3.2.1 demonstrates.

A model for the calculation of wet-bulb temperature for drying of a porous solid wetted with binary mixtures was presented by Thurner & Schlunder (1985); a criteria for non-

selective drying within the porous solid based on a penetration depth was developed, and the wet-bulb temperature was found by solving heat and mass balances together with an expression for phase equilibrium assuming gas-phase control. A simplified picture of the mass transfer was used, employing binary mass transfer coefficients. Pakowski (1989) presented a simple model for binary wet-bulb calculations using a mass transfer model derived by Newbald & Amundson (1973) which accounts for the cross-effects of one component on another using an effective diffusivity concept. The model presented in this work incorporates mass transfer fluxes solved using the explicit solution of the Maxwell-Stefan equations for mass transfer, outlined in section 3.1.1.

Equilibrium at the vapour-liquid interface is assumed to apply. Thus, for a ternary liquid mixture, there is an equilibrium expression for each component:

$$F_4 \equiv K_1 x_1 - y_1^I = 0 \quad (3.38)$$

$$F_5 \equiv K_2 x_2 - y_2^I = 0 \quad (3.39)$$

$$F_6 \equiv K_3 x_3 - y_3^I = 0 \quad (3.40)$$

where

$$K_i = \gamma_i p_i / P \quad (3.41)$$

The activity coefficients γ_i are found from the NRTL equation (see appendix B.1). The requirement that the summation of vapour mole-fractions is unity is expressed by:

$$F_7 \equiv \sum y_i^I - 1 \quad (3.42)$$

The rate of heat transfer at the interface of a liquid undergoing heat and mass transfer with its surroundings is the sum of that due to the temperature gradient, and that due to enthalpy transferred by the shift of material from the interface:

$$q_I = q_G + \sum_{i=1}^n N_i (\bar{H}_i^G - \bar{H}_i^L) \quad (3.43)$$

Implicit in the definition of wet-bulb temperature is that the heat transfer to the evaporating liquid is used for evaporation of the liquid, thus the q_I term is zero.

To compute the wet-bulb temperature for a ternary mixture, the discrepancy functions $F_1 - F_3$ for the mass transfer fluxes $N_1 - N_3$ (section 3.1.2) can be augmented with the heat balance F_8 :

$$F_8 \equiv h_G^\bullet(T^G - T^L) - \sum_{i=1}^3 N_i \Delta H_i^{vap} - \sum_{i=1}^3 N_i M_i C_{p_i}^G (T^G - T^L) = 0 \quad (3.44)$$

The right-hand side of the heat balance also appears in the differential heat balance in equation 3.33.

Thus, for a ternary liquid, the wet-bulb model has 8 equations ($F_1 - F_8$) in 8 unknowns ($N_1, N_2, N_3, y_1^I, y_2^I, y_3^I, y_4^I, T^L$). A Newton-method approach to solving $F_1 - F_8$ is used in section 3.2.

3.1.5 Pseudoazeotrope Compositions

To complete a residue curve map for a given mixture, the nature of all azeotropes in the mixture must be known *a priori* (the residue curves themselves can be computed without knowledge of the azeotropes); each azeotrope in the mixture can be characterised as a stable node, an unstable node or a saddle (Widagdo & Seider 1996). For evaporation maps, similar logic applies, except that the corresponding fixed points are now *pseudo-azeotropes*, which are determined using the concept of *selectivity*. The selectivity of a component i is defined (Riede & Schlunder 1990) as the difference between the relative molar evaporation flux of component i , and the mole fraction of component i in the liquid:

$$S_i = \frac{N_i}{\sum_{i=1}^n N_i} - x_i \quad (3.45)$$

For values of $S_i > 0$, component i is preferentially removed and its concentration in the liquid phase decreases, while for $S_i < 0$ the reverse occurs. At $S_i = 0$, evaporation is non-selective for component i , which is analogous to the distillation of a liquid mixture at its azeotropic composition. For gas phase controlled evaporation, a non-selective process may occur at liquid compositions that are different to those of the thermodynamic azeotrope due to the fact that the process depends *both* on vapour-liquid equilibria *and* on diffusion in the gas phase (Viduarre & Martinez 1997). These non-selective liquid compositions are known as pseudo-azeotropes or *dynamic azeotropes* (Schlunder 1989a,b). Just as thermodynamic azeotropes represent the fixed points of a simple distillation process (Doherty & Malone 2001), the pseudo-azeotropes represent the singular or fixed-points for the gas-phase limited system. For a ternary mixture, each of the binary pseudo-azeotropes (where they exist) are found by equating the selectivity for the relevant pair, i.e. $S_1 = S_2$, or $S_1 = S_3$ or $S_2 = S_3$. The ternary azeotrope (where it exists) is found by solving two equal-selectivity equations simultaneously, $S_1 = S_2$ and $S_1 = S_3$ for example. For the calculation of binary pseudo-azeotropes, in which case the liquid composition is not specified *a priori*, the problem statement for the wet-bulb temperature ($F_1 - F_8$) is augmented by 3 additional equations for the liquid mole-fractions. In the case where the binary is the pair 1-2, the discrepancy function

for equal selectivity ($S_1 = S_2$) is

$$F_9 \equiv \left[\frac{N_1}{\sum N_i} - x_1 \right] - \left[\frac{N_2}{\sum N_i} - x_2 \right] = 0 \quad (3.46)$$

For a binary pseudo-azeotrope, the third component in the mixture is obviously zero:

$$F_{10} \equiv x_3 = 0 \quad (3.47)$$

Similar expressions apply for the 1-3 and 2-3 pairs. Where the composition of a ternary pseudo-azeotrope to be computed, replace F_{10} with:

$$F_{10} \equiv \left[\frac{N_1}{\sum N_i} - x_1 \right] - \left[\frac{N_3}{\sum N_i} - x_3 \right] = 0$$

for pair 1-3 or, for pair 2-3:

$$F_{10} \equiv \left[\frac{N_2}{\sum N_i} - x_2 \right] - \left[\frac{N_3}{\sum N_i} - x_3 \right] = 0$$

The summation of the liquid mole-fractions completes the model:

$$F_{11} \equiv \sum x_i - 1 = 0 \quad (3.48)$$

For a ternary liquid, the pseudo-component model has 11 equations ($F_1 - F_{11}$) in 11 unknowns: $N_1, N_2, N_3, y_1^I, y_2^I, y_3^I, y_4^I, T^L, x_1, x_2$ and x_3). A Newton-method approach to solving $F_1 - F_{11}$ is presented in section 3.2.3.

3.2 Numerical Methods

3.2.1 Evaporation Trajectories

The system of equations describing total evaporation fluxes in the gas phase is summarised by equations $\mathbf{F}(\bar{\mathbf{x}}) = 0$ given by 3.17. To solve this set of nonlinear equations, we use Newton's (or Newton-Raphson) method, which requires both the evaluation of $\mathbf{F}(\bar{\mathbf{x}})$ and the derivative of $\mathbf{F}(\bar{\mathbf{x}})$. This method provides a very efficient means of converging to a root if a sufficiently good guess is provided (Press et al. 1992). The Newton-Raphson method is based on a Taylor series expansion of $\mathbf{F}(\bar{\mathbf{x}})$ in the neighbourhood of $\bar{\mathbf{x}}$:

$$F_i(\bar{\mathbf{x}} + \delta\bar{\mathbf{x}}) = F_i(\bar{\mathbf{x}}) + \sum_{j=1}^N \frac{\partial F_i}{\partial x_j} \delta x_j + \mathcal{O}(\delta\mathbf{x}^2)$$

The matrix of partial derivatives is the Jacobian matrix \mathbf{J} :

$$\mathbf{J}(\mathbf{x}) = \left[\frac{\partial F_i}{\partial \bar{x}_j} \right]$$

By neglecting terms of order $\delta \bar{x}^2$ and higher, a set of linear equations for $\delta \bar{x}$ is obtained:

$$\mathbf{J} \cdot \delta \bar{\mathbf{x}} = -\mathbf{F}$$

which can be solved by the so-called LU (lower-upper) decomposition (Kelley 1995). The corrections are then added to the solution vector

$$\bar{\mathbf{x}}_{new} = \bar{\mathbf{x}}_{old} + \delta \bar{\mathbf{x}}$$

and iterated until satisfactory convergence is reached. For the discrepancy functions $F_1 - F_3$ (equation 3.17), the Jacobian can be found analytically:

$$\mathbf{J} = \frac{\partial F_i}{\partial x_j} = \begin{bmatrix} y_1^G - 1 & y_1^G & y_1^G \\ y_2^G & y_2^G - 1 & y_2^G \\ y_3^G & y_3^G & y_3^G - 1 \end{bmatrix} \quad (3.49)$$

It is assumed that the mass transfer coefficients in calculation of the Jacobian can be considered constant. Following Taylor & Krishna (1993), the algorithm for calculation of the mass transfer fluxes in the film is shown in table 3.1. This is detailed here as it forms the basis for algorithms to determine the wet-bulb temperature, and pseudo-azeotrope compositions which follow.

By numerically integrating the governing equations for the multicomponent evaporation model (equations 3.28, 3.30 and 3.33), coupled with fluxes calculated from table 3.1 at each time step, together with suitable initial conditions, the composition-temperature trajectory (evolution of concentration and temperature over time) can be found. A simulation code was written in "C" using the LAPACK package of routines for matrix manipulation. These were incorporated via "mex" files into the Matlab programming environment. Numerical integration was performed using the ode15s routine within Matlab. Physical properties for the components as a function of temperature were generated from AspenPlus, with liquid-phase non-ideality represented by the NRTL model.

The initial conditions for the integration are compositions in the neighbourhood of unstable nodes of the evaporation maps. Similarly, the termination criteria are compositions in the neighbourhood of stable nodes. This is detailed in section 3.2.4.

Table 3.1: Calculation of multicomponent fluxes using Newton method

Given: $y_i^I, y_i^G, T^L, T^G, u^G, D_{ij}$
1. Using y_i^I and y_i^G , calculate mean vapour film properties
2. Calculate c (from ideal gas), and κ_{ij} from correlations
3. Estimate the N_i
4. Calculate Φ , Ξ , k_{ij}^\bullet and J_i
5. Evaluate the vector of discrepancy functions (residuals) $\mathbf{F} = [F_1 F_2 F_3]$
6. Compute the Jacobian matrix \mathbf{J}
7. Update the estimates of N_i : $[\mathbf{N}^{NEW}] = \mathbf{N} + \mathbf{J} \backslash \mathbf{F}$
8. If $\text{err} < \text{tolerance}$, stop, else return to step 4

3.2.2 Multicomponent Wet-bulb Temperature

To compute the wet-bulb temperature, a Newton-method solution to the discrepancy functions $F_1 - F_8$, outlined in table 3.2 is used. As with the case for the calculation of mass fluxes, the Jacobian (J_{wb}) for the wet-bulb computation can be found analytically and is given in table 3.4 (shaded terms).

All the terms in J_{wb} are straightforward with the exception of those involving partial derivatives with respect to liquid temperature ($\partial F_5 / \partial T^L$ - $\partial F_7 / \partial T^L$). For these, J_{wb} includes terms with:

$$\frac{\partial K_i}{\partial T} = K_i \frac{d \ln p_i}{dT} \quad (3.50)$$

where K_i is given by equation 3.41. To determine the partial derivatives of vapour pressure with respect to temperature, an expression of the following form is used (Prausnitz et al. 1986):

$$p_i = P_i^c \exp \left\{ \frac{1}{1 - (1 - T/T_i^c)} \left(A_i \left(1 - \frac{T}{T_i^c} \right) + B_i \left(1 - \frac{T}{T_i^c} \right)^{1.5} - D_i \left(1 - \frac{T}{T_i^c} \right)^6 \right) \right\} \quad (3.51)$$

where the A_i , B_i , C_i and D_i are constants for each component, and T_i^c is critical temperature. Differentiating equation 3.51 with respect to temperature gives

$$\frac{d \ln(p_i)}{dT} = \frac{T_i^c}{T^2} [A_i z_i + B_i z_i^{1.5} + C_i z_i^3 - D_i z_i^6] - \frac{1}{T} [A_i - 1.5 B_i z_i^{0.5} + 3 C_i z_i^2 - 6 D_i z_i^5] \quad (3.52)$$

where $z_i = T/T_i^c - 1$, from which the numerical values of the required derivatives in equation 3.50, and thence the required terms in J_{WB} can be found. The algorithm for the Newton-method solution for multicomponent wet-bulb temperature (with analytic

Table 3.2: Algorithm for computation of wet-bulb temperature

$$\bar{x}_{WB} = (N_1, N_2, N_3, y_1^I, y_2^I, y_3^I, y_4^I, T^L)$$

Given: $y_i^G, T^G, u^G, D_{ij}, x_i$

1. Establish initial values for vector of unknowns \bar{x}_{wb}
 2. For given (estimated) x_i , calculate y_i^I
 3. Using y_i^I and y_i^G , calculate mean vapour film properties
 4. Calculate $c, \Phi, \Xi, k_{ij}^\bullet$ and J_i (as for calculation of fluxes in table 3.1)
 5. Calculate $h_V^\bullet = h_V \Xi_H$
 6. Evaluate F_{WB} the vector of discrepancy functions $F_1 \dots F_8$
 7. Compute the Jacobian matrix J_{WB} for $F_1 \dots F_8$ from table 3.4
 8. Calculate $\Delta x_{WB} = -J_{WB} \backslash F_{WB}$
 9. Update the estimates of solution: $[\bar{x}_{WB}^{NEW}] = \bar{x}_{WB} + \Delta x_{WB}$
 10. If $\Delta x_{WB} < \text{tolerance}$, stop, else return to step 2
-

Table 3.3: Algorithm for computation of pseudo-azeotrope composition (and temperature). $\bar{x}_{AZ} = (N_1, N_2, N_3, y_1^I, y_2^I, y_3^I, y_4^I, T^L, x_1, x_2, x_3)$

Given: y_i^G, T^G, u^G, D_{ij}

1. Establish initial values for vector of unknowns \bar{x}_{az}
 2. For given (estimated) x_i , calculate y_i^I
 3. Using y_i^I and y_i^G , calculate mean vapour film properties
 4. Calculate $c, \Phi, \Xi, k_{ij}^\bullet$ and J_i (as for calculation of fluxes in table 3.1)
 5. Calculate $h_V^\bullet = h_V \Xi_H$
 6. Evaluate F_{AZ} the vector of discrepancy functions $F_1 \dots F_{11}$
 7. Compute the Jacobian matrix J_{AZ} for $F_1 \dots F_{11}$ from table 3.4
 8. Calculate $\Delta x_{AZ} = -J_{AZ} \backslash F_{AZ}$
 9. Update the estimates of solution: $[\bar{x}_{AZ}^{NEW}] = \bar{x}_{AZ} + \Delta x_{AZ}$
 10. If $\Delta x_{AZ} < \text{tolerance}$, stop, else return to step 2
-

Jacobian) is given in table 3.2.

3.2.3 Computation of Pseudo-Azeotrope Compositions

To compute the pseudo-azeotrope compositions, a Newton-method solution to $F_1 - F_{11}$, outlined in table 3.3 is employed. Note that the wet-bulb temperature at the pseudo-azeotropic composition is an additional output of the pseudo-azeotrope algorithm. As with the case for the calculation of mass fluxes and wet-bulb temperature, the Jacobian for the functions $F_1 - F_{11}$ can be found analytically and is given in table 3.4. Just as the discrepancy functions $F_1 - F_8$ for the wet-bulb temperature are augmented with $F_9 - F_{11}$ for calculation of pseudo-azeotrope composition, the Jacobian J_{AZ} is an augmented

form of the wet-bulb Jacobian J_{WB} . The shaded portion of table 3.4 represents the common part of the Jacobians. The new terms involve $\partial K_i / \partial x_j$ which are given by

$$\begin{aligned} \frac{\partial K_i}{\partial x_i} &= K_i + x_i \frac{d \ln \gamma_i}{d x_i} & \text{for } i = j \\ \frac{\partial K_i}{\partial x_j} &= x_i \frac{d \ln \gamma_i}{d x_j} & \text{for } i \neq j \end{aligned} \quad (3.53)$$

The derivative term for $\ln \gamma_i$ is a lengthy expression involving the terms of the NRTL expression for γ_i (see appendix B.2). The derivatives of the equal-selectivity function F_9 with respect to the fluxes for the 1-2 pair are given by

$$\begin{aligned} \frac{\partial F_9}{\partial N_1} &= \frac{N_2 - N_1}{(\sum N_i)^2} + \frac{1}{\sum N_i} \\ \frac{\partial F_9}{\partial N_2} &= \frac{N_2 - N_1}{(\sum N_i)^2} - \frac{1}{\sum N_i} \\ \frac{\partial F_9}{\partial N_3} &= \frac{N_2 - N_1}{\sum N_i} \end{aligned} \quad (3.54)$$

Similar expressions apply for the 1-3 and 2-3 pairs. In the case where a ternary pseudo-azeotrope is sought, the derivatives for the second equal-selectivity function F_{10} are

$$\begin{aligned} \frac{\partial F_{10}}{\partial N_1} &= \frac{N_3 - N_1}{(\sum N_i)^2} + \frac{1}{\sum N_i} \\ \frac{\partial F_{10}}{\partial N_2} &= \frac{N_2 - N_1}{(\sum N_i)^2} - \frac{1}{\sum N_i} \\ \frac{\partial F_{10}}{\partial N_3} &= \frac{N_2 - N_1}{\sum N_i} \end{aligned} \quad (3.55)$$

3.2.4 Construction of Evaporation Maps

To obtain a spread of trajectories over the evaporation map, points x^s are defined through which the trajectories are desired to pass (within a pre-defined tolerance ϵ_3). Figure 3.3 outlines the construction of an evaporation map schematically. Two scenarios are considered. In the first (figure 3.3(a)), trajectories run from a ϵ_1 -neighbourhood of an unstable node (on chloroform-methanol axis) to a ϵ_2 -neighbourhood of a stable node (on acetone-chloroform axis). In the second scenario (figure 3.3(b)), pre-loading of the gas phase changes the topology so that unstable node does not exist along the binary axis as before. In that case, trajectories are initiated from a ϵ_4 -neighbourhood of the axis (chloroform-methanol).

Note that while figure 3.3(a) shows trajectories initiating at an unstable binary node, and terminating at a stable binary node, trajectories may also initiate and terminate at

	N_1	N_1	N_1	y_1^I	y_2^I	y_3^I	y_4^I	T^L	x_1	x_2	x_3
F_1	$y_1 - 1$	y_1	y_1	ck_{11}^\bullet	ck_{12}^\bullet	ck_{13}^\bullet	0	0	0	0	0
F_2	y_2	$y_2 - 1$	y_2	ck_{21}^\bullet	ck_{22}^\bullet	ck_{23}^\bullet	0	0	0	0	0
F_3	y_3	y_3	$y_3 - 1$	ck_{31}^\bullet	ck_{32}^\bullet	ck_{33}^\bullet	0	0	0	0	0
F_4	$\frac{\Delta H_1^{vap} + C_{p1}^G(T^G - T^L)}{C_{p1}^G(T^G - T^L)}$	$\frac{\Delta H_2^{vap} + C_{p2}^G(T^G - T^L)}{C_{p2}^G(T^G - T^L)}$	$\frac{\Delta H_3^{vap} + C_{p3}^G(T^G - T^L)}{C_{p3}^G(T^G - T^L)}$	0	0	0	0	$-\frac{h^G \Phi}{\sum N_i C_{pi}^G M_i} - \frac{exp(\Phi) - 1}{\sum N_i C_{pi}^G M_i}$	0	0	0
F_5	0	0	0	-1	0	0	0	$x_1 \frac{\partial K_1}{\partial T}$	$x_1 \frac{\partial K_1}{\partial x_1} + K_1$	$x_1 \frac{\partial K_1}{\partial x_2}$	$x_1 \frac{\partial K_1}{\partial x_3}$
F_6	0	0	0	0	-1	0	0	$x_2 \frac{\partial K_2}{\partial T}$	$x_2 \frac{\partial K_2}{\partial x_1} + K_2$	$x_2 \frac{\partial K_2}{\partial x_2} + K_2$	$x_2 \frac{\partial K_2}{\partial x_3}$
F_7	0	0	0	0	0	-1	0	$x_3 \frac{\partial K_3}{\partial T}$	$x_3 \frac{\partial K_3}{\partial x_1} + K_3$	$x_3 \frac{\partial K_3}{\partial x_2} + K_3$	$x_3 \frac{\partial K_3}{\partial x_3} + K_3$
F_8	0	0	0	1	1	1	1	0	0	0	0
F_9	$\frac{N_2 - N_1}{(\sum_{N_i}^1)^2} + \frac{1}{\sum_{N_i}^1}$	$\frac{N_2 - N_1}{(\sum_{N_i}^1)^2} - \frac{1}{\sum_{N_i}^1}$	$\frac{N_2 - N_1}{(\sum_{N_i}^1)^2}$	0	0	0	0	-1	1	0	0
F_{10}	0	0	0	0	0	0	0	0	0	0	1
F_{11}	0	0	0	0	0	0	0	0	1	1	1

Table 3.4: Jacobian J_{AZ} (11x11) for binary pseudo-azeotrope procedure (pair 1-2); shaded cells are the Jacobian J_{WB} (8x8) for Newton-method wet-bulb computation.

Table 3.5: Algorithm for generation of evaporation maps

-
1. Locate binary and ternary pseudo-azeotropes for the given mixture (see table 3.2, and the continuation procedure of section 4.2.4).
 2. For a given unstable node specify the radius ϵ_1 around the node which defines the locus of possible initial concentrations
 3. Specify the point $x^s = (x_1^s, x_2^s)$ through which the desired trajectory should pass
 4. Initialize value for θ (via optimization routine); set constraints for θ : $\theta_{min} < \theta < \theta_{max}$ e.g. $0^\circ < \theta < 90^\circ$
 5. Calculate initial composition $x_1^\theta = x_1^o + \epsilon_1 \cos(\theta)$, and $x_2^\theta = x_2^o + \epsilon_1 \sin(\theta)$; x_1^o and x_2^o are the compositions of the starting unstable node (either a pure component, or a binary pseudo-azeotrope)
 6. Generate the evaporation trajectory by numerically integrating the system of governing equations 3.28, 3.30 & 3.33, coupled with the multicomponent flux calculation from table 3.1; the integration is terminated when x approaches a stable node x^f within a certain distance ϵ_2 .
 7. From computed trajectory, find point of intersection x^{AB} with the line AB
 8. Find approach to x^s : $\Delta_{AB} = \|x^s - x^{AB}\|$
 9. Adjust value of θ (via optimization routine) until $\Delta_{AB} < \epsilon_3$
 10. For optimal value of θ , project the solution in $T - x$ space onto the ternary diagram
 11. Repeat from step 3 as required
-

pure component nodes. The angle θ governs the starting composition x_θ ; by finding the intersection point x_{AB} , the value of θ that minimises length Δ_{AB} can be determined by numerical optimization. The approach used to generate the trajectories is outlined in table 3.5. The Matlab optimization function `fminbnd` was used in this work for numerical optimization of θ .

For each ternary mixture, the stable and unstable nodes must be identified prior to generation of an evaporation map, as they form the starting and end-points respectively of evaporation trajectories. This procedure involves calculating all binary and ternary pseudo-azeotropes by the methods of section 3.2.3, and their corresponding wet-bulb temperatures. The wet-bulb temperatures of the pure components in the mixture must also be found, by the method of section 3.2.2. The unstable nodes for the mixture are those whose wet-bulb temperature is a local minimum, while the stable nodes are those whose wet-bulb temperature is a local maximum.

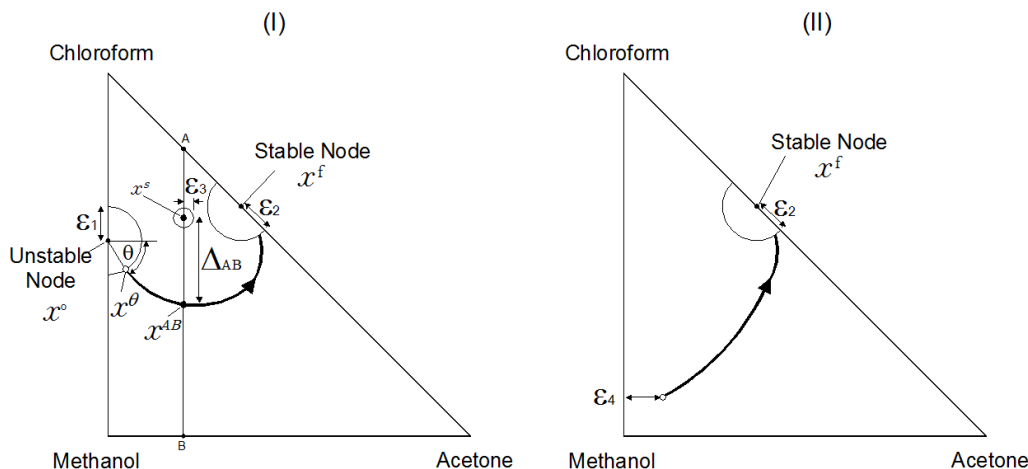


Figure 3.3: Geometric construction of evaporation map

3.3 Simulation Results and Discussion

3.3.1 Validation of Evaporation Model

The multicomponent evaporation model may be compared to data available for evaporation of binary and ternary mixtures. While the evaporation maps of subsequent sections are generated for a planar geometry only, the evaporation model is applicable to other geometries such as droplets, provided the appropriate forms of the heat and mass transfer correlations are used. Thus, data for both droplets and planar films are used for model validation purposes.

Multicomponent Droplets Figure 3.4 shows a comparison of model predictions to data (Pakowski 1994) for evaporation of droplets of a binary IPA/water mixture, under two different conditions of surrounding gas flow and relative humidity. There is reasonably good agreement with the experimental data for droplet temperature and diameter (plotted as d^2). Note that there are no adjustable parameters in this model. As noted in section 3.2.1, the model predictions are found by numerically integrating the governing equations for the multicomponent evaporation model (equations 3.28, 3.30 and 3.33), coupled with fluxes calculated from table 3.1 at each time step, together with suitable initial conditions. For data set 2, there is some variation in the agreement of the model with the data at smaller values of d^2 ; this may be due to larger relative heat losses in the filament supporting the droplet at smaller droplet sizes. The droplet temperature falls rapidly in the initial seconds due to evaporative cooling, followed by a gradual rise as time progresses, and the droplet becomes depleted of IPA.

For the case of IPA-water droplet evaporation, the computed values of wet-bulb temperature, calculated using concentrations at specific time points are shown in figure 3.4, indicating good agreement with experiment. As droplet evaporation progresses, the simulated droplet temperature and computed wet-bulb temperatures converge as expected. The simulated temperature and droplet diameter (d^2) have been extended in time for data set 1 in order to show how the droplet diameter tends to zero as the evaporation progresses.

Multicomponent Films The evaporation of a ternary ethanol/MEK/toluene mixture from a planar film was studied by Martinez & Setterwall (1991). Comparison of model predictions with their work is shown in figure 3.5-3.7, showing generally good agreement with the data. The fit is less good for figure 3.6. This may be due to the fact the initial concentration therein has a higher percentage of the most volatile component (ethanol) than in figures 3.5 and 3.7 so that the rate of evaporation is more rapid; consequently, the liquid film recedes below the edge of the container holding the liquid which may effect the gas flow conditions and the heat and mass transfer coefficients at the vapour-liquid interface. Also, as the most volatile component is eliminated, the viscosity of the residual liquid may increase (being mostly MEK and toluene which have higher viscosities) which might lead to a gradients in concentration due to reduced level of natural circulation. In that case the assumption of gas-phase limited heat and mass transfer may not be strictly valid.

Note from figure 3.8 that pure toluene forms the stable node for mixtures (a) and (b), while pure ethanol is the stable node for mixture (c). This behaviour is consistent with the evaporation map in figure 3.21. Note also from figures 3.6 in particular that a significant portion of the total mass is evaporated before the final composition (pure toluene) is approached.

3.3.2 Binary and Ternary Pseudo-Azeotropes

Pseudo-azeotropes for the various ternary mixtures are shown (as filled circles) on the ternary diagrams of figures 3.19-3.23. Table 3.6 below summarises the pseudo-azeotropic compositions and temperatures for each of these cases. The pure components and pseudo-azeotropes are denoted as stable/unstable nodes or saddles as appropriate; the unstable nodes form the starting point for the evaporation trajectories in each of the maps, while the stable nodes are the terminal points.

3. EVAPORATION MAPS FOR GAS PHASE LIMITED CONDITIONS

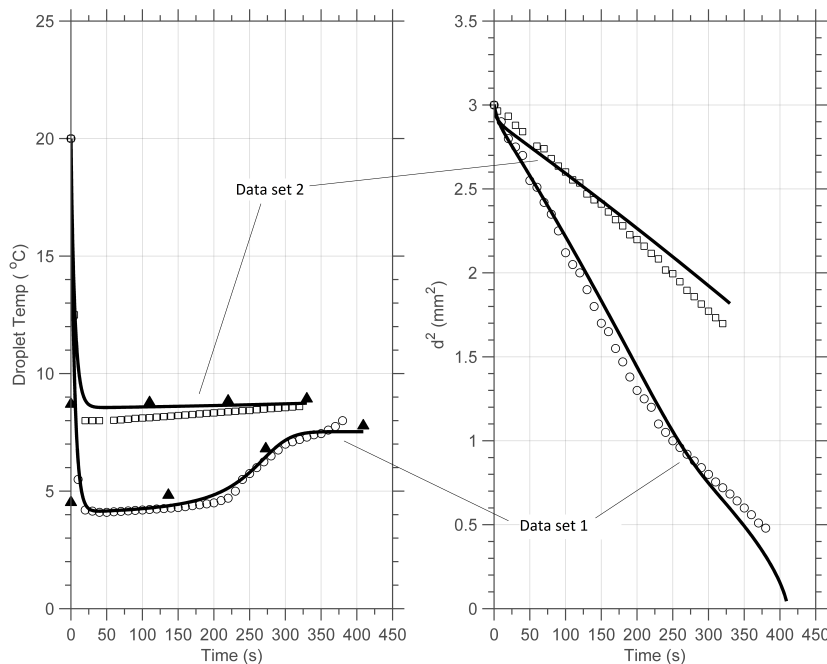


Figure 3.4: IPA-water droplet evaporation (Pakowski 1990); \blacktriangle : computed wet-bulb temperature; \circ : data set 1 ($T^G = 20C$, $u^G = 0.324m/s$; $RH_{IPA} = 0\%$; $RH_{H_2O} = 5.6\%$); \square : data set 2 ($T^G = 20C$, $u^G = 0.19m/s$; $RH_{IPA} = 15.3\%$; $RH_{H_2O} = 15.3\%$)

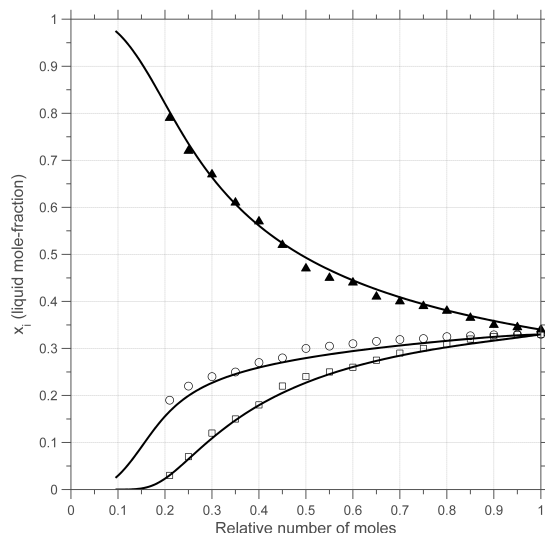


Figure 3.5: Evaporation of ethanol(1)-MEK(2)-toluene(3) mixture; comparison of model with experimental data (Martinez & Setterwall (1991), $x_1 = 0.33$, $x_2 = 0.33$, $x_3 = 0.34$; $T^G = 298K$, $T^L = 298K$, $u^G = 0.1m/s$; $d = 0.03m$). Horizontal axis represents progress of the evaporation from right to left; \square : ethanol, \circ : MEK, \blacktriangle : toluene

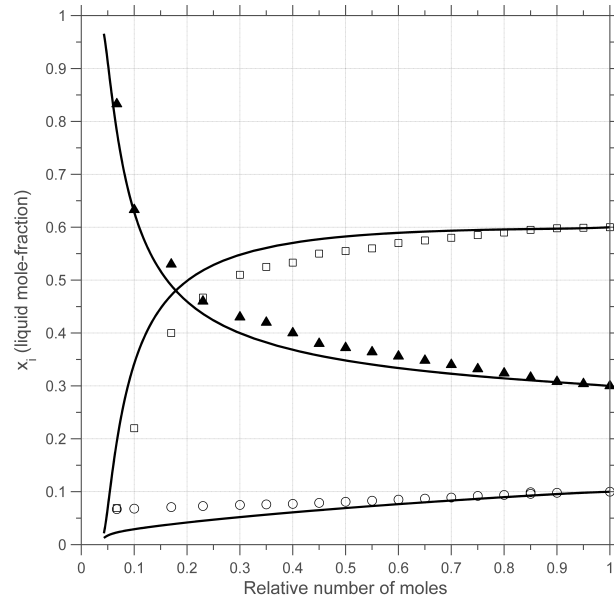


Figure 3.6: Evaporation of ethanol(1)-MEK(2)-toluene(3) mixture; comparison of model with experimental data (Martinez & Setterwall (1991)); $x_1 = 0.6, x_2 = 0.1, x_3 = 0.3$; $T^G = 298K, T^L = 298K, u^G = 0.1m/s$; \square : ethanol, \circ : MEK, \blacktriangle : toluene

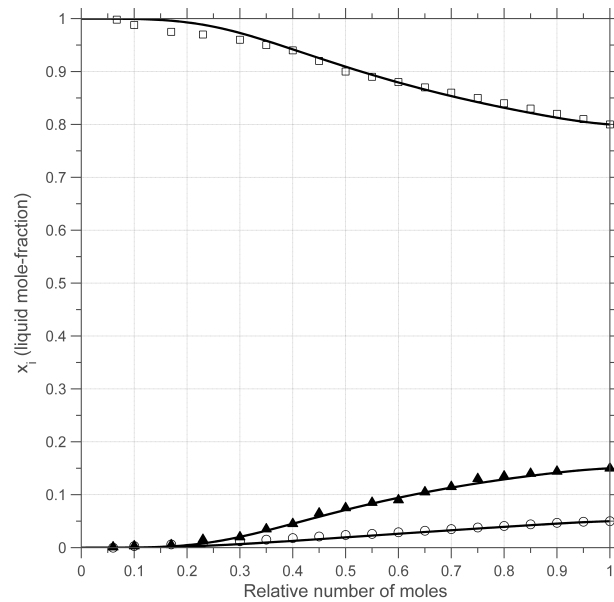


Figure 3.7: Evaporation of ethanol(1)-MEK(2)-toluene(3) mixture; comparison of model with experimental data (Martinez & Setterwall (1991)); $x_1 = 0.8, x_2 = 0.05, x_3 = 0.15$; $T^G = 296K, T^L = 294K, u^G = 0.07m/s$; \square : ethanol, \circ : MEK, \blacktriangle : toluene

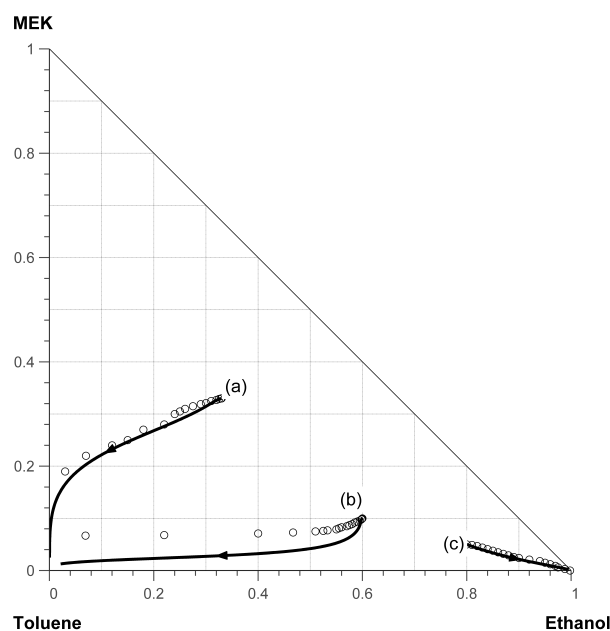


Figure 3.8: Figures 3.5-3.7 on ternary co-ordinates

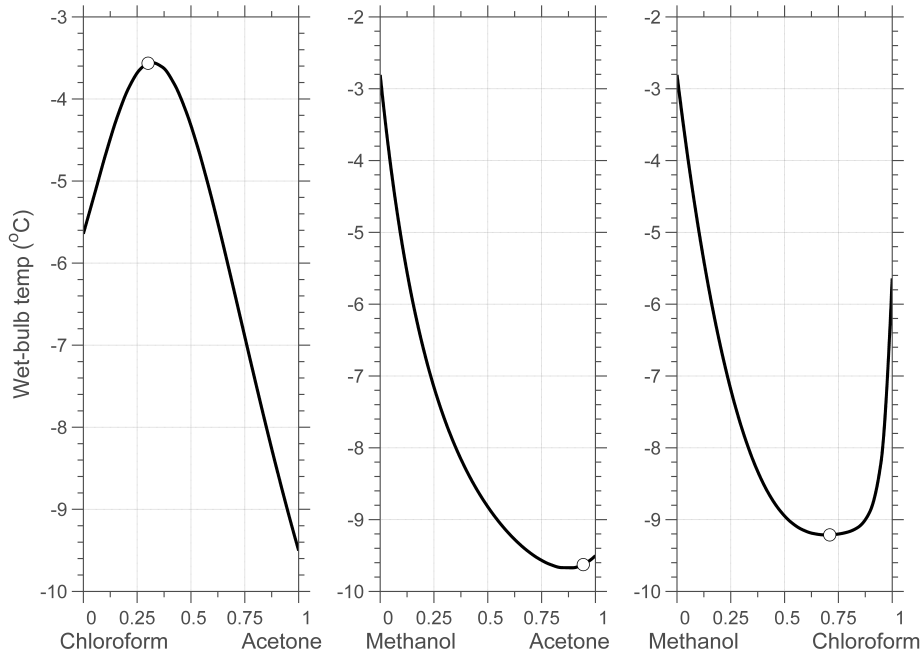
3.3.3 Multicomponent Wet-Bulb Temperature

Using the algorithm of table 3.2, the wet-bulb temperature can be computed for binary and ternary mixtures. Figure 3.9a shows wet-bulb temperatures for the three binary mixtures in the acetone/chloroform/methanol ternary mixture, together with the pseudo-azeotropic composition found from the algorithm of table 3.3. The wet-bulb temperature lies near a minimum or maximum at the pseudo-azeotropic composition in each case.

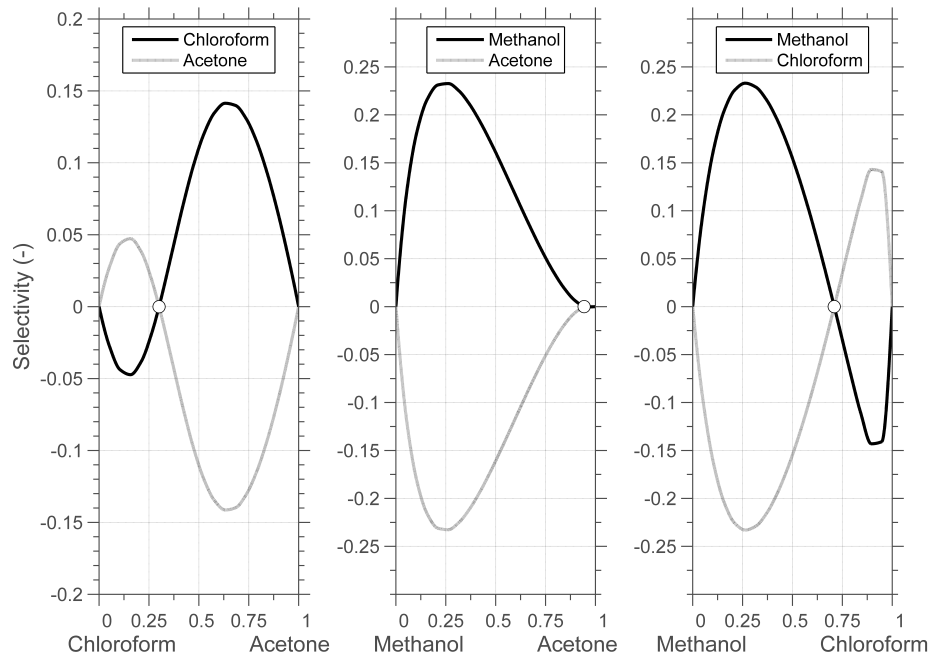
Figure 3.9b shows the corresponding binary selectivities as defined by equation 3.45. As required by the definition of a pseudo-azeotrope, the selectivities are zero at the pseudo-azeotropic compositions.

Whereas binary azeotropes lie at the maximum or minimum bubble-point for a given binary mixture (Prausnitz et al. 1986), the minimum or maximum wet-bulb temperature is not constrained to coincide with the pseudo-azeotropic composition. Figure 3.10 shows a magnified portion of the plots in figure 3.9a for the acetone/chloroform/methanol mixture, showing this effect. This can be explained by the fact that conventional azeotrope composition is a function of pressure only (assuming an accurate model of the vapour-liquid equilibria), while the pseudo-azeotrope composition is a function also of mass transfer rates in the gas phase.

Figure 3.11 shows multicomponent wet-bulb temperature lines computed by table 3.2 for binary IPA/water mixtures for four different relative humidity levels. These show



(a) Wet-bulb temperature for binary mixtures



(b) Selectivity for binary mixtures

Figure 3.9: Wet-bulb temperature and selectivities for binary mixtures in acetone/chloroform/ methanol mixture; evaporation into pure air; open circles denote pseudo-azeotrope compositions; $T^G = 40^\circ\text{C}$, $u^G = 0.5\text{m/s}$, $d = 0.03\text{m}$

Table 3.6: Results of pseudo-azeotrope calculations; $T^G = 20^\circ C$,
 $u^G = 0.5m/s$, $d = 0.03m$; SN=stable node, UN=unstable node,
 S=saddle

Components & pseudo-azeotropes	Pseudo-azeotrope composition (mole fractions)	T_{WB}	Type	Figure
(1) IPA	-	$12.58^\circ C$	SN	3.18
(2) Ethanol	-	$8.00^\circ C$	S	
(3) Methanol	-	$-2.81^\circ C$	UN	
(1) Water	-	$15.86^\circ C$	SN	3.19
(2) Ethanol	-	$8.00^\circ C$	SN	
(3) Methanol	-	$-2.81^\circ C$	UN	
Water/Ethanol	0.15, 0.85	$7.81^\circ C$	S	
(1) IPA	-	$20^\circ C$	SN	3.20
(2) Water	-	$12.58^\circ C$	SN	
(3) Ethanol	-	$15.86^\circ C$	SN	
IPA/Water	0.53, 0.47	$10.65^\circ C$	S	
Water/Ethanol	0.16, 0.85	$7.81^\circ C$	UN	
(1) Ethanol	-	$8.00^\circ C$	SN	3.21
(2) MEK	-	$7.92^\circ C$	S	
(3) Toluene	-	$20.86^\circ C$	SN	
Ethanol/MEK	0.35, 0.65	$5.57^\circ C$	UN	
Ethanol/Toluene	0.75, 0.25	$6.83^\circ C$	S	
(1) DCM	-	$-16.67^\circ C$	S	3.22
(2) Methanol	-	$-2.81^\circ C$	SN	
(3) Ethyl Acetate	-	$4.19^\circ C$	SN	
DCM/Methanol	0.89, 0.11	$-18.08^\circ C$	UN	
Methanol/Ethyl-acetate	0.74, 0.26	$-3.99^\circ C$	S	
(1) Acetone	-	$-9.52^\circ C$	S	3.23
(2) Chloroform	-	$-5.64^\circ C$	S	
(3) Methanol	-	$-2.81^\circ C$	SN	
Acetone/Chloroform	0.30, 0.70	$-3.56^\circ C$	SN	
Chloroform/Methanol	0.71, 0.29	$-9.21^\circ C$	UN	
Methanol/Acetone	0.94, 0.06	$-9.63^\circ C$	UN	
Acetone/Chloroform/methanol	0.27, 0.35, 0.38	$-7.42^\circ C$	S	

the same qualitative behaviour as those computed by Pakowski (1989) for IPA/water droplets, using the effective diffusivity approach of Newbald & Amundson (1973). The gas phase molefraction is found from the specified relative humidity using

$$y_i^G = \frac{p_i \gamma_i}{P} \frac{RH}{100}$$

The plot for 50%:50% relative humidity also shows a temperature of non-selective drying, T_{NS} (Pakowski 1989); non-selective process implies drying occurs at constant composition. T_{NS} is found by computing the pseudo-azeotropic composition (at which

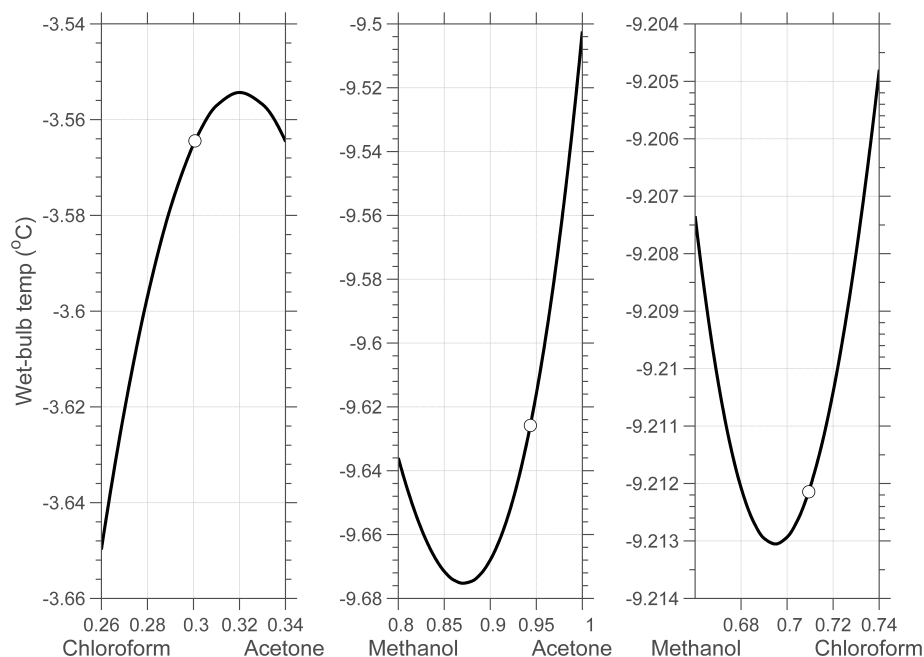


Figure 3.10: Magnified portion of figure 3.9a; open circles denote pseudo-azeotrope compositions; pseudo-azeotropes are not constrained to lie at extrema of wet-bulb temperature curves

selectivity $S_i = 0$), and the corresponding wet-bulb temperature at increasing values of the air (dry-bulb) temperature.

Note from the plot of $RH_{Ethanol} = 100\%$ that the wet-bulb temperature exceeds the dry-bulb temperature (20°C) at lower ethanol concentration; this is due to condensation of ethanol at the vapour-liquid interface when the gas-phase concentration is high, and the liquid-phase concentration is low.

Figures 3.12-3.14 show wet-bulb temperature surfaces for three ternary mixtures. Note that these are temperature surfaces for mixtures undergoing a rate-based (mass transfer limited) evaporation/drying; bubble-point surfaces are the analogous surfaces for mixtures at thermodynamic equilibrium. The ethyl acetate/dichloromethane/methanol surface in figure 3.12 shows peaks at pure methanol -2.8°C and pure ethyl acetate 4.2°C , with a minimum at dichloromethane -16.7°C . A minimum in the wet-bulb surface can be seen along the methanol/ethyl acetate edge at -4.0°C , while another minimum lies along the methanol/dichloromethane edge at 18.1°C . The ethanol/MEK/toluene surface in figure 3.13 shows a peak at pure toluene at 20.9°C , and a smaller peak at pure ethanol at 8.0°C . Note that minima in the surface occur along the toluene-ethanol and the ethanol-MEK edges; these minima correspond approximately to minimum-temperature pseudo-azeotropes. The acetone/chloroform/methanol surface in figure 3.14 has a minimum at pure acetone at -9.5°C and a maximum at pure

3. EVAPORATION MAPS FOR GAS PHASE LIMITED CONDITIONS

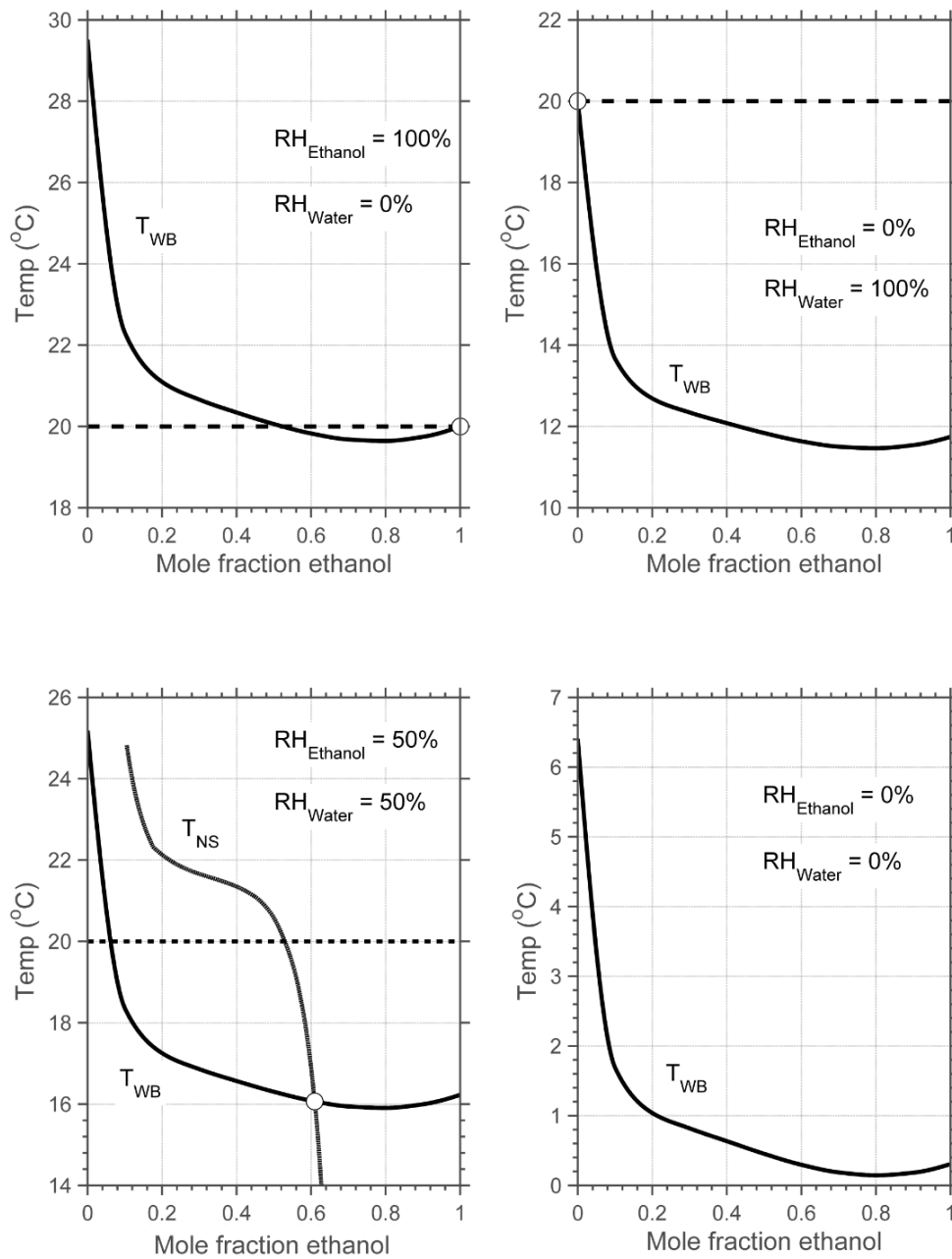


Figure 3.11: Ethanol/water multicomponent wet-bulb lines; $T^G = 20^\circ\text{C}$,
 $u^G = 0.5\text{m/s}$, $d = 0.03\text{m}$

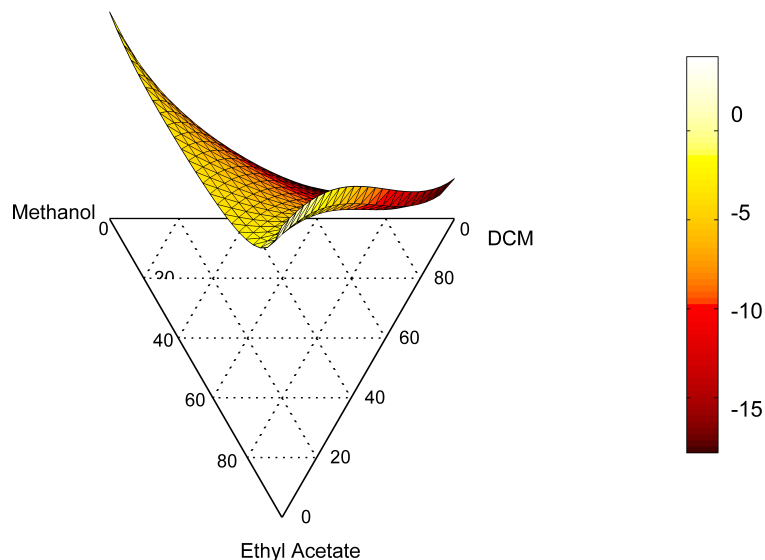


Figure 3.12: Wet-bulb temperature (deg C) surface for ethyl acetate/dichloromethane/methanol; $T^G = 20^\circ C$, $u^G = 0.5 m/s$, $d = 0.03 m$

methanol at $-2.8^\circ C$; a further maximum occurs along the acetone-chloroform edge, corresponding to a maximum temperature pseudo-azeotrope at $-3.5^\circ C$.

The peaks and troughs in the wet-bulb temperature surface are explored in more detail in section 6.3. Visualisation of wet-bulb temperature surfaces (or manifolds) in for mixtures with more than three components is not feasible, although the algorithms described here may be directly extended to higher dimensions.

3.3.4 Evaporation Trajectories - IPA/Ethanol/Water Example

To demonstrate the general features of evaporation trajectories, an example trajectory for IPA/ethanol/water is considered here. For a given ternary mixture, with an assumed planar geometry (i.e. evaporation from a flat surface such as a film), an evaporation trajectory may be found by numerically integrating the governing equations for gas-phase limited evaporation. Equation 3.28 describes the molar hold-up, while equation 3.33 describes the energy balance. By coupling these equations with the multicomponent flux calculation from table 3.1, the system of equations may be integrated forward in time from any desired initial composition until the composition approaches a stable node within a certain pre-specified tolerance.

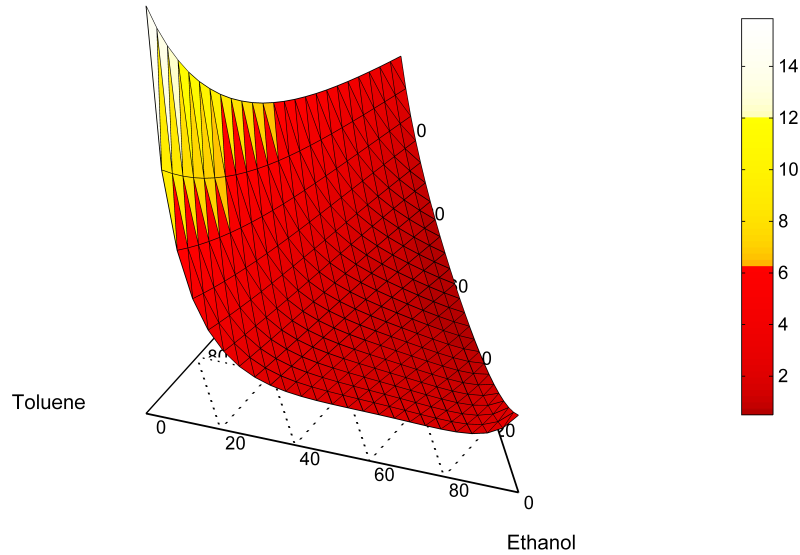


Figure 3.13: Wet-bulb temperature (deg C) surface for ethanol/MEK/toluene;
 $T^G = 20^\circ C$, $u^G = 0.5m/s$, $d = 0.03m$

Figure 3.15 shows such an example evaporation trajectory for the IPA/ethanol/water mixture. For this example, the initial composition is in the neighbourhood of pure methanol (most volatile component). The trajectory becomes richer in ethanol and leaner in methanol as it moves through point A towards point B; after point B, it becomes leaner in ethanol and richer in IPA, all the while becoming also leaner in methanol. The trajectory is terminated when it approaches pure IPA (least volatile component).

Also shown at each of three points A, B and C in figure 3.15 are matrices which indicate the degree of multicomponent interaction between the diffusing species in the gas phase. Multicomponent interaction effects (the degree to which the process is non-Fickian) can be assessed by considering the relative magnitude of the off-diagonal contributions to the diffusive fluxes. Recall from 3.18 that the diffusive flux for component i is given by:

$$J_i = c \sum_{j=1}^3 k_{ij}^{\bullet} \Delta y_j \quad \text{for} \quad i = 1, 2, 3$$

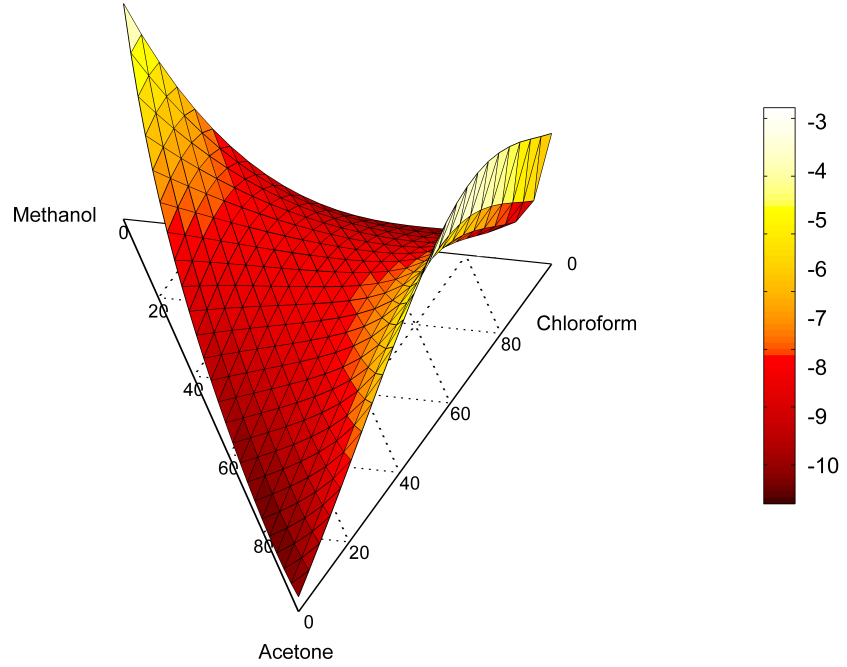


Figure 3.14: Wet-bulb temperature (deg C) surface for acetone/chloroform/methanol; $T^G = 20^\circ C$, $u^G = 0.5m/s$, $d = 0.03m$

A measure of the contribution of an off-diagonal (multicomponent) terms is given by:

$$\left| \frac{k_{ij}^\bullet \Delta y_j}{k_{ii}^\bullet \Delta y_i} \right| \quad (3.56)$$

The ij term refers to the off-diagonal contribution, while the ii term is the diagonal, or Fickian term. The interaction effect is notable when the ratio of the interaction term (denominator) to the Fickian term (numerator) is significant. For the ternary liquid mixture, diffusing in air, the matrix of relative interaction terms shown in figure 3.15 is simply:

$$\begin{pmatrix} - & \frac{k_{12}^\bullet \Delta y_2}{k_{11}^\bullet \Delta y_1} & \frac{k_{13}^\bullet \Delta y_3}{k_{11}^\bullet \Delta y_1} \\ \frac{k_{21}^\bullet \Delta y_1}{k_{22}^\bullet \Delta y_2} & - & \frac{k_{23}^\bullet \Delta y_3}{k_{22}^\bullet \Delta y_2} \\ \frac{k_{31}^\bullet \Delta y_1}{k_{33}^\bullet \Delta y_3} & \frac{k_{32}^\bullet \Delta y_2}{k_{33}^\bullet \Delta y_3} & - \end{pmatrix} \quad (3.57)$$

where 1=IPA, 2=ethanol, 3=methanol. So, for example, the second term in the first row indicates the ratio of diffusive flux of component 1 (IPA) caused by concentra-

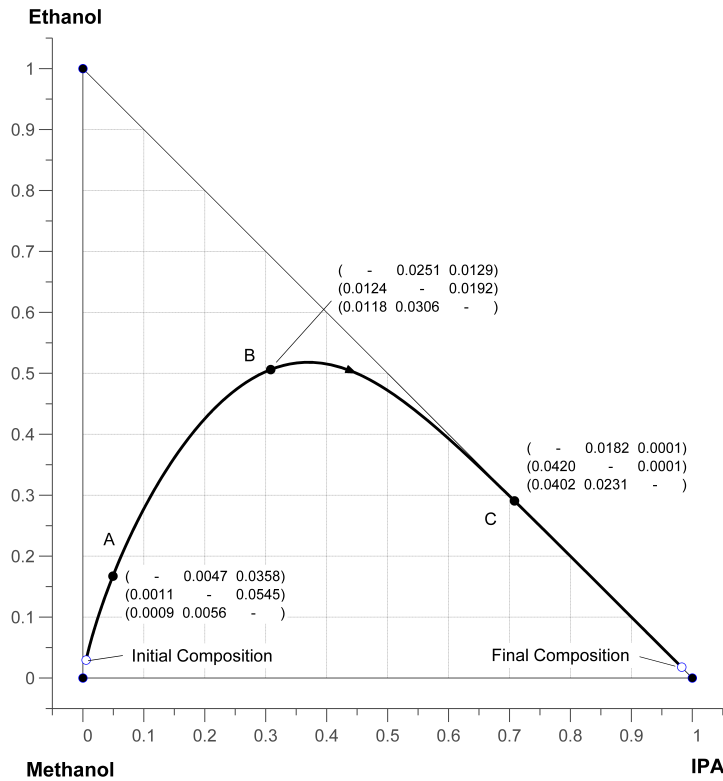


Figure 3.15: Example evaporation trajectory for IPA/ethanol/water; $T^G = 80^\circ\text{C}$, $u^G = 0.5\text{m/s}$, $d = 0.03\text{m}$

tion difference of component 2 (ethanol), to simple Fickian diffusion of component 1 (caused by its own concentration gradient). For the conditions of figure 3.15, the largest off-diagonal term at point A is 0.0545 (5.4%), for point B the largest terms is 0.0306 (3.6%), while for point C the largest off-diagonal term is 0.0402 (4.02%). These figures suggest that the interaction terms are not very significant under the chosen conditions. Under other circumstances however, the interaction terms may be an important factor; section 4.4 examines interaction effects where the gas-phase is pre-loaded with one component of the ternary mixture, in which cases the interaction terms may be significant.

Figure 3.16 shows composition profiles in the notional film at the vapour-liquid interface at each of the highlighted points of interest A, B, and C of figure 3.15. The composition profiles are found from equation 3.10 and are linear in the dimensionless film thickness η ($\eta = 0$ is the vapour-liquid interface, while $\eta = 1$ is the edge of the notional film, at which point the gas phase concentration is that of the bulk gas phase). For IPA, which increases in concentration from A to B to C, the profiles likewise increase from A to B to C. For ethanol, the liquid concentration increases from A to B,

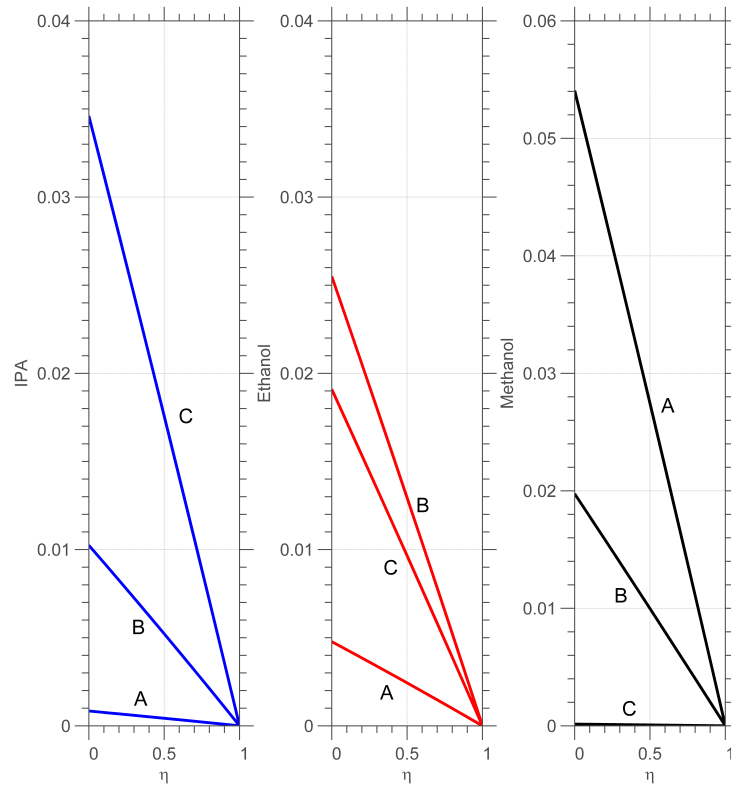


Figure 3.16: Example film concentration profiles (mole-fractions) for IPA/ethanol/water; the profiles A, B, C correspond to the points A, B and C on figure 3.15; $T^G = 80^\circ\text{C}$, $u^G = 0.5\text{m/s}$, $d = 0.03\text{m}$; gas-phase is pure air

then decreases to C; this pattern is evident in the profiles of figure 3.16 also. Finally, the methanol concentration decreases from A to B to C, which pattern is also replicated in the composition profiles.

The component fluxes along the evaporation trajectory of figure 3.15 are represented by the curves in figure 3.17, where the fluxes are plotted against a dimensionless path length ζ for the evaporation trajectory. The arrows in the figure indicate the relative directions of the diffusive fluxes; air diffuses in the direction opposite to the components of the ternary mixture. The flux for methanol is initially high then falls as the liquid becomes leaner in methanol over the course of the trajectory. The ethanol flux is initially small, then rises as trajectory moves from point A to B on figure 3.15, before falling again as the trajectory tends towards pure IPA. The IPA flux is initially near zero as there is almost no IPA in starting composition, before rising as the residual liquid becomes steadily richer in IPA.

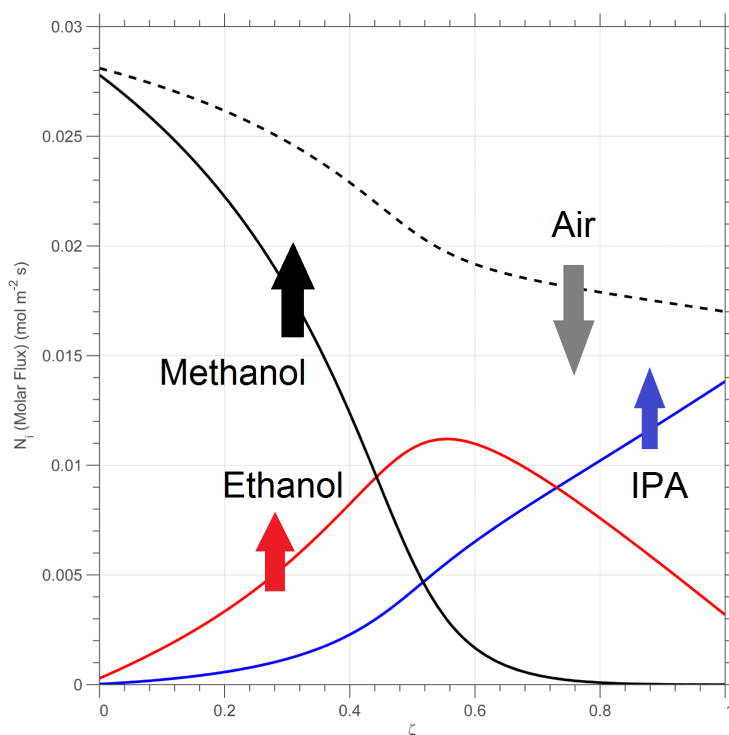


Figure 3.17: Component fluxes along trajectory of figure 3.15 for IPA/ethanol/water; x-axis is dimensionless path length; $T^G = 80^\circ\text{C}$, $u^G = 0.5\text{m/s}$, $d = 0.03\text{m}$

3.3.5 Ternary Evaporation Maps

Using the algorithm for generation of evaporation maps in table 3.5, evaporation maps have been computed for 6 example ternary mixtures listed in table 2.1, and are shown in figures 3.18-3.23. Each of these maps involve evaporation into pure air; the effect of pre-loading the gas phase with one of the ternary components is considered in section 4.3. Note that the evaporation trajectories in the various maps are computed using the same model used to compute composition trajectories of experimental data in figures 3.5-3.8. The solvents employed in the following maps are commonly used (apart from chloroform) in various mixtures, in the pharmaceutical industry (Paudel et al. 2013). A number of the mixtures exhibit separation boundaries which are the subject of chapter 6.

IPA-ethanol-methanol Figure 3.15 showed a single evaporation trajectory; when a complete set of trajectories is developed, the map shown in figure 3.18 results, where the trajectories run from the (unstable) methanol node to the (stable) IPA node; pure ethanol is a saddle in this case. This represents a relatively simple topology, containing no pseudo-azeotropes. The corresponding residue curve map in figure 2.2a shows

qualitatively similar behaviour, with no azeotropes. The pure component nodes have been annotated with the calculated wet-bulb temperatures from table 3.6. The unstable methanol node has the lowest T_{WB} of the components in the mixture (-2.8°C), while the stable IPA node has the highest (12.6°C), with an intermediate value for ethanol (8.0°C). This follows the same pattern as the normal boiling points for these components (as would be required for the map evaporation map to be qualitatively similar to the residue curve map for the mixture). In this mixture, and all those that follow, unstable nodes correspond to locally lowest values of T_{WB} , while stable nodes correspond to locally highest values. All evaporation trajectories in this case (evaporation into pure air) end at pure IPA; in other words, the final (differentially small) drop of mixture will be pure IPA, regardless of the initial composition. The trajectories tend to hug the IPA/ethanol edge rather closely when methanol is eliminated from the mixture, so that the final stage of evaporation/drying will be of an essentially binary IPA/ethanol mixture. Note that the final composition is not dependent on the initial composition, as this mixture does not contain any separation boundaries.

Water-ethanol-methanol The water-ethanol-methanol map in figure 3.19 has a single binary pseudo-azeotrope on the IPA-water axis. For this mixture, the trajectories run from the pure methanol node to either the pure ethanol or pure water nodes. The ethanol-water pseudo-azeotrope is a saddle in this mixture. The wet-bulb temperatures shown on figure 3.19 show how trajectories flow from a low value of T_{WB} to a high value, e.g. from methanol (-2.8°C) to ethanol (8.0°C). Just as in the *distillation boundaries* that occur in residue-curve maps, there is a separation boundary running from the pure methanol (unstable) node to the water-ethanol saddle. This boundary divides the ternary diagram into two regions, one for which all initial compositions terminate at the ethanol node, and one for which all compositions terminate at the water node. Thus, the final drop of liquid will be pure water in some cases, and pure ethanol otherwise, depending on the initial composition. Note that the wet-bulb temperature of the water/ethanol saddle node is intermediate in value to the T_{WB} of ethanol and water, so that one would expect it to be a saddle (Chapter 5 demonstrates numerical method for determining stability of the various nodes in evaporation maps). Trajectories that initiate on one side of the boundary remain on that side; thus, a relatively small difference in the initial composition can lead to a large difference in the residual composition (either pure ethanol or pure water). The corresponding residue curve map in figure 2.2b shows qualitatively similar behaviour, with a single azeotrope between water and ethanol.

IPA-water-ethanol The IPA-water-ethanol mixture in figure 3.20 has two pseudo-azeotropes, one on the IPA-water axis and one on the ethanol-water axis. In this case, the map consists of trajectories running from the ethanol-water binary (unstable) node,

to either the pure water or pure IPA node. The wet-bulb temperature of the unstable ethanol-water node (7.8°C) is the lowest of the fixed points of the mixture; trajectories between it and the stable IPA node ($T_{WB} = 20.0^{\circ}\text{C}$) pass by the saddles at pure ethanol ($T_{WB} = 15.9^{\circ}\text{C}$) and IPA/water ($T_{WB} = 10.7^{\circ}\text{C}$), which is consistent in that each of these saddles has a wet-bulb temperature between those of pure IPA and water. A separation boundary runs from the ethanol-water binary pseudo-azeotrope to the IPA-water pseudo-azeotrope. Thus, the terminal composition of the evaporating mixture will be pure IPA in some cases and pure water otherwise, depending on the initial composition. Figure 2.2c shows the equivalent residue curve map, which displays qualitatively similar features - an unstable binary azeotrope between water and ethanol, and a saddle azeotrope between IPA and water.

Ethanol-MEK-toluene The ethanol-MEK-toluene mixture in figure 3.21 has topology similar to the IPA-water-ethanol mixture in terms of number and type of unstable/stable/saddle nodes. Trajectories flow from the unstable ethanol/MEK node ($T_{WB} = 5.6^{\circ}\text{C}$) to either the stable ethanol node ($T_{WB} = 8.0^{\circ}\text{C}$) or the stable toluene node ($T_{WB} = 20.9^{\circ}\text{C}$). Pure MEK ($T_{WB} = 7.9^{\circ}\text{C}$) and the ethanol/toluene node ($T_{WB} = 6.8^{\circ}\text{C}$) are saddles in this mixture. As with the IPA-water-ethanol mixture, a separation boundary runs between the binary pseudo-azeotropes. In the region of low ethanol concentration, the evaporation trajectories tend to hug the MEK/toluene edge, so that the residual liquid is essentially a binary MEK/toluene mixture during the final stages of evaporation. The residue curve map of figure 2.2d displays similar features, with two binary azeotropes: ethanol/MEK and ethanol/toluene.

Dichloromethane/methanol/ ethyl acetate The topology for DCM/methanol/ethyl acetate in figure figure 3.22 is similar to those of IPA/ethanol/water and ethanol/MEK/toluene, one with one unstable node at the DCM-methanol pseudo-azeotrope, and one saddle at the ethanol/toluene azeotrope. Trajectories run from the DCM/methanol unstable node ($T_{WB} = -18.1^{\circ}\text{C}$) to either the methanol node ($T_{WB} = -2.8^{\circ}\text{C}$) or the ethyl-acetate node ($T_{WB} = 4.2^{\circ}\text{C}$). Pure DCM ($T_{WB} = -16.7^{\circ}\text{C}$) and the ethyl-acetate/methanol binary pseudo-azeotrope ($T_{WB} = -4.0^{\circ}\text{C}$) are saddles in this mixture. A separation boundary runs between the binary pseudo-azeotropes, separating the composition space into a region where the terminal composition is pure methanol, and one where the terminal composition is pure ethyl-acetate.

As with the preceding mixtures, the qualitative features of the corresponding residue curve map, shown in figure 2.2e, are similar.

Acetone-chloroform-methanol Figure 3.23 shows the evaporation map for acetone/chloroform/methanol, which has 3 binary pseudo-azeotropes, and a single ternary

pseudo-azeotrope. Trajectories run from the acetone-methanol stable node ($T_{WB} = -9.2^\circ\text{C}$) to either the acetone-chloroform binary node ($T_{WB} = -3.6^\circ\text{C}$), or to the pure methanol node ($T_{WB} = -2.8^\circ\text{C}$). Similarly, trajectories from the chloroform-methanol binary node ($T_{WB} = -9.6^\circ\text{C}$) run to either the acetone-chloroform binary node, or to pure methanol. In this mixture, pure acetone ($T_{WB} = -9.5^\circ\text{C}$) and pure methanol are saddles. The ternary pseudo-azeotrope is also a saddle. Separation boundaries run from the acetone-methanol binary to the chloroform-methanol binary, and from the pure methanol node to the acetone-chloroform node. The final composition of an evaporating mixture will thus either be pure methanol or that of the acetone/chloroform binary pseudo-azeotrope, depending on the initial liquid composition. Figure 2.2f shows the equivalent residue curve map which shows qualitatively similar characteristics.

As noted for each of the mixtures above, the topology of the evaporation maps are similar to those of the corresponding RCMs; the topology is also consistent in the sense of Guirikov (1958) who showed that for ternary simple distillation the combination of the singular points of different types satisfies the rule:

$$2N_3 + N_2 + N_1 = 2S_3 + S_2 + 2 \quad (3.58)$$

where $N_3(S_3)$ is the number of ternary nodes (saddles), $N_2(S_2)$ is the number of binary nodes (saddles), and N_1 is the number of pure component nodes (Kiva et al. 2003). This consistency does not hold when the gas phase is loaded with a component as section 4.3 demonstrates. The qualitative similarity of residue curve maps and evaporation maps is not surprising when one considers the fixed points of each type of map. For residue curve maps the topology in terms of the location of azeotropes is governed by consideration of vapour-liquid equilibria (VLE) only - see section 2.2. So, at a given pressure, the location of the azeotropes is dictated by the VLE model only. For evaporation maps, the topology in terms of pseudo-azeotropes is due to both VLE and mass transfer considerations in the film at the vapour-liquid interface - see section 3.1. It is the solution of the combination of factors that causes the azeotrope (RCM) and pseudo-azeotrope (Evaporation Maps) to have different compositions. Computed values of azeotropes and pseudo-azeotropes can be compared by examining table 4.2 (for azeotropes) and table 3.6 (for pseudo-azeotropes).

3. EVAPORATION MAPS FOR GAS PHASE LIMITED CONDITIONS

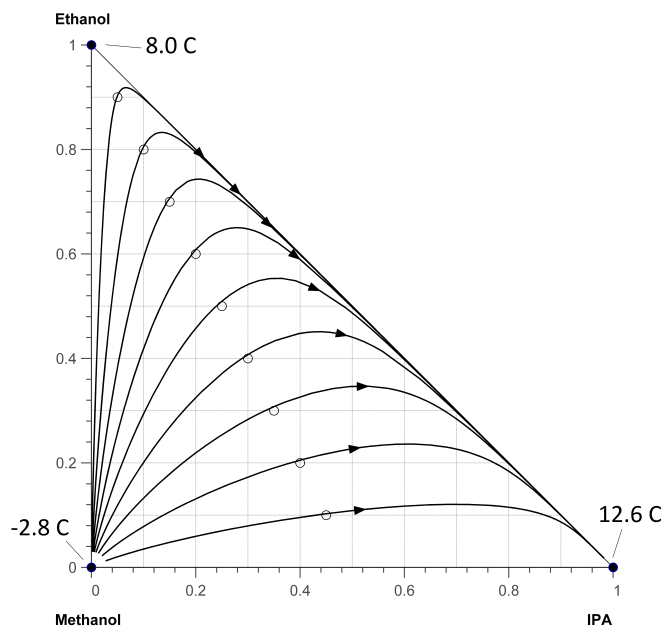


Figure 3.18: Evaporation map for IPA-ethanol-methanol; closed circles denote fixed points; open circles denote pre-specified points for trajectories; arrows indicate direction of composition changes; annotations are wet-bulb temperatures; $T^G = 20^\circ\text{C}$, $u^G = 0.5\text{m/s}$, $d = 0.03\text{m}$

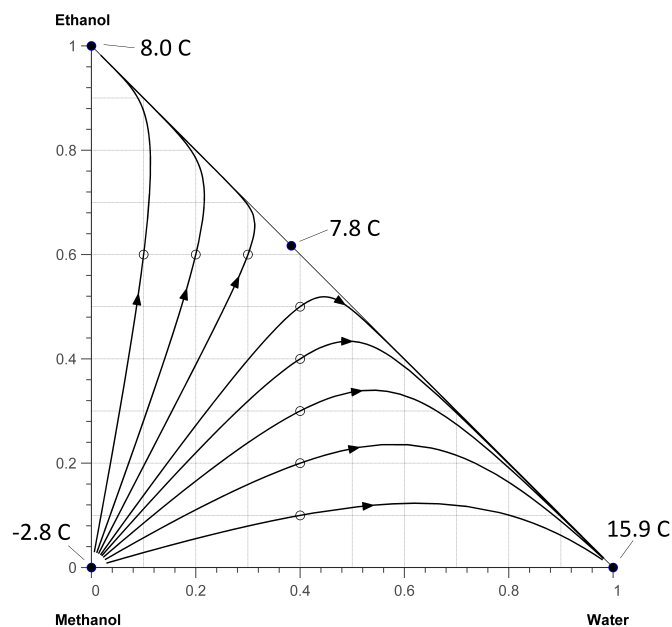


Figure 3.19: Evaporation map for water-ethanol-methanol; annotations are wet-bulb temperatures; $T^G = 20^\circ\text{C}$, $u^G = 0.5\text{m/s}$, $d = 0.03\text{m}$

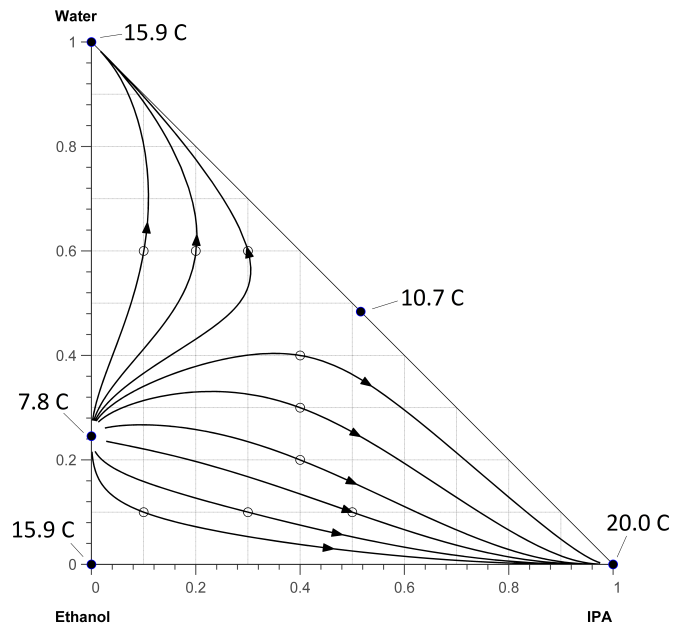


Figure 3.20: Evaporation map for IPA-water-ethanol; annotations are wet-bulb temperatures; $T^G = 20^\circ\text{C}$, $u^G = 0.5\text{m/s}$, $d = 0.03\text{m}$

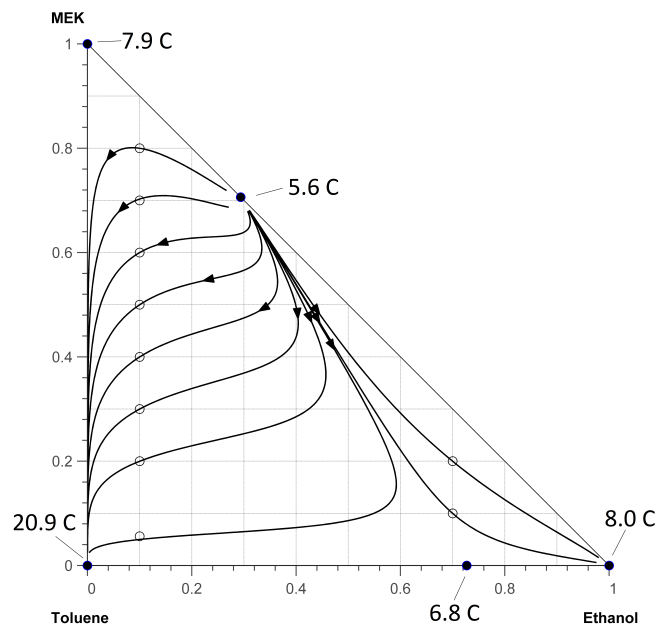


Figure 3.21: Evaporation map for Ethanol-MEK-Toluene; annotations are wet-bulb temperatures; $T^G = 20^\circ\text{C}$, $u^G = 0.5\text{m/s}$, $d = 0.03\text{m}$

3. EVAPORATION MAPS FOR GAS PHASE LIMITED CONDITIONS

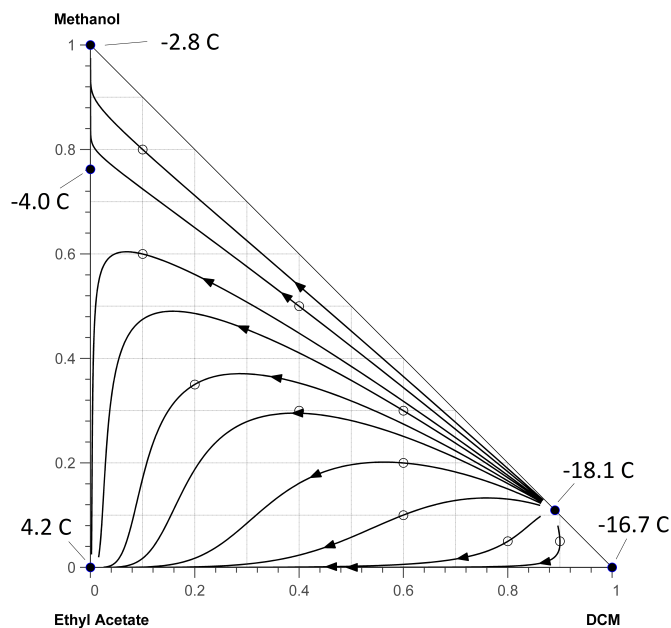


Figure 3.22: Evaporation map for Dichloromethane/methanol/ethyl acetate; annotations are wet-bulb temperatures; $T^G = 20^\circ\text{C}$, $u^G = 0.5\text{m/s}$, $d = 0.03\text{m}$

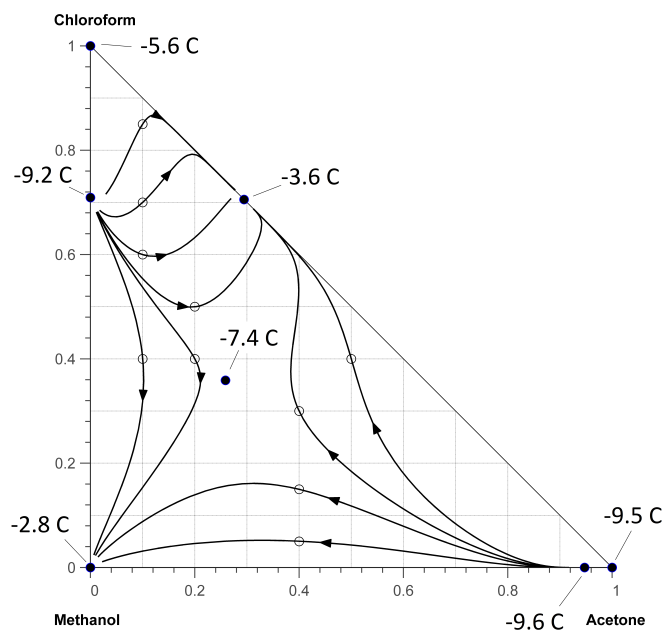


Figure 3.23: Evaporation map for Acetone/chloroform/methanol; annotations are wet-bulb temperatures; $T^G = 20^\circ\text{C}$, $u^G = 0.5\text{m/s}$, $d = 0.03\text{m}$

3.4 Reduction of Multicomponent Wet-Bulb Model to Single Component Case

The formulation of the multicomponent wet-bulb model in section 3.1.4 can be reduced to a more familiar form for a single liquid component in an inert gas (e.g. air-water) as follows. The multicomponent form of the heat balance in equation 3.44 is implicit in the multicomponent mass fluxes N_i . When the explicit solution to the Maxwell-Stefan equations for the film is used, the expressions for the fluxes must be solved together with the equilibrium expressions for each of the ternary components (equations 3.38, 3.39, 3.40) and the summation of vapour mole-fractions in 3.42. However, for a single liquid component A and pure air as the gas phase, equation 3.44 (recalling that q_I is zero), reduces to:

$$q_V = h_V \Xi (T^G - T^I) = N_A \left\{ \bar{H}_A^G - \bar{H}_A^L \right\} = N_A \Delta H_A^{vap} - N_A M_A C_{pA} (T^G - T^I) \quad (3.59)$$

We may neglect the last term above as it is small relative to the latent heat term, allowing an expression for the wet-bulb temperature T^I to be found. Expanding Ξ , and solving for N_A gives

$$N_A = \frac{h^G}{\Delta H^{vap}} \left[\frac{\Phi}{\exp(\Phi) - 1} \right] (T^G - T^I) \quad (3.60)$$

The mass-transfer and heat-transfer factors ϕ and ϕ_H^G are given by (Taylor & Krishna 1993):

$$\phi = \frac{N_A}{ck_A} \quad \text{and} \quad \phi_H^G = \frac{N_A C_{pA}}{h^G}$$

where k_A is a binary mass transfer coefficient, so that eliminating N_A gives:

$$\phi = \phi_H^G \frac{h^G}{C_{pA} k_A} \quad (3.61)$$

For the film theory of mass transfer (Bird et al. 2002) we can write ϕ and ϕ_H^G as

$$\phi = \ln \left[1 + \frac{y_A^I - y_A^G}{1 - y_A^G} \right] \quad \text{and} \quad \phi_H^G = \ln \left[1 + \frac{C_{pA} (T^G - T^I)}{\Delta H_A^{vap}} \right]$$

so that

$$\ln \left[1 + \frac{y_A^I - y_A^G}{1 - y_A^G} \right] = \frac{h^G}{C_{pA} k_A} \ln \left[1 + \frac{C_{pA} (T^G - T^I)}{\Delta H_A^{vap}} \right] \quad (3.62)$$

which is the equation for wet-bulb temperature of a pure component (corrected for mass transfer rate) derived in Bird et al. (2002)¹. Solving for T^I gives the wet-bulb

¹Ref. equation 22.8-34 of Bird et al. (2002)

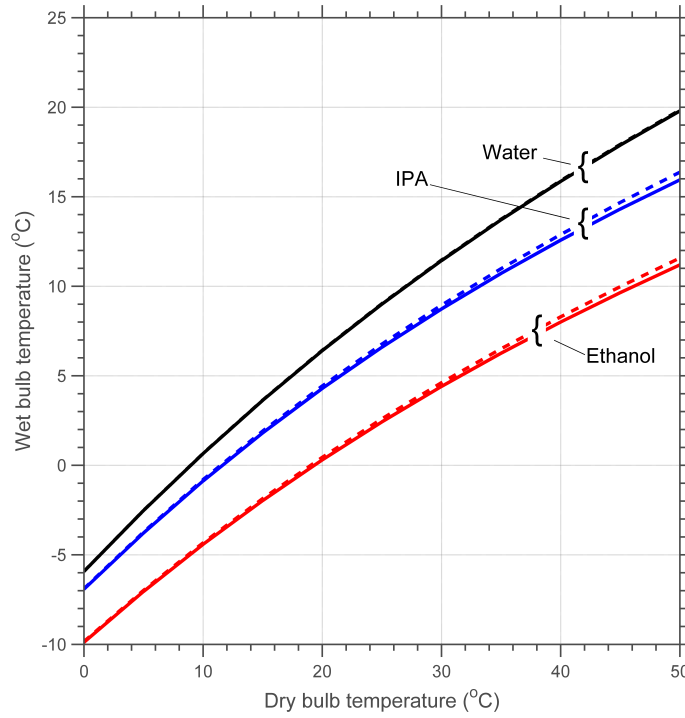


Figure 3.24: Comparison of multicomponent algorithm (solid lines) with prediction from equation 3.63 (dashed lines); gas phase is pure air, $u^G = 0.5\text{m/s}$, $d = 0.03\text{m}$

temperature for pure component A:

$$T^I = \frac{\Delta H_A^{vap}}{Cp_A} \left[\frac{Cp_A T^G}{\Delta H_A^{vap}} - \left[1 + \frac{y_A^I - y_A^G}{1 - y_A^G} \right] \left(\frac{Cp_A k_A}{h^G} \right) + 1 \right] \quad (3.63)$$

This equation is actually implicit in T^I due to the dependence of y_A^I on T^I via the partial pressure at the wet-bulb temperature: $y_A^I = p_A(T^I)/P$. Equation 3.63 (or equation 3.62) may be solved numerically for T^I when y_G and T^G are given (using `fsolve` method in Matlab (Matlab 2010)). The pure-component wet-bulb temperatures, obtained from numerical solution to equation 3.63, can be compared with the calculated values from the full multicomponent formulation. Figure 3.24 shows such a comparison for water, IPA and ethanol in pure air, as a function of the dry-bulb (air) temperature. The values obtained by both methods are in close agreement, considering that the method of equation 3.63 ignores sensible heat terms.

3.5 Chapter Summary and Conclusions

A scheme for computation of evaporation maps for non-ideal ternary liquid mixtures was developed, for conditions of gas-phase limited heat and mass-transfer. These maps are analogous to residue curve maps employed in the analysis of distillation processes, but include non-equilibrium effects caused by diffusion in the gas film at the vapour-liquid interface. In order to construct the maps, it is firstly necessary to (1) determine the location of the *pseudo-azeotropes* that are fixed points of the maps, and (2) determine the wet-bulb temperature of mixtures in a neighbourhood of the unstable nodes in the mixture. Related algorithms were developed for calculating (1) and (2) using a Newton's-method approach with analytic forms for the Jacobian matrices. A multicomponent Maxwell-Stefan mass transfer model has been used throughout. The use of the same basis for the calculation of fluxes, wet-bulb temperature and pseudo-azeotropes ensures that there is consistency between the pseudo-azeotrope locations and the computed evaporation trajectories.

The calculated evaporation trajectories are at the equivalent mixture wet-bulb temperature at every point on the map and therefore follow a wet-bulb temperature surface for a given set of conditions; it is the projection of the compositions of the trajectories onto the ternary diagram that forms the evaporation map. For a given geometry and evaporation conditions (y^G , T^G , u^G), it is possible in principle to determine the composition of the residual solvent composition for any particular initial composition (provided the assumption of gas-phase limited mass transfer applies).

This analysis of this chapter has used a planar geometry as a basis. The evaporation maps track composition changes that occur in ternary mixtures in such situations as horizontal liquid films, or trays of solvent-wet material in a tray dryer, where the resistance to heat and mass transfer lies in the gas phase, and where the gas concentration does not vary significantly with length in the direction of gas flow. In the next several chapters, certain features of evaporation maps are developed and analysed.

Chapter 4

Bifurcations in Evaporation Maps

4.1 Introduction

In this chapter there are two areas of focus related to the topology of evaporation maps. Firstly, a method to calculate all pseudo-azeotropes in a ternary mixture is addressed and secondly, bifurcations which occur in evaporation maps with varying concentrations in the gas phase are studied. From the viewpoint of practical application of a drying or evaporation process, gas composition, temperature and velocity are normally available as design variables. We focus in this work on the effect of gas composition only in the bifurcation analysis of the maps. Where the gas is pre-loaded with a component of the ternary mixture, bifurcations are shown to occur in the maps and the topology of the map changes, with the appearance and disappearance of various nodes and saddles. By appropriate selection of the gas pre-loading concentration, the composition of a pseudo-azeotrope (where it exists) can be manipulated, up to a point where the pseudo-azeotrope disappears, leaving a pure component as the residue.

In chapter 3 a Newton-based method for the computation of pseudo-azeotropes under specified conditions of gas-phase composition, velocity and temperature was developed. For pure gas phase, the Newton method described therein (see table 3.2) may be used to determine the pseudo-azeotrope composition (and wet-bulb temperature), provided a reasonable initial estimate of the variables is provided. The location of *all* pseudo-azeotropes for a given mixture is more problematic, since the Newton-method approach will only converge to a single (local) solution if one exists; consequently, it may converge to a pure component, rather than the actual required solution if the initial estimate is not appropriate, and will not identify multiple solutions.

For the analogous problem of thermodynamic azeotropes, the computation of *all* such azeotropes is a surprisingly difficult task. Fidkowski et al. (1993a) developed a method based on a simple homotopy process to calculate all azeotropes in a homogeneous

mixture (single liquid phase); this method can also locate multiple solutions, although cases of multiple azeotropy are fortunately rare (Gaw & Swinton 1966). The method of Fidkowski et al. was extended to heterogeneous mixtures by Tolsma & Barton (2000a,b). Refer to section 2.2 for introductory material on azeotropy. In section 4.2.3 a method to track the various azeotropes in a ternary mixture is presented based on a separate tracking of each possible azeotrope (excluding multiple azeotropy). In section 4.2.4 a homotopy method is applied to track the various pseudo-azeotropes for ternary mixtures, under specified conditions of gas velocity, temperature and composition.

The maps generated were in chapter 3 were for a pure gas phase (pure air). In practice, the gas phase in a real evaporation or drying process will often be partially laden (pre-loaded) with one or more components of the liquid mixture, so it is of interest to know how the vapour phase concentration affects the topology of evaporation maps. Luna & Martinez (1998, 1999) analysed evaporation of batch and continuous processes and demonstrated by simulation how changes in the gas composition affected the location and existence of pseudo-azeotropes in ternary mixtures. Motivated by that work, in section 4.3 an approach is developed for quantifying the changes in topology of the evaporation maps as the gas phase concentration is varied. The acetone-chloroform-methanol mixture is used as an example, as it has the most complex topology of the ternary mixtures considered so far. The loading of the gas phase with each of the three components in the mixture is considered separately. Ultimately, there is a qualitative change in the evaporation map known as a *bifurcation* as the concentration parameter increases. In section 4.3 a numerical continuation method is developed to show systematically how the topology of evaporation maps is affected by gas composition. Bifurcation diagrams for the various pseudo-azeotropes show how the topology of the maps changes with pre-loading of the gas phase.

Finally, in section 4.4 an analysis of interaction effects due to multicomponent mass transfer in the gas phase is presented. In particular, interaction effects due to the phase pre-loading is considered.

4.2 Azeotropes and Pseudo-Azeotropes via Homotopy

In this section the homotopy method for computation of azeotropes is presented, and a method for location of pseudo-azeotropes is developed by analogy. Firstly, in section 4.2.1, a method for computation of azeotropes using a Newton-method approach is discussed; this uses an analytic form of the Jacobian of the governing equations which is an approach that, to the author's knowledge, has not been previously published. Computed results are compared with azeotropic compositions of a number of mixtures from AspenPlus. This approach has parallels with the Newton-method approach for location of pseudo-azeotropes from section 3.2.3.

4.2.1 Computation of Azeotropes By Newton's Method

The definition of the condition for an azeotrope to exist is given by:

$$f(\mathbf{x}) \equiv \mathbf{y}^*(\mathbf{x}) - \mathbf{x} = \mathbf{0} \quad (4.1)$$

where $\mathbf{y}^*(\mathbf{x})$ represents the vapour in thermodynamic equilibrium with liquid of composition \mathbf{x} . For an n -component mixture there are $n - 1$ independent compositions (mole fractions) in each phase with the additional constraints that

$$\sum_{i=1}^n x_i = 1 \quad (4.2a)$$

$$\sum_{i=1}^n y_i = 1 \quad (4.2b)$$

$$x_i \geq 0 \quad i = 1, 2, \dots, n \quad (4.2c)$$

The elements of the equilibrium vapour composition \mathbf{y}^* can be expressed in terms of the liquid composition by

$$y_i^* = \frac{x_i \gamma_i(x_i, T) p_i}{P} \quad (4.3)$$

where the non-ideality in the liquid phase is captured by the activity coefficient γ_i , which in this work is described by the NRTL equation (Prausnitz et al. 1986). Equations 4.1-4.3 is a system of $2c+1$ equations in $2c+1$ unknowns: $x_1 \cdots x_n$, y_1, \dots, y_n and temperature T . This reduces to a problem of $c + 1$ unknowns in $c + 1$ variables ($\bar{\mathbf{x}} = x_1 \cdots x_n, T$) by relating the y_i^* and x_i using equation 4.3 directly, so that for a ternary mixture an equivalent statement to the azeotrope condition of equation 2.25 is

$$\mathbf{F}(\bar{\mathbf{x}}) = \begin{bmatrix} x_1 \left(\frac{\gamma_1 p_1}{P} - 1 \right) \\ x_2 \left(\frac{\gamma_2 p_2}{P} - 1 \right) \\ x_3 \left(\frac{\gamma_3 p_3}{P} - 1 \right) \\ \sum_{i=1}^3 x_i - 1 \end{bmatrix} = \mathbf{0} \quad (4.4)$$

The Jacobian for the set of equations 4.4 is

$$\mathbf{J}(\bar{\mathbf{x}}) = \left[\frac{\partial F_i}{\partial \bar{x}_j} \right]_{\mathbf{x}=\mathbf{x}^s} = \begin{pmatrix} \frac{p_1}{P} \left(1 + x_1 \frac{\partial \gamma_1}{\partial x_1} \right) - 1 & x_1 \frac{p_1}{P} \frac{\partial \gamma_1}{\partial x_1} & x_1 \frac{p_1}{P} \frac{\partial \gamma_1}{\partial x_3} & -x_1 \frac{p_1}{P} \frac{\partial p_1}{\partial T} \\ x_2 \frac{p_2}{P} \frac{\partial \gamma_2}{\partial x_1} & \frac{p_2}{P} \left(1 + x_2 \frac{\partial \gamma_2}{\partial x_2} \right) - 1 & x_2 \frac{p_2}{P} \frac{\partial \gamma_2}{\partial x_3} & -x_2 \frac{p_2}{P} \frac{\partial p_2}{\partial T} \\ x_3 \frac{p_3}{P} \frac{\partial \gamma_3}{\partial x_1} & x_2 \frac{p_3}{P} \frac{\partial \gamma_3}{\partial x_2} & \frac{p_3}{P} \left(1 + x_3 \frac{\partial \gamma_3}{\partial x_3} \right) - 1 & -x_3 \frac{p_3}{P} \frac{\partial p_3}{\partial T} \\ 1 & 1 & 1 & 0 \end{pmatrix} \quad (4.5)$$

To calculate the terms in equation 4.5 involving composition derivatives $\partial \gamma_i / \partial x_j$, the form derived by Taylor & Kooijman (1991) for $\partial \ln \gamma_i / \partial x_j$ is used, summarised in appendix B.2. This is then converted to the form required using the following relationship:

$$\frac{\partial \gamma_i}{\partial x_j} = \gamma_i \frac{\partial \ln \gamma_i}{\partial x_j} \quad (4.6)$$

The derivatives of vapour pressure with respect to temperature in the Jacobian of equation 4.5 are found from the Antoine equation given by equation 3.52 and the fact that

$$\frac{\partial p_i}{\partial T} = p_i \frac{\partial \ln p_i}{\partial T} \quad (4.7)$$

The method for the computation of the azeotropes is summarised in table 4.1. The solution of the linearised set of equations in step 4 is accomplished using lower/upper (LU) decomposition by the "backslash" operator in Matlab (Matlab 2010).

Table 4.2 shows computed values of the azeotropes that appear in figures 2.2b-2.2f. The table also shows comparison with values generated using AspenPlus (AspenTech 2014), indicating reasonably good agreement between both sets of values. The vapour pressures used in these calculations are based on correlation from Prausnitz et al. (1986) (see appendix B.3), whereas AspenPlus uses its own internal database; consequently, some disparity would not be unexpected.

4.2.2 Overview of Homotopy Methods

In chapter 3 a method for computation of binary and ternary pseudo-azeotropes was outlined. In essence, the solution scheme (see table 3.3) solves for the roots of a sys-

Table 4.1: Calculation of azeotropes using Newton's method (with analytic Jacobian)

Given: operating pressure P
1. Initial estimate of compositions \mathbf{x} and temperature T ; $\bar{\mathbf{x}} = x_1 \cdots x_n, T$
2. Evaluate the residuals $F(\mathbf{x}) = 0$ (equation 4.4)
3. Compute the Jacobian matrix \mathbf{J} (equation 4.5) using analytic form of $\partial\gamma_i/\partial x_j$ (equation 4.6) and appendix B.2
4. Compute $\delta\bar{\mathbf{x}} = \mathbf{J} \backslash \mathbf{F}$
5. Update the estimates of $\bar{\mathbf{x}}$: $[\bar{\mathbf{x}}^{NEW}] = \bar{\mathbf{x}} + \delta\bar{\mathbf{x}}$
6. If $\text{err} < \text{tolerance}$, stop, else return to step 1

tem of coupled non-linear (algebraic) equations (for a ternary system) using Newton's method with an analytic Jacobian. In section 4.2.1, a method for computation of binary and ternary azeotropes was presented, again using a Newton-method approach. However, Newton's (or Newton-Raphson) method suffers from certain well-known shortcomings (Kuno & Seader 1988):

- the starting point must be in the vicinity of a root (i.e. the method is only locally convergent)
- Newton's method can locate (at best) a single root even though multiple solutions may exist

While certain other approaches, such as the global terrain method of Lucia & Feng (2002) are able to avoid these deficiencies, conventional root-finders cannot be used to robustly locate all of the solutions to equation 4.4 for a multicomponent mixture since in general it is a nonlinear constrained problem with multiple solutions (Fidkowski et al. 1993b). A homotopy procedure is an approach to solving a "difficult" problem $\mathbf{D}(\mathbf{x}) = 0$ by firstly solving an "easy" problem $\mathbf{E}(\mathbf{x}) = 0$ that has a similar structure and the same number of variables (Bausa & Marquardt 2000). The homotopy function is defined by

$$\mathbf{H}(\mathbf{x}, \lambda) = \lambda \mathbf{D}(\mathbf{x}) + (1 - \lambda) \mathbf{E}(\mathbf{x}) \quad (4.8)$$

which involves both the easy and hard problems and the homotopy parameter λ . The solution of $\mathbf{H}(\mathbf{x})$ for $0 \leq \lambda \leq 1$ is found by solving the "easy" problem $\mathbf{H}(\mathbf{x}, \lambda = 0) = \mathbf{E}(\mathbf{x}) = 0$ and then gradually moved to the "difficult" problem $\mathbf{H}(\mathbf{x}, \lambda = 1) = \mathbf{D}(\mathbf{x}) = 0$ by increasing value of the parameter λ from zero to 1.

In the following sections, a homotopy method is outlined that tracks *all* azeotropes in a given mixture starting from a pure component (at $\lambda = 0$) to the actual value (at $\lambda = 1$). This approach is based on the method of Fidkowski et al. (1993a). A similar

Azeotropes	Calculated composition	AspenPlus Composition	Calculated $T(^{\circ}C)$	AspenPlus $T(^{\circ}C)$	Type	Figure
(1) Water	0.0837	0.0864	78.16	78.22	S, UN	2.2b, 2.2c
(2) Ethanol	0.9163	0.9136				
(1) IPA	0.6712	0.6728	80.21	80.18	S	2.2c
(3) Water	0.3288	0.3227				
(1) Ethanol	0.4908	0.4794	74.10	73.96	UN	2.2d
(3) MEK	0.5092	0.5206				
(1) Ethanol	0.7993	0.7985	76.21	76.27	S	
(3) Toluene	0.2007	0.2015				
(1) DCM	0.8641	0.8613	37.73	37.60	UN	2.2e
(2) Methanol	0.1359	0.1387				
(2) Methanol	0.7008	0.7035	62.16	62.25	S	
(3) Ethyl-acetate	0.2992	0.2965				
(1) Acetone	0.3513	0.3534	65.08	65.05	SN	
(2) Chloroform	0.6487	0.6466				
(2) Chloroform	0.6560	0.6575	53.77	53.74	UN	2.2f
(3) Methanol	0.3440	0.3425				
(3) Methanol	0.2220	0.2225				
(1) Acetone	0.7780	0.7775	55.20	55.24	UN	
(1) Acetone	0.3249	0.3272				
(2) Chloroform	0.2333	0.2322	57.30	57.31	S	
(3) Methanol	0.4418	0.4406				

Table 4.2: Azeotrope computation by Newton's method using analytic Jacobian, and comparison with values generated by AspenPlus; compositions in mole-fractions; $P = 1.013\text{bar}$; SN=stable node, UN=unstable node, S=saddle

approach is then used in section 4.2.4 to compute the pseudo-azeotropes of a mixture, given known gas-phase conditions.

4.2.3 Computation of Azeotropes by Homotopy Method

In this section a simple homotopy method is given to track the azeotropes in a given mixture. For this problem the component terms in $\mathbf{E}(\mathbf{x})$ and $\mathbf{D}(\mathbf{x})$ are given by

$$E_i(x_i) = \frac{x_i p_i}{P} \quad \text{and} \quad D_i(x_i) = \frac{x_i p_i \gamma_i}{P} \quad (4.9)$$

so that the homotopy is given by

$$H_i(x_i, \lambda) = \lambda \frac{x_i p_i}{P} + (1 - \lambda) \frac{x_i p_i \gamma_i}{P} \quad (4.10)$$

The expression for $E_i(x_i)$ above is simply Raoult's law, which applies to ideal mixtures. By gradually increasing λ from zero to 1, the effect of non-ideality in the liquid mixture is gradually introduced. Figure 4.1 shows the effect of the homotopy parameter on two binary mixtures. The acetone-chloroform mixture in figure 4.1a shows a maximum-boiling azeotrope, while the chloroform-methanol mixture in figure 4.1b has a minimum-boiling azeotrope. The degree of non-ideality increases as $\lambda \rightarrow 1$, as evidenced by the shape of the bubble-point curve which deviates more significantly from the near-straight line behaviour at $\lambda = 0$ (Raoult's law). At some value of λ , the binary azeotrope "appears", indicated by an intersection between the $y-x$ curve and the $y = x$ line; the binary azeotrope is a "bifurcation" of equation 4.10. The homotopy map of equation 4.10 can be expressed in the following form:

$$\mathbf{H}(\bar{\mathbf{x}}) = \begin{bmatrix} ((1 - \lambda) + \lambda\gamma_1) \left(\frac{x_1 p_1}{P} - 1 \right) - x_1 \\ ((1 - \lambda) + \lambda\gamma_2) \left(\frac{x_2 p_2}{P} - 1 \right) - x_2 \\ ((1 - \lambda) + \lambda\gamma_3) \left(\frac{x_3 p_3}{P} - 1 \right) - x_3 \\ \sum_{i=1}^n x_i - 1 \end{bmatrix} = \mathbf{0} \quad (4.11)$$

The Jacobian of the homotopy function can be written as (Tolsma & Barton 2000a):

$$\mathbf{J}_H(\bar{\mathbf{x}}) = \left[\frac{\partial H_i}{\partial x_j} \right]_{\mathbf{x}=\bar{\mathbf{x}}} = \begin{pmatrix} \alpha_1 - \lambda x_1 K_{11} & -\lambda x_1 K_{12} & -\lambda x_1 K_{13} & -x_1 \beta_1 \\ -\lambda x_2 K_{21} & \alpha_2 - \lambda x_2 K_{22} & -\lambda x_2 K_{23} & -x_2 \beta_2 \\ -\lambda x_3 K_{31} & -\lambda x_3 K_{32} & \alpha_3 - \lambda x_2 K_{23} & -x_3 \beta_3 \\ 1 & 1 & 1 & 0 \end{pmatrix} \quad (4.12)$$

where

$$\alpha_i = 1 - (\lambda K_i + (1 - \lambda)) \frac{p_i}{P}$$

$$\beta_i = \lambda \frac{\partial K_i}{\partial T} + \frac{1 - \lambda}{P} \frac{dp_i}{dT}$$

$$K_i = \gamma_i \frac{p_i}{P}$$

$$K_{ij} = \left(\frac{\partial K_i}{\partial x_j} \right)_{x_i(j), T, P}$$

and where the subscript $x_i(j)$ denotes that all mole fractions are held constant except x_j . In this work γ_i is assumed not to be a function of temperature, so that β_i is given by

$$\beta_i = \lambda \frac{p_i}{P} \frac{dp_i}{dT} + \frac{1 - \lambda}{P} \frac{dp_i}{dT}$$

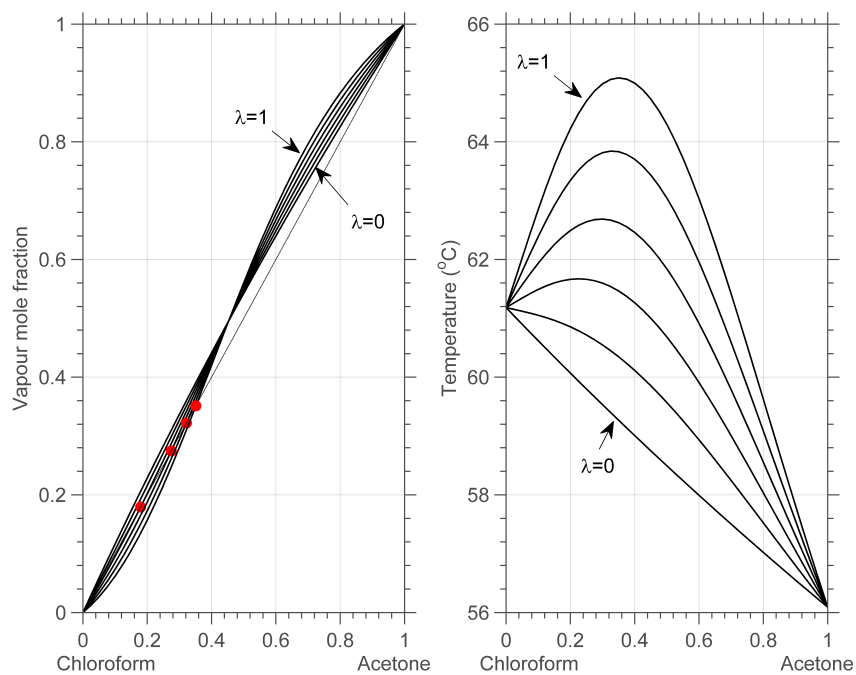
where the derivative of vapour pressure with respect to temperature is computed using equation 4.7. The K_{ij} when expanded are

$$K_{ij} = \frac{p_i}{P} \frac{d\gamma_i}{dx_j}$$

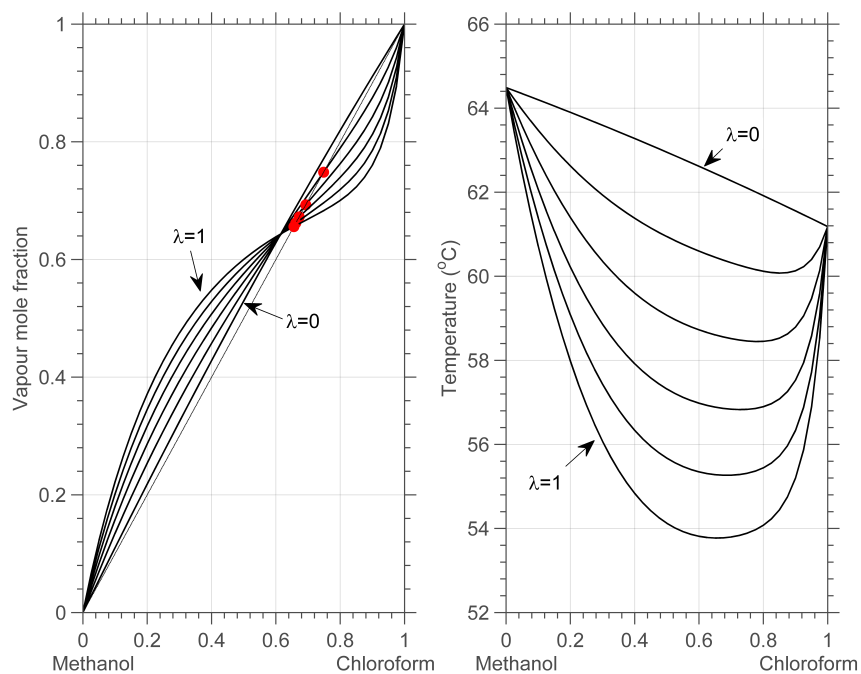
in which equation 4.6 is used for the derivative term, with the composition derivatives $\partial \ln \gamma_i / \partial x_j$ from appendix B.2.

The homotopy procedure adopted here is to gradually increase the value of λ in increments from 0 to 1, and to track the solutions to equation 4.11 for each possible azeotrope (namely three binary and a ternary azeotrope). The procedure is summarized in table 4.3.

Figure 4.2 shows the computed branches for the azeotropes of the acetone-chloroform-methanol mixture. For the binary pairs (AC,AM,CM) azeotropes are "born" at a certain value of λ from a solution on the branch corresponding to a pure component. The



(a) Acetone-chloroform mixture



(b) Chloroform-methanol mixture

Figure 4.1: Hypothetical $y - x$ composition and bubble-point at various values of homotopy parameter λ for binary mixtures; filled circles denote hypothetical azeotropic compositions

chloroform-methanol (CM) azeotrope appears at $\lambda \approx 0.05$, ending with a composition of $x_{Chloro} = 0.66$, $x_{MeOH} = 0.34$ at $\lambda = 1$. For acetone-chloroform (AC) the azeotrope first appears at $\lambda \approx 0.25$, ending with an azeotropic composition of $x_{Ace} = 0.35$, $x_{Chloro} = 0.65$ at $\lambda = 1$. Figure 4.2 also shows how the computed ternary azeotrope forms from a branch on the CM-binary branch at $\lambda \approx 0.21$, ending with $x_{Ace} = 0.33$, $x_{Chloro} = 0.23$, $x_{MeOH} = 0.44$ at $\lambda = 1$. These values at $\lambda = 1$ compare well with the azeotropic compositions computed directly in table 4.2. The azeotrope temperatures for each branch are also shown in figure 4.2; the temperatures at $\lambda = 1$ correspond to those computed directly in table 4.2.

Table 4.3: Homotopy method for tracking location of azeotropes in ternary mixture

-
1. Initialise homotopy parameter $\lambda = 0$
 2. Initialize \bar{x} ; for the AC (acetone-chloroform, 1-2) branch, initialise with $\bar{x} = [0.5, 0.5, 0.0, 60.0]$
 3. Compute the values of $\mathbf{H}(\bar{x})$ (equation 4.11)
 4. Compute the Jacobian matrix $\mathbf{J}_H(\bar{x})$ (equation 4.12)
 5. Compute $\delta\bar{x} = \mathbf{J}_H(\bar{x}) \setminus \mathbf{H}(\bar{x})$
 6. Update the estimates of \bar{x} : $[\bar{x}^{NEW}] = \bar{x} + \delta\bar{x}$
 7. If $\text{err} < \text{tolerance}$, stop, else return to step 3
 8. Increment λ and repeat from step 2 using updated \bar{x}
 9. Repeat for CM, AM and ACM (ternary) branches, using appropriate initialisation
-

4.2.4 Computation of Pseudo-Azeotropes by Homotopy Method

In this section, a similar homotopy approach to that adopted in the previous section is combined with the algorithm for pseudo-azeotrope computation developed in section 3.1.5. This allows the branches of the various pseudo-azeotropes to be tracked individually as the homotopy parameter λ is varied from 0 to 1. This homotopy procedure addresses the effect of increasing liquid-phase non-ideality on the location of the pseudo-azeotropes; it does not address mass-transfer effects in the gas phase directly.

The effects of the homotopy procedure on the location of the pseudo-azeotropes can be seen in the selectivity and wet-bulb temperature plots in figure 4.3. The acetone-chloroform mixture (4.3a) has a maximum wet-bulb temperature, while the chloroform/methanol mixture (4.3b) has a minimum wet-bulb temperature; the corresponding mixtures have maximum-boiling and minimum boiling azeotropes respectively. The degree of non-ideality incorporated in the problem increases as $\lambda \rightarrow 1$; the shape of the wet-bulb temperature curve deviates more strongly from the near straight-line

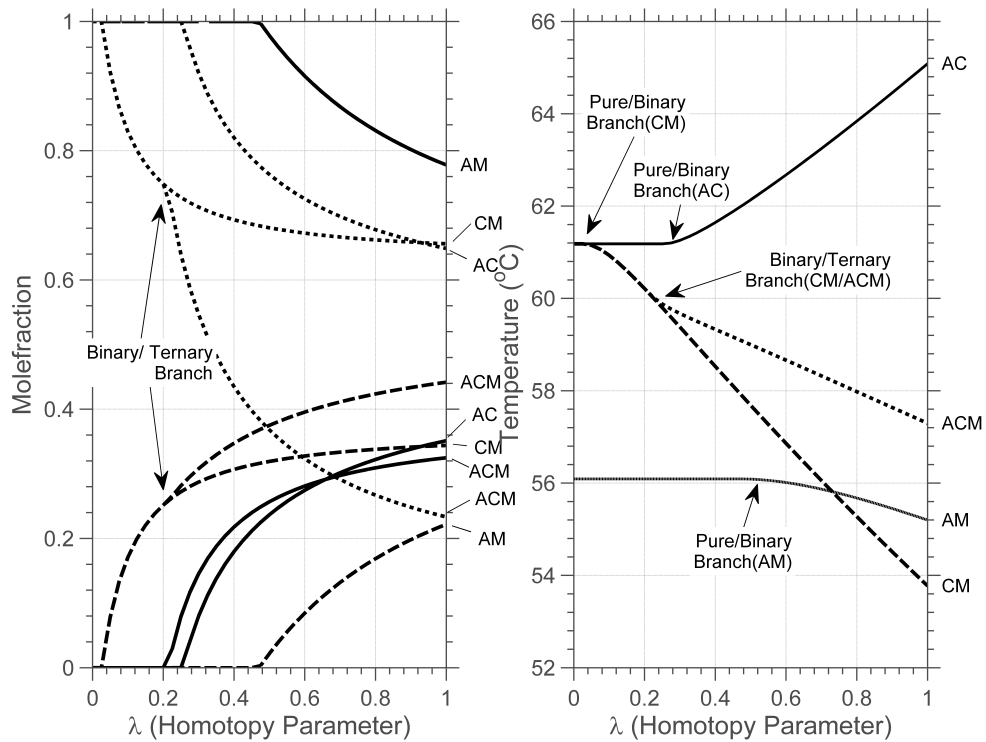


Figure 4.2: Location of azeotropes in acetone(A)-chloroform(C)-methanol(M) mixture by homotopy method; solid=acetone, dotted=chloroform, dashed=methanol

behaviour at $\lambda = 0$. The pseudo-azeotropic compositions correspond to selectivities $S_i = 0$ (see equation 3.45 for definition). Note that the pseudo-azeotropes do not in general correspond to minima or maxima in the wet-bulb temperature surface, unlike conventional azeotropes which do correspond to extrema in bubble-point temperature (see section 3.3.3 for discussion).

The pseudo-azeotropy homotopy map for the ternary mixture (which is analogous to the azeotropy map of equation 4.11) can be summarised by:

$$\mathbf{H}(\bar{\mathbf{x}}_{pAZ}) = \begin{bmatrix} F_1 \equiv J_1 + y_1^G \sum_{j=1}^3 N_j - N_1 \\ F_2 \equiv J_2 + y_2^G \sum_{j=1}^3 N_j - N_2 \\ F_3 \equiv J_3 + y_3^G \sum_{j=1}^3 N_j - N_3 \\ F_4 \equiv K_1 x_1 - y_1^I \\ F_5 \equiv K_2 x_2 - y_2^I \\ F_6 \equiv K_3 x_3 - y_3^I \\ F_7 \equiv \sum_{i=1}^n y_i - 1 \\ F_8 \equiv h_G^\bullet(T^G - T^L) - \sum_{i=1}^3 N_i \Delta H_i^{vap} - \sum_{i=1}^3 N_i M_i C p_i^G (T^G - T^L) \\ F_9 \equiv \left[\frac{N_1}{\sum N_i} - x_1 \right] - \left[\frac{N_2}{\sum N_i} - x_2 \right] \\ F_{10} \equiv \left[\frac{N_1}{\sum N_i} - x_1 \right] - \left[\frac{N_3}{\sum N_i} - x_3 \right] \\ F_{11} \equiv \sum_{i=1}^n x_i - 1 \end{bmatrix} = \mathbf{0} \quad (4.13)$$

where

$$\bar{\mathbf{x}}_{pAZ} = (N_1, N_2, N_3, y_1^I, y_2^I, y_3^I, y_4^I, T^L, x_1, x_2, x_3) \quad (4.14)$$

is the array of variables to be solved. The formula for the $F_1 \cdots F_{11}$ are derived in section 3.1.5. Similar forms apply for each of the binary pairs in the mixture, as described in section 3.1.5. The Jacobian for this set of equations is similar in form to that shown in table 3.4; the key difference being the definition of K_i in terms of the homotopy parameter λ :

$$K_i = \lambda \gamma_i \frac{p_i}{P} + (1 - \lambda) \frac{p_i}{P} \quad (4.15)$$

Table 4.4 summarises the procedure for pseudo-azeotrope location by homotopy.

Figure 4.4 shows the computed branches for the pseudo-azeotropes of the acetone-chloroform-methanol mixture, which has evident similarities to that for the azeotropes of figure 4.2. As with conventional azeotropes, the pseudo-azeotropes of the binary pairs (AC,AM,CM) are "born" at a certain value of λ from a solution on the branch corresponding to a pure component. The chloroform-methanol (CM) pseudo-azeotrope appears at $\lambda \approx 0.05$, ending with a composition of $x_{Chloro} = 0.71$, $x_{MeOH} = 0.29$ at $\lambda = 1$. For acetone-chloroform (AC) the pseudo-azeotrope first appears at $\lambda \approx 0.40$, ending with a pseudo-azeotropic composition of $x_{Ace} = 0.30$, $x_{Chloro} = 0.70$ at $\lambda = 1$. For acetone-methanol (AM) the pseudo-azeotrope first appears at $\lambda \approx 0.40$, with a pseudo-azeotropic composition of $x_{Ace} = 0.94$, $x_{Chloro} = 0.06$ at $\lambda = 1$.

Figure 4.4 also shows how the computed ternary pseudo-azeotrope forms from a branch

Table 4.4: Homotopy method for location of pseudo-azeotropes

-
1. Initialise homotopy parameter $\lambda = 0$
 2. Initialize \bar{x}_{pAZ} ; for the AC (acetone-chloroform, 1-2) branch, initialise with $x_1 = 0.5$, $x_2 = 0.5$, plus suitable values for other terms.
 3. Calculate homotopy map $\mathbf{H}(\bar{x})$ (equation 4.13);
 4. Compute the Jacobian matrix \mathbf{J}_{HpAZ} from table 3.4, using modified definition of K_i from equation 4.15
 5. Compute $\delta\bar{x}_{pAZ} = \mathbf{J}_{HpAZ} \setminus \mathbf{H}$
 6. Update the estimates of \bar{x}_{pAZ} : $[\bar{x}_{pAZ}^{NEW}] = \bar{x}_{pAZ} + \delta\bar{x}_{pAZ}$
 7. If $\text{err} < \text{tolerance}$, stop, else return to step 3
 8. Increment λ and repeat from step 2 using updated \bar{x}
 9. Repeat for CM, AM and ACM (ternary) branches, using appropriate initialisation
-

on the CM-binary $\lambda \approx 0.21$, ending with $x_{Ace} = 0.33$, $x_{Chloro} = 0.23$, $x_{MeOH} = 0.44$ at $\lambda = 1$. These values at $\lambda = 1$ compare well with the pseudo-azeotropic compositions computed directly in table 3.6. The pseudo-azeotrope (wet-bulb) temperatures for each branch are also shown in figure 4.4; the temperatures at $\lambda = 1$ correspond to those computed directly in table 3.6.

4.3 Bifurcations in Evaporation Maps

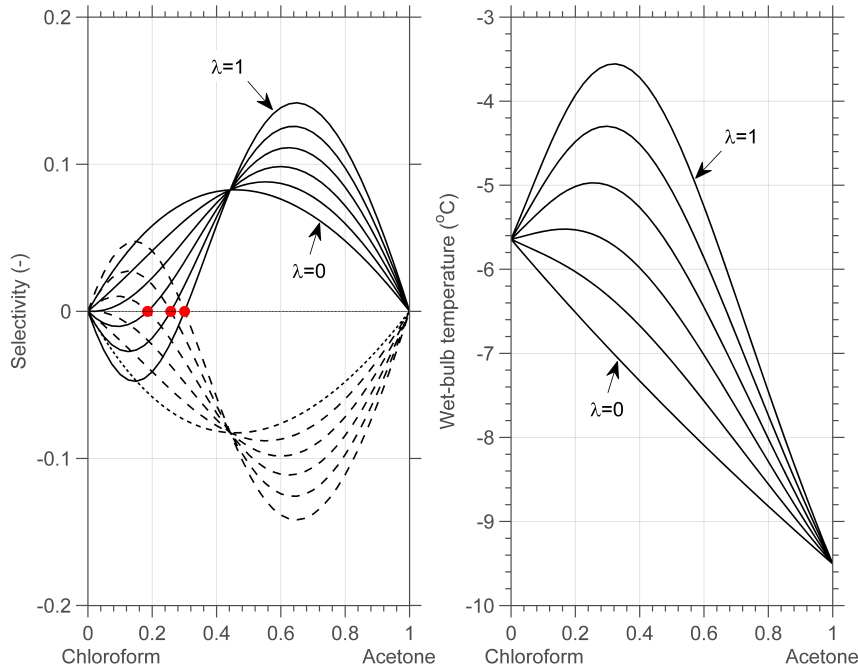
In this section the background to bifurcation analysis is presented, and some applications are reviewed. An analysis of the bifurcations that occur in evaporation maps with varying gas-phase concentration is then presented.

4.3.1 Overview of Bifurcations and Numerical Continuation

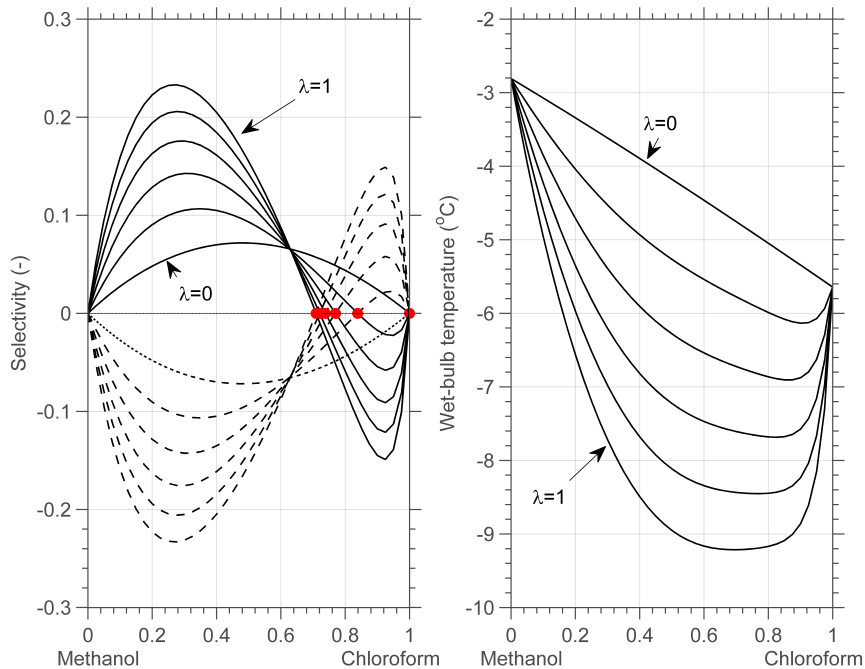
The study of bifurcation theory is aimed at mapping different regions of parameter space that have qualitatively different behaviour. The existence of multiple steady states in CSTRs (continuous stirred tank reactors) or in distillation columns are examples of such nonlinear behaviour in real systems (Bekiaris et al. 1995, Kohout et al. 2002). Nonlinear phenomena such as those just described can often be usefully represented (Seydel 2010) as a system of nonlinear ODEs (ordinary differential equations)

$$\frac{dy}{dt} = \mathbf{f}(\mathbf{y}, \lambda) \quad (4.16)$$

4. BIFURCATIONS IN EVAPORATION MAPS



(a) Acetone-chloroform; for selectivity plot: solid=acetone, dashed=chloroform



(b) Chloroform-methanol; for selectivity plot: solid=chloroform, dashed=methanol

Figure 4.3: Hypothetical selectivity and wet-bulb temperature at various values of homotopy parameter λ for binary mixtures; filled circles denote hypothetical pseudo-azeotropic compositions; $T^G = 40^\circ\text{C}$, $u^G = 0.5\text{m/s}$

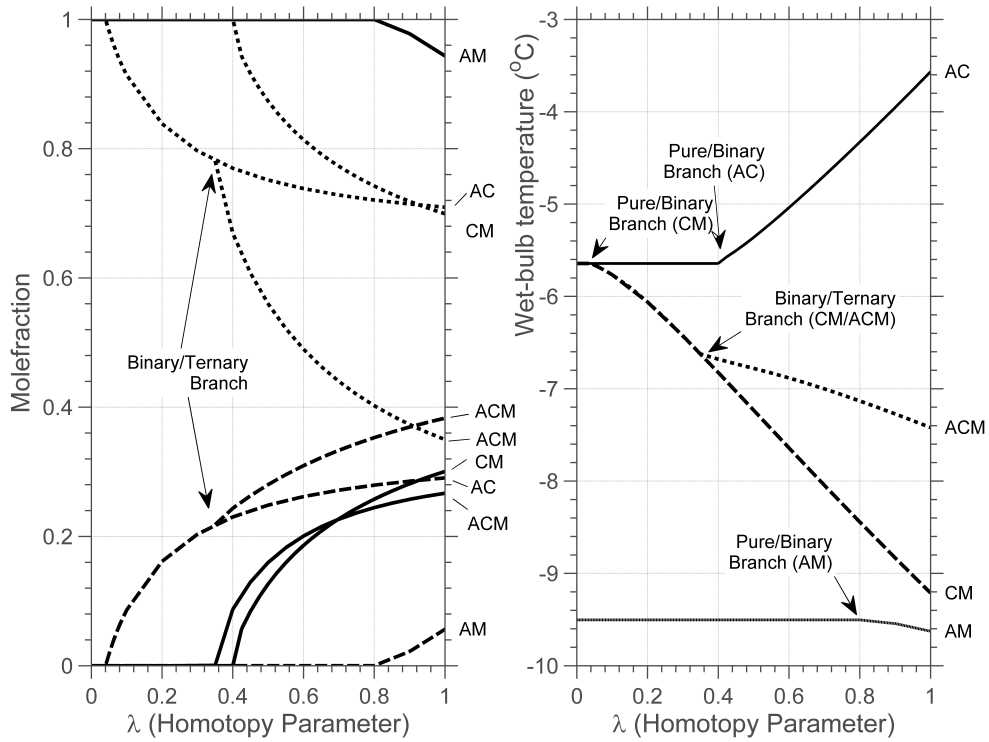


Figure 4.4: Location of pseudo-azeotropes in acetone(A)-chloroform(C)-methanol(M) mixture by homotopy method

or, as solutions to a system of nonlinear algebraic equations.

$$\mathbf{0} = \mathbf{f}(\mathbf{y}, \lambda) \quad (4.17)$$

for a set of states \mathbf{y} , and parameter λ . For some nonlinear processes, the qualitative structure of the *flow*¹ can change as the parameter λ is varied. These qualitative changes in the flow are called *bifurcations*, and the parameter values at which the changes occur are called *bifurcation points* or *branch points* (Strogatz 1994). More strictly, a bifurcation point (with respect to λ) is a solution $(\mathbf{y}_0, \lambda_0)$ of equation 4.16 or 4.17 where the number of solutions changes when λ passes λ_0 (Seydel 2010). Several types of bifurcation are possible, depending on the physics of the system (Strogatz 1994); in this work the *saddle-node* bifurcation is of interest. Figure 4.5 shows a prototypical example given by the first-order function

$$\frac{dx}{dt} = \dot{x} = \lambda + x^2 \quad (4.18)$$

As the parameter λ is varied, two fixed points move towards each other, collide and mutually annihilate. Equation 4.18 represents a *vector field*; the velocity vector \dot{x} is sketched on the horizontal axis in figure 4.5; arrows point right when $\dot{x} > 0$ and

¹Loosely speaking the *flow* is the set of solutions to 4.16 or 4.17 (Hale & Kocak 1991)

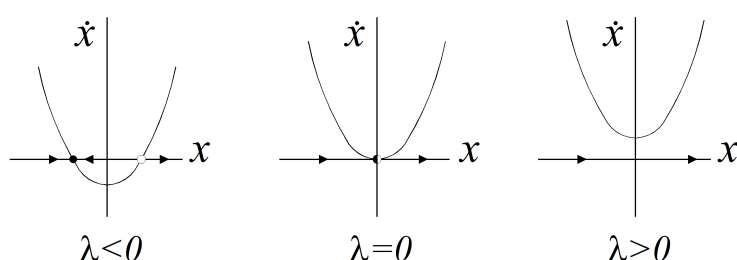


Figure 4.5: Saddle-node bifurcation (Strogatz 1994)

left when $\dot{x} < 0$. The filled circle denotes a stable node while the open circle is an unstable node. When $\lambda < 0$ there are two fixed points, one stable and one unstable. As λ reaches zero from below the solution curve moves up and the two fixed points approach each other. When $\lambda = 0$ a half-stable fixed point exists, while at $\lambda > 0$ the fixed points have disappeared. Section 4.3.2 demonstrates the analogous type of saddle-node bifurcations that occur in evaporation maps as the gas-phase concentration is varied.

The fundamentals and mathematical background of numerical continuation methods are described in detail by Govaerts (2000), Seydel (2010), and Kuznetsov (1998). Many of the analyses presented in the literature are developed using bifurcation software such as AUTO (Doedel et al. 1997), and MATCONT (Dhooge et al. 2003). Bekiaris et al. (1993, 1995) investigated multiple steady states in numerical models of homogeneous and heterogeneous azeotropic distillation using the AUTO package, with the distillate flow rate as a bifurcation parameter. Experimental evidence for multiple steady states was subsequently provided for the case of homogeneous azeotropic distillation by Guttinger et al. (1997) and for heterogeneous azeotropic distillation by Muller & Marquardt (1997). Knapp & Doherty (1994) analysed bifurcations in extractive distillation processes with reflux ratio and entrainer:feed ratio as bifurcation parameters using the AUTO package; they found maximum reflux ratios and minimum entrainer:feed ratios beyond which separation via extractive distillation was not feasible. Garhyan et al. (2003) explored the oscillatory behaviour of an ethanol fermentor using AUTO, while Zavala-Tejeda et al. (2006) used MATCONT to study a continuous polyurethane reactor, focusing on impact of conventional feed-back control, and on disturbance variables such as cooling water flow. Other examples include that of Kohout et al. (2002) who developed a fortran-based tool (*CONT*) for bifurcation analysis of chemical engineering problems and demonstrated examples for stirred and tubular reactors.

Software for bifurcation analysis has also been coupled to commercial flowsheeting

software (Chokshi 2006, Ramzan et al. 2010). Vadapalli & Seader (2001) presented a general framework for computation of bifurcation diagrams using Aspen Plus (Aspen-Tech 2014), and demonstrated examples for an adiabatic CSTR, as well as azeotropic and reactive distillation columns. Restrepo et al. (2014) developed a method to perform bifurcation and eigenvalue analysis using dynamic models generated using Aspen Dynamics and Aspen Custom Modeler (AspenTech 2014). Other researchers have developed customised software packages to directly incorporate bifurcation-tracking capabilities in a dynamic simulation environment. Mangold et al. (2000) developed the DIVA flowsheeting software package and presented examples of a circulation-loop reactor for abatement of VOC (volatile organic compounds), and a reactive distillation process for production of fuel ethers. Radichkov et al. (2006) used the DIVA package for a numerical study of nonlinear oscillations in a continuous fluidized bed spray granulator, using a simple population-balance model. The book by Strogatz (1994) gives an introductory exposition of nonlinear dynamics (including bifurcations). Hirsch et al. (2004) offer a more technical but accessible approach, while the texts of Wiggins (1990), Guckenheimer & Holmes (1985) and Hale & Kocak (1991) provide a more advanced treatment.

In this section, the focus is on bifurcations of the evaporation maps. The governing equations are the discrepancy functions $F_1 - F_{11}$ of chapter 3. One can attempt to track the branches of fixed points by stating the problem analogous to the system of equations 4.17 as

$$F_i(\bar{x}, y_i^G) = 0 \quad (4.19)$$

where \bar{x} is vector of variables, F is the vector of the discrepancy functions $F_1 - F_{11}$, and y_i^G (bulk gas phase concentration of component i) acts as the continuation (or bifurcation) parameter. A naive approach would be to attempt to simply follow the branch by gradually increasing the value of y_i^G , using the most recently calculated value of \bar{x} as an initial guess for a new point on the branch. However, this approach fails when the Jacobian of F becomes singular which happens at a *limit* or *turning* point (Seydel 2010). In addition, as the limit point is approached, the steps in y_i^G must be modified to properly track the branch. To address this problem, the path of the branches can be followed numerically by using a numerical continuation procedure (Kuznetsov 1998). The continuation process is initialized by locating the pseudo-azeotrope composition at zero gas pre-loading ($y_i^G = 0$, for $i = 1, 2, 3$) using the algorithm of table 3.2. The analytic Jacobian used in the continuation method is given in table 3.4.

In this work the CL-Matcont toolbox (Govaerts 2011) is used to track the branches of the fixed points of equation 4.19. This involves using a Moore-Penrose adaptation of the "pseudo arclength" continuation method (Dhooge et al. 2003, Seydel 2010). A convergence-dependent step-size control to negotiate limit points. Such bifurcations caused by varying a single parameter are called *codimension-one*.

4.3.2 Bifurcation Analysis of Evaporation Maps

To demonstrate the saddle-node bifurcations that may occur, the ternary acetone/ chloroform/methanol mixture has been selected for study; this is the most complex of the mixtures originally selected in table 2.1, and is therefore likely to yield the most interesting behaviour.

This section focuses only on bifurcations due to gas-phase pre-loading. As the concentration difference between the bulk gas and the interface provides the driving force for mass transfer, gas-phase pre-loading has a pronounced influence on the dynamics of the evaporative process (Luna & Martinez 1999). Other bifurcation parameters could be used, such as gas-phase temperature T^G or velocity u^G . However, it is not expected that variations in gas velocity or temperature would lead to bifurcations in evaporation maps as changes in gas velocity and temperature affect each component in a broadly similar way via their effect on Nusselt and Schmidt numbers; these dimensionless numbers in turn lead to heat transfer coefficient and binary mass transfer coefficients respectively (see equations 3.19 and 3.36). There may be a possible temperature effect if temperature variations were to affect binary gas diffusion coefficients for the various components to differing extents, but this has not been explored in this work.

Bifurcation diagrams for each of the 3 binary pseudo-azeotropes in the acetone/ chloroform/methanol mixture are shown in figure 4.6. For each binary pair, the locus of the pseudo-azeotrope (fixed point) may be tracked using the gas-phase concentration of each of the components in the pair as a bifurcation parameter as discussed below.

Acetone/chloroform pseudo-azeotrope:

Figure 4.6aII shows how the acetone- chloroform pseudo-azeotrope composition tends towards pure acetone as the loading of acetone in the gas phase increases, and disappears when $y_{Acetone}^G > 0.085$. In other words, increasing the composition of acetone in the vapour phase causes the composition of the pseudo-azeotrope in liquid phase to also increase in acetone content. This is intuitively correct in that the driving force for evaporation of acetone declines as the difference in concentration between liquid and gas phases diminishes, whereas the driving forces for evaporation of chloroform and methanol are less affected (in fact, for a non-multicomponent mass transfer model, they would be completely unaffected). The liquid phase therefore becomes enriched in acetone as the tendency for acetone to evaporate is reduced, relative to that of chloroform and methanol. Qualitatively similar behaviour of the acetone-chloroform mixture was observed by Luna & Martinez (1999) in a study of isothermal batch evaporation. The arrowed lines on figure 4.6(a)-(c) indicate qualitatively the direction of the vector field of liquid concentration which is

directed towards the stable branch and away from the unstable.

The behaviour of the acetone-chloroform pseudo-azeotrope can also be analyzed in terms of evaporative fluxes of acetone and chloroform as shown in figure 4.7. As the acetone pre-loading increases, the normalized flux of acetone increases to 1.0, while that of chloroform decreases to zero as figure 4.7aII indicates. This is evidence of the enrichment of the liquid phase with acetone due to decreasing flux of chloroform. Note however that the selectivity of each component remains at zero at each point on the curves of figure 4.7 (as required by definition of pseudo-azeotrope, see section 3.1.5). The normalized fluxes have the same numerical values as the pseudo-azeotrope composition by virtue of the definition of selectivity (from equation 3.45):

$$S_i = \frac{N_i}{\sum_{i=1}^n N_i} - x_i$$

As the selectivity S_i is by definition zero along the pseudo-azeotrope branches, the ratio of fluxes therefore equals the liquid (pseudo-azeotrope) composition. In a similar way, the pseudo-azeotrope composition tends towards pure chloroform as the loading of chloroform increases (part I of figure), and disappears when $y_{\text{Chloroform}}^G > 0.075$ approximately. In this case, the driving force for chloroform evaporation declines as the gas phase pre-loading of chloroform increases, while the driving forces for acetone and methanol evaporation are largely unaffected (or completely unaffected in the case of a non-multicomponent mass transfer model). As the chloroform pre-loading increases, the chloroform normalized flux increases to 1.0, while that of acetone declines to zero as shown in figure 4.7aI; this is caused by the relative decline in chloroform flux relative to acetone, due to lower concentration difference between liquid and gas phase for chloroform.

Beyond $y_{\text{Acetone}}^G > 0.085$ (for acetone loading), or $y_{\text{Chloroform}}^G > 0.075$ (for chloroform loading) the pseudo-azeotrope no longer exists; the effect this has on the evaporation maps is shown in figures 4.9 and 4.10 and discussed in section 4.3.3.

Acetone/methanol pseudo-azeotrope:

For the acetone-methanol binary, figure 4.6b shows the stable (solid line) and unstable (dotted line) branches of the acetone-methanol pair. As the acetone gas concentration increases above zero (part II) of figure), a stable branch originates at pure methanol. Ultimately, the branches coalesce at the limit point (LP) at approximately $y_{\text{Acetone}}^G = 0.023$. This coalescence and disappearance of two fixed points constitutes what is termed a *saddle-node* bifurcation, although in the binary case it involves branches of two nodes, one stable, and one unstable. Increasing the acetone content in the vapour phase therefore pushes the location of the $y_{\text{Acetone}}^G = 0$ pseudo-azeotrope to a more acetone-lean composition (points 1B, 2B etc.) as y_{Acetone}^G in-

creases, while also giving rise to an additional (unstable) pseudo-azeotrope at pure methanol that becomes richer in acetone (points 1A, 2A etc). The physical explanation for the appearance of a second binary pseudo-azeotrope branch at $y_{Acetone}^G > 0$ is not straightforward, but is due to the combination of non-linearity of the vapour-liquid equilibria in the liquid phase and multicomponent mass transfer in the vapour phase. Qualitatively similar behaviour for the acetone-methanol binary was also found by Luna & Martinez (1999) in a study of isothermal batch evaporation.

Comparing the component evaporative fluxes along the solution branches (see figure 4.7bII), it can be seen that the normalized fluxes show a similar pattern to the bifurcation diagrams of figure 4.6b, i.e. a convex shape that turns at the limit-point concentration of $y_{Acetone}^G = 0.023$. The maximum in normalized acetone flux tends to a maximum value of 1.0 as the pseudo-azeotrope tends to pure acetone, while the maximum in methanol flux occurs as it tends to pure methanol.

A similar situation occurs when the gas-phase is pre-loaded with methanol (figure 4.7bI). Increasing the methanol content of the y_{MeOH}^G moves the (unstable) pseudo-azeotrope to a more methanol-rich composition, and gives rise to a stable pseudo-azeotrope at pure acetone. The stable and unstable branches coalesce and disappear at the limit point (LP) of $y_{MeOH}^G = 6 \times 10^{-5}$ as the methanol pre-loading increases. Luna & Martinez (1999) also found that the acetone-methanol disappeared as methanol pre-loading increased, although they did not track the pseudo-azeotrope composition over its full range as is done in this work.

The corresponding evaporative fluxes (figure 4.7bI) along the solution branches shows analogous behaviour to that for acetone pre-loading; the convex shapes mirror the shape of the bifurcation diagram of figure 4.6bI. The normalized methanol flux tends to a maximum value of 0.0 (i.e. $N_{Acetone}/\Sigma N_i = 0$ so $N_{Chloroform}/\Sigma N_i = 1.0$) as the pseudo-azeotrope tends to pure methanol.

Chloroform/methanol pseudo-azeotrope:

The chloroform- methanol pseudo-azeotrope (figure 4.6c) shows similar behaviour to the acetone-methanol azeotrope discussed above. As pre-loading with methanol increases from zero (part II of figure), a stable branch originates at pure methanol. Ultimately, the stable and unstable branches coalesce at the limit point $y_{Chloroform}^G = 0.027$ approximately. Increasing the gas phase content of chloroform moves the position of the $y_{Chloroform}^G = 0.0$ pseudo-azeotrope to a more chloroform-lean composition (points 1A, 2A etc.) while also introducing an additional pseudo-azeotrope at pure methanol that becomes richer in chloroform as the pre-loading with chloroform increase (points 1B, 2B etc.)

As the gas-phase is pre-loaded with methanol (part I of figure 4.6c) a stable branch

appears at pure chloroform, leading ultimately to a saddle-node bifurcation at the limit point. Beyond the limit point, the pseudo-azeotrope no longer exists; the effect this has on the evaporation maps is shown in figure 4.11 and discussed in section 4.3.3.

Qualitatively similar behaviour for the chloroform-methanol binary was also found by Luna & Martinez (1999) who found a second pseudo-azeotrope appeared at finite gas pre-loading, which then disappeared above a certain concentration. That work did not involve tracking the pseudo-azeotrope location over the full range of composition however.

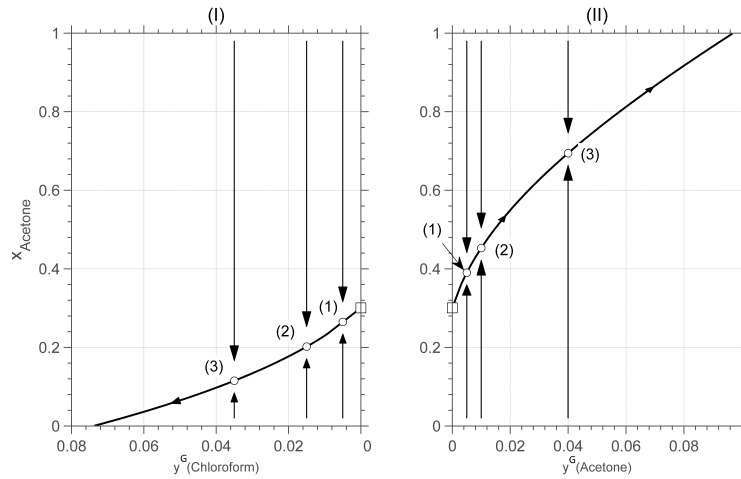
The corresponding evaporative fluxes for chloroform loading (figure 4.7cII) along the solution branches show the convex shapes that mirror the shape of the bifurcation diagram of figure 4.6cII. The normalized chloroform flux tends to a maximum value of 1.0 as the pseudo-azeotrope tends to pure chloroform.

The binary bifurcation diagrams in figure 4.6 show in principle how to select a gas-phase concentration that yields a desired point on a stable branch, noting that each point on a stable branch represents a terminal concentration of an evaporating binary liquid mixture (at given gas-phase conditions u^G and T^G). Taking figure 4.6aII as an example, the use of a gas phase mole-fraction of $y_{Acetone}^G = 0.04$ (point (3) on diagram) will yield a terminal composition $x_{Acetone} = 0.7$; the evaporation map in figure 4.9c shows liquid composition trajectories converging to this composition (the binary composition trajectories lie along the acetone-chloroform edge of the diagram).

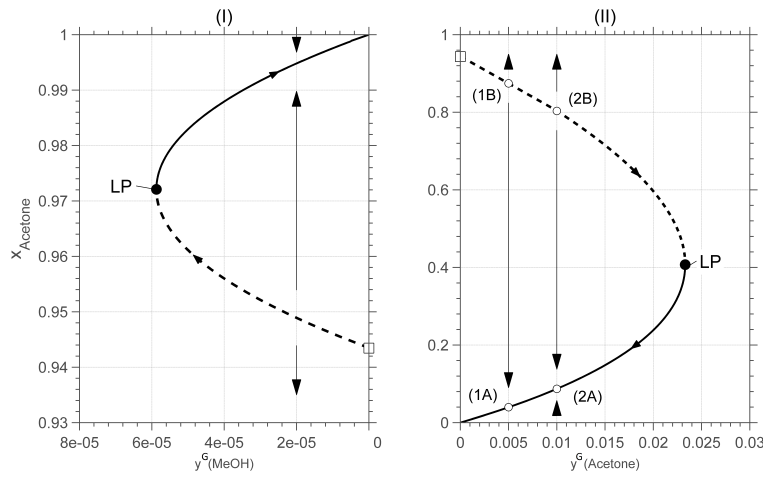
Ternary acetone/chloroform/methanol pseudo-azeotrope:

Bifurcation diagrams may also be developed for ternary pseudo-azeotropes, as depicted in figure 4.8. As acetone pre-loading increases (figure 4.8a), the ternary azeotrope shifts towards the acetone-methanol axis. The continuation path for the ternary ultimately meets that of the binary acetone-methanol pseudo-azeotrope (shown on the horizontal plane) at which point the ternary disappears. As the gas-phase is loaded with chloroform (figure 4.8b), the continuation path for the ternary pseudo-azeotrope approaches and meets the chloroform-methanol binary (shown on the horizontal plane). In figure 4.8c, showing methanol pre-loading, the ternary exhibits a turning point, so that for methanol concentrations between zero and the limit point concentration there are 2 ternary pseudo-azeotropes, one stable node and one saddle. This bifurcation of a ternary pseudo-azeotrope is a higher dimensional example of the saddle-node bifurcations seen in figure 4.6a and 4.6b for binary pseudo-azeotropes.

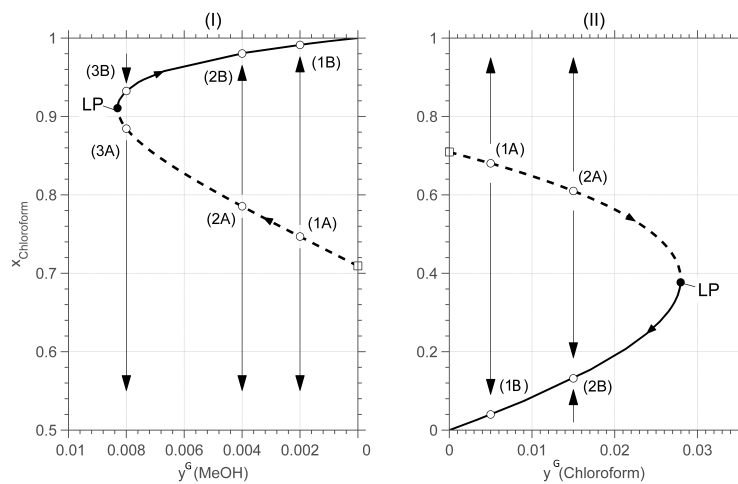
4. BIFURCATIONS IN EVAPORATION MAPS



(a) Acetone-chloroform pseudo-azeotrope: (I) chloroform (II) acetone loading

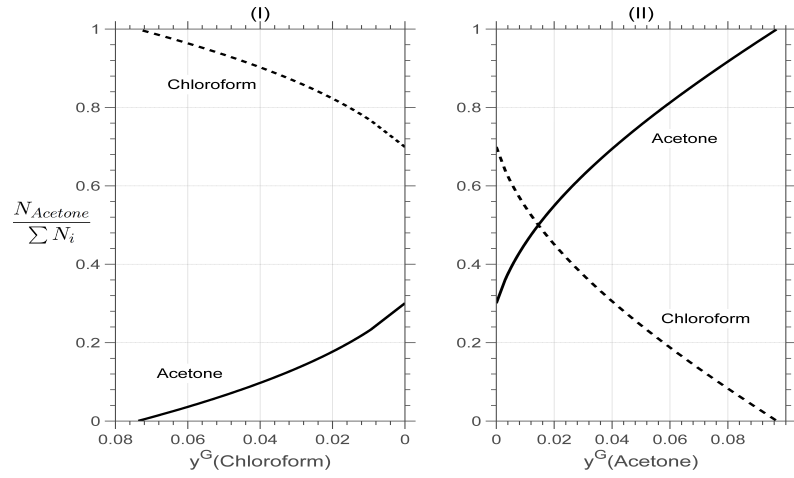


(b) Acetone-methanol pseudo-azeotrope: (I) methanol (II) acetone loading

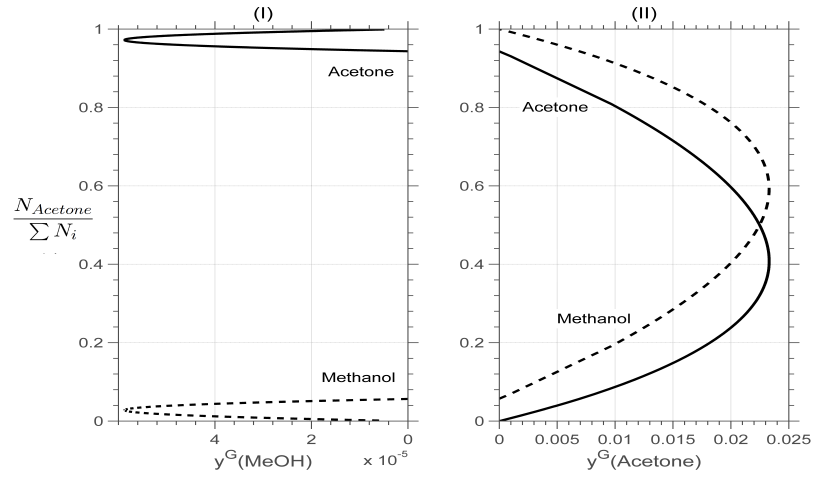


(c) Chloroform-methanol pseudo-azeotrope: (I) methanol (II) chloroform loading

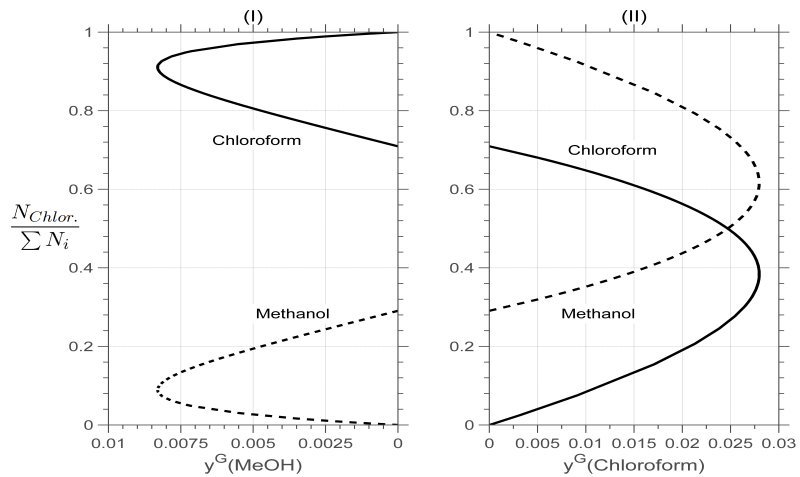
Figure 4.6: Bifurcation diagrams for acetone-chloroform-methanol;
 $T^G = 40^\circ\text{C}$, $u^G = 0.5\text{m/s}$, $d = 0.03\text{m}$



(a) Acetone-chloroform pseudo-azeotrope: (I) chloroform (II) acetone loading



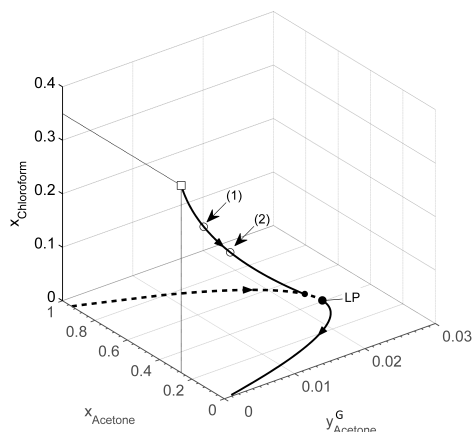
(b) Acetone-methanol pseudo-azeotrope: (I) methanol (II) acetone loading



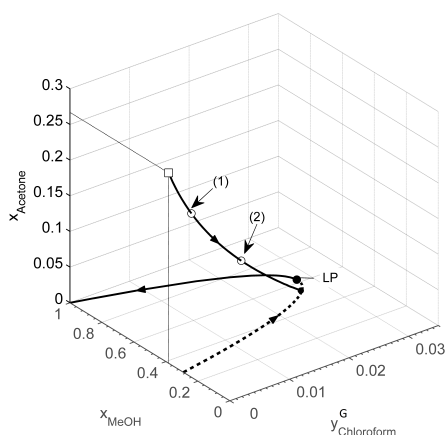
(c) Chloroform-methanol pseudo-azeotrope: (I) methanol (II) chloroform loading

 Figure 4.7: Normalized evaporative fluxes for acetone-chloroform-methanol; $T^G = 40^\circ\text{C}$, $u^G = 0.5\text{m/s}$, $d = 0.03\text{m}$

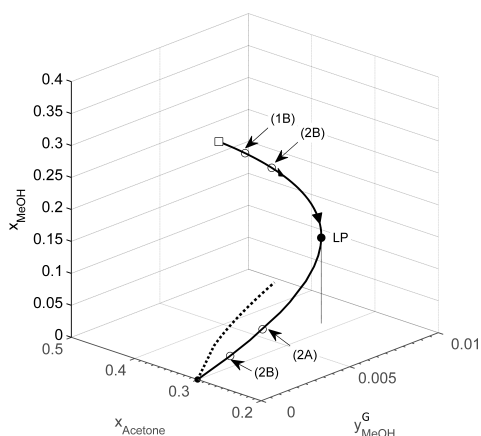
4. BIFURCATIONS IN EVAPORATION MAPS



(a) Acetone pre-loading; horizontal plane corresponds to figure 4.6bII; points (1)-(2) correspond to composition of ternary in figure 4.9a-b



(b) Chloroform pre-loading; horizontal plane corresponds to figure 4.6cII; points (1)-(2) correspond to composition of ternary in figure 4.10a-b



(c) Methanol pre-loading; horizontal plane corresponds to figure 4.6aII; points (1A)/(1B)-(2A)/(2B) correspond to figure 4.11a-b

Figure 4.8: Bifurcation diagrams for ternary azeotrope; numbered points correspond to gas-phase concentrations in maps of figure 4.9, 4.10 and 4.11.

4.3.3 Effect of Gas Pre-Loading on Evaporation Maps

The effect of pre-loading the gas phase on the evaporation maps can be related to the bifurcation diagrams. Figure 4.9, 4.10 and 4.11 show how the topology of the evaporation maps for the acetone-chloroform-methanol mixture are affected by the pre-loading of the gas phase with each component in turn. As the gas-phase concentration changes, there are significant changes in the numbers of fixed points (binary and ternary pseudo-azeotropes), as well as in the flow of evaporation trajectories, as detailed in the following paragraphs.

Acetone Pre-Loading

In figure 4.9, as $y_{Acetone}^G$ increases, the acetone-chloroform binary moves towards the pure acetone corner, the ternary moves towards the acetone-methanol axis, and the two pseudo-azeotropes on the acetone-methanol vertex approach each other before coalescing and disappearing. In figure 4.9c, the ternary has disappeared, leaving the acetone-chloroform pseudo-azeotrope as the terminal point. At higher acetone concentrations (figure 4.9d), this pseudo-azeotrope also disappears. These behaviours are consistent with the bifurcations in figures 4.6aII (which shows effect of acetone loading on acetone-chloroform binary), 4.6bII (which shows effect of acetone loading on acetone-methanol binary), and 4.8a which shows effect of acetone loading on the ternary pseudo-azeotrope. The overall effect of increasing acetone content in the vapour phase is to eventually eliminate the various binary and ternary pseudo-azeotrope fixed points in favour of a single end-point at pure acetone. This is physically reasonable in that an increasing acetone gas phase concentration reduces the driving force for acetone evaporation, while not significantly affecting the evaporation of chloroform and methanol.

Luna & Martinez (1999) studied isothermal batch drying of the acetone/chloroform mixture and found qualitatively similar behaviour to that described above:

- binary acetone-chloroform azeotrope increased in acetone content as $y_{Acetone}^G$ increased
- new acetone-methanol pseudo-azeotrope appeared for $y_{Acetone}^G > 0$
- chloroform-methanol pseudo-azeotrope disappeared for $y_{Acetone}^G > 0$
- ternary pseudo-azeotrope moved toward acetone-methanol edge as $y_{Acetone}^G$ increased, disappearing at a finite value

Chloroform Pre-Loading

In figure 4.10, as $y_{Chloroform}^G$ increases, the acetone-chloroform binary moves towards the pure chloroform corner, the ternary pseudo-azeotrope moves towards the

chloroform- methanol axis and the two binary pseudo-azeotropes on the acetone-methanol axis move towards each other before coalescing and disappearing. In figure 4.10c, the ternary has disappeared, while in (figure 4.10d chloroform remains as the terminal composition. These phenomena are consistent with the bifurcations in figures 4.6aI (which shows effect of chloroform loading on acetone-chloroform binary), 4.6cII (which shows effect of chloroform loading on chloroform-methanol binary), and 4.8b which shows effect of chloroform loading on the ternary pseudo-azeotrope. Analogous to the case of acetone pre-loading, the net effect of increasing chloroform content in the vapour phase is to eliminate the pseudo-azeotropes to give a single evaporation end-point at pure chloroform. This is physically reasonable in that an increasing chloroform gas phase loading reduces the driving force for chloroform evaporation, while not significantly affecting the evaporation of acetone and methanol.

Methanol Pre-Loading

For methanol pre-loading, increasing concentration causes the two ternary pseudo-azeotropes to converge before ultimately converging at their limit point. The binary pseudo-azeotropes on the chloroform-methanol axis also converge as y_{MeOH}^G increases. Ultimately, the pseudo-azeotropes all disappear, leaving methanol as the stable node in figure 4.11d. The bifurcations in figures 4.6bI (for effect of methanol loading on acetone-chloroform binary), 4.6cI (for effect of chloroform loading on chloroform-methanol binary), and 4.8c (for effect of methanol loading on the ternary pseudo-azeotrope) show behaviour consistent with that of the evaporation maps of figure 4.11. As methanol concentration in the gas-phase is increased, the binary and ternary pseudo-azeotropes are eventually eliminated to yield a single end-point at pure methanol. This is intuitively correct in that the driving force for methanol evaporation is reduced as the methanol gas-phase concentration increases, whereas the driving forces for acetone and chloroform are not significantly affected.

Work by Luna & Martinez (1999) found qualitatively similar behaviour to that described above for methanol pre-loading:

- binary acetone-chloroform azeotrope increased in acetone content as $y_{Acetone}^G$ increased
- new chloroform-methanol pseudo-azeotrope appeared for $y_{MeOH}^G > 0$
- acetone-methanol pseudo-azeotrope disappeared for $y_{MeOH}^G > 0$
- acetone-chloroform pseudo-azeotrope disappeared for $y_{MeOH}^G > 0$
- new ternary pseudo-azeotrope formed for $y_{MeOH}^G > 0$, and moved in direction of pure methanol as the methanol pre-loading increased

- the pair of ternary pseudo-azeotropes moved closer together with increasing y_{MeOH}^G , before ultimately coalescing and disappearing

The evaporation maps in figures 4.11-4.9 show the changing locations of the pseudo-azeotropes as the gas phase concentration is varied; this movement can be tracked continuously on a ternary diagram as shown in figure 4.12, which replicates the information shown in figure 4.8 in an alternate form. The ternary pseudo-azeotrope moves towards the acetone-methanol edge before disappearing as the pre-loading of acetone increases, and towards the methanol-chloroform edge as the chloroform pre-loading increases, again disappearing at the edge. With methanol pre-loading, the ternary moves towards a limit point, while a secondary ternary appears on the acetone-chloroform edge and moves towards the same limit point. Both branches meet at the limit point, after which the ternary disappears. The binary limit points from figures 4.6b and 4.6c are also shown on the ternary in figure 4.12.

4.4 Interaction Effects

In a similar approach to that adopted in section 3.3.4, multicomponent interaction effects (the degree to which the process is non-Fickian) can be assessed by considering the relative magnitude of the off-diagonal contributions to the diffusive fluxes. A measure of the contribution of an off-diagonal (multicomponent) term is given by:

$$\left| \frac{k_{ij}^{\bullet} \Delta y_j}{k_{ii}^{\bullet} \Delta y_i} \right| \quad (4.20)$$

The interaction effect is notable when the ratio of the interaction term (denominator) to the Fickian term (numerator) is significant. As an example of this approach, values of the ratios along the branches of the binary pseudo-azeotropes in the acetone-chloroform-methanol mixture are shown in figure 4.13. These correspond to the bifurcation diagrams in figure 4.6. For the acetone-chloroform pair (figure 4.13a), the term with denominator $k_{12}^{\bullet} \Delta y_2$ represents the contribution of a chloroform concentration gradient to the diffusive flux of acetone. This term tends to zero with increasing $y_{Acetone}^G$ as the composition of the binary pseudo-azeotrope in figure 4.6a approaches pure acetone (in which case $x_2 = 0$, so that $\Delta y_2 = 0$). As the liquid composition tends to that of a pure acetone, the gas-phase diffusion is purely binary (air + acetone), in which case multicomponent effects do not exist. The size of the term involving $k_{12}^{\bullet} \Delta y_2$ in figure 4.6a is 0-0.1 over the region of interest, so that while not the dominant term, it is not generally negligible. Similarly, the term with denominator $k_{21}^{\bullet} \Delta y_1$ represents the contribution of an acetone concentration gradient to the diffusive flux of chloroform. This tends to zero with increasing $y_{Chloroform}^G$, as the pseudo-azeotrope composition tends to pure chloroform (in which case $x_1 = 0$, so that $\Delta y_1 = 0$). This

4. BIFURCATIONS IN EVAPORATION MAPS

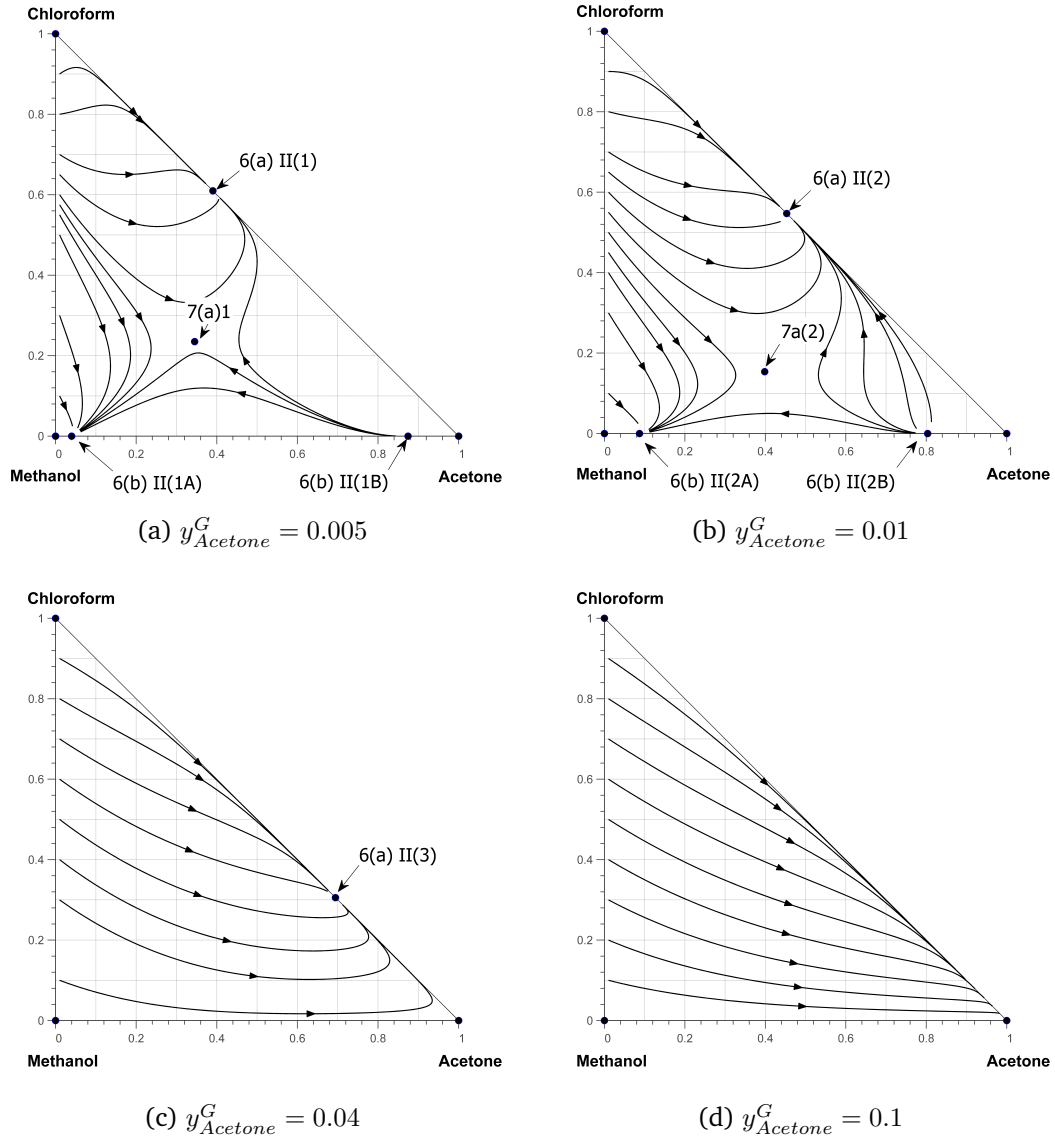


Figure 4.9: Evaporation maps for acetone-chloroform-methanol, gas phase pre-loaded with acetone, $T^G = 40^\circ C$, $u^G = 0.5 m/s$, $d = 0.03 m$; closed circles denote fixed points; annotations correspond to pseudo-azeotrope compositions in figure 4.6 a(II) and 4.6 b(II)

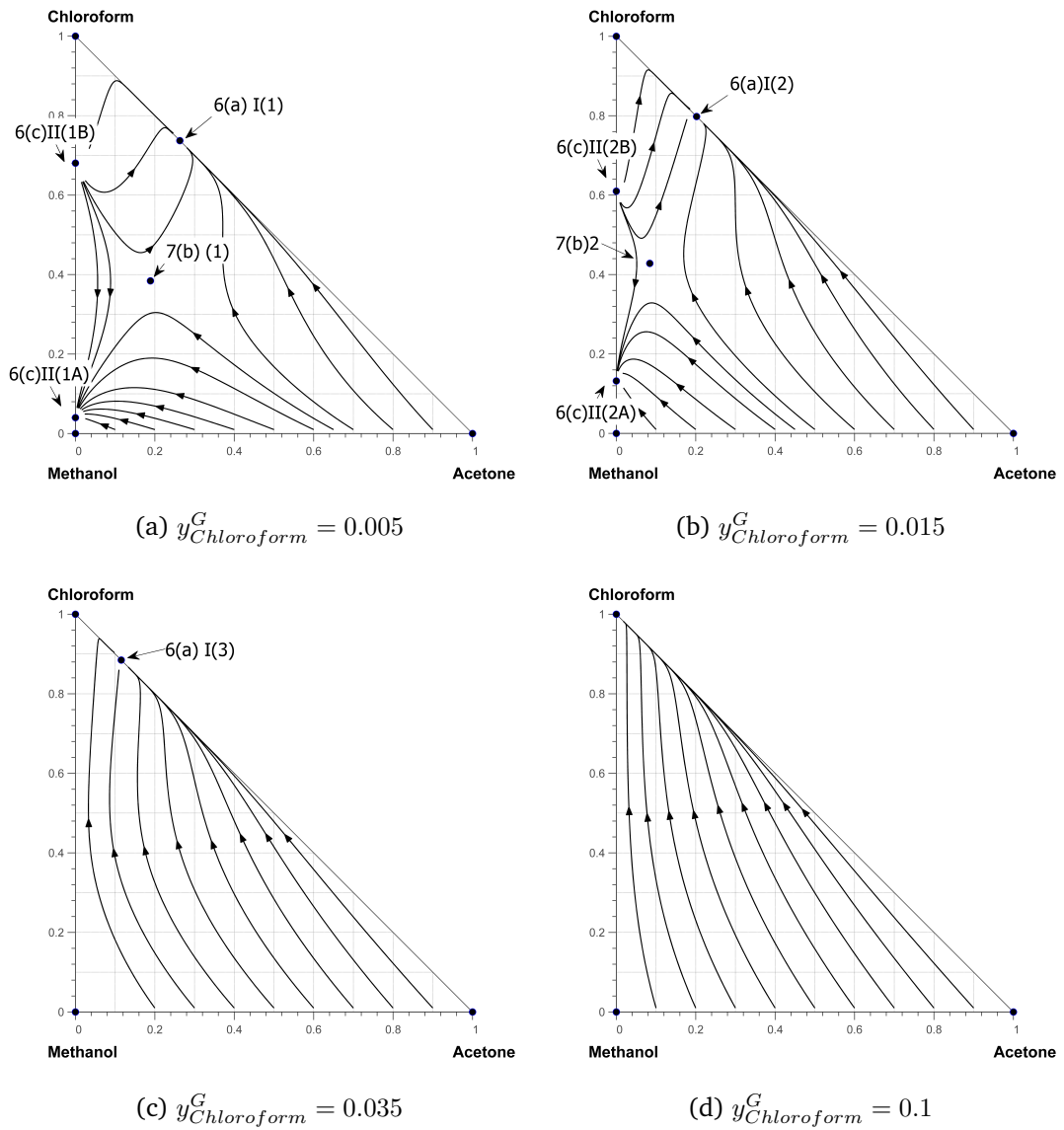
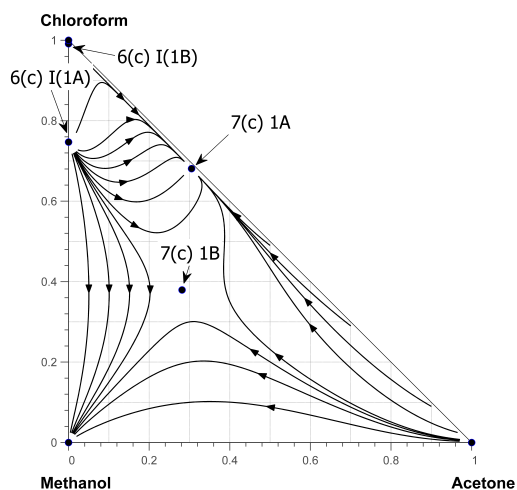
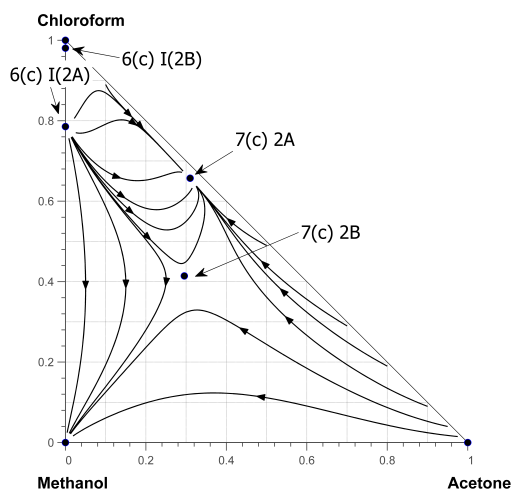


Figure 4.10: Evaporation maps for acetone-chloroform-methanol, gas phase pre-loaded with chloroform; $T^G = 40^\circ\text{C}$, $u^G = 0.5\text{m/s}$, $d = 0.03\text{m}$; closed circles denote fixed points; annotations correspond to pseudo-azeotrope compositions in figure 4.6 a(I) and 4.6 c(II)

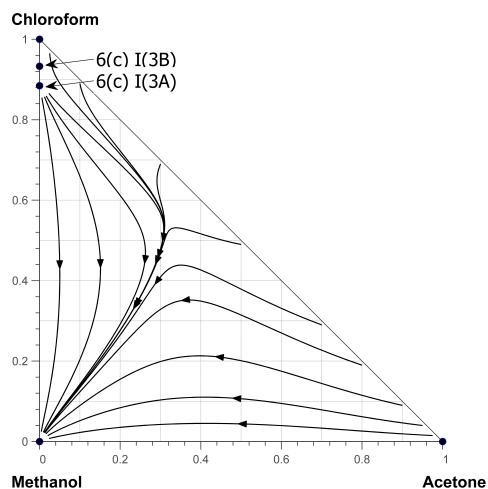
4. BIFURCATIONS IN EVAPORATION MAPS



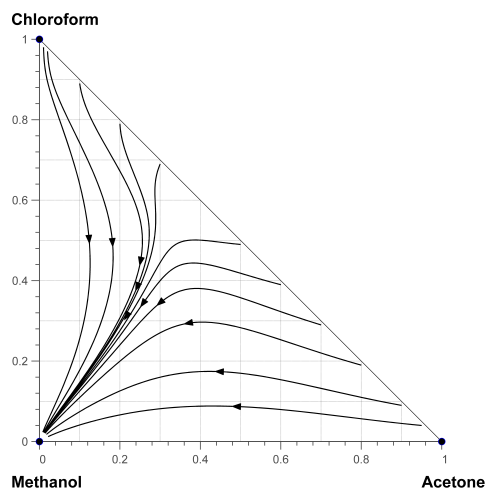
(a) $y_{MeOH}^G = 0.002$



(b) $y_{MeOH}^G = 0.004$



(c) $y_{MeOH}^G = 0.006$



(d) $y_{MeOH}^G = 0.01$

Figure 4.11: Evaporation maps for acetone-chloroform-methanol, gas phase pre-loaded with methanol; $T^G = 20^\circ\text{C}$, $u^G = 0.5\text{m/s}$; annotations correspond to pseudo-azeotrope compositions in figure 4.6b(II) and 4.6c(I)

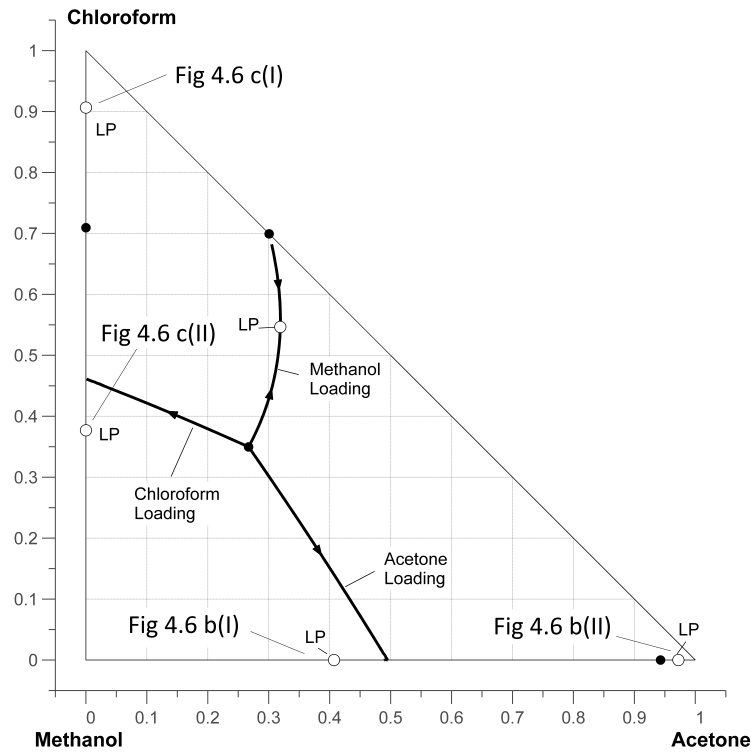
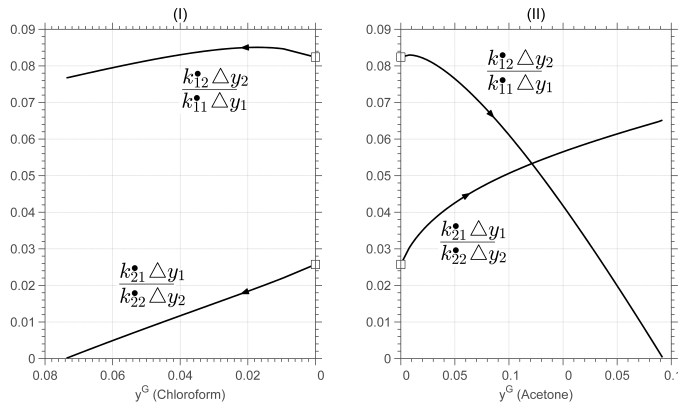


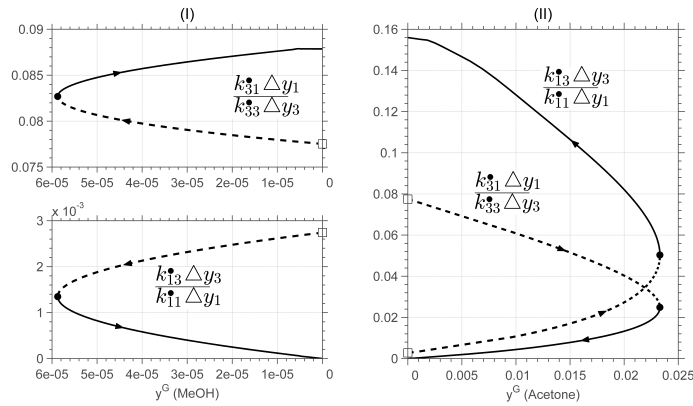
Figure 4.12: Path of ternary pseudo-azeotrope of acetone-chloroform-methanol mixture during continuation procedure; limit points shown as open circles, pseudo-azeotropes at pure gas phase (non pre-loaded) are filled circles. Paths correspond to those shown in figure 4.8

term is 0-0.07 over the range of interest. For other process conditions involving higher component fluxes, such as at higher bulk gas temperatures and velocities, the interaction effects may be more significant. Figures 4.13b and 4.13c, show the interaction effects for the other binary pairs; most notable is the term involving $k_{32}^{\bullet} \Delta y_2$ in figure 4.13c, where the ratio is $\mathcal{O}(1)$ along part of the stable branch as the azeotrope composition tends to pure chloroform, indicating significant interaction. In this region, the pseudo-azeotrope composition approaches pure chloroform, so that the concentration difference for methanol (Δy_3) approaches zero, even as that for chloroform (Δy_2) remains significant; thus, although the actual flux of methanol approaches zero in this area, because the flux of chloroform is relatively large, the effect of the chloroform concentration gradient on the methanol flux is significant, indicated by the large value of the ratio. The ratio in equation 4.20 is not evaluated where the Δy_i term in the denominator is zero.

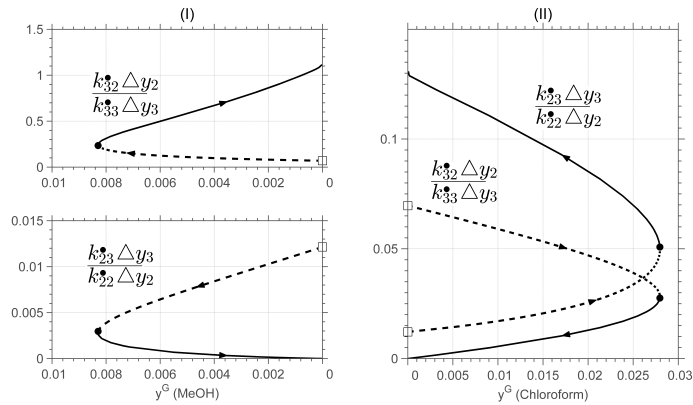
4. BIFURCATIONS IN EVAPORATION MAPS



(a) Acetone-chloroform pseudo-azeotrope: (I) chloroform loading (II) acetone loading.



(b) Acetone-methanol binary pseudo-azeotrope: (I) acetone loading (II) methanol loading



(c) Chloroform-methanol binary pseudo-azeotrope: (I) chloroform loading (II) methanol loading

Figure 4.13: Off-diagonal contributions to diffusive fluxes for binary pseudo-azeotropes of acetone(1)-chloroform(2)-methanol(3) mixture; \square = pseudo-azeotrope location for evaporation into pure gas; \bullet = limit point; solid lines are stable branches, dashed lines are unstable, corresponding to figure 4.6. Arrows show direction of continuation procedure.

4.5 Chapter Summary and Conclusions

The initial portion of this chapter focused on calculation methods for azeotropes and pseudo-azeotropes. A Newton's method approach to calculation of azeotropes using an analytic form of the Jacobian was presented, and compared with results from a commercial simulation package. While there is nothing novel in the calculation of azeotropes per se, an approach employing Newton's method with an analytic form of the Jacobian matrix has not been previously published, to the best of the author's knowledge. Homotopy methods were then used to assess how azeotropes and pseudo-azeotropes form as functions of a homotopy parameter which described the degree of non-ideality in the liquid phase. These methods were able to successfully identify the various solution branches in a complex ternary mixture.

The second development of this chapter has been the numerical continuation procedure used to track the pseudo-azeotrope fixed points for ternary evaporation maps. A numerical continuation procedure was used to analyse the bifurcations that occur in the maps, using the gas-phase concentration as a bifurcation parameter. This analysis, and the bifurcation diagrams generated, allow one to find the required gas-phase composition that results in a desired terminal composition for the evaporation of a ternary mixture.

Finally, the extent of multicomponent interaction along the binary azeotrope branches was investigated; the ratio of diagonal to non-diagonal diffusive flux terms was used as a measure of the extent of interaction. For the acetone/chloroform/methanol mixture considered, the off-diagonal (interaction) terms were generally $< 10\%$ of the diagonal (Fickian) terms, although in the case of methanol loading of the chloroform-methanol azeotrope there is significant interaction along the stable branch in the neighbourhood of pure chloroform.

Chapter 5

Stability Analysis

The stability of the fixed points (pure components and azeotropes) of residue curve maps can be evaluated by linearizing the dynamic behaviour in the vicinity of the fixed points. A similar approach is adopted in this chapter for evaporation maps, by linearizing the governing equations for the gas-phase limited process.

In the following sections the linearization and stability analysis approach for residue curve maps is firstly addressed; an analytic form of the Jacobian is derived that uses the NRTL equation to describe vapour-liquid non-ideality. However, an analytic form for the Jacobian cannot be found for evaporation maps. For that reason, a finite-difference method is used to compute the required gradients of the Jacobian at the fixed points of evaporation maps. The linearization process allows the fixed points of both residue curve maps and evaporation maps to be characterised in terms of the eigenvalues of the Jacobian matrices evaluated at their respective fixed points. In tandem with the eigenvalues, the corresponding eigenvectors may also be found at the fixed points. The eigenvalues are useful for analysing the stability of the fixed points (pure components and azeotropes or pseudo-azeotropes), while the eigenvectors show the asymptotic behaviour of residue curves and of evaporation trajectories in the vicinity of the fixed points. The eigenvectors are also used in the location of separation boundaries in chapter 6.

5.1 Stability of Fixed Points in Residue Curve Maps

While the stability of a particular node (pure component or azeotrope) can be predicted based on the behaviour of trajectories in the vicinity of that node, a more exact direct approach is desirable. Doherty & Perkins (1978a,b) analysed the dynamics of simple distillation processes, elaborating many of the mathematical features of residue curve maps. They also showed how to determine the stability of fixed points of residue

curve maps using the well-known theory of ordinary differential equations. Theorems due to Liapunov and Hartman-Grobmann (Varma & Morbidelli 1997) imply that an autonomous, non-linear system $\mathbf{f}(\mathbf{x})$ is asymptotically stable if the corresponding linearized system is stable, and unstable if the linearized system is unstable (no conclusion can be drawn if linearized system is marginally stable). Thus, the nature of an isolated singular point is topologically similar to the singular point of the linearized equations at that point. Recall that residue curves are described mathematically by (see also equation 2.18)

$$-\frac{d\mathbf{x}}{d\tau} = \mathbf{f}(\mathbf{x}) = \mathbf{y}(\mathbf{x}) - \mathbf{x} \quad (5.1)$$

where \mathbf{x} is a vector of liquid mole fractions, $\mathbf{y}(\mathbf{x})$ is a relationship for vapour-liquid equilibria, and τ is a dimensionless *warped time* that incorporates molar liquid holdup (Doherty & Malone 2001). By linearizing the system described by equation 5.1 at fixed points (pure components and azeotropes), the stability characteristics at the fixed points can be assessed using the eigenvalues computed at those fixed points. For the residue curve described by equation 5.1 we have (Doherty & Perkins 1978a)

$$\begin{aligned} -\frac{d\mathbf{u}}{d\tau} &= [\mathbf{J}(\mathbf{x}^s)](\mathbf{u}) \\ \mathbf{u} &= \mathbf{x} - \mathbf{x}^s \\ \mathbf{J}(\mathbf{x}_s) &= \left[\frac{\partial f_i}{\partial x_j} \right]_{\mathbf{x}=\mathbf{x}^s} \end{aligned} \quad (5.2)$$

provided that $\det(\mathbf{J}(\mathbf{x}^s)) \neq 0$

where $\mathbf{J}(\mathbf{x}^s)$ is the Jacobian matrix at the fixed point \mathbf{x}^s , and $\mathbf{u} = \mathbf{x} - \mathbf{x}^s$ represents a deviation from the fixed point. Solutions to the system of linear ordinary differential equations given by equation 5.2 are of the form

$$\mathbf{u}(t) = \sum_{i=1}^n c_i e^{\beta_i t} \cdot \mathbf{v} \quad (5.3)$$

where β are the eigenvalues of $\mathbf{J}(\mathbf{x}_s)$, and \mathbf{v} are the corresponding eigenvectors. For the ternary systems considered here, there are two eigenvalues and two corresponding eigenvectors solution, and the solution form is

$$u_1(t) = c_1 e^{\beta_1 \tau} v_1(1) + c_2 e^{\beta_2 \tau} v_2(1) \quad (5.4a)$$

$$u_2(t) = c_1 e^{\beta_1 \tau} v_1(2) + c_2 e^{\beta_2 \tau} v_2(2) \quad (5.4b)$$

with the summation of molefractions $\sum u_i = 0$ providing the closure of the problem, and where $v_1(1)$ and $v_1(2)$ represent the first and second elements of the column eigenvector v_1 . The fixed points of residue curve maps can be stable or unstable nodes, or saddle nodes depending on the eigenvalues β_i of the Jacobian in equation 5.2 (Hirsch et al. 2004):

- Eigenvalues real and both positive - unstable node
- Eigenvalues real and both negative - stable node
- Eigenvalues real and opposite sign - saddle

See figures 5.1 and 5.2b below for example residue curve map displaying these characteristics. Doherty & Perkins (1978a) also showed that complex and pure imaginary eigenvalues do not occur for the simple distillation described by equation 5.1.

If the deviation \mathbf{u} is small, so that the composition \mathbf{x} differs only slightly from the composition of the fixed point (at which $\mathbf{x} = \mathbf{y}(\mathbf{x})$), then an alternate form of the Jacobian is given by Pollmann et al. (1996):

$$\mathbf{J}'(\mathbf{x}_S) = \begin{pmatrix} \frac{\partial y_1}{\partial x_1} - \frac{\partial y_1}{\partial x_n} & \cdots & \frac{\partial y_1}{\partial x_{n-1}} - \frac{\partial y_1}{\partial x_n} \\ \vdots & & \vdots \\ \frac{\partial y_{n-1}}{\partial x_1} - \frac{\partial y_{n-1}}{\partial x_n} & \cdots & \frac{\partial y_{n-1}}{\partial x_{n-1}} - \frac{\partial y_{n-1}}{\partial x_n} \end{pmatrix} \quad (5.5)$$

which has eigenvalues denoted by λ_i . The subtraction of the partial derivative with respect to the n th components arises from the fact that the sum of the mole fractions sums to unity. The partial derivatives with respect to mole fractions are calculated (analytically in this work) as if all mole fractions are independent (Salomone & Espinosa 2001), and the choice of the n th component is arbitrary. The eigenvectors for $\mathbf{J}(\mathbf{x}^s)$ and $\mathbf{J}'(\mathbf{x}^s)$ are the same, but the eigenvalues are related by $\beta_i = 1 - \lambda_i$ (Pollmann et al. 1996).

For a ternary mixture (selecting 1 and 2 as the primary components and component 3 as the n th), equation 5.5 reduces to

$$\mathbf{J}'(\mathbf{x}_S) = \begin{pmatrix} \frac{\partial y_1}{\partial x_1} - \frac{\partial y_1}{\partial x_3} & \frac{\partial y_1}{\partial x_2} - \frac{\partial y_1}{\partial x_3} \\ \frac{\partial y_2}{\partial x_1} - \frac{\partial y_2}{\partial x_3} & \frac{\partial y_2}{\partial x_2} - \frac{\partial y_2}{\partial x_3} \end{pmatrix} \quad (5.6)$$

For an isobaric system the vapour compositions are given by an equation of the form (see also equation 3.27):

$$y_i = \frac{p_i T(\mathbf{x})}{P} \gamma_i(T(\mathbf{x}), \mathbf{x}) x_i \quad (5.7)$$

and the composition derivatives are given by (Doherty & Perkins 1978b) as

$$\frac{\partial y_i}{\partial x_j} = \delta_{ij} \left(\frac{p_i}{P} \right) + x_i \left(\frac{p_i}{P} \right) \frac{d\gamma_i}{dx_j} + \frac{1}{P} \frac{dp_i}{dT} \left(\frac{\partial T}{\partial x_j} \right) x_i \gamma_i \quad (5.8)$$

The partial derivative of temperature with respect to composition (underlined terms above) is zero at an azeotrope, so that equation 5.6 becomes (at an azeotropic fixed

Table 5.1: Procedure for calculation of eigenvalues and eigenvectors (with analytic Jacobian); optionally, compute linearized trajectories around a fixed point.

Given: operating pressure P

1. For pure component, calculate bubble/dew point (Smith & vanNess 1987)
 2. For binary/ternary azeotrope, calculate azeotropic composition and temperature via continuation algorithm (section 4.2.3)
 3. Calculate activity coefficients γ_i (appendix B.1) and derivatives of activity coefficients (appendix B.2) at the known compositions and temperature
 4. Compute Jacobian $\mathbf{J}'(\mathbf{x}_S)$ using equation 5.9 and the `eig` function (similar forms apply for the 1-3 and 2-3 pairs in a ternary mixture)
 5. Calculate eigenvalues and eigenvectors from \mathbf{J}' (using standard linear algebra techniques)
 6. To solve for linearized trajectories:
 - 6.1. Pick a start point (x_1^0, x_2^0) linearized trajectory
 - 6.2. Using the computed eigenvalues and eigenvectors, solve equations 5.4 simultaneously for the constants c_1 and c_2 (e.g. using Matlab `fsolve` function) for $u_1(0) = x_1^0 - x_1^s$ and $u_2(0) = x_2^0 - x_2^s$
 - 6.3. With the calculated values of c_1 and c_2 , project equations 5.4 forward and backwards in dimensionless time τ in a vicinity of \mathbf{x}^s
-

point)

$$\mathbf{J}'(\mathbf{x}_S) = \begin{pmatrix} \frac{p_1}{P} \left(x_1 \left[\frac{\partial \gamma_1}{\partial x_1} - \frac{\partial \gamma_1}{\partial x_3} \right] + \gamma_1 \right) & x_1 \frac{p_1}{P} \left[\frac{\partial \gamma_1}{\partial x_2} - \frac{\partial \gamma_1}{\partial x_3} \right] \\ x_2 \frac{p_2}{P} \left[\frac{\partial \gamma_2}{\partial x_1} - \frac{\partial \gamma_2}{\partial x_3} \right] & \frac{p_2}{P} \left(x_2 \left[\frac{\partial \gamma_2}{\partial x_2} - \frac{\partial \gamma_2}{\partial x_3} \right] + \gamma_2 \right) \end{pmatrix} \quad (5.9)$$

The derivatives in equation 5.9 are constrained by the fact that the x_i sum to unity. The constrained derivatives (denoted by subscript Σ) are given in terms of the unconstrained derivatives by (Taylor & Kooijman 1991)

$$\left. \frac{\partial \ln \gamma_i}{\partial x_j} \right|_{\Sigma} = \frac{\partial \ln \gamma_i}{\partial x_j} - \frac{\partial \ln \gamma_i}{\partial x_n} \quad (5.10)$$

The Jacobian thus requires evaluation of composition derivatives of the NRTL activity coefficients. Appendix B.2 gives the form of the unconstrained derivatives of $\ln x_i$; these can be used in equation 5.9 by employing the relationship

$$\frac{\partial \gamma_i}{\partial x_j} = \gamma_i \frac{\partial \ln \gamma_i}{\partial x_j}$$

The eigenvalues and eigenvectors of the Jacobians of equations 5.9 can be found directly using standard formulas of linear algebra (Lay 2006), or conveniently using the `eig` function in Matlab. Table 5.1 summarises the procedure.

Figure 5.1a shows a residue curve map for the benzene-acetone-chloroform mixture overlaid with linearized trajectories and eigen-directions, and annotated with eigenvalues at the fixed points. A portion of figure 5.1a is shown magnified in figure 5.1b. The stable node at pure benzene is characterised by negative eigenvalues (β_i), while the unstable nodes at pure acetone and pure chloroform have positive β_i . The saddle at the acetone-chloroform azeotrope has one positive and one negative eigenvalue. At each fixed point two intersecting eigen-directed lines are shown; these lines indicate the direction of influence of the exponential parts of equation 5.4. At pure chloroform, both eigenvalues β_1 and β_2 are of similar size so that the residue curves departing the pure vertex does not favour either the chloroform-benzene or the chloroform-acetone side. At pure benzene one eigenvalue (β_1) is significantly more negative than the other (β_2), so that the residue curve favours an approach along the chloroform-benzene side associated with the more negative value. A similar but less pronounced situation exists at the pure acetone vertex, with the residue curves approaching via the acetone-benzene side. For the pure component vertices, the eigen-directions point along the edges of the composition diagram; these represent the direction of changes of binary mixtures.

At the acetone-chloroform saddle azeotrope in figure 5.1b and one eigenvector passes along the acetone-chloroform edge, while the other is directed towards the interior. A number of linearized trajectories (solutions to equation 5.4) are shown adjacent to the saddle, generally following the direction of the residue curves from either of the two unstable nodes (acetone and chloroform) towards the stable node (benzene). Note that the linearized trajectories are only valid in the neighbourhood of the fixed point at which they were computed, and so do not follow the path of the residue curves very well at a distance from the fixed point.

The eigenvalues calculated using the approach of table 5.1 are compared with values found by Pollmann et al. (1996) in table 5.2, showing reasonably good agreement between the two approaches, considering that different activity coefficient models are used (Wilson model for Pollmann et al., NRTL model for this work).

Also shown in table 5.1 are the eigenvalues β_i for the form of the linearized residue curve in equation 5.2. The type of node (stable, unstable, saddle) is consistent with the sign of the β_i obtained in this way, so that the pure benzene stable node has two negative eigenvalues, the pure acetone and pure chloroform unstable nodes have two positive eigenvalues, while the saddle azeotrope of acetone-chloroform has one positive and one negative eigenvalue.

The residue curve map for ethanol/MEK/toluene in figure 5.2a has an unstable mode at the ethanol/MEK azeotrope (positive β_i), and stable nodes at pure ethanol and pure

Table 5.2: Comparison of computed eigenvalues of equation 5.9 (NRTL model) with calculations of Pollmann et al. (1996) (Wilson model); also shown are eigenvalues β_i for open evaporation (equation 5.2; SN = stable node, UN = unstable node, S = saddle; $P = 1.0$ bar

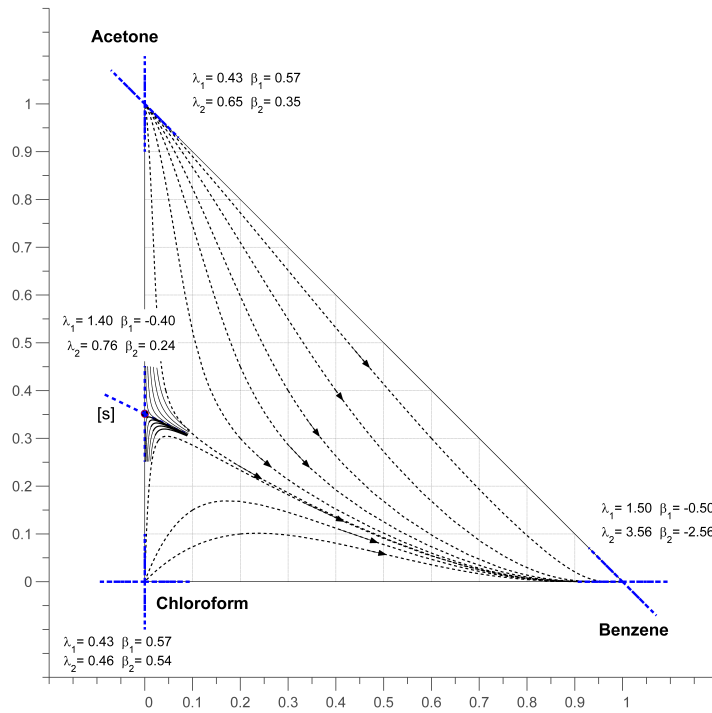
Pure components & azeotropes	Calculated Eigenvalues	Eigenvalues (Pollmann et al. 1996)	Eigenvalues (Open Evaporation)
Benzene (SN)	$\lambda_1 = 1.50$	$\lambda_1 = 1.6$	$\beta_1 = -0.50$
	$\lambda_2 = 3.56$	$\lambda_1 = 3.4$	$\beta_2 = -2.56$
Acetone (UN)	$\lambda_1 = 0.43$	$\lambda_1 = 0.46$	$\beta_1 = 0.57$
	$\lambda_2 = 0.65$	$\lambda_1 = 0.62$	$\beta_2 = 0.35$
Chloroform (UN)	$\lambda_1 = 0.43$	$\lambda_1 = 0.44$	$\beta_1 = 0.57$
	$\lambda_2 = 0.46$	$\lambda_1 = 0.49$	$\beta_2 = 0.54$
Acetone/Chloroform (S)	$\lambda_1 = 1.40$	$\lambda_1 = 1.4$	$\beta_1 = -0.4$
	$\lambda_2 = 0.76$	$\lambda_1 = 0.73$	$\beta_2 = 0.24$

toluene (negative β_i). The saddles at pure MEK and the ethanol/toluene azeotrope have β_i of opposite sign. There is a large disparity in size of the eigenvalues at pure toluene, so that the residue curves track toward the node along one particular eigen-direction, the MEK/toluene edge.

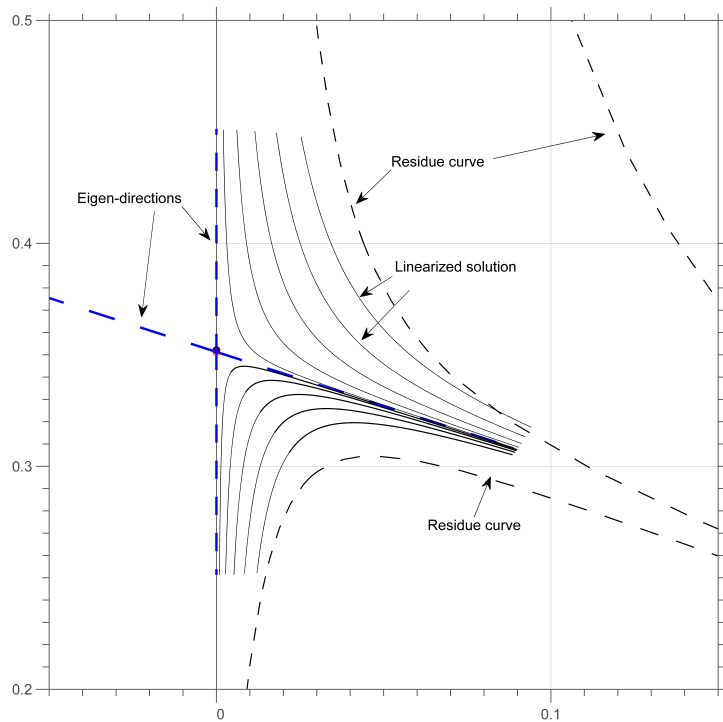
As a more complex example, figure 5.2b shows the residue curve map for acetone/chloroform/methanol, including eigenvalues and eigen-directed lines at each of the fixed points. The stable nodes of this mixture are pure methanol and the maximum-boiling acetone/chloroform azeotrope, which have two negative eigenvalues (β_i). The acetone/methanol and chloroform/methanol minimum-boiling azeotropes are unstable nodes, characterized by two positive eigenvalues each. Pure acetone and pure chloroform are binary saddles, having one positive and one negative eigenvalue. Finally, the ternary azeotrope is a saddle, with one positive and one negative azeotrope. At the ternary azeotrope, it can be seen that the eigen-directed lines are oriented in the direction of the residue curves at that point.

5.2 Stability of Fixed Points in Evaporation Maps

The previous section demonstrated the approach for assessing the stability of residue curve maps via calculation of eigen-values and eigen-vectors at the fixed points. In this section an analogous approach is adopted for evaporation maps. Luna & Martinez (1998, 1999) developed criteria for stability of pseudo-azeotropes in gas-phase controlled drying of liquid mixtures. They posited that the stability of the non-isothermal system could be derived from an analysis of the equivalent isothermal system, using arguments based on a continuously rising temperature profile during evaporation. However, as section 6.3 demonstrates, temperature does not rise monotonously dur-



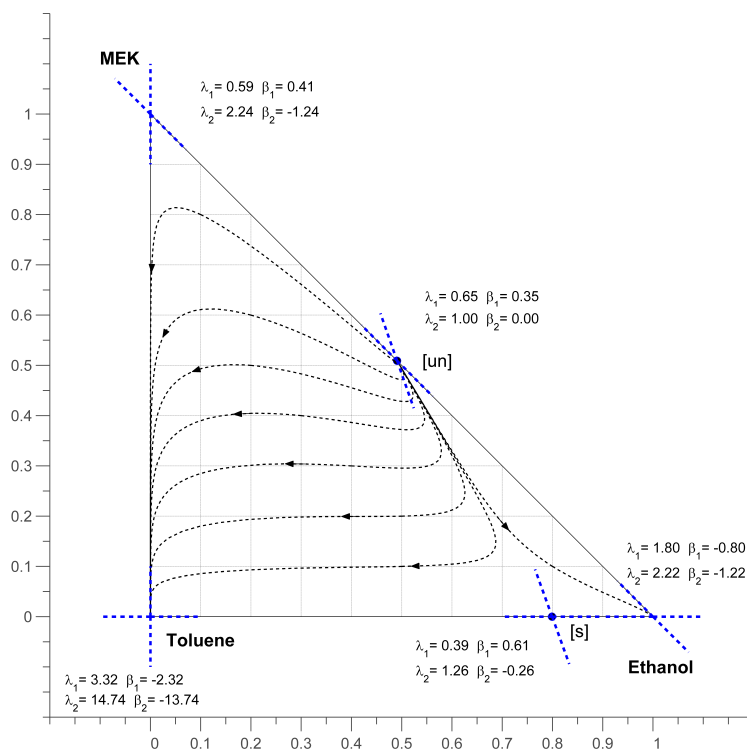
(a) Benzene-acetone-chloroform



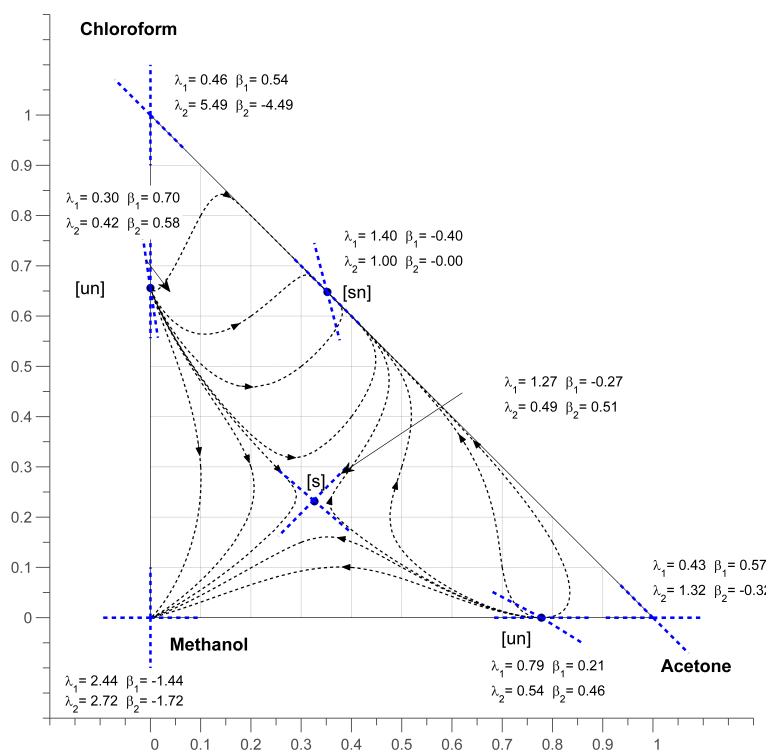
(b) Magnified portion around azeotrope showing linearized approximations

Figure 5.1: Eigen-values and eigen-directions for residue curve map of benzene-acetone-chloroform.; dashed lines are eigen-directions.

5. STABILITY ANALYSIS



(a) Ethanol-MEK-toluene



(b) Acetone-chloroform-methanol

Figure 5.2: Eigen-values and eigen-directions for RCM example mixture; $P = 1.0$ bar.
 Heavy dashed lines are eigen-directions at the fixed points.

ing evaporation of a multicomponent mixture, and ridges and valleys in the wet-bulb temperature surface are crossed during the multicomponent evaporation process. Rev (1992) reached a similar conclusion in a study of residue curve maps, finding that temperature does not rise monotonously during open evaporation (simple distillation) processes. Nevertheless, we may use the assumption that *in the neighbourhood of the stable fixed points* the wet-bulb temperature does continuously rise; this is evident in the wet-bulb temperature surfaces of figures 3.12-3.14, so that the approach of Luna & Martinez (1998, 1999) is valid in those neighbourhoods.

Recall that the component balance for gas-phase limited drying (equation 3.28) is given by:

$$\frac{dx_i}{dt} = -\frac{A}{h_T^L} \left(\frac{x_i}{N_t} - N_i \right) \quad (5.11)$$

and the corresponding energy balance is given by equation 3.33. For the isothermal case, the energy balance is not required, and at a fixed point (pure component or pseudo-azeotrope) x_i^s , the right-hand side of equation 5.11 will be zero:

$$F(x_i^s) = 0 = \frac{A}{h_T^L} (x_i N_t - N_i) \quad (5.12)$$

As the term involving A/h_T^L will always be ≥ 0 , the stability characteristics can be analysed by taking calculating the eigen-values of the Jacobian of the term in brackets at the fixed point:

$$\mathbf{J}(\mathbf{x}_s) = \left[\frac{\partial F_i}{\partial x_j} \right]_{\mathbf{x}=\mathbf{x}^s} \quad (5.13)$$

$$= \begin{pmatrix} x_1 \frac{\partial N_t}{\partial x_1} - \frac{\partial N_1}{\partial x_1} + N_t & x_1 \frac{\partial N_t}{\partial x_2} - \frac{\partial N_1}{\partial x_2} \\ x_2 \frac{\partial N_t}{\partial x_1} - \frac{\partial N_2}{\partial x_1} & x_2 \frac{\partial N_t}{\partial x_2} - \frac{\partial N_2}{\partial x_2} + N_t \end{pmatrix} \quad (5.14)$$

The Jacobian includes terms for $i = 1 \dots n - 1$ with the n th mole-fraction given by $\sum x_i = 1$. Calculation of the Jacobian involves firstly finding the component and total fluxes at points over the entire composition space, using the multicomponent fluxes algorithm of table 3.1. A finite-difference approximation is then used to compute the flux gradients over the x_1 - x_2 composition space, represented by indices k, j below. For points on the edge of the composition triangle, a 3-point asymmetric forward difference approximation is used. For gradients in the x_1 direction, this gives:

$$\frac{\partial N_i}{\partial x_1}(k, j) = \frac{-3N_i(j, k) + 4N_i(j, k + 1) - N_i(j, k + 2)}{2\Delta x_1}$$

Table 5.3: Algorithm for calculation of eigenvalues and eigenvectors of evaporation maps

-
1. Establish a grid of $n_p \times n_p$ points over the ternary composition space
 2. At each composition point $\mathbf{x}(j)$, $j = 1 \cdots n_p$, calculate the component fluxes $N_i(j)$ and the wet-bulb temperature $T_{WB}(\mathbf{x}(j))$
 3. Normalize the fluxes for each component i (by dividing by the largest flux of each component)
 4. Locate binary and ternary pseudo-azeotropes for the mixture (see chapters 3 and 4.
 5. At each fixed point (pure components + pseudo-azeotropes), calculate flux gradients using forward-difference or centered difference formula
 6. Assemble Jacobian at each fixed point from calculated flux gradients (equation 5.14)
 7. Compute eigen-values and eigen-vectors from Jacobian at each fixed point
-

which is $\mathcal{O}(\Delta x^2)$ accurate (Selebi & Schiesser 1992). Similar formulations are used for gradients in the x_2 and x_3 directions. For points in the interior of the composition space, a 5-point centered difference approximation which is $\mathcal{O}(\Delta x^4)$ accurate (Selebi & Schiesser 1992) is used:

$$\frac{\partial N_i}{\partial x_1}(k, j) = \frac{-N_i(j, k+2) + 8N_i(j, k+1) - 8N_i(j, k-1) - N_i(j, k-2)}{12\Delta x_1}$$

Table 5.3 summarises the numerical procedure for calculation of eigenvalues and eigenvectors for evaporation maps. Figure 5.3 shows computed component and total fluxes for the acetone-chloroform-methanol mixture calculated at points over the composition space; it is from such composition data the the flux gradients $\partial N_i / \partial x_j$ are determined. Figure 5.4 shows evaporation maps for two example mixtures, over-laid with eigen-directions at the fixed points, and annotated with the eigenvalues of equation 5.14. As with residue curve maps, the stability of the fixed points can be assessed in terms of the eigenvalues. For the ethanol-MEK-toluene mixture in figure 5.4a, the eigenvalues are both negative at the pure ethanol and pure toluene stable nodes (where evaporation trajectories terminate). Similarly, the eigenvalues are both positive at the ethanol-MEK pseudo-azeotrope which is an unstable node, while the ethanol-toluene saddle has eigenvalues with mixed sign.

In figure 5.4b, the unstable nodes at the acetone-methanol and chloroform-methanol pseudo-azeotropes have eigenvalues with postive sign, while the stable nodes at the

acetone-chloroform pseudo-azeotrope and at pure methanol have negative signs. The saddle at pure chloroform and that at the ternary azeotrope have eigenvalues with mixed signs.

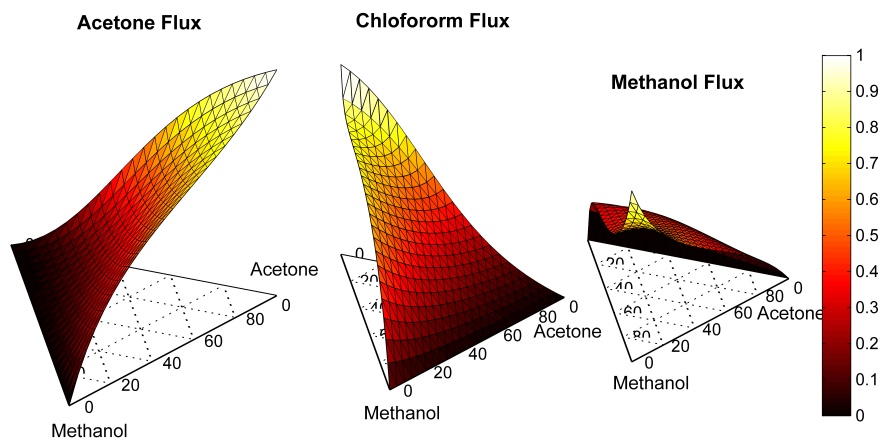
Recalling that the eigenvalues represent a linearized approximation in the vicinity of the fixed points, the eigenvalues of the stable toluene node in figure 5.4a can be compared with those of the stable methanol node in figure 5.4a to examine the significance of the relative sizes of the eigenvalues. For the methanol node, the eigenvalues are similar in size, so that trajectories approach the node without tending to favour either the acetone-methanol or the chloroform-methanol edge. By contrast, for the toluene node the disparity in size of the eigenvalues is indicative of trajectories to hug one particular edge. This is borne out by the trajectories in the neighbourhood of the toluene node which hug the chloroform-methanol edge.

5.3 Chapter Summary and Conclusions

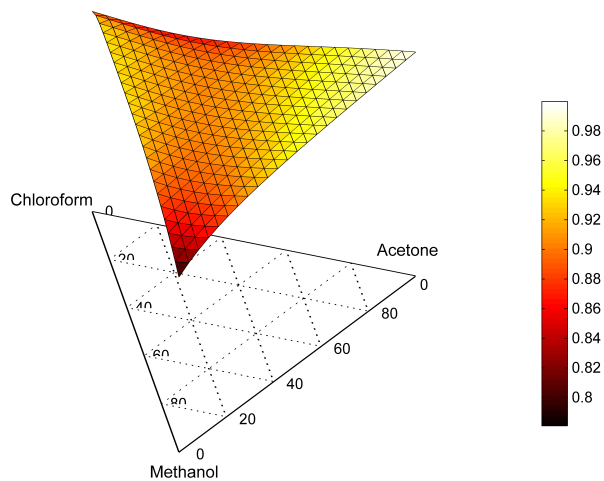
The stability of an evaporation or drying process can be characterized by the eigenvalues of the linearized process at the fixed points of the system. The stability in this case refers to the mathematical stability of the system of non-linear ordinary differential equations (ODEs) that are used to model the process. The eigen-directions at the fixed points show the asymptotic behaviour of trajectories in the neighbourhood of the fixed points. In this chapter, methods for calculation of eigenvalues and eigen-directions for residue curve maps and evaporation maps have been developed. The method used for residue curve maps is motivated by existing work by Doherty & Perkins (1978a,b) and Pollmann et al. (1996), and uses an analytic form of the Jacobian matrix at the fixed points to calculate the eigenvalues. The method used for evaporation maps is guided by work of Luna & Martinez (1998, 1999) for batch drying of multicomponent mixture, and locates eigenvalues and eigen-directions by firstly calculating derivatives of component fluxes at the fixed points using a numerical finite difference method.

The characteristics of a number of non-ideal ternary mixtures have been evaluated in terms of the eigenvalues of the fixed points, and have been shown to qualitatively describe the stability; nodes with two negative eigenvalues are stable, nodes with two positive eigenvalues are unstable, while nodes with eigenvalues of opposing sign are saddles. In addition to indicating the asymptotic flow of residue curve and evaporation trajectories, the eigen-directions are used in chapter 6 in a method for location of separation boundaries.

5. STABILITY ANALYSIS

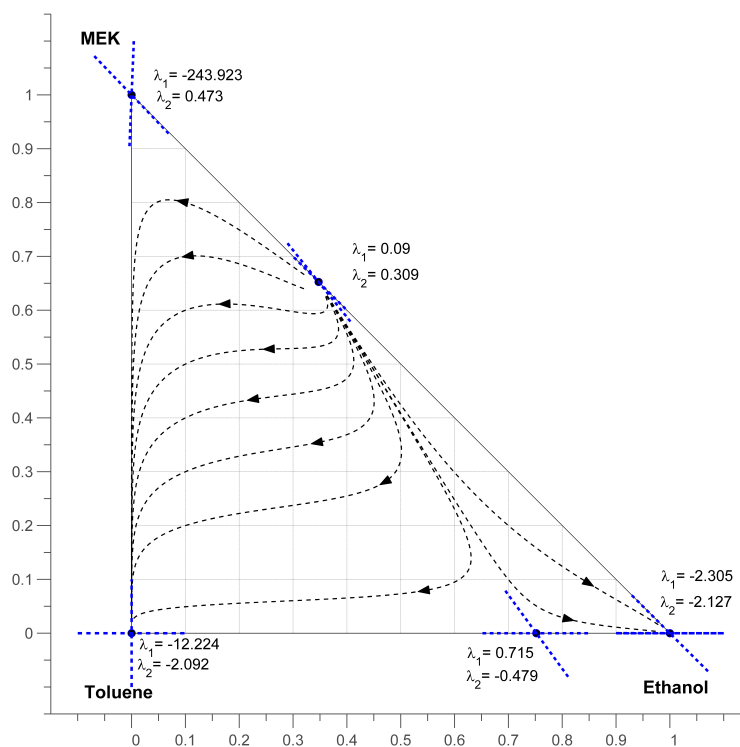


(a) Component fluxes (normalised)

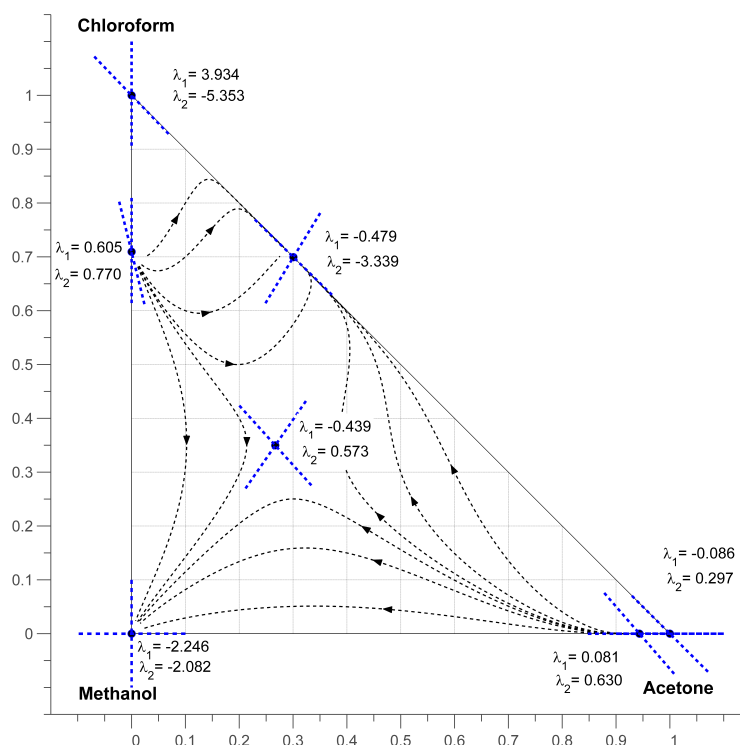


(b) Total flux

Figure 5.3: Surface plots of component and total fluxes (normalized) in acetone/chloroform/methanol mixture ; $T^G = 20^\circ\text{C}$, $u^G = 0.5\text{m/s}$, $d = 0.03\text{m}$



(a) Ethanol-MEK-toluene



(b) Acetone-chloroform-methanol

Figure 5.4: Eigen-values and eigen-directions for evaporation map example mixtures; heavy dashed lines are eigen-directions at the fixed points.

Chapter 6

Separation Boundaries

The location of separation boundaries is an important issue in practice, as boundaries separate the composition space into regions where different product compositions are obtained during distillation (for residue curve maps) or evaporation/drying (for evaporation maps). In this chapter numerical methods for the location of separation boundaries in both types of maps are investigated. For evaporation maps, a method employing eigenvectors derived from the linearized analysis is firstly developed by analogy with existing methods for residue curve maps. For both types of maps, a novel approach for calculation of separation boundaries using an optimization-based maximum-area method is presented. The flexure of the wet-bulb temperature surface (ridges and valleys) is explored, and it is shown how evaporation trajectories cross ridges and valleys, so that ridges and valleys do not coincide with separation boundaries.

An analysis of the residue curve maps shown in figure 2.2 suggests the existence of limiting residue curves that connect saddle azeotropes to other fixed points (pure components, or other azeotropes). In figure 2.2b, the limiting curve is between the water-ethanol saddle azeotrope and pure methanol. In figure 2.2b, the limiting curve is between the IPA-water azeotrope and the ethanol-water azeotrope. Figure 2.2f suggests a limiting curves connecting the acetone-chloroform azeotrope to pure methanol via the ternary saddle azeotrope, and a further limiting curve connecting the chloroform-methanol azeotrope to the acetone-methanol azeotrope via the ternary saddle. Residue curve map boundaries for two example ternary mixtures are shown more explicitly in figure 6.2.

Such boundaries based on limiting residue curves are termed *simple distillation boundaries* (SDB). For higher dimensional systems ($n > 3$), the boundaries form multidimensional hypersurfaces (Bruggemann & Marquardt 2011). A separation boundary is a *separatrix* or *invariant manifold* in a mathematical context; each ternary saddle is characterized by two such manifolds, one unstable and one stable, so that the saddle is an attractor for its stable manifold and a repellor for its unstable manifold (Blagov

& Hasse 2002). A *distillation region* is defined as a subset of the composition space in which all residue curves originate from the same locally minimum-boiling fixed point, and terminate at the same local maximum boiling fixed point. Mathematically, a distillation region is a *basin of attraction* for the governing system of equations expressed by 2.17 (Strogatz 1994).

The evaporation maps shown in figures 3.18-3.23 show analogous behaviour to that of the residue curve maps. In this case, the fixed points are pure components and pseudo-azeotropes; separation boundaries connect saddles and fixed points as with residue curve maps. Boundaries are also present in the evaporation maps with pre-loaded gas phase shown in figures 4.9-4.11, with the location of the boundary changing (and ultimately disappearing) as the concentration of pre-loaded gas increases.

Despite the extensive literature on residue curve maps, there exist few methods for exact calculation of separation boundaries. Approximate numerical approaches include those of Foucher et al. (1991), Peterson & Partin (1997), Rooks et al. (1998) and Popken & Gmehling (2004). Each of these methods finds approximate separation boundaries of equation 2.17. In industrial practice, the most common approach to computation of separation boundaries for a residue curve map involves firstly determining the eigen-directions of the ternary saddle azeotropes of the mixture, if one exists (see section 5.1). The integration of equation 2.17 is then initiated from a point a small distance along each of the eigen-directions, and proceeds forwards or backwards in dimensionless time τ until a fixed point (stable or unstable node) is reached (AspenTech 2015).

Reyes-Labarta et al. (2010) proposed a method for approximate location of boundaries based on optimizing the location of a spline-fit to a set of points joining two azeotropic points. The method of Lucia & Taylor (2006) involves maximizing line integrals derived from individual residue curves. This approach however requires a global optimization over the line integrals (trajectory-lengths), as the integrals do not necessarily display a single, global optimum within a given separation region. The method of Lucia & Taylor locates an initial local maximum, then employs a terrain optimization method to verify that the computed trajectory is optimal within that region.

In section 6.1 the linearized analyses of chapter 5 is used as a means to initiate the computation of separation boundaries for both residue curve and evaporation maps. In section 6.2 a "maximum-area" method for computation of boundaries in both types of maps is developed. In section 6.3 the flexure of the wet-bulb temperature is explored.

6.1 Separation boundaries from linearized analysis

For residue curve maps, separation boundaries may be calculated by integrating the ordinary differential equations that describe the residue curves from a point adjacent to a saddle azeotrope up to a stable or unstable node. This is done by firstly calculating the eigenvectors/eigen-directions at the saddle, then taking a small step in the direction of the eigenvector towards the node. The basis for calculating eigen-vectors at fixed points of residue curve maps was discussed In section 5.1.

For residue curve maps, having determined the initial composition on the eigenvector, the differential equations are then integrated forward in dimensionless time τ until a stable node is reached, or backwards in τ until an unstable node is reached. For evaporation maps a similar forward or backwards integration can be used.

Figure 6.1 shows the procedure for calculating boundaries using eigenvectors to initialize the integration procedure. The approach is summarised for residue curve maps is summarised in table 6.1, and for evaporation maps in table 6.2. The approaches for residue curve maps and evaporation maps are analagous, although the fixed points are different, and the generation of the eigenvectors is achieved in different ways as discussed in detail in chapter 5.

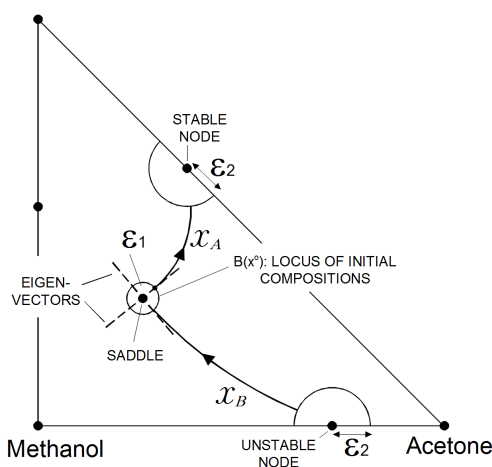


Figure 6.1: Schematic for determination of separation boundaries in ternary mixture (acetone-chloroform-methanol)

Computed Boundaries in Residue Curve Maps Figure 6.2a shows calculated separation boundary for the residue curve map for benzene-acetone-chloroform mixture; the corresponding eigen-directed lines for this mixture are shown in figure 5.1a. The separation boundary connects the binary saddle on the acetone-chloroform edge to the pure benzene vertex.

Table 6.1: Algorithm for generation of separation boundaries in residue curve maps using eigenvector calculated at saddle node

-
1. Locate binary and ternary azeotropes for the mixture
 2. For a given saddle node specify the radius ϵ_1 around the node which defines the locus of possible initial concentrations as $B(x^o) = \{x : \|x - x^o\| = \epsilon_1\}$ (see figure 6.1)
 3. Calculate the eigenvectors at the saddle node by the methods outlined in section 5.1
 4. Calculate the composition a small distance ϵ_1 along the eigenvector in the direction of a node (see figure 6.1)
 5. Generate the boundary (limiting residue curve) by numerically integrating equation 2.17 forwards in τ to a stable node, or backwards in τ to an unstable node; the integration is terminated when x approaches a node within a certain distance ϵ_2
 6. If no ternary saddle exist, apply the procedure above to any binary saddles in the mixture
-

Figure 6.2b shows the computed residue curve map separation boundaries for acetone/chloroform/methanol mixture; the eigen-directed lines for this mixture are shown in figure 5.2b. In this case the separation boundary runs from the unstable chloroform-methanol node through the ternary saddle to the stable acetone-chloroform node, and from the unstable acetone-methanol node through the ternary to the stable methanol node.

Computed Boundaries in Evaporation Maps Figure 6.3a shows calculated separation boundary for the evaporation map for benzene-acetone-chloroform mixture. Figure 6.3b shows the separation boundaries for the acetone-chloroform evaporation map. Refer to figure 5.4b for the corresponding analysis of eigenvalues and eigen-vectors.

6.2 Separation boundaries by optimization

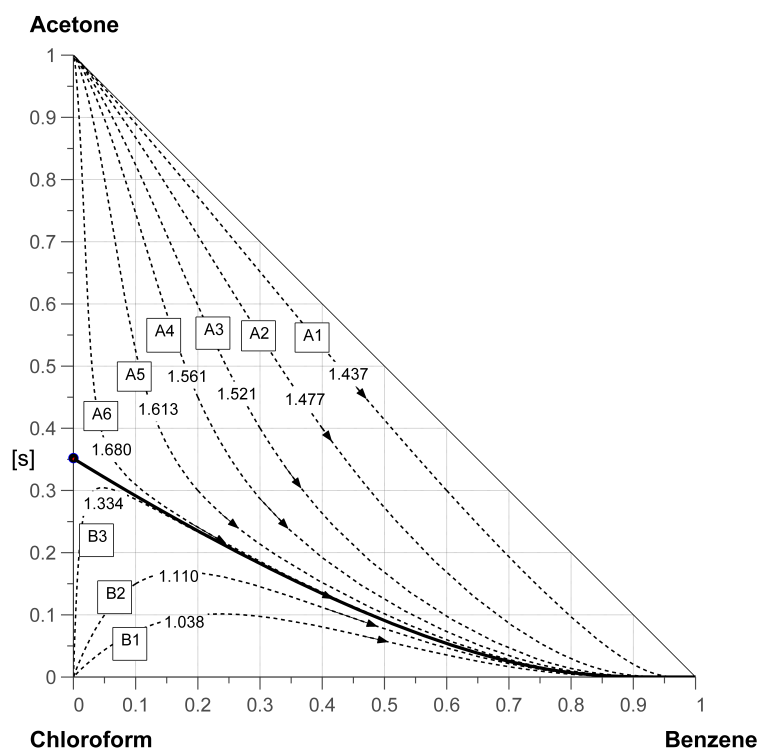
Lucia & Taylor (2006) presented a geometric characterization of separation boundaries in residue curve maps for homogeneous mixtures. Their key observation was that the line integral (or trajectory-lengths along residue curve) from an unstable node to a reachable stable node is a local extremum along a boundary. In their formulation, a residue curve between an unstable and a stable node can be represented as a parameterized trajectory $x(\alpha)$ for $\alpha \in [0, T]$, where $x(0)$ and $x(T)$ are the beginning and end-points of the residue curve (Lucia & Taylor 2006). This approach was extended to reactive systems by Taylor et al. (2006).

Table 6.2: Algorithm for generation of separation boundaries in evaporation maps using eigenvector calculated at saddle node

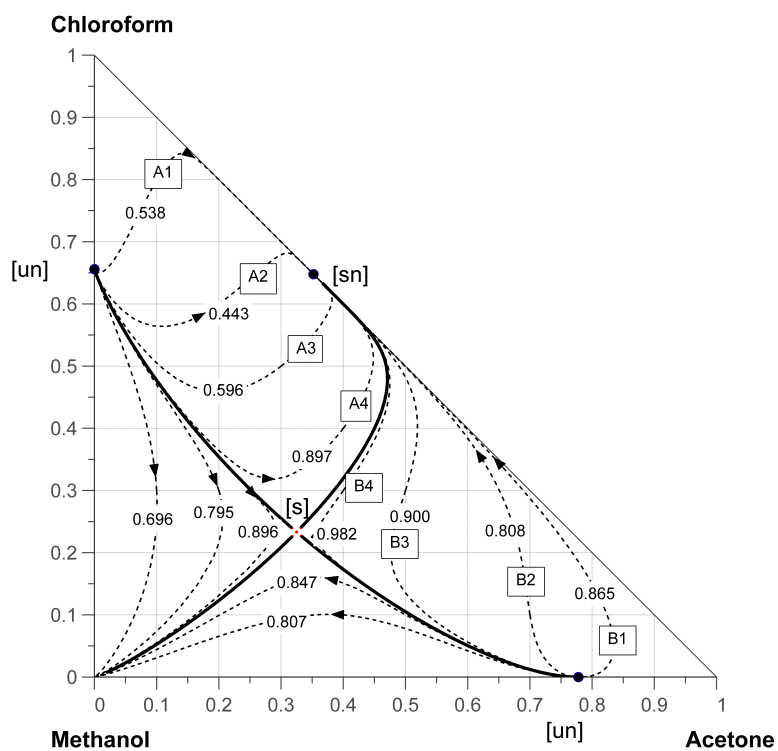
-
1. Locate binary and ternary pseudo-azeotropes for the mixture
 2. For a given unstable node specify the radius ϵ_1 around the node which defines the locus of possible initial concentrations as $B(x^o) = \{x : \|x - x^o\| = \epsilon_1\}$.
 3. Calculate the eigenvectors at the unstable node by the methods outlined in section 5.2
 4. Calculate the composition a small distance ϵ_1 along the eigenvector in the direction of a stable node (see figure 6.1)
 5. Generate the boundary (limiting evaporation trajectory) by numerically integrating the system of governing equations 3.28, 3.30 & 3.33, coupled with the multicomponent flux calculation from table 3.1; the integration is terminated when x approaches a stable node within a certain distance ϵ_2
 6. Repeat from step 2 for any further unstable nodes in the mixture
-

Figure 6.2 shows example residue curve maps for two ternary mixtures, with computed arc lengths shown for a number of residue curves. Consider firstly the benzene-acetone-chloroform mixture in figure 6.2a, which has a single distillation boundary that runs between pure benzene and the acetone-chloroform saddle azeotrope. It can be seen from the figure that the arc length increases for the curves denoted A1-A6, as they progress from the benzene-acetone edge towards a maximum value along the separation boundary. Similarly, the arc length also increases for the curves denoted B1-B3, as they approach the separation boundary from the benzene-chloroform edge. A more complex example is that of figure 6.2b, which has three binary azeotropes and one ternary azeotrope. The acetone-methanol and chloroform-methanol azeotropes are unstable nodes, while pure methanol and the acetone-chloroform azeotrope are stable nodes. As with the preceding example, when any residue curve from either of the unstable nodes to a reachable stable node is considered, the integral length (arc length) along the separation boundary is greater than any other trajectory in the same region. However, considering the progression from A1-A4, it can be seen that there is more than one maximum in the integral length as the length of curve A2 is shorter than A1 or A3. A similar situation exists for the progression from B1-B4, where B2 is shorter than B1 or B3. This demonstrates that when using maximum integral length as an optimization variable, it is necessary to find *all* the line integrals of maximum length in all separation regions to define separation boundaries with certainty.

A similar situation exists with the evaporation maps shown in figure 6.3. Arc lengths in figure 6.3a become increasingly longer as they progress from the edges towards the



(a) Benzene/chloroform/methanol



(b) Acetone/chloroform/methanol

Figure 6.2: Trajectory-lengths and separation boundaries for example residue curve maps; filled circles represent pure components and azeotropes; $P = 1.0$ bar

separation boundary, while for 6.3b this does not hold.

In this section an approach for determining the separation boundaries in residue curve maps and evaporation maps based on a maximum circumscribed area is developed; this method is based on the intuitive observation that separation boundaries are lines which circumscribe a maximum area in a separation region. This approach is an alternative to the maximum trajectory-length approach of Lucia & Taylor (2006), and obviates the requirement for an additional step to ensure that the trajectory-length is in fact optimal in the separation region. In the following discussion, the approach by optimization of trajectory length is first considered for each type of map, followed by the maximum-area approach.

6.2.1 Optimization of integral trajectory length

Residue Curve Maps Recall that the governing equation for residue curve map (see equation 2.17) is

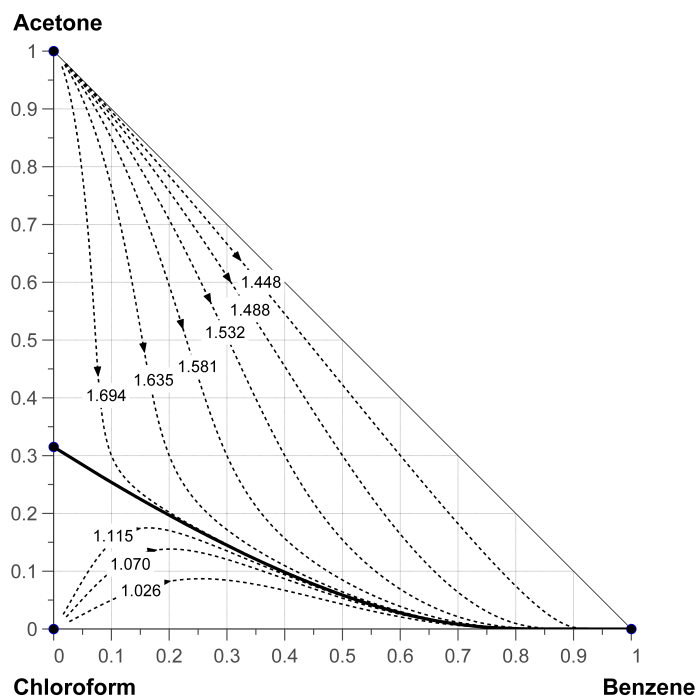
$$-\frac{d\mathbf{x}}{d\tau} = \mathbf{y}(\mathbf{x}) - \mathbf{x} \quad (6.1)$$

In the method of Lucia & Taylor (2006) the separation boundary for a residue curve map is the trajectory associated with the solution to the following optimization problem for the line integral D :

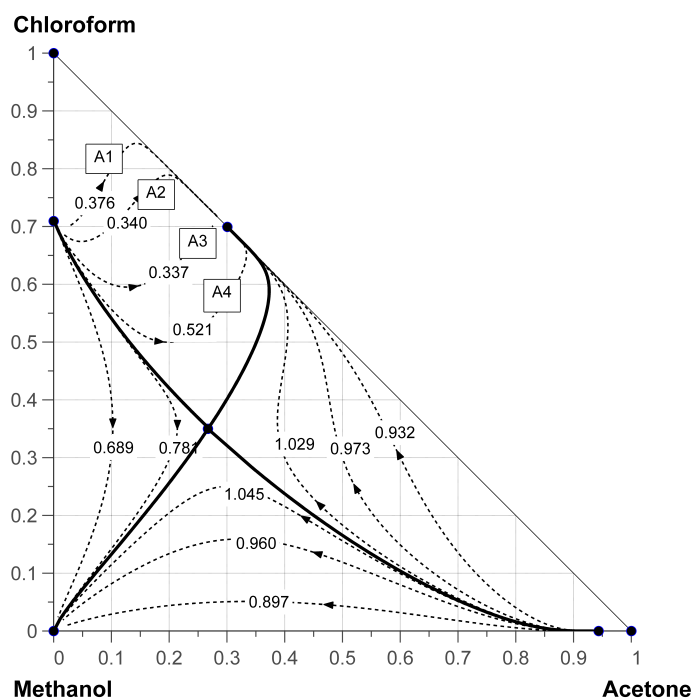
$$\begin{aligned} \max_{\mathbf{x}^\theta} D &= \int_0^T \left\| \frac{d\mathbf{x}(\alpha)}{d\tau} \right\| d\alpha \approx \sum_{k=0}^N \|\Delta x_k\| \\ -\frac{d\mathbf{x}(\alpha)}{d\tau} &= \mathbf{y}(\mathbf{x}(\alpha)) - \mathbf{x}(\alpha) \\ \mathbf{x}(T) &= \mathbf{x}^T \end{aligned} \quad (6.2)$$

where $\|\cdot\|$ denotes the two-norm, $\mathbf{x}^\theta = (x_1^\theta, x_2^\theta)$ is a feasible set of initial conditions on the circle of radius ϵ surrounding the unstable node \mathbf{x}^o (depending only on θ), α is a dummy length variable and \mathbf{x}^T is a stable node. The line integral D represents the line integral or distance along a solution curve obtained from the numerical integration of $d\mathbf{x}(\alpha)/d\tau$. The integral is in turn approximated by the summation of the norm between successive points on the solution for \mathbf{x} between 0 and T . Note that \mathbf{x} is an $n - 1$ dimension array, with the $n - th$ mole-fraction obtained from $\sum x_i = 1.0$.

Evaporation Maps The analogous optimization expression for an evaporation map in this work uses the governing equations that describe the gas-phase limited evaporation process. Using the component material balance from equation 3.28 and the energy



(a) Benzene/chloroform/methanol



(b) Acetone/chloroform/methanol

Figure 6.3: Trajectory-lengths and separation boundaries for example evaporation maps; filled circles represent pure components and pseudo-azeotropes; $T^G = 20^\circ\text{C}$, $u^G = 0.5\text{ m/s}$, $d = 0.03\text{ m}$

balance from equation 3.33 gives the optimization problem as:

$$\begin{aligned}
 \max_{\mathbf{x}^\theta} D &= \int_0^T \left\| \frac{d\mathbf{x}(\alpha)}{d\alpha} \right\| d\alpha \approx \sum_{k=0}^N \|\Delta \mathbf{x}_k\| \\
 \frac{dx_i}{dt} &= -\frac{A}{h_T^L} (N_i - x_i N_t) \\
 \frac{dT^L}{dt} &= \frac{\left[h_V^\bullet (T^G - T^L) - \sum_{i=1}^3 N_i \Delta H_i^{vap} - \sum_{i=1}^3 N_i M_i C p_i^G (T^G - T^L) \right]}{\sum_{i=1}^3 h_i^L M_i C p_i^L} \\
 \mathbf{x}(T) &= \mathbf{x}^T
 \end{aligned} \tag{6.3}$$

where, at each time increment of integration, the fluxes N_i are determined using the algorithm of table 3.1. Note that in the formulation of equation 6.3, the heat & mass-transfer area A and hold-up h_T^L could be subsumed into a dimensionless time as was implicitly done for liquid hold-up in the residue curve optimization (time τ) of equation 6.2.

To ensure that the integral length is optimal for a given unstable node, Lucia & Taylor (2006) used the terrain methodology of Lucia & Feng (2002) to explore the range of feasible rotation angles, $\theta_{min} \leq \theta \leq \theta_{max}$; for the benzene vertex in figure 6.2a, the range of feasible angles is $0 \leq \theta \leq 45^\circ$, as the ternary map is presented on a right-angle triangle. Similarly, for the acetone/methanol unstable node in figure 6.2b, the range of feasible angles is $0 \leq \theta \leq 180^\circ$. The idea in the method of Lucia & Taylor (2006) is to firstly determine the optimal angle θ^* and corresponding separation boundary $\mathbf{x}^*(\alpha)$, and then search over the feasible rotation angles $\theta_{min} \leq \theta \leq \theta_{max}$ using the terrain method to either verify that θ^* is optimal, or to locate the actual optimal value.

Figure 6.4 shows schematically how the optimization procedure for maximising the integral length is performed, for either type of map. Starting from a point \mathbf{x}_j^θ which is located a distance ϵ_1 from an unstable node, the integration progresses until a neighbourhood ϵ_2 of a stable node is reached. In the case of figure 6.4a, the integration may terminate in an ϵ_2 neighbourhood of either the acetone/chloroform node or the methanol node. At each value of θ_j , the governing differential equations are integrated forward in time (τ or t) until a termination criterion is met, and the line length is computed from the integrated trajectory \mathbf{x} . Two trajectories of maximum length correspond to the separation boundaries that run (1) from acetone/methanol node to the acetone/chloroform node or (2) from acetone/methanol node to the pure methanol node. In the case of figure 6.4b, the integration starts at the chloroform/methanol node, but terminates at the same stable nodes as before. In the implementation of the maximum trajectory length approach used here, the selection of feasible angles is done using *ad-hoc* approach; the range is sub-divided into a number of sub-ranges over which the optimization is performed. The optimal length is then found by taking the

maximum over the sub-ranges. This does not definitively ensure that the maximum length is located, but is adequate to demonstrate the method for comparison purposes with the maximum-area approach.

Note that trajectories that lie along the edges of the composition simplex are also feasible. Table 6.5 summarises the algorithm for residue curve map boundaries, for both the maximum trajectory length and maximum area approaches.

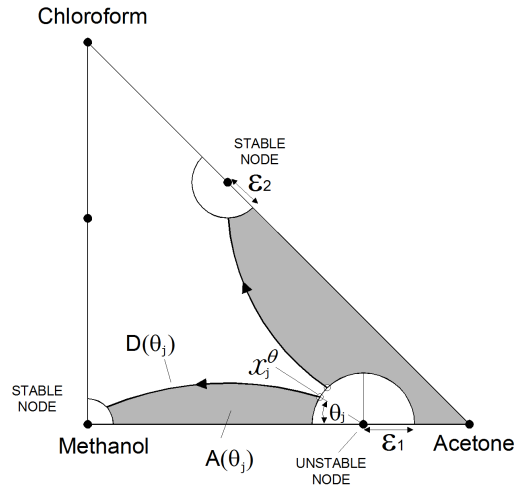
6.2.2 Optimization of integral area

Residue Curve Maps The integral length approach involves a parameterisation along the trajectory length (arc-length) α . The area circumscribed by the trajectory is the primary concern with the alternative approach described here. The optimization is based on the area circumscribed by a trajectory; the curve under which the area is to be calculated is the output of the numerical integration of $d\mathbf{x}(\alpha)/d\tau$, which is a function of θ (see figure 6.4):

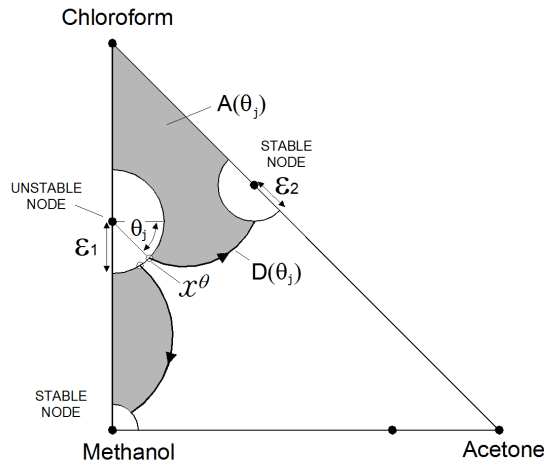
$$\begin{aligned} \max_{\mathbf{x}^\theta} A &= \int_0^T \int_{A(\alpha)} \frac{d\mathbf{x}(\alpha)}{d\tau} da d\alpha \approx \frac{1}{2} \sum_{k=0}^N (x^{k+1} - x_1^k) \left(\frac{d\mathbf{x}(x_1^k)}{d\tau} - \frac{d\mathbf{x}(x^{k+1})}{d\tau} \right) \\ - \frac{d\mathbf{x}(\alpha)}{d\tau} &= \mathbf{y}(\mathbf{x}) - \mathbf{x} \\ \mathbf{x}(T) &= \mathbf{x}^T \end{aligned} \quad (6.4)$$

A trapezoidal approximation to the area integral is used above, and the derivative terms underlined represent computed values from the numerical integration of $d\mathbf{x}(\alpha)/d\tau$. The shaded areas in figure 6.4 depict the areas from a typical integration; the areas may be bounded by any of the edges of the ternary diagram depending on the starting point (unstable node) and the termination point (stable node). Where the trajectory begins and terminates on a single edge of the ternary diagram, the independent variable for area integration is the mole-fraction along that edge; for example the acetone/methanol edge in the case of the $A(\theta_j)$ shown in figure 6.4a. A slightly more complex integration is required where the trajectory begins and ends on different edges of the ternary diagram, such as the case of the $A(\theta_j)$ shown in figure 6.4b. In that case, the area is subdivided into areas that can be integrated separately.

The maximum-area method has the advantage of being able to locate the globally optimal (maximum) residue curve in a residue curve map without the additional optimization step required by the method of Lucia & Taylor (2006).



(a) Integration from chloroform/methanol unstable node



(b) Integration from acetone/methanol unstable node

Figure 6.4: Trajectory-lengths $D(\theta_j)$ and areas $A(\theta_j)$ for acetone-methanol-chloroform mixture

Evaporation Maps Similarly, the optimization expression for an evaporation trajectory is given by:

$$\begin{aligned}
 \max_{x^\theta} A &= \int_0^T \int_{A(\alpha)} \frac{d\mathbf{x}(\alpha)}{dt} da d\alpha \approx \frac{1}{2} \sum_{k=0}^N (x^{k+1} - x_1^k) \left(\frac{d\mathbf{x}(x_1^k)}{dt} - \frac{d\mathbf{x}(x^{k+1})}{dt} \right) \\
 \frac{dx_i}{dt} &= -\frac{A}{h_T^L} (N_i - x_i N_t) \\
 \frac{dT^L}{dt} &= \frac{\left[h_V^\bullet(T^G - T^L) - \sum_{i=1}^3 N_i \Delta H_i^{vap} - \sum_{i=1}^3 N_i M_i C p_i^G (T^G - T^L) \right]}{\sum_{i=1}^3 h_i^L M_i C p_i^L} \\
 \mathbf{x}(T) &= \mathbf{x}^T
 \end{aligned} \tag{6.5}$$

The Matlab function `fminbnd` was used to obtain the optimum values of θ in this work for the optimization problems 6.2-6.5; `fminbnd` uses *golden section* search and parabolic interpolation to find minima for single-variable functions on fixed intervals (Matlab 2010); consequently, to find the maxima, the negative of the objective functions in 6.2-6.5 were actually used.

6.2.3 Computed Separation Boundaries

Residue Curve Maps Figure 6.5 shows computed values of integral trajectory lengths and areas for the residue curve map of the homogeneous acetone-chloroform-methanol mixture (see figure 6.2 for the map with some trajectory lengths indicated). While the integral lengths and areas are smooth within each region, they show a discontinuity at the maximum values where $D(\theta)$ and $A(\theta)$ are shaped like a one-sided cusp in each region. This is due to the different line lengths and areas that occur on either side of a boundary - evidence for this can also be seen in figure 6.2. The open and closed circles on the plots represent either end of the smooth portions which lie either side of the separation boundary; in figure 6.5a and 6.5b, angles to the left of the cusp (open circle) converge to the pure methanol node, while angles to the right converge to the acetone-chloroform node, while in figure 6.5c and 6.5d angles to the left of the cusp (closed circle) converge to the acetone-chloroform node, while angles to the right converge to pure methanol. Table 6.3 summarises the optimum values of θ and the corresponding values of line-integral and area for the residue curve map of figure 6.2b, corresponding to the peak values in figure 6.5. For all the computations, a high degree of precision is required for the values of the optimization angle θ ; both the arc length (trajectory length) and the integral area are very sensitive to θ , as can be seen from the very sharp peaks that occur in figure 6.5.

The key feature to note here is that the computed area shows a single maximum value over the range of θ , whereas the trajectory length may have in general more than one maximum, and requires additional measures to determine which local maximum corresponds to the separation boundary. The separation boundaries determined using the optimization method are shown in figure 6.2, and essentially overlie the boundaries obtained via the eigenvector approach of section 6.1.

Table 6.3: Maximum line integral and maximum areas for location of separation boundary in residue curve map of acetone-chloroform-methanol mixture in figure 6.2b; angles measured with respect to horizontal axis; $P = 1.0$ bar

Unstable Node	Optimum Angle θ^*	Maximum Line Integral	Maximum Area
Acetone-chloroform	179.3866°	1.0044	0.1463
Chloroform-methanol	-71.6557°	1.0414	0.1788

Evaporation Maps Figure 6.3 shows the separation boundaries for the evaporation maps of the same mixtures shown in 6.2, computed using the optimization algorithm of table 6.6. The boundaries run between stable and unstable nodes, passing through the ternary saddle. The optimum rotation angles for these conditions are summarised in table 6.4.

Table 6.4: Maximum line integral and maximum areas for location of separation boundary in evaporation map of acetone-chloroform-methanol mixture in figure 6.3b; angles measured with respect to horizontal axis; $T^G = 20C$, $u^G = 0.5m/s$, $d = 0.03m$

Unstable Node	Optimum Angle θ^*	Maximum Line Integral	Maximum Area
Acetone-chloroform	179.9075°	1.0685	0.1584
Chloroform-methanol	-59.6298°	0.8604	0.1645

The discussion here has been limited to ternary mixtures in which case the boundary is a curve which is found by optimizing an area. In principle the method should be extensible to higher dimensions so that for example for quaternary mixtures, the separation boundary would be a surface determined by optimizing (maximizing) a volume.

6.3 Flexure of the wet-bulb temperature surface

The temperature $T(x)$ of the simple distillation process that is the basis of the residue curve map increases monotonically with dimensionless time τ ; the temperature in this case is the bubble point temperature of the mixture. This phenomenon is captured in the theorem that $T(x)$ is a *Liapunov* surface for the ordinary differential equations in 2.17 (Doherty & Perkins 1978a). Indeed, azeotropic compositions can be found by experimentally examining the $T(x)$ surface as the temperature is either a minimum or a maximum at the azeotropic composition for binary mixtures. The topology of the residue curve map (RCM) diagram and the boiling point surface for a ternary mixture coincide, which is to say that their stable nodes (peaks), unstable nodes (pits) and saddle points are the same (Kiva et al. 2003). Early research in the field concluded that ridges and valleys in the temperature surface also coincided with distillation boundaries for the mixture (Doherty & Perkins 1978a). This is an important practical issue in the analysis of distillation systems; to assume that material balance lines joining distillate, feed and bottoms compositions in a continuous distillation column cannot cross distillation region boundaries potentially excludes some separation schemes (Laroche et al. 1992). However, as demonstrated by van Dongen & Doherty (1984) and Rev (1992), the flexures (ridges and valleys) in the boiling point surface do not in general coincide with the separatrices (separation boundaries) of residue curve maps. The reason for the confusion is that while the temperature surface is a naturally-occurring

6. SEPARATION BOUNDARIES

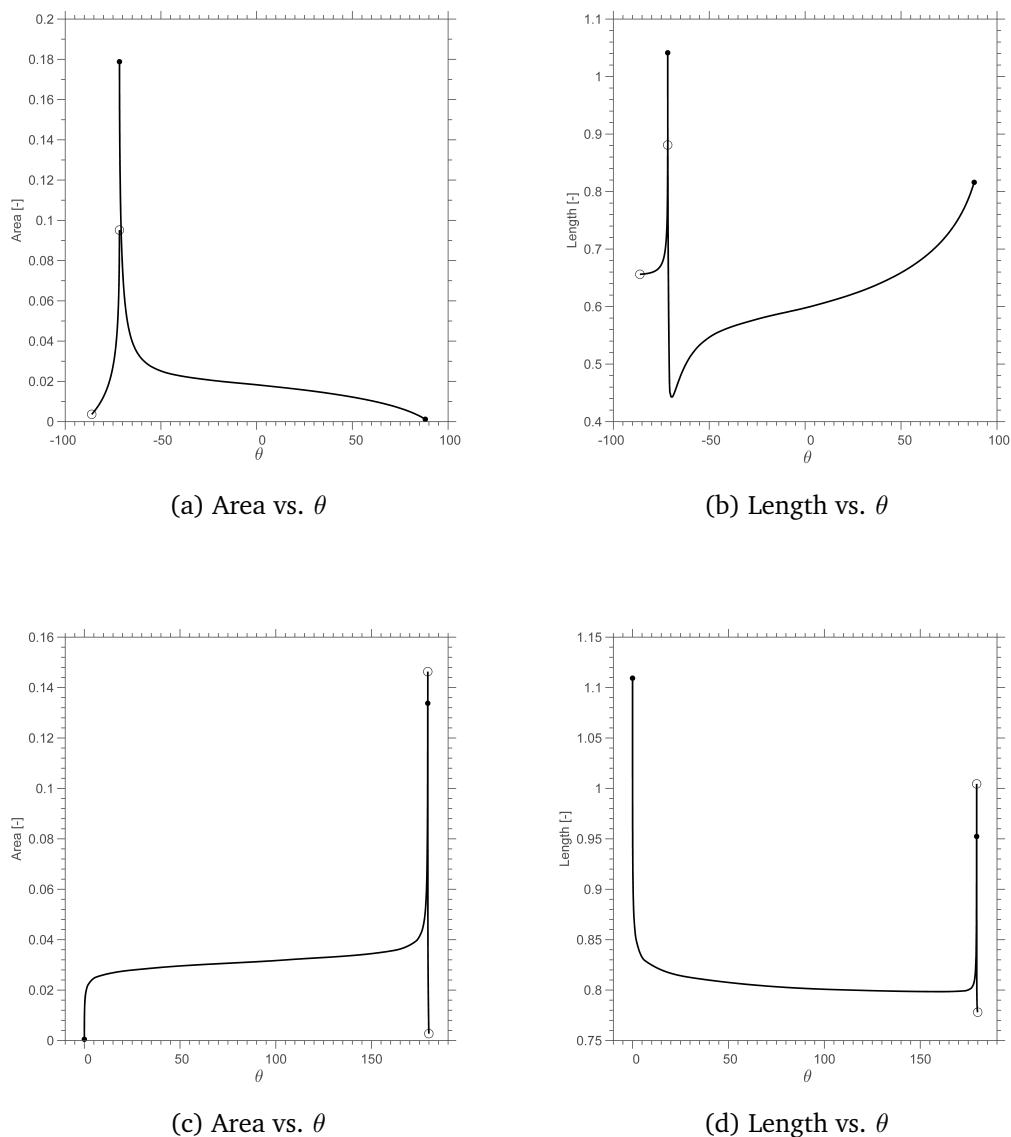


Figure 6.5: Area and residue curve length for acetone-chloroform-methanol mixture; (a) and (b) originating at chloroform-methanol azeotrope, (c) and (d) originate at acetone-methanol azeotrope; closed and open circles represent sides of "cusp"

Liapunov surface of equation 2.17 (Doherty & Perkins 1978a), it is not necessarily a scalar potential function over the vector field of vapour-liquid tie lines, as shown by Rev (1992).

In this section, some features of the wet-bulb temperature surface $T_{WB}(\mathbf{x})$ that are analogous to the bubble-point $T(\mathbf{x})$ surface of residue curve maps are explored. In particular, the relationship between ridges and valleys in the wet-bulb surface and the separation boundaries in evaporation maps is investigated. An optimization method for location of minima and maxima in the wet-bulb temperature is first discussed, fol-

lowed by an approximate finite difference based on directly-calculated gradients of the surface.

6.3.1 Location of ridges and valleys in wet-bulb surface by optimization

An algorithm for calculation of the wet-bulb temperature for a multicomponent mixture was presented in chapter 3. In figure 3.9a, a number of wet-bulb/composition diagrams for binary mixtures were shown. For the binary mixtures considered, the pseudo-azeotropic temperature was located near (but not coincident with) either a minimum or a maximum (in case of acetone-chloroform) of the wet-bulb temperature over the composition range. Wet-bulb surfaces for a number of ternary mixtures were presented (see figures 3.12-3.14) displaying ridges and valleys of varying complexity. In this section we analyze a number of ternary systems as follows:

1. The $T_{WB}(\mathbf{x})$ surface is scanned in each of the three composition directions (x_1, x_2, x_3), along sections parallel to the edges, and the minimum or maximum wet-bulb temperature is located using a numerical optimization algorithm along each direction; this approach is summarised in table 6.7
2. Several evaporation trajectories are plotted, in the same manner as that used to generate the evaporation maps, to demonstrate the extent of crossing of separation boundaries by the trajectories

Taking the x_1 (i.e. x_{EtOH}) valley in the ethanol-MEK-toluene mixture in figure 6.6a as an example, the wet-bulb search begins on the ethanol-toluene edge at $x_2(j) = 0$ (i.e. $x_{MEK} = 0$, and increments until $x_2(j) = 1$. At each increment of $x_2(j)$ the minimum wet-bulb is determined from the following optimization problem:

$$\begin{aligned} \min_{x_1} T_{WB} &= T_{WB}(\mathbf{x}, u^G, T^G, d, P) \\ x_2 &= x_2(j) \\ \sum_i^n x_i &= 1.0 \end{aligned} \tag{6.6}$$

where $T_{WB}(\mathbf{x}, u^G, T^G, d, P)$ is found from the algorithm of table 3.2. In this case the optimization is a function of a single variable x_1 and so a suitable optimization routine such as `fminbnd` (Matlab 2010) can be used to locate the optimum (minimum value). The algorithm is summarised in table 6.7.

The computed flexures (ridges and valleys) are shown in figure 6.6a for the ethanol/MEK/toluene mixture. Three valleys are shown in the figure:

1. A valley runs in the x_1 search direction from the ethanol-MEK edge to a point around 0.95 molefraction ethanol on the ethanol-toluene edge.

2. A valley runs in the x_2 search direction from a point near the minimum temperature ethanol/toluene pseudo-azeotrope to a point on the ethanol-toluene edge. The minimum wet-bulb temperature (with respect to the valley in the x_2 direction) then lies along the ethanol-toluene edge thereafter.
3. A further valley runs in the x_3 direction from near the mid-point on the ethanol-MEK edge to a point on the ethanol-toluene edge

In this case valleys are perceptible in each of the possible search directions. The dashed lines in figure 6.6a represent evaporation trajectories; it can be seen that there is no restriction to the crossing of valleys by the trajectories. A further example is shown in figure 6.6b for the acetone/chloroform/methanol mixture. Two valleys and a ridge are shown for this mixture:

1. A valley runs from a point on the acetone-methanol edge near the acetone-methanol pseudo-azeotrope to a point on the chloroform-methanol edge.
2. A valley also runs from the vicinity of the chloroform-methanol pseudo-azeotrope to the methanol-acetone edge
3. A ridge runs from near the acetone-chloroform pseudo-azeotrope to the chloroform/ methanol edge, near pure methanol.

As with the the previous example, there is no restriction to the crossing of valleys by the evaporation trajectories. The three computed paths intersect at the saddle of the wet-bulb surface near (but not coincident with) the ternary pseudo-azeotrope. A comparison with the separation boundaries in figure 6.3b shows that the valleys and ridges in the ternary mixture do not coincide with the separation boundaries.

6.3.2 Location of ridges and valleys by finite difference method

An alternative approximate method for calculation of the ridges and valleys involves direct calculation of of gradients (first derivatives) of the $T_{WB}(x)$ surface. The surface is firstly calculated at discrete points over the composition space. Gradients are then calculated using a finite difference method in each of the x_1 , x_2 and x_3 directions over the surface. For edge points ($x = 0$ and $x = 1.0$) *one-sided* differences are used. For gradients in x_1 this gives:

$$\left. \frac{\partial T_{WB}}{\partial x_1} \right|_{x_1=0} \approx \frac{T_{WB}^{j+1} - T_{WB}^j}{\Delta x_1} \quad \text{and} \quad \left. \frac{\partial T_{WB}}{\partial x_1} \right|_{x_1=1} \approx \frac{T_{WB}^j - T_{WB}^{j-1}}{\Delta x_1}$$

For interior points *central* differences are used:

$$\frac{\partial T_{WB}}{\partial x_1} \approx \frac{T_{WB}^{j+1} - T_{WB}^{j-1}}{2\Delta x_1}$$

Similar expressions apply for gradients in x_1 and x_2 . Second derivatives are used to distinguish minima (valleys) from maxima (ridges). At edge points this gives

$$\left. \frac{\partial^2 T_{WB}}{\partial x_1^2} \right|_{x_1=0} \approx \frac{T_{WB}^{j+2} - 2T_{WB}^{j+1} + T_{WB}^j}{\Delta x_1^2} \quad \text{and} \quad \left. \frac{\partial^2 T_{WB}}{\partial x_1^2} \right|_{x_1=1} \approx \frac{T_{WB}^j - 2T_{WB}^{j-1} + T_{WB}^{j-2}}{\Delta x_1^2}$$

while the interior points are given by:

$$\frac{\partial^2 T_{WB}}{\partial x_1^2} \approx \frac{T_{WB}^{j+1} - 2T_{WB}^j + T_{WB}^{j-1}}{2\Delta x_1^2}$$

The contours are calculated at points where each of the first-derivatives are zero using the contour function in Matlab (Matlab 2010); points where zero-contours of each derivative cross is a saddle point or a local extremum; if second-derivatives are same sign and positive, the extremum is a minimum, if second-derivatives are same sign and negative, the extremum is a maximum, if opposite signs, a saddle. The algorithm is summarised in table 6.8. When a sufficiently fine grid is used the results of the gradient approach are similar to the optimization approach above; figure 6.6a shows the valleys in the x_1 and x_2 search directions for the acetone/chloroform/methanol mixture. For each valley, the computed results for the two approaches agree well in the region between the starting point for the optimization algorithm (the unstable node) and the ternary saddle. Thereafter there is some divergence in the location of the valleys. This is due to the nature of the wet-bulb temperature optimization (table 6.7) which can only locate a single minimum parallel to each edge; thus, as the search increment passes the ternary saddle the algorithm can only locate minima along the line of the current increment i.e. cannot double-back on itself.

Algorithm 6.8 is more efficient than 6.7 if the grid of $T_{WB}(\mathbf{x})$ has already been computed i.e. in the case where flux-plots over the ternary composition space are being calculated (see figure 5.3), especially if the grid of points is not too fine. Algorithm 6.7 requires that an optimization problem be solved at each increment along the valley or ridge path, and so the time required for computation is dependent on the number of points selected to represent the path.

6.4 Chapter Summary and Conclusions

In this chapter numerical methods for location of separation boundaries in evaporation maps have been developed. A method using eigen-vectors obtained from the linearized analysis in chapter 5 was firstly used, and demonstrated for both residue curve maps and evaporation maps.

Optimization methods using maximum trajectory length (based on work of Lucia & Taylor (2006)), and a novel maximum area approach were also developed. The max-

imum area method does not require an additional optimization step required in the method of Lucia & Taylor. A high degree of numerical precision is required with both optimization methods, due to extreme sensitivity of the trajectory length and integral area to the optimization angle θ . For a number of ternary mixtures considered, the same boundaries were obtained by each method.

The flexure of the wet-bulb temperature surface, which is the temperature at each point on an evaporation map, was also investigated. Numerical methods for location of ridges and valleys in wet-bulb surfaces were presented, one involving an optimization (minimization) of the wet-bulb temperature in each of three search directions, and a further approach based on a finite difference method applied directly to the wet-bulb surface. Computations for a number of ternary mixtures show that ridges and valleys do not correspond to separation boundaries in evaporation maps.

Table 6.5: Algorithm for generation of separation boundaries in residue curve map

-
1. Locate binary and ternary azeotropes for the given mixture
 2. For a given unstable node specify the radius ϵ_1 around the node which defines the locus of possible initial concentrations as $B(x^o) = \{x : \|x - x^o\| = \epsilon_1\}$.
 3. Define θ_{min} and θ_{max} for the given unstable node
 4. Maximization of trajectory length:
 - (a) Subdivide feasible range of θ_{min} and θ_{max} into n_θ sub-ranges; let θ_1 and θ_2 be the lower and upper end of a particular sub-range
 - (b) Initialize value for θ between θ_1 and θ_2 (via optimization routine)
 - (c) Calculate initial composition $x_1^\theta = x_1^o + \epsilon_1 \cos(\theta)$, and $x_2^\theta = x_2^o + \epsilon_1 \sin(\theta)$; x_1^o and x_2^o are the compositions of the starting unstable node (either a pure component, or a binary pseudo-azeotrope)
 - (d) Generate the residue curve by numerically integrating equation 2.17; the integration is terminated when x approaches a stable node within a certain distance ϵ_2
 - (e) Accumulate $D(\theta_j) = \sum \|\Delta x_k\|$ where the summation is over the output of the ODE solver
 - (f) Check for a maximum value in D , such that $\|D(\theta_k) - D(\theta_{k-1})\| < \delta$, where δ is a tolerance for successive iterations. If the tolerance is satisfied stop, otherwise adjust value of θ within θ_1 and θ_2 (via optimization routine)
 - (g) Repeat for each sub-range within θ_{min} and θ_{max}
 - (h) Determine optimum value (θ^*) over the sub-ranges
 5. Maximization of circumscribed area:
 - (a) Initialize value for θ within θ_{min} and θ_{max} (via optimization routine)
 - (b) Calculate initial composition $x_1^\theta = x_1^o + \epsilon_1 \cos(\theta)$, and $x_2^\theta = x_2^o + \epsilon_1 \sin(\theta)$
 - (c) Generate the residue curve by numerically integrating equation 2.17; the integration is terminated when x approaches a stable node within a certain distance ϵ_2
 - (d) Accumulate $A(\theta_j)$ using numerical integration
 - (e) Check for a maximum value in A , such that $\|A(\theta_k) - A(\theta_{k-1})\| < \delta$. If the tolerance is satisfied stop, otherwise adjust value of θ (via optimization routine) and repeat from step 5a
 6. For optimal value (θ^*), project the solution in $T - x$ space onto the ternary diagram; the projected curve lies on the separation boundary.
 7. Repeat from step 2 for any further unstable nodes in the mixture
-

Table 6.6: Algorithm for generation of separation boundaries in evaporation map

-
1. Locate binary and ternary azeotropes for the given mixture
 2. For a given unstable node specify the radius ϵ_1 around the node which defines the locus of possible initial concentrations as $B(x^o) = \{x : \|x - x^o\| = \epsilon_1\}$.
 3. Define θ_{min} and θ_{max} for the given unstable node
 4. Maximization of trajectory length:
 - (a) Subdivide feasible range of θ_{min} and θ_{max} into n_θ sub-ranges; let θ_1 and θ_2 be the lower and upper end of a particular sub-range
 - (b) Initialize value for θ between θ_1 and θ_2 (via optimization routine)
 - (c) Calculate initial composition $x_1^\theta = x_1^o + \epsilon_1 \cos(\theta)$, and $x_2^\theta = x_2^o + \epsilon_1 \sin(\theta)$; x_1^o and x_2^o are the compositions of the starting unstable node
 - (d) Calculate wet-bulb temperature from algorithm table 3.2
 - (e) Generate the evaporation trajectory by numerically integrating the system of governing equations 3.28, 3.30 & 3.33, coupled with the multicomponent flux calculation from table 3.1; the integration is terminated when x approaches a stable node within a certain distance ϵ_2
 - (f) Accumulate $D(\theta_j) = \sum \|\Delta x_k\|$ where the summation is over the output of the ODE solver
 - (g) Check for a maximum value in D , such that $\|D(\theta_k) - D(\theta_{k-1})\| < \delta$, where δ is a tolerance for successive iterations. If the tolerance is satisfied stop, otherwise adjust value of θ within θ_1 and θ_2 (via optimization routine)
 - (h) Repeat for each sub-range within θ_{min} and θ_{max}
 - (i) Determine optimum value (θ^*) over the sub-ranges
 5. Maximization of circumscribed area:
 - (a) Initialize value for θ within θ_{min} and θ_{max}
 - (b) Calculate initial composition $x_1^\theta = x_1^o + \epsilon_1 \cos(\theta)$, and $x_2^\theta = x_2^o + \epsilon_1 \sin(\theta)$
 - (c) Generate the evaporation trajectory by numerically integrating the system of governing equations 3.28, 3.30 & 3.33, coupled with the multicomponent flux calculation from table 3.1; the integration is terminated when x approaches a stable node within a certain distance ϵ_2
 - (d) Accumulate $A(\theta_j)$ using numerical integration
 - (e) Check for a maximum value in A , such that $\|A(\theta_k) - A(\theta_{k-1})\| < \delta$. If the tolerance is satisfied stop, otherwise adjust value of θ (via optimization routine) and repeat from step 5a
 6. For optimal value (θ^*), project the solution in $T - x$ space onto the ternary diagram; the projected curve lies on the separation boundary.
 7. Repeat from step 2 for any further unstable nodes in the mixture
-

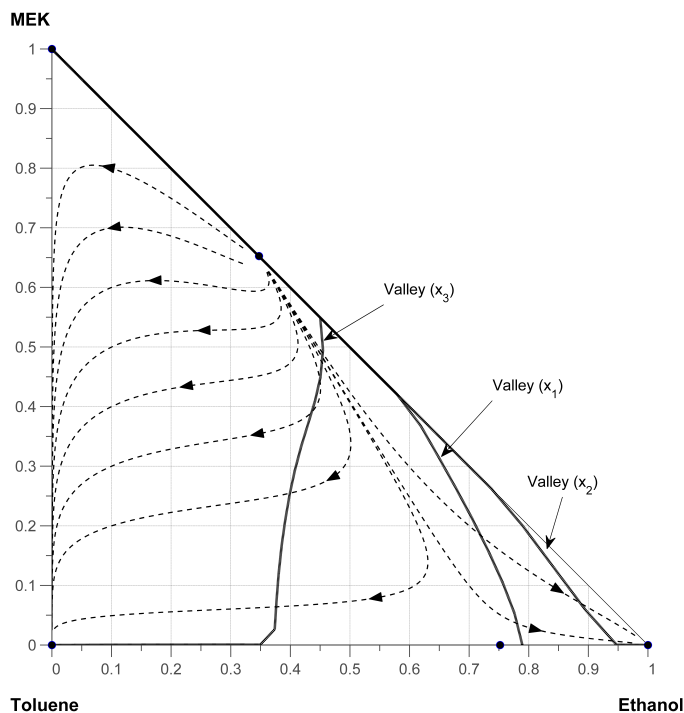
Table 6.7: Algorithm for location of valleys and ridges in wet-bulb temperature surface via optimization

-
1. Initialize $x_1 = 0$ (or $x_1 = 0$ or $x_1 = 0$ depending on required direction of movement)
 2. At each increment of x_1 , solve optimization problem of equation 6.6 to find $\min T_{WB}(x_2)$ along line of constant x_1 , with $x_3 = 1 - x_1 - x_2$; to locate a ridge, solve for $\max T_{WB}(x_2)$
 3. Iterate with increasing value of x_1 until a boundary (edge of composition triangle) is reached
 4. Repeat in x_2 and x_3 search directions
-

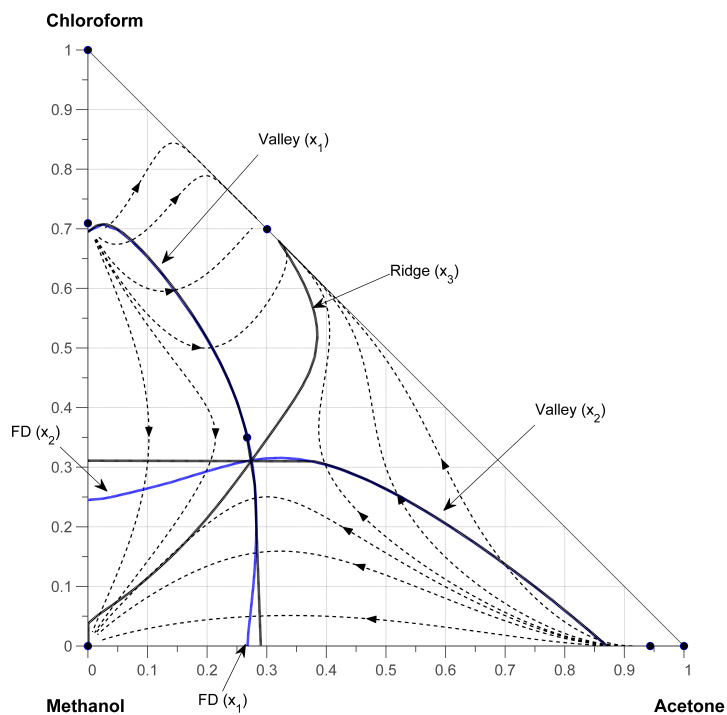
Table 6.8: Algorithm for location of valleys & ridges in wet-bulb temperature surface via gradients

-
1. Calculate $T_{WB}(\mathbf{x})$ over ternary composition space \mathbf{x} using a discrete grid of points
 2. Calculate gradient (first derivatives) $\partial T_{WB}/\partial x_1$ in x_1 direction using finite difference method; at edges ($x_1 = 0$ and $x_1 = 1.0$), use *single-sided* differences, at interior points use *central difference* approximation. Repeat gradient calculations for $\partial T_{WB}/\partial x_2$ in x_2 direction, and $\partial T_{WB}/\partial x_3$ in x_3 direction
 3. Calculate zero-contours for gradients in each direction (using contour function in Matlab)
 4. Valleys in $T_{WB}(\mathbf{x})$ surface in x_1 direction are identified by $\partial^2 T_{WB}/\partial x_1^2 < 0$, and ridges by $\partial^2 T_{WB}/\partial x_1^2 > 0$; similarly for x_2 and x_3 directions
-

6. SEPARATION BOUNDARIES



(a) ethanol/MEK/ toluene



(b) Acetone/chloroform/methanol

Figure 6.6: Valleys and ridges in wet-bulb temperature surfaces, obtained by optimization method of table 6.7; FD denotes valleys obtained by gradient method of table 6.8; $T^G = 40C$, $u^G = 0.5m/s$, $d = 0.03m$

Chapter 7

Evaporation maps including diffusion effects in liquid

The model developed in chapter 3 addressed evaporation from a liquid surface, considering only heat and mass transfer limitations in the gas phase; a lumped model was applied to the liquid. In this chapter the lumped model is extended to include diffusion within the liquid phase giving a distributed model, described by partial differential equations (PDEs); a lumped model is however retained for the purposes of heat transfer in the liquid. The goal of this chapter is to examine how diffusion in the liquid phase affects the evaporation paths of the non-ideal mixtures, in particular with respect to the terminal compositions which in some cases may be pseudo-azeotropes.

To numerically solve the equations of mass transfer in the liquid phase, a *finite volume* method is employed. The finite volume method is used extensively in the field of computational fluid dynamics (CFD) to reduce the governing equations to a form suitable for linear solvers (Guyer et al. 2009). Further details of the origin and derivation of the method can be found in Ferziger & Peric (1999) and Patankar (1980). The finite volume technique is mass conservative regardless of the number of nodes in the spatial discretization, or the number of time steps (Botte et al. 2000). In this chapter, a specific formulation of the method is derived to account for multicomponent diffusion effects in the liquid phase. Stockie et al. (2003) and Kermani & Stockie (2004) used a related approach for the modeling of multicomponent gas transport in porous fuel cell electrodes. Finite volume methods for coupled mass transfer are also discussed by Kumar & Mazumder (2009), Peerenboom et al. (2011) and Padoin et al. (2014).

The model developed in this chapter uses an exact solution to the Maxwell-Stefan equations for mass transfer developed in chapter 3 to calculate mass (and heat) fluxes in the gas film at the vapour-liquid interface. Diffusion gradients in the quiescent liquid phase are included by employing a generalized multicomponent Fickian model for the diffusive fluxes in the liquid, based on a Maxwell-Stefan approach. The gas-phase

and liquid phase models are coupled at the receding vapour-liquid interface in the numerical scheme as the evaporation progresses. For the liquid phase, a one-dimensional (1-D) finite volume method is used to discretize the governing partial differential equations in space, while a *method-of-lines* approach is used for the temporal integration. The calculated gas-phase fluxes act as Neumann-type boundary conditions for the distributed model in the liquid. Solutions to the overall model take the form of trajectories in temperature-composition space, which are then projected onto a ternary diagram. The fixed points (including pseudo-azeotropes) computed from the gas-phase-limited model (chapter 3) apply also to the distributed model developed here. The composition profiles from the distributed model are shown to reduce to those of a the gas-phase-limited model as an effective diffusivity parameter in the liquid increases.

7.1 Governing Equations

The equations that describe the heat and mass transfer in the gas and liquid phases are developed in the following sections, and follow from the conservation equations outlined in section 2.1. The coupling between transfer processes in the liquid and gas is captured by the boundary conditions for the liquid phase.

7.1.1 Mass and Heat Transfer in Gas Phase

The model for heat and mass transfer in the gas phase was developed in chapter 3, and is summarised in table 7.1. At each time increment, the multicomponent fluxes N_i are solved using an analytical method due to Krishna & Standart (1976), which is detailed in section 3.1.1. The heat flux is coupled to the mass fluxes through equation 7.4.

7.1.2 Mass Transfer in Liquid Phase

Whereas for the gas phase heat and mass transfer coefficients are employed to determine the fluxes, in the liquid phase the composition profiles can be resolved directly by solving the partial differential equations that govern the mass transfer process. Figure 7.1 shows the situation schematically. The conservation equations for mass, heat and momentum were outlined briefly in section A.2; the conservation of a species i in a multicomponent mixture is given by equation A.15 which (neglecting reaction terms) is

$$\frac{\partial \rho^L \omega_i}{\partial t} = -\nabla \cdot \mathbf{n}_i = -\nabla \cdot (\rho^L \omega_i \mathbf{v}) - \nabla \cdot \mathbf{j}_i \quad i = 1, 2, 3 \quad (7.5)$$

where \mathbf{n}_i and \mathbf{j}_i are total and diffusive mass fluxes respectively, ρ^L is the total mass density of liquid phase, ω_i is mass fraction of component i , and \mathbf{v} is the mass-averaged

Table 7.1: Summary of gas-phase heat and mass transfer; see chapter 3 for derivations

Mass Transfer The $n - 1$ diffusive fluxes J_i are given by

$$J_i = c \sum_{j=1}^3 k_{ij}^{\bullet} \Delta y_i \quad \text{for} \quad i = 1, 2, 3 \quad (7.1)$$

where k_{ij}^{\bullet} are the multicomponent mass transfer coefficients corrected for finite mass transfer rates given by equation 3.16, which is based on analytic solution to mass transfer in the notional film at the vapour-liquid interface. The form of the binary mass transfer coefficients required to find k_{ij}^{\bullet} for flat geometry is:

$$Sh_{ij} = \frac{d\kappa_{ij}}{D_{ij}} = \left(0.65 Re^{1/2} Sc_{ij}^{1/3}\right) \quad (7.2)$$

Discrepancy functions for the total fluxes N_i are written as:

$$F_i \equiv J_i + y_i^G \sum_{j=1}^3 N_j - N_i = 0 \quad \text{for} \quad i = 1, 2, 3 \quad (7.3)$$

and are solved for the N_i using a Newton method as described in section 3.2.1, for specified y_i^G , T^L , T^G , u^G and D_{ij} .

Heat Transfer Heat flux at the vapour-liquid interface is given by:

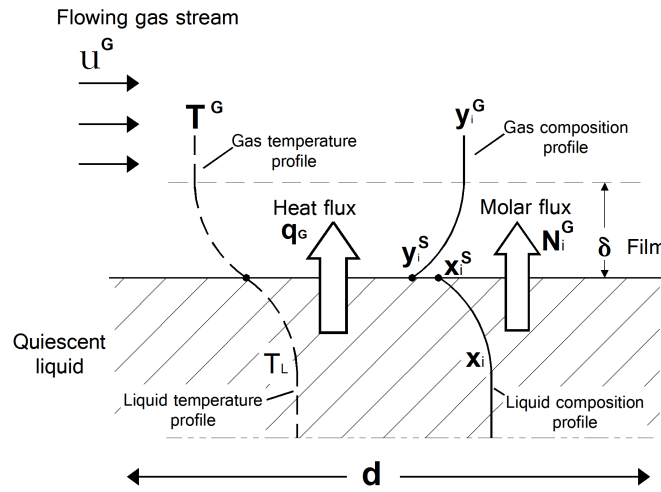
$$q_I = h_G^{\bullet}(T^G - T^L) - \sum_{i=1}^3 N_i \Delta H_i^{vap} - \sum_{i=1}^3 N_i M_i C p_i^G (T^G - T^L) \quad (7.4)$$

where

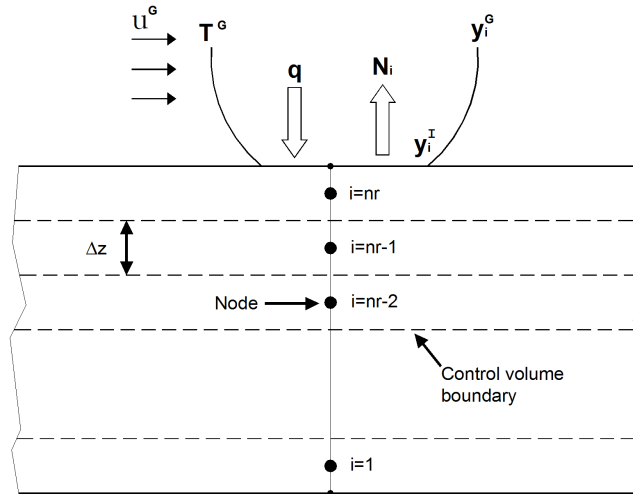
$$h_G^{\bullet} = h_G \Xi_H = h_G \left[\frac{\Phi_H^G}{\exp(\Phi_H^G) - 1} \right] \quad \text{and} \quad \Phi_H^G = \frac{\sum_{i=1}^3 n_i C p_i^G}{h_G}$$

The form of the heat transfer coefficient used for flat geometry is

$$Nu = \frac{h_G d}{k} = \left(0.65 Re^{1/2} Pr^{1/3}\right)$$



(a) Schematic of heat and mass transfer fluxes



(b) Finite-volume discretization within film

Figure 7.1: Schematic of heat and mass transfer from liquid film surface, and finite-volume discretization within film

velocity.

To calculate the diffusive fluxes j_i in the liquid phase, the generalised Fick equations are used. As outlined in section A.3, Maxwell and Stefan developed a theory of diffusion based on equilibrium of molecular friction and thermodynamic interaction that is physically more consistent than Fick's law (Krishna & Wesselingh 1997). The generalised driving force for diffusion, d_i is related to the relative species velocities ($u_i - u_j$) and is given by equation 2.9 (Taylor & Krishna 1993):

$$d_i = \frac{x_i}{RT} \cdot \nabla_{T,P} \mu_i = \sum_{j=1}^{n-1} \frac{x_i x_j}{\mathfrak{D}_{ij}} (u_i - u_j) = \sum_{j=1}^{n-1} \Gamma_{ij} \nabla_{ij} x_j \quad (7.6)$$

where $\nabla_{T,P}\mu_i$ is the chemical potential gradient, and n is the number of components. Here \mathfrak{D}_{ij} are the liquid-phase Maxwell-Stefan diffusivities which can be viewed as inverse drag coefficients between components i and j . The thermodynamic correction factor Γ_{ij} is found from the activity coefficients Γ_i which are in turn calculated from an appropriate model of vapour-liquid equilibrium (NRTL equation in this work):

$$\Gamma_{ij} = \delta_{ij} + x_i \left. \frac{\partial \ln \gamma_i}{\partial x_j} \right|_{T,P} \quad \text{with} \quad \delta_{ij} = 1 \quad \text{for} \quad i = j \quad \text{and} \quad \delta_{ij} = 0 \quad \text{for} \quad i \neq j \quad (7.7)$$

Taylor & Kooijman (1991) present details of the calculation of $\frac{\partial \ln \gamma_i}{\partial x_j}$ which are also employed here, and are detailed in appendix B.2. It should be noted that liquid diffusion coefficients can be quite sensitive to the model use to compute Γ , in part because Γ requires the first derivative of the activity coefficient with respect to composition. Model parameters (binary interaction parameters) for activity coefficient modes are determined by curve-fitting to experimental VLE data; although different models may provide estimates of $\ln \gamma_i$ that fit the experimental data equally well, the derivatives of $\ln \gamma_i$ (and, therefore Γ) may differ significantly (Taylor & Kooijman 1991).

The generalized form of Fick's law for molar and mass diffusive fluxes J_i and j_i was developed in section A.3 and is given by equation 2.15 (Taylor & Krishna 1993):

$$(J) = -c[B]^{-1}[\Gamma](\nabla x) = -c[D](\nabla x) \quad (7.8a)$$

$$(j) = -\rho^L[D^o](\nabla \omega) \quad (7.8b)$$

where the normal brackets indicate a column vector of terms, and the square brackets a two-dimensional matrix. The terms in the $n-1$ dimensional $[B]$ matrix are given by equation 2.12:

$$B_{ii} = \frac{x_i}{\mathfrak{D}_{in}} + \sum_{\substack{k=1 \\ i \neq k}}^n \frac{x_k}{\mathfrak{D}_{ik}} \quad (7.9a)$$

$$B_{ij} = -x_i \left(\frac{1}{\mathfrak{D}_{ij}} + \frac{1}{\mathfrak{D}_{in}} \right) \quad (7.9b)$$

To convert from a molar-averaged velocity frame to a mass-averaged velocity frame, the following expression (Taylor & Krishna 1993) is employed:

$$[D^o] = [B^{uo}]^{-1} [\omega] [x]^{-1} [D][x][\omega]^{-1} [B^{uo}] \quad \text{where} \quad [D] = [B]^{-1}[\Gamma] \quad (7.10)$$

and where $[\omega]$ and $[x]$ are diagonal matrices whose non-zero elements are the mass-fractions and mole-fractions respectively. The elements of $[B^{uo}]$ and $[B^{uo}]$ are in turn

given by

$$B_{ik}^{uo} = \delta_{ik} - \omega_i \left(\frac{x_k}{\omega_k} - \frac{x_n}{\omega_n} \right) \quad (7.11a)$$

$$B_{ik}^{ou} = \delta_{ik} - \omega_i \left(1 - \frac{\omega_n x_k}{x_n \omega_k} \right) \quad (7.11b)$$

where ω_i is the mass-fraction of component i and δ_{ij} is the Kronecker delta. Writing equation 7.5 explicitly for components 1 and 2 in one-dimensional form, and inserting the expanded form of equation 7.8(b) for the diffusive mass fluxes gives:

$$\frac{\partial \rho^L \omega_1}{\partial t} = -\frac{\partial}{\partial z} \left[\rho^L v \omega_1 - \left(\rho^L D_{11}^o \frac{\partial \omega_1}{\partial z} + \rho^L D_{12}^o \frac{\partial \omega_2}{\partial z} \right) \right] \quad (7.12a)$$

$$\frac{\partial \rho^L \omega_2}{\partial t} = -\frac{\partial}{\partial z} \left[\rho^L v \omega_2 - \left(\rho^L D_{21}^o \frac{\partial \omega_1}{\partial z} + \rho^L D_{22}^o \frac{\partial \omega_2}{\partial z} \right) \right] \quad (7.12b)$$

where z is the depth co-ordinate in the liquid phase. By solving for ω_1 and ω_2 , the concentration of the final component is found from a summation of the mass fractions:

$$\sum_{i=1}^n \omega_i = 1 \quad (7.13)$$

In addition to the component balances above, an overall material balance (continuity equation) can be expressed in one-dimensional form as:

$$\frac{\partial \rho^L}{\partial t} = -\nabla \cdot (\rho^L \mathbf{v}) = -\frac{\partial (\rho^L v)}{\partial z} \quad (7.14)$$

This equation is used to calculate the mass-averaged velocity during the evolution of composition profiles in the liquid, following the approach of Torres et al. (2003). An overall balance on the liquid also yields the following equation for the interface velocity (Pakowski 1992):

$$\frac{dz}{dt} = \frac{1}{\bar{\rho}^L} \left(\sum_{i=1}^{n-1} n_i^G + z \frac{d\bar{\rho}^L}{dt} \right) \quad (7.15)$$

where $\bar{\rho}^L$ is the average liquid density of the liquid phase, and n_i^G is the vapour phase mass flux of component i . This equation allows the rate of regression of the interface to be tracked over time. The finite-volume mesh is re-calculated at each time point and integrated forward in time using an ODE solver as described below.

7.1.3 Boundary Conditions for Mass Transfer

At the vapour-liquid interface, the receding interface is accounted for in the boundary conditions. Taking a balance on a differential volume enclosing the interface gives (Pakowski 1990):

$$n_i^L - \rho^L \omega_{iL}^I \frac{dz}{dt} = n_i^G - \rho^G \omega_{iV}^I \frac{dz}{dt} \quad (7.16)$$

where n_i^L and n_i^G are total molar fluxes on the liquid and vapour side of the interface respectively, ρ^L and ρ^V are the total mass concentrations, and dz/dt is the velocity of the receding interface. The gas-phase flux terms n_i^G provide the coupling between the explicit form of the Maxwell-Stefan equations for the gas phase and the numerical solution required for the liquid phase. Summing the i components gives the total liquid-phase flux at the interface:

$$n_t^L = n_t^G + (\rho^L - \rho^V) \frac{dz}{dt} \quad (7.17)$$

In mass units, the boundary conditions at the interface are:

$$\rho^L D_{11} \frac{\partial \omega_1}{\partial z} + \rho^L D_{12} \frac{\partial \omega_2}{\partial z} = n_t^L \left(\omega_1^I - \frac{n_1^L}{n_t} \right) \quad (7.18a)$$

$$\rho^L D_{21} \frac{\partial \omega_1}{\partial z} + \rho^L D_{22} \frac{\partial \omega_2}{\partial z} = n_t^L \left(\omega_2^I - \frac{n_2^L}{n_t} \right) \quad (7.18b)$$

while at the bottom of the liquid film, the boundary conditions are simply

$$\rho^L D_{11}^o \frac{\partial \omega_1}{\partial z} + \rho^L D_{12}^o \frac{\partial \omega_2}{\partial z} = 0 \quad (7.19a)$$

$$\rho^L D_{21}^o \frac{\partial \omega_1}{\partial z} + \rho^L D_{22}^o \frac{\partial \omega_2}{\partial z} = 0 \quad (7.19b)$$

Due to the coupled nature of the mass transfer, the composition derivatives at the vapour-liquid interface ($\partial \omega_1 / \partial z$ and $\partial \omega_2 / \partial z$) must be found numerically at each time step. The boundary conditions in equations 7.18 are a system of two equations in two unknowns (the derivatives). Values for the derivatives are found by solving equations 7.18 simultaneously at each time increment; the Matlab `fsolve` solver was used in this work. The composition derivatives at the bottom are identically zero as there is no flux through the bottom boundary.

The mass-averaged velocity v is determined implicitly from equations 7.12 and 7.14, together with a correlation for the temperature-dependence of component densities ρ_i . The validity of assuming that pure component densities are functions of temperature only was examined by Torres et al. (2003) for fuel mixtures using a van der Waals equation of state. They found it to be a good assumption for pressures < 10

bar.

7.1.4 Heat Transfer in Liquid Phase

Whereas a distributed model is used for composition in the liquid phase, a lumped model is employed for the energy balance, following the derivation in chapter 3. The energy balance for the liquid may be written in terms of liquid temperature T^L as the independent variable:

$$\frac{dT^L}{dt} = \frac{A \left[q_G - \sum_{i=1}^3 N_i (\bar{H}_i^G - \bar{H}_i^L) \right]}{\sum_{i=1}^3 N_i M_i C p_i^L} \quad (7.20)$$

where \bar{H}_i^G and \bar{H}_i^L are the partial molar vapour and liquid molar enthalpies respectively of component i . Expanding the enthalpy terms \bar{H}_i^G and \bar{H}_i^L , and the heat flux term gives

$$\frac{dT^L}{dt} = \frac{\left[h_G^\bullet (T^G - T^L) - \sum_{i=1}^3 N_i \Delta H_i^{vap} - \sum_{i=1}^3 N_i M_i C p_i^G (T^G - T^L) \right]}{\sum_{i=1}^3 h_i^L M_i C p_i^L} \quad (7.21)$$

The fluxes are summed from $i = 1 - 3$ only, as the flux of the inert gas (air) is zero. Table 7.1 summarises the form of the heat transfer coefficient h_G^\bullet .

7.1.5 Vapour-Liquid Equilibria and Physical Properties

Using a pseudo steady-state assumption, the gas-phase and liquid phase concentrations at the interface are linked by a vapour-liquid equilibrium expression:

$$y_i^I = x_i^I \gamma_i p_i / P \quad (7.22)$$

where γ_i are the activity coefficients representing non-ideality in the liquid phase, p_i is the vapour pressure of component i and P is the total pressure. See equation 3.24 *et seq.* for background to this expression. The liquid interface concentration x_i^I differs from that in the bulk liquid, due to diffusion effects, while the vapour concentration y_i^I differs from that of the bulk gas y_i^G into which the evaporation occurs. The NRTL equation (Prausnitz et al. 1986) is used to represent the activity coefficients in this work, using binary interaction parameters from the Aspen Properties data-base (AspenTech 2014). It is assumed in equation 7.22 that the gas phase is ideal; non-ideal behaviour could be included by incorporating an appropriate expression for fugacity coefficients of the gas-phase components. Physical properties for the gas and liquid phases (den-

sity, viscosity, thermal conductivity etc.) are correlated with temperature using data extracted from Aspen Properties (AspenTech 2014).

7.1.6 Liquid Diffusion Coefficients

Taylor & Krishna (1993) suggest the following expression for the binary Maxwell-Stefan diffusivities in a multicomponent system:

$$\mathfrak{D}_{ij} = \left(\mathfrak{D}_{ij}^o \right)^{(1+x_j-x_i)/2} \left(\mathfrak{D}_{ji}^o \right)^{(1+x_i-x_j)/2} \quad (7.23)$$

where the \mathfrak{D}_{ij}^o are the infinite dilution diffusion coefficients. The Wilke-Chang correlation (Prausnitz et al. 1986) is used to estimate the infinite dilution coefficients; see appendix B.4 for details.

7.1.7 Initial Conditions

The evaporation trajectories computed under gas-phase limited conditions in chapter 3 originated in the vicinity of unstable nodes, and terminated at stable nodes. The nodes may be either pure components or pseudo-azeotropes. In this chapter the gas-phase limited model has been extended to allow for diffusion gradients in the liquid phase which evolve over time. To initialize the numerical solution scheme, it is assumed that the liquid phase is at a uniform concentration (typically that of the initial composition near an unstable node) and at a uniform temperature (the wet-bulb temperature at that uniform composition). The method for calculating the wet-bulb temperature for known liquid composition is detailed in section 3.2.2.

7.2 Numerical Methods

The partial differential equations 7.12 and 7.14, with boundary conditions 7.18 and 7.19, together with interface regression equation 7.15 and the energy balance equation 7.21 and the scheme for the gas phase multicomponent mass fluxes in table 7.1 constitute the system of equations to be solved. By numerically integrating the governing equations the composition-temperature trajectory (evolution of concentration and temperature over time) can be found. In this work, a finite-volume technique is used to obtain the desired numerical solution. The liquid and gas phases are coupled via the mass-flux boundary conditions; the fluxes in turn are obtained from the explicit solution to the Maxwell-Stefan equations in the vapour film adjacent to the vapour-liquid interface, evaluated at each time-step of the integration. In the following sections, the form of the finite-volume technique used to solve the system of equations is outlined.

7.2.1 Finite Volume Formulation for Mass Transport in Liquid Phase

The development of the finite volume method used in this work is outlined below. This treatment differs from the conventional approach to be found for example in Patankar (1980) and Versteeg & Malalasekera (2007) in that multicomponent diffusion terms are included so that coupling occurs between species diffusive fluxes in the liquid.

For *finite difference* methods the solution domain is discretized into a finite number of points, and the equations are solved at each point. With the *finite volume* technique, the domain is divided into a finite number of control volumes, with the centre of each control volume (or *cell*) representing the value of the variables over that volume. Integration of the PDEs over the control volume ensures that the discretized equation is cast in a form that ensures conservation of mass. The key steps in the finite volume approach are (Schafer 2006):

1. Decompose problem domain into control volumes
2. Develop integral balance equations
3. Incorporate boundary conditions (Dirichlet, Neumann, Robin etc).
4. Approximate integrals by numerical integration
5. Approximate function values and derivatives by interpolation of values at neighbouring cells
6. For method-of-lines approach, solve system of ODEs at nodes (using a standard ODE solver)

7.2.2 Component Material Balances

The finite difference method use the strong or differential form of the governing equations. The finite element and finite volume method use the weak or integral form. The integral form has the advantage of providing a more intuitive treatment of Neumann boundary conditions; finite volume methods are better suited to complex geometries as the integral forms do not require a specific mesh structure (Schafer 2006).

The starting point for the finite volume method is the integral (weak) form of the balance or transport equation, where each term applies to a control volume (Jakobsen 2008). Taking the species conservation equation for species i from equation 7.5 and

integrating over a control volume V and time t gives:

$$\underbrace{\int_t \int_V \frac{\partial \rho \omega_i}{\partial t} dv dt}_{\text{rate of increase of mass of } i} + \underbrace{\int_t \int_A \rho \omega_i \mathbf{v} \cdot \hat{\mathbf{n}} da dt}_{\text{net rate of addition of mass of } i \text{ by convection}} = \underbrace{\int_t \int_A \mathbf{j}_i \cdot \hat{\mathbf{n}} da dt}_{\text{net rate of addition of mass of } i \text{ by diffusion}} + \underbrace{\int_t \int_V S_i dv dt}_{\text{net rate of addition of mass of } i \text{ by source terms}} \quad (7.24)$$

where $\hat{\mathbf{n}}$ is a unit normal and S_i represents a source term for i , neglected hereafter. Considering only the spatial integration, and neglecting source terms, we can group terms in equation 7.24 to yield:

$$\int_V \frac{\partial \rho \omega_i}{\partial t} = \int_A (\rho \omega_i \mathbf{v} - \mathbf{j}_i) \cdot \hat{\mathbf{n}} da \quad (7.25)$$

A Maxwell-Stefan description of diffusion in the liquid is used here, so the diffusive mass fluxes \mathbf{j}_i are coupled (see equation 7.8):

$$\begin{pmatrix} j_1 \\ j_2 \end{pmatrix} = -\rho \mathbf{D}^o \begin{pmatrix} \nabla \omega_1 \\ \nabla \omega_2 \end{pmatrix} \quad (7.26)$$

The terms of the 2x2 diffusivity matrix \mathbf{D} are given by

$$\mathbf{D}^o = \begin{pmatrix} D_{11}^o & D_{12}^o \\ D_{21}^o & D_{22}^o \end{pmatrix} \quad (7.27)$$

where the D_{ij}^o are the multicomponent diffusion coefficients. The off-diagonal terms D_{12}^o and D_{21}^o represent the interaction terms; when these are zero, the diffusion process is Fickian.

Finite volume methods ensure that the discretization is conservative so that mass is explicitly conserved for each control volume. The spatial discretization of the transport equation 7.25 is considered next.

7.2.3 Spatial Discretization

Figure 7.2 shows a schematic finite-volume cell arrangement for the two-dimensional case (Patankar 1980, Versteeg & Malalasekera 2007). Using the conventional notation, each cell center (grid node) is identified by "P", with neighbouring east "E", west "W", south "S" and north "N" nodes. Cell faces are located at "e", "w", "s" and "n" respectively. Grids may be in general be non-orthogonal (figure 7.2(b)) or orthogonal (figure 7.2(c)). Unit normals from each cell face are identified by n_e , n_w , n_s and n_n . For the orthogonal grid, the cell dimensions are $y_n - y_s$ and $x_e - x_w$. Figure 7.3 shows

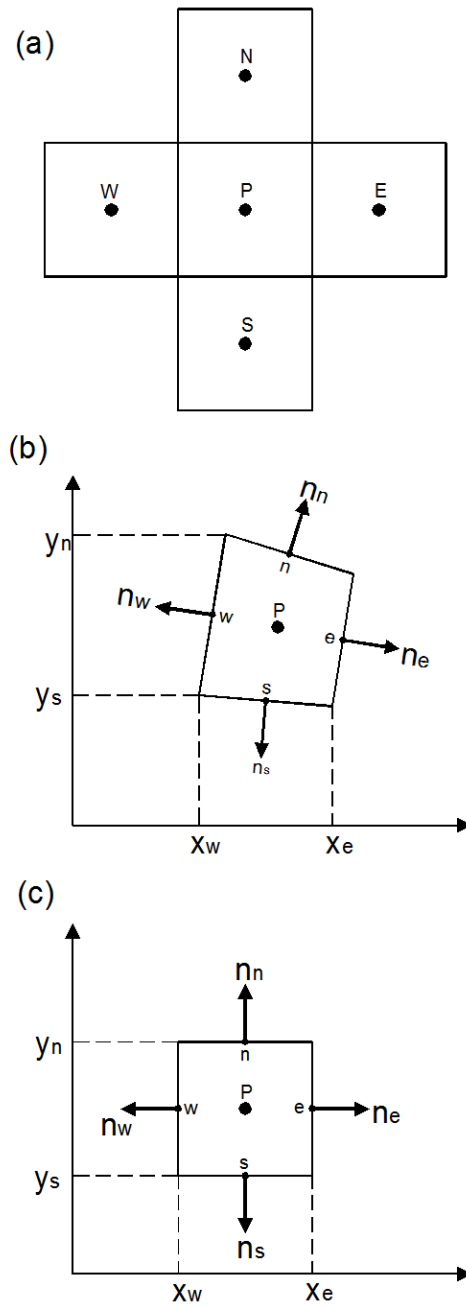


Figure 7.2: Control volumes for general 2-D finite-volume method (Schafer 2006)

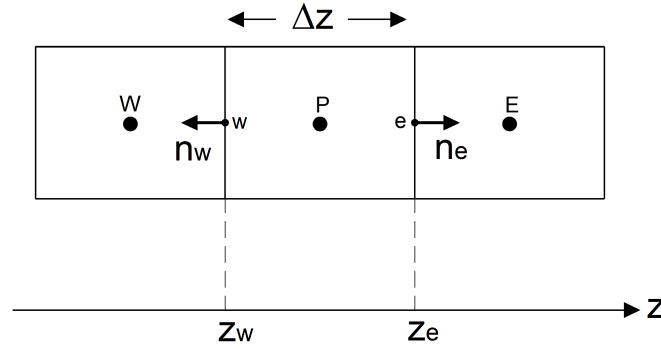


Figure 7.3: Control volumes for 1-D finite-volume method

a schematic cell arrangement for the one-dimensional case. In this work, the focus is on diffusion in a single direction, normal to the vapour-liquid interface; consequently the following development uses figure 7.3 as a basis.

The surface integral in equation 7.25 may be split into the sum of the 2 surface integrals at opposing cell faces:

$$\int_V \frac{\partial \rho \omega_i}{\partial t} = \sum_c \int_{A_c} (\rho \omega_i \mathbf{v} - \mathbf{j}_i) \cdot \hat{\mathbf{n}}_c \, da_c \quad (7.28)$$

where c represents each of the cell faces e, w (east and west). Assuming the cell volume ΔV is constant over time, and has unit cross-sectional area (so that $\Delta V = \Delta z \times m^2$) gives the following balance equation for each control volume:

$$\frac{\partial \rho \omega_i}{\partial t} = \frac{1}{\Delta z} \left(\sum_c \int_{A_c} (\rho \omega_i \mathbf{v} - \mathbf{j}_i) \cdot \hat{\mathbf{n}}_c \, da_c \right) \quad (7.29)$$

The surface integrals (fluxes) in equation 7.29 may be computed by firstly approximating the fluxes by values on the control-volume faces ("e" and "w") and then by approximating values of variables at the control faces by values at adjacent nodes. A simple mid-point rule is employed here in which case the summation in brackets in equation 7.29 is simply

$$\sum_c \left((\rho \omega_i)_c \mathbf{v} - \sum_c \mathbf{j}_{ic} \right) \Delta z \quad (7.30)$$

summed over east and west faces, where ΔS is the (unit) width. To perform the required spatial discretization, a first order-accurate upwind differencing scheme (UDS) is employed for the convective fluxes, and a second order-accurate central-difference scheme (CDS) for the diffusive fluxes. Recall that the diffusive flux term \mathbf{j}_i includes two terms for a ternary system to capture the multicomponent or interaction effects. Using the generalised Ficks law from equation 7.8 for the \mathbf{j}_i , and neglecting the time-

dependence for the moment, the following expressions for the spatial discretization of equation 7.30 (see also equation 7.12) are obtained:

$$\begin{aligned} \text{Component 1: } & \left(\rho v \omega_{1P} - \hat{\rho} D_{11}^o \frac{\omega_{1E} - \omega_{1P}}{z_E - z_P} - \underbrace{\hat{\rho} D_{12}^o \frac{\omega_{2E} - \omega_{2P}}{z_E - z_P}}_{\text{off-diagonal term}} \right) \Delta z \\ & - \left(\rho v \omega_{1W} - \hat{\rho} D_{11}^o \frac{\omega_{1P} - \omega_{1W}}{z_P - z_W} - \underbrace{\hat{\rho} D_{12}^o \frac{\omega_{2P} - \omega_{2W}}{z_P - z_W}}_{\text{off-diagonal term}} \right) \Delta z = 0 \end{aligned} \quad (7.31a)$$

$$\begin{aligned} \text{Component 2: } & \left(\rho v \omega_{2P} - \underbrace{\hat{\rho} D_{21}^o \frac{\omega_{1E} - \omega_{1P}}{z_E - z_P}}_{\text{off-diagonal term}} - \hat{\rho} D_{22}^o \frac{\omega_{2E} - \omega_{2P}}{z_E - z_P} \right) \Delta z \\ & - \left(\rho v \omega_{2W} - \underbrace{\hat{\rho} D_{21}^o \frac{\omega_{1P} - \omega_{1W}}{z_P - z_W}}_{\text{off-diagonal term}} - \hat{\rho} D_{22}^o \frac{\omega_{2P} - \omega_{2W}}{z_P - z_W} \right) \Delta z = 0 \end{aligned} \quad (7.31b)$$

where $\hat{\rho}$ is the value of ρ at the cell face of interest and Δz is the control volume length. The mass-averaged velocity v is assumed to be constant through the control volume in the direction W to E . The under-lined terms in equation 7.31 indicate the off-diagonal terms which represent the non-Fickian contribution to diffusive mass transfer. Re-arranging the component balance equation 7.31 gives the following relationships between nodal (cell-centre) values:

$$\text{Component 1: } a_1^P \omega_1^P + a_2^P \omega_1^P + a_1^E \omega_1^E + a_2^E \omega_2^E + a_1^W \omega_1^W + a_2^W \omega_2^W = a^{BC} \quad (7.32a)$$

$$\text{Component 2: } b_1^P \omega_1^P + b_2^P \omega_1^P + b_1^E \omega_1^E + b_2^E \omega_2^E + b_1^W \omega_1^W + b_2^W \omega_2^W = b^{BC} \quad (7.32b)$$

where a^{BC} and b^{BC} are coefficients that incorporate source terms for component 1 and 2 respectively. The terms in the coefficient relationships of equation 7.32 are:

$$\begin{aligned} a_1^P &= \frac{\rho v}{(z_e - z_w)} + \frac{\rho D_{11}^o (z_E - z_W)}{(z_E - z_P)(z_e - z_w)(z_P - z_W)} \\ &= \frac{\rho v}{\Delta z} + \frac{2\rho D_{11}^o}{\Delta z^2} \\ a_2^P &= \frac{\rho D_{12}^o (z_E - z_P)}{(z_E - z_P)(z_e - z_w)(z_P - z_W)} \\ &= \frac{2\rho D_{12}^o}{\Delta z^2} \\ a_1^E &= -\frac{\rho D_{11}^o}{(z_E - z_W)(z_e - z_w)} \end{aligned}$$

$$= -\frac{\rho D_{11}^o}{\Delta z^2}$$

$$\begin{aligned} a_2^E &= -\frac{\rho D_{12}^o}{(z_P - z_W)(z_e - z_w)} \\ &= -\frac{\rho D_{12}^o}{\Delta z^2} \end{aligned}$$

$$\begin{aligned} a_1^W &= -\frac{\rho v}{(z_e - z_w)} - \frac{\rho D_{11}^o}{(z_P - z_W)(z_e - z_w)} \\ &= -\frac{\rho v}{\Delta z} - \frac{\rho D_{11}^o}{\Delta z^2} \end{aligned}$$

$$\begin{aligned} a_2^W &= -\frac{\rho D_{12}^o}{(z_P - z_W)(z_e - z_w)} \\ &= -\frac{\rho D_{12}^o}{\Delta z^2} \end{aligned}$$

$$\begin{aligned} b_1^P &= \frac{\rho D_{21}^o (z_E - z_P)}{(z_P - z_W)(z_e - z_w)(z_E - z_P)} \\ &= \frac{2\rho D_{21}^o}{\Delta z^2} \end{aligned}$$

$$\begin{aligned} b_2^P &= \frac{\rho v}{(z_e - z_w)} + \frac{\rho D_{22}^o (z_E - z_W)}{(z_E - z_P)(z_e - z_w)(z_P - z_W)} \\ &= \frac{\rho v}{\Delta z} + \frac{\rho D_{22}^o}{\Delta z^2} \end{aligned}$$

$$\begin{aligned} b_1^E &= -\frac{\rho D_{21}^o}{(z_E - z_P)(z_e - z_w)} \\ &= \frac{\rho D_{21}^o}{\Delta z^2} \end{aligned}$$

$$\begin{aligned} b_2^E &= -\frac{\rho D_{22}^o}{(z_E - z_P)(z_e - z_w)} \\ &= -\frac{\rho D_{22}^o}{\Delta z^2} \end{aligned}$$

$$\begin{aligned} b_1^W &= -\frac{\rho D_{21}^o}{(z_P - z_W)(z_e - z_w)} \\ &= \frac{\rho D_{21}^o}{\Delta z^2} \end{aligned}$$

$$\begin{aligned}
b_2^W &= -\frac{\rho v}{(z_e - z_w)} - \frac{\rho D_{22}^o}{(z_P - z_W)(z_e - z_w)} \\
&= -\frac{\rho v}{\Delta z} - \frac{\rho D_{22}^o}{\Delta z^2} \\
a^{BC} &= 0 \\
b^{BC} &= 0
\end{aligned}$$

The simplifications involving Δz above apply only when the grid is equally spaced, with grid spacing Δz . In this work, a non-evenly spaced grid was used so that grid-spacing was smaller near the vapour-liquid interface. As concentration changes are expected to be more pronounced near the interface, this allows more accurate representation of the composition profile, without incurring the computational cost of a uniformly dense spacing. The grid spacing $z_p(i)$ for a total length z with nr cell volumes is given by:

$$z_p(i) = z \left(\frac{i-1}{nr} \right)^f \quad (7.33)$$

where f is a factor used to adjust the spacing. In this work $f = 2$.

7.2.4 Treatment of Boundary Conditions

The development outlined above applies to interior cells in a one-dimensional domain. To account for evaporation from the liquid to the vapour phase at the vapour-liquid interface, the mass fluxes must be accounted for at the domain boundaries. The treatment of gas-phase mass transfer in section 7.1.1 yields component mass fluxes n_i^G at the vapour-liquid interface; these fluxes can be considered Neumann-type boundary conditions for the partial differential equations for mass transfer in the liquid phase. The Neumann boundary conditions are implemented by applying the flux condition from right-hand side of 7.18 and 7.19 at the east and west faces of boundary cells (at $i = 1$ and $i = nr$), representing the vapour-liquid interface and the base of the liquid film respectively (see figure 7.1b).

A prescribed flux boundary condition for the "west" boundary of figure 7.3 yields the similar component relationships to those of the non-boundary nodes of equation 7.32, but with the specified mass fluxes at the interface (n_1^G and n_2^G) explicitly included:

$$\text{Component 1 : } a_1^P \omega_1^P + a_2^P \omega_1^P + a_1^E \omega_1^E + a_2^E \omega_2^E + a_1^W \omega_1^W + a_2^W \omega_2^W = -n_1^G \quad (7.34)$$

$$\text{Component 2 : } b_1^P \omega_1^P + b_2^P \omega_1^P + b_1^E \omega_1^E + b_2^E \omega_2^E + b_1^W \omega_1^W + b_2^W \omega_2^W = -n_2^G \quad (7.35)$$

The fluxes at the base of the liquid film ($i = 1$ in figure 7.1b) are zero. The coefficients

for the interface boundary node are then given by:

$$\begin{aligned} a_1^P &= \frac{\rho v}{(z_e - z_w)} + \frac{\rho D_{11}^o}{(z_E - z_P)(z_e - z_w)} \\ &= \frac{\rho v}{\Delta z} + \frac{2\rho D_{11}^o}{\Delta z^2} \end{aligned}$$

$$\begin{aligned} a_2^P &= \frac{\rho D_{12}^o}{(z_E - z_P)(z_e - z_w)} \\ &= \frac{\rho D_{12}^o}{\Delta z^2} \end{aligned}$$

$$\begin{aligned} a_1^E &= -\frac{\rho D_{11}^o}{(z_E - z_P)(z_e - z_w)} \\ &= -\frac{2\rho D_{11}^o}{\Delta z^2} \end{aligned}$$

$$\begin{aligned} a_2^E &= -\frac{\rho D_{12}^o}{(z_E - z_P)(z_e - z_w)} \\ &= -\frac{\rho D_{12}^o}{\Delta z^2} \end{aligned}$$

$$a_1^W = 0$$

$$a_2^W = 0$$

$$\begin{aligned} b_1^P &= \frac{\rho D_{21}^o}{(z_E - z_P)(z_e - z_w)} \\ &= \frac{\rho v}{\Delta z} + \frac{2\rho D_{11}^o}{\Delta z^2} \end{aligned}$$

$$\begin{aligned} b_2^P &= \frac{\rho v}{(z_e - z_w)} + \frac{\rho D_{22}^o}{(z_E - z_P)(z_e - z_w)} \\ &= \frac{\rho D_{12}^o}{\Delta z^2} \end{aligned}$$

$$\begin{aligned} b_1^E &= -\frac{\rho D_{21}^o}{(z_E - z_P)(z_e - z_w)} \\ &= -\frac{2\rho D_{21}^o}{\Delta z^2} \end{aligned}$$

$$\begin{aligned} b_2^E &= -\frac{\rho D_{22}^o}{(z_E - z_P)(z_e - z_w)} \\ &= -\frac{\rho D_{22}^o}{\Delta z^2} \end{aligned}$$

$$b_1^W = 0$$

$$b_2^W = 0$$

$$a^{BC} = -n_1^G$$

$$b^{BC} = -n_2^G$$

The key feature here is the incorporation of the component mass fluxes from the boundary conditions into the source terms a^{BC} and b^{BC} . Similar equations apply for the base of the liquid film, with $a^{BC} = 0$ and $b^{BC} = 0$.

7.2.5 Time Discretization

In order to solve the time-dependent problem, the spatial discretization of the previous section, when combined with the transport equation 7.29 results in a system of ordinary differential equations (ODEs) with respect to time for each 1-D control volume:

$$\frac{d\rho\omega_1}{dt} = \frac{1}{\Delta z} \left(-a_1^P(t)\omega_1^P + -a_2^P(t)\omega_2^P + \sum_c a_1^E(t)\omega_1^E + \sum_c a_2^E(t)\omega_2^E + \sum_c a_1^W(t)\omega_1^W + \sum_c a_2^W(t)\omega_2^W + a_1^{BC}(t) \right) \quad (7.36a)$$

$$\frac{d\rho\omega_2}{dt} = \frac{1}{\Delta z} \left(-b_1^P(t)\omega_1^P + -b_2^P(t)\omega_2^P + \sum_c b_1^E(t)\omega_1^E + \sum_c b_2^E(t)\omega_2^E + \sum_c b_1^W(t)\omega_1^W + \sum_c b_2^W(t)\omega_2^W + b_1^{BC}(t) \right) \quad (7.36b)$$

These can be re-cast in a matrix-like form suitable for solution by an ODE-solver:

$$\begin{pmatrix} \frac{d(\rho\omega_1)}{dt} \\ \frac{d(\rho\omega_2)}{dt} \end{pmatrix} = \begin{pmatrix} A & 0 \\ 0 & B \end{pmatrix} \begin{pmatrix} (\omega_1) \\ (\omega_2) \end{pmatrix} - \begin{pmatrix} (a^{BC}) \\ (b^{BC}) \end{pmatrix} \quad (7.37)$$

where $(\rho\omega_1)$ and $(\rho\omega_2)$ are the $nr \times 1$ arrays of mass density of components 1 and 2 at each of the nr cells depicted in the schematic of figure 7.1b. The Matlab *ODE15s* solver for numerically stiff systems was used in this work. In a finite difference setting, this approach is referred to as the *method of lines* (Schafer 2006). The A and B matrices in equation 7.37 are given by

$$A = \frac{1}{\Delta z} \begin{pmatrix} a_1^{P(1)} + a_2^{P(1)} & a_1^{E(1)} + a_2^{E(1)} & 0 & \cdots & 0 \\ a_1^{W(2)} + a_2^{W(2)} & a_1^{P(2)} + a_2^{P(2)} & a_1^{E(2)} + a_2^{E(2)} & 0 & 0 \\ 0 & 0 & \ddots & \ddots & 0 \\ 0 & \cdots & \ddots & \ddots & a_1^{E(nr-1)} + a_2^{E(nr-1)} \\ 0 & \cdots & 0 & a_1^{W(nr)} + a_2^{W(nr)} & a_1^{P(nr)} + a_2^{P(nr)} \end{pmatrix} \quad (7.38a)$$

$$B = \frac{1}{\Delta z} \begin{pmatrix} b_1^{P(1)} + b_2^{P(1)} & b_1^{E(1)} + b_2^{E(1)} & 0 & \cdots & 0 \\ b_1^{W(2)} + b_2^{W(2)} & b_1^{P(2)} + b_2^{P(2)} & b_1^{E(2)} + b_2^{E(2)} & 0 & 0 \\ 0 & 0 & \ddots & \ddots & 0 \\ 0 & \cdots & \ddots & \ddots & b_1^{E(nr-1)} + b_2^{E(nr-1)} \\ 0 & \cdots & 0 & b_1^{W(nr)} + b_2^{W(nr)} & b_1^{P(nr)} + b_2^{P(nr)} \end{pmatrix} \quad (7.38b)$$

where the bracketed superscript is the cell-centre index, and the subscript refers to the component.

In the following simulations, the time integration for the distributed model was continued forward in time until the averaged film concentration approached a stable node to within a pre-specified tolerance, typically 0.01 mole-fraction. The nodes for each mixture are known *a priori*, and include pure components and pseudo-azeotropes as described in chapter 3 and 4.

7.3 Simulation Results and Discussion

A Matlab code was written for the distributed model described in the previous section. In the following sections a comparison with some experimental data is presented, followed by a study of evaporation paths for a number of ternary mixtures.

7.3.1 Comparison with Experimental Data

The evaporation of ternary ethanol/methyl-ethyl-ketone(MEK)/toluene mixtures from a flat geometry was studied by Martinez & Setterwall (1991). Data from that work was used in chapter 3 to compare predictions of the gas-phase-limited evaporation model. In this section, computed results from the distributed model are compared with those of the gas-phase-limited model. Figure 7.4, 7.5 and 7.6 show computed results compared to the data of Martinez & Setterwall (1991).

Figure 7.4 shows computed ternary compositions for the gas-phase-limited model (dotted lines) and the distributed model (solid lines), for an initial liquid composition of $x_{EtOH} = 0.33$, $x_{MEK} = 0.33$, $x_{Toluene} = 0.34$. It has already been established in chapter 3 that the gas-phase limited model agrees well with the experimental data of for this mixture. Consequently, a model directly incorporating the effects of liquid diffusion might not be expected to agree well with the same data. This is borne out by the solid lines in figure 7.4; although the composition paths terminate at the correct node (pure toluene), the distributed model does not accurately match the experimental composition profile during the course of the evaporation process. This is probably due to some mixing and natural circulation within the liquid phase caused by the effect of the gas stream moving over the liquid surface, which in turn causes concentration gradients within the liquid to be wiped out. However, by employing an effective diffusivity with a nominal value of $D_e = 1.5 \times 10^{-10} m^2/s$ (an adjustable parameter essentially), the agreement is better, as indicated by the dashed lines in the figure; in that case the generalized Fick matrix \mathbf{D} is simply

$$\mathbf{D}^o = \begin{pmatrix} D_e & 0 \\ 0 & D_e \end{pmatrix}$$

so that multicomponent effects (normally captured in the off-diagonal terms) are zero.

Figure 7.5 and 7.6 shows similar composition profiles for two different initial liquid compositions, where the solids lines are obtained using the same value for \mathbf{D}^o as above. In each case the gas-phase limited model provides better agreement, indicating that the assumption of a quiescent liquid phase is not valid.

Each of the figures 7.4-7.6 also shows a plot of the *characteristic number for liquid-side mass transfer* K_L suggested by Thurner & Schlunder (1986) as an indicator of mass transfer resistance.

$$K_L = \exp\left(\frac{-v_L}{k_L}\right) \quad (7.39)$$

where k_L is a liquid mass transfer coefficient, and v_L is the bulk liquid phase velocity towards the interface. In this work we use a form for k_L based on the computed film

thickness $z(t)$ and the total liquid concentration:

$$k_L = c \frac{D_e}{z} \quad (7.40)$$

The characteristic number can then be expressed in terms of the molar evaporation rate N_t^G :

$$K_L = \exp \left(\frac{-N_t^G}{\frac{cD_e}{z}} \right) \quad (7.41)$$

In the development outlined by Thurner & Schlunder (1986), as $K_L \rightarrow 1$ no concentration profiles exist in the liquid phase, and the selectivity depends on gas-side mass transfer and thermodynamic equilibrium. At high evaporation rates and/or low liquid-side mass transfer coefficients, $K_L \rightarrow 0$, and liquid-side resistance is the limiting step. In figures 7.4-7.6, K_L is initially near zero, implying significant mass transfer resistance in the liquid phase. As the evaporation progresses and the film becomes thinner K_L increases, implying minimal liquid phase resistance. Consequently, there is a predicted change in the controlling mechanism from liquid side to gas side as the evaporation progresses.

The terms of the generalized Fickian diffusivity matrix \mathbf{D}^o during the course of the evaporation of figure 7.4 (calculated using equations 7.9, 7.10 7.11 and 7.23) are shown in figure 7.7. The diagonal terms of \mathbf{D}^o have values that are reasonably constant over most of the process: $D_{11} \approx 2.0 \times 10^{-11}$ and $D_{22} \approx 5.0 \times 10^{-11}$. As the process tends towards pure toluene ($\xi \rightarrow 0$), the off-diagonal contributions D_{12} and D_{21} tend to zero; this is intuitively correct, as no interaction effects occur with pure components. There is an increase in diffusivity also due the increase in liquid (wet-bulb) temperature as pure toluene is approached; this is to be expected based on the form of the Wilke-Chang correlation used to predict binary diffusivities, see appendix B.4. Note that the off-diagonal diffusivity D_{21} is negative throughout the process, indicating that a positive ethanol(1) gradient Δx_1 acts against the diffusion of ethanol(1). Conversely, D_{12} is negative throughout the process indicating that a positive MEK gradient Δx_2 enhances the diffusion of ethanol.

It can be seen from figures 7.4-7.6 that by using an effective diffusivity $D_e = 1.5 \times 10^{-10} \text{ m}^2/\text{s}$, the computed profiles more closely match the gas-phase-limited model; this higher effective diffusivity accounts for the fact that the liquid is presumably not quiescent during the evaporation process, due to the natural circulation and surface agitation effects noted above. Note that pure toluene forms the stable node for the mixtures in figure 7.4 and 7.5, while pure ethanol is the stable node for the mixture in figure 7.6.

Composition gradients as function of relative time τ are shown in figure 7.8. The effect of the film thinning due to evaporation is evident as the dimensionless film thickness

η declines with increasing τ . Figure 7.8a shows how the surface of the liquid becomes rapidly leaner in the more volatile ethanol and MEK components, while become richer in less volatile toluene. The different diffusivity values for ethanol and MEK (in particular D_{11} and D_{22} , see figure 7.7) give rise to different gradients in the composition profiles; thus the changes in MEK composition propagate more deeply into the liquid than those for ethanol because $D_{22} > D_{11}$. The use of a single effective diffusivity D_e in figures 7.8b and 7.8c causes the composition profiles to display the same rates of change within the liquid for each component, so the curvature in the profiles in figures 7.8b and 7.8c is similar.

In addition to the characteristic number K_L described above, the *Biot* number is conventionally used to describe the ratio of diffusive resistance within a phase (solid or liquid) to the convective resistance outside (liquid or gas phase respectively). The Biot numbers for mass and heat transfer are given by (Pakowski & Mujumdar 2006):

$$Bi_M = \frac{z/D_L}{1/k_G} = \frac{zk_G}{D_L} \quad \text{and} \quad Bi_H = \frac{zh_G}{k_L} \quad (7.42)$$

For heat transfer a lumped-parameter analysis suggests that if $Bi \ll 0.1$ (typically $Bi < 0.1$ is sufficient) a lumped parameter model can be used, whereas for $Bi > 0.1$ a more complex distributed parameter model should be used (Krieth et al. 2010, Bergman et al. 2011). For heat-transfer applications, equilibrium between a vapour and liquid phase generally implies equal temperature at the interface i.e. there is generally no *contact resistance* between phases. For mass transfer applications however, there is a contact resistance in the form of the distribution coefficient for components between vapour and liquid phases. Thus, using the definition of Bi_M and Bi_H as written above, equality of the Biot numbers does not imply similarity between a heat-transfer and a mass-transfer application at a vapour-liquid interface. In addition, because of the multicomponent mass transfer model employed here, involving a mass transfer coefficient matrix k_{ij}^\bullet in the vapour phase and a diffusivity matrix D in the liquid phase, single values of k^G and D_L in the Biot number definition are not accessible. The appropriate definition that implies similarity is given by (Parti 1994):

$$Bi'_{Mi} = m_i Bi_M = \frac{x_i^I - x_i^B}{y_i^I - y_i^V} \quad (7.43)$$

where $m = p_i \gamma_i / P$ is a distribution coefficient for component i (Benitez 2009), and a Biot number is defined for each component. Values of Bi'_{Mi} may be determined as the evaporation process proceeds using computed values of the concentration and equation 7.43. Note that this is not a computation directly involving mass-transfer coefficients and diffusivities; rather it is a method of "back"-calculating a Biot number from computed values of the vapour and liquid molefractions, and the distribution coefficient m . An example of this calculation is shown in the next section.

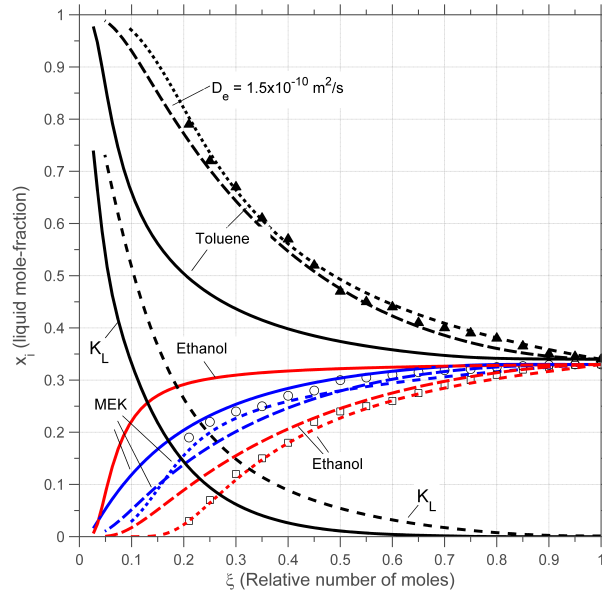


Figure 7.4: Composition profiles for ethanol(1)-MEK(2)-toluene(3) mixture; initial conditions: $x_1 = 0.33, x_2 = 0.33, x_3 = 0.34$; $T^G = 298K, T^L = 298K$, $u^G = 0.1m/s$; \square : ethanol, \circ : MEK, \blacktriangle : toluene. Solid line is distributed (PDE) model, dashed line is model with effective diffusivity, short dashed line is gas-phase-limited model

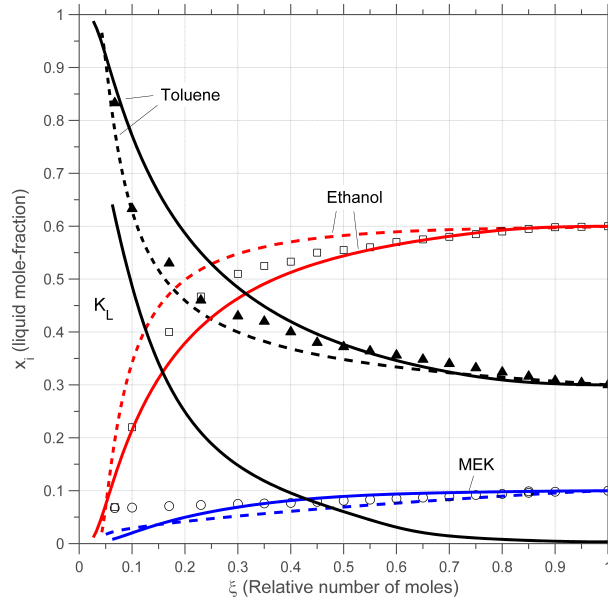


Figure 7.5: Composition profiles for ethanol(1)-MEK(2)-toluene(3) mixture; initial conditions: $x_1 = 0.6, x_2 = 0.1, x_3 = 0.3$; $T^G = 298K, T^L = 298K$, $u^G = 0.1m/s$; \square : ethanol, \circ : MEK, \blacktriangle : toluene. Solid line is distributed (PDE) model, dashed line is model with effective diffusivity, short dashed line is gas-phase-limited model

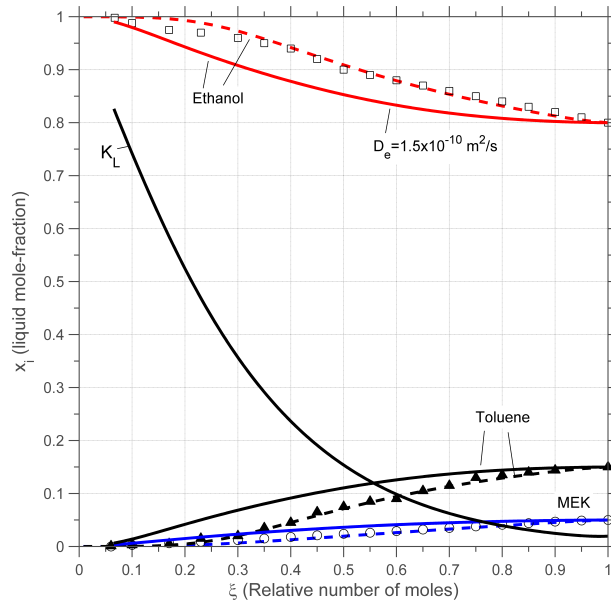


Figure 7.6: Composition profiles for ethanol(1)-MEK(2)-toluene(3) mixture; initial conditions: $x_1 = 0.8, x_2 = 0.05, x_3 = 0.1$; $T^G = 295K, T^L = 298K$, $u^G = 0.07m/s$; \square : ethanol, \circ : MEK, \blacktriangle : toluene. Solid line is distributed (PDE) model, dashed line is model with effective diffusivity, short dashed line is gas-phase-limited model

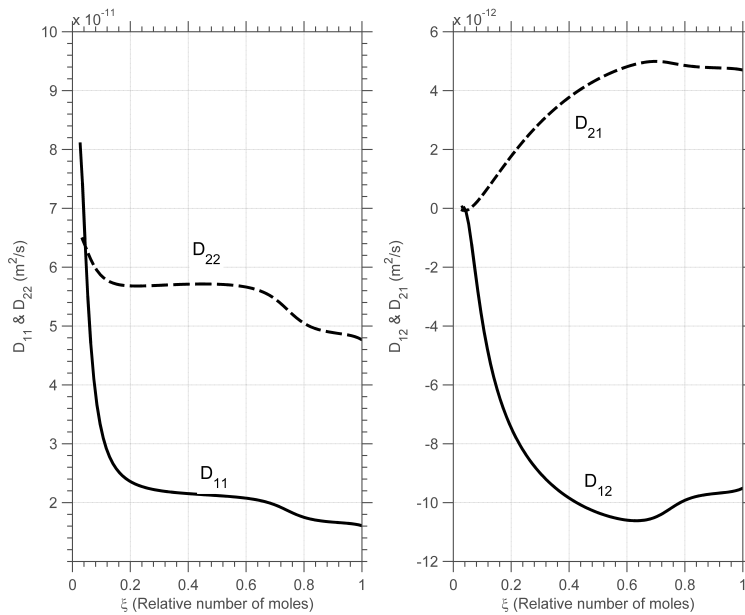
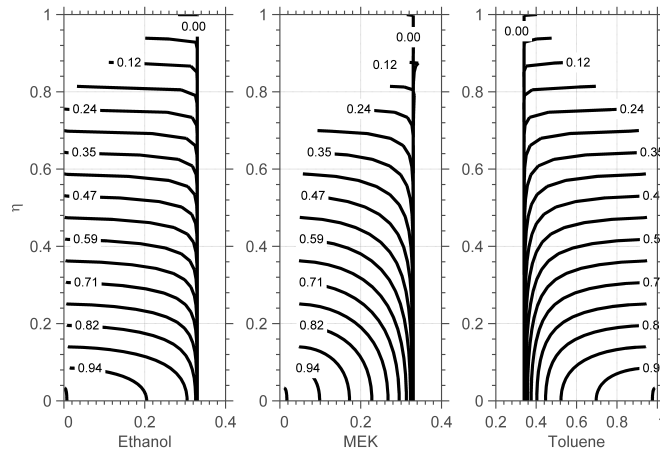
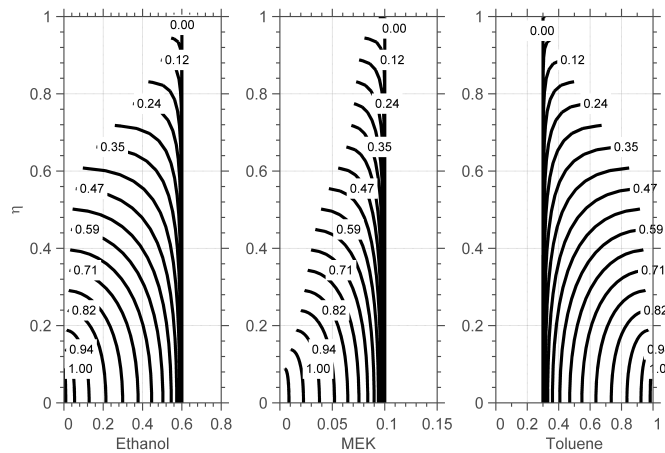


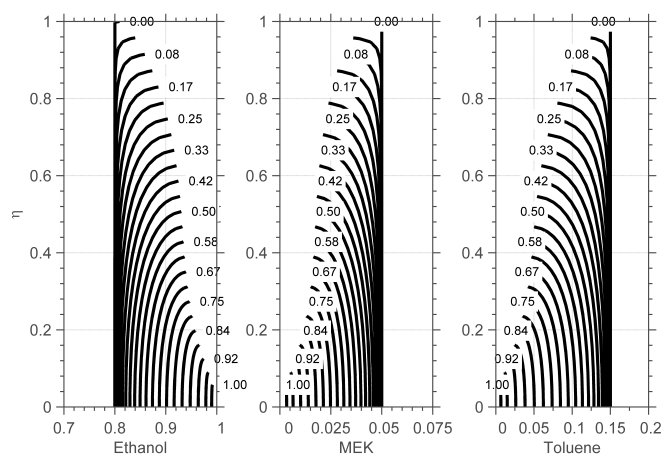
Figure 7.7: Elements of generalized Fick diffusivity matrix for ethanol-MEK-toluene mixture in figure 7.5



(a) Composition profiles corresponding to figure 7.4; multicomponent liquid diffusivity



(b) Composition profiles corresponding to figure 7.5; effective liquid diffusivity



(c) Composition profiles corresponding to figure 7.6; effective liquid diffusivity

Figure 7.8: Composition profiles for ethanol(1)-MEK(2)-toluene(3); y-axis is η (dimensionless thickness); composition profiles annotated with τ (dimensionless time)

7.3.2 Evaporation Paths for Selected Ternary Mixtures

Computed trajectories for a number of ternary mixtures are discussed in this section. A number of features that distinguish the results of the distributed model from the lumped model of evaporation are discussed.

IPA-ethanol-methanol Figure 7.9 show trajectories for two initial compositions of the IPA-ethanol-methanol mixture in the vicinity of the unstable methanol node. Lines of constant τ (relative time) and η (relative distance) are also shown. When the drying/evaporating rate is slow or the film is thin, the drying/evaporation is controlled by the resistance in the gas film at the interface. This is equivalent to Biot numbers that are much less than unity, in which case concentration profiles do not vary significantly with depth in the film. In the case of the mixtures in figure 7.9, the concentration profile is initially flat due to the initial condition of uniform concentration; the initial concentration profile is represented by a point on the diagram. The lines of composition at constant relative time τ collapse onto a single path approximately when $\tau > 0.83$, after which composition does not vary significantly with depth in the film. In the distributed model, the surface of the film is depleted of the volatile components more rapidly than the base, in particular at larger values of Bi_{Mi} . Consequently, the profiles at constant relative depth η are fanned out from the initial point; closer to the the film surface, the composition profiles are leaner in the more volatile methanol component.

The composition profiles and component Biot numbers (from definition of equation 7.43) corresponding to the IPA-ethanol-methanol mixture of figure 7.9b are shown in figure 7.10. The Biot numbers are initially zero at $\tau = 0$ as there is no composition profile in the liquid phase (so numerator is zero), then rise during the evaporation process before declining again as the mixture composition approaches a pure component, at which point the liquid composition gradients diminish to zero. It can be seen from figure 7.10b that the Biot numbers are large enough over most of the time period for a distributed parameter model to be required. Note that the Biot number for ethanol has a secondary small peak near $\tau = 1$; this is associated with the averaged liquid composition that becomes initially richer in ethanol, as evident in the ternary diagram of figure 7.9b), before finally becoming lean in ethanol as the final liquid concentration tends to pure IPA.

Composition paths for the lumped model of chapter 3 are also shown in figure 7.9. The average compositions of the distributed model in general follow a path that tends more directly from the initial composition to the IPA node than the path of the lumped model. Early in the process, the surface ($\eta = 0$) concentration approximately tracks the path of the lumped model; this occurs because the concentration profile is initially uniform, which is by definition also the case with the lumped model. Late in the process, both the distributed and lumped-model paths coincide along the IPA-ethanol

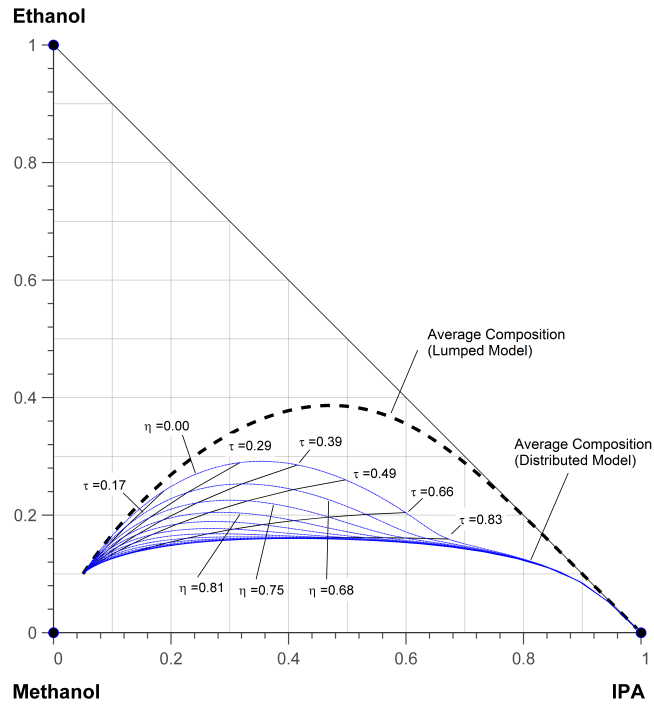
edge. At large values of Bi_{Mi} the rate of mass transfer from the depths of the film is controlled largely by the component diffusivities (i.e. by diffusion in the liquid phase), whereas for the lumped model, the gas-phase component diffusivities, partial pressures and activity coefficients dictate the relative changes in composition. At large values of Bi_{Mi} , the average composition would therefore tend to follow a path directly towards the final composition with the shape of the path affected only by the relative values of the diffusivities. At intermediate Biot numbers (e.g. $Bi_{Mi} \approx \mathcal{O}(1)$, as in much of the duration of figure 7.10b), the mass transfer resistances within the gas and liquid phases are comparable. Consequently, the paths followed by the average composition (distributed model) of the mixtures in figure 7.9 are curved as both the diffusivity in the liquid and the volatility of the components affect the behaviour of the mixture.

Ethanol-MEK-toluene Figure 7.11a for the ethanol-MEK-toluene mixture has an initial composition of $\{x_{EtOH} = 0.3, x_{MEK} = 0.6, x_{Toluene} = 0.1\}$. The composition throughout the liquid is initially uniform (at $\tau = 0$), after which the compositions at different values of η start to fan out, with the most rapid changes at the liquid surface ($\eta = 0$). When relative time $\tau \approx 0.62$, the composition profiles have been substantially wiped out, and the bulk of the liquid follows the distributed (PDE) model average composition. The lumped model average composition tends towards the MEK-toluene edge, whereas the distributed model tends more directly towards the pure toluene node. In the distributed model the surface becomes rapidly depleted of ethanol, then gradually more depleted of MEK; consequently, the profile for $\eta = 0$ tends initially towards the MEK-Toluene edge (becoming lean in ethanol), before turning towards the pure toluene node (becoming lean in MEK). As the residual liquid is relatively richer in MEK and toluene, the rate at which they diffuse to the liquid surface dictates the composition profile; in this case the diffusivities are equal, so the average concentration profile follows a near direct path to the pure toluene node.

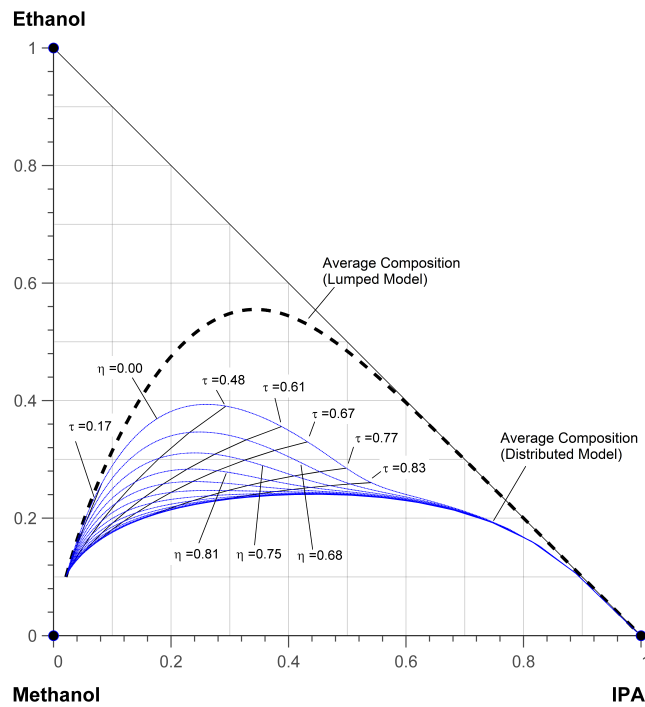
A slightly different picture emerges from figure 7.11b, where the initial composition is $\{x_{EtOH} = 0.5, x_{MEK} = 0.4, x_{Toluene} = 0.1\}$. Contrary to the previous example, the surface of the liquid initially becomes slightly enriched with ethanol and leaner in MEK, reaching a peak around $\tau = 0.26$; in that period the selectivity for ethanol is greater than for MEK. Thereafter, selectivity for ethanol and MEK is reversed, the surface becomes rapidly leaner in ethanol, while the MEK concentration remains nearly constant (evidenced by the flat portion of the $\eta = 0$ profile between ethanol concentration of 0.5 and 0.2). The lines of composition at constant relative time τ collapse onto a single path approximately when $\tau > 0.75$, after which composition does not vary significantly with depth in film.

Acetone-chloroform-methanol A ternary diagram for the more complex acetone-chloroform-methanol mixture is shown in figure 7.12. Composition paths are compared

7. EVAPORATION MAPS INCLUDING DIFFUSION EFFECTS IN LIQUID

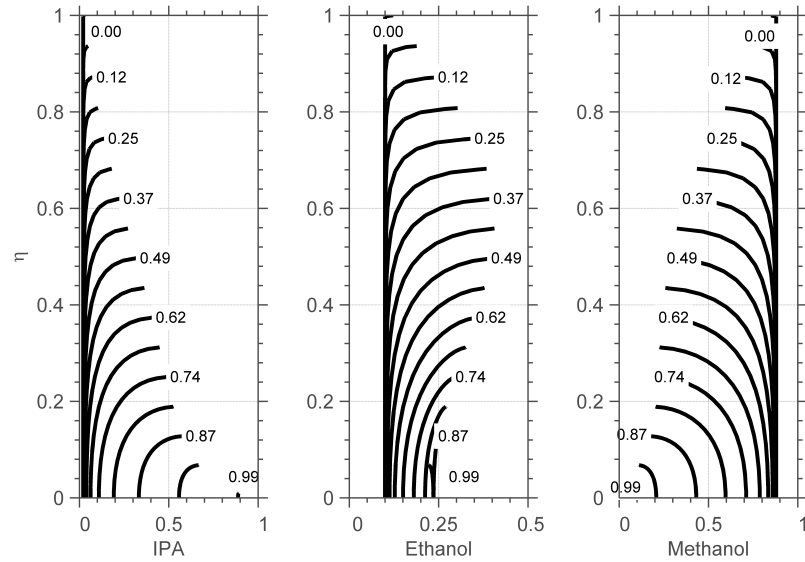


(a) Initial conditions: $x_1 = 0.05, x_2 = 0.1, x_3 = 0.85$; $T^G = 40^\circ\text{C}$, $u^G = 0.5\text{m/s}$

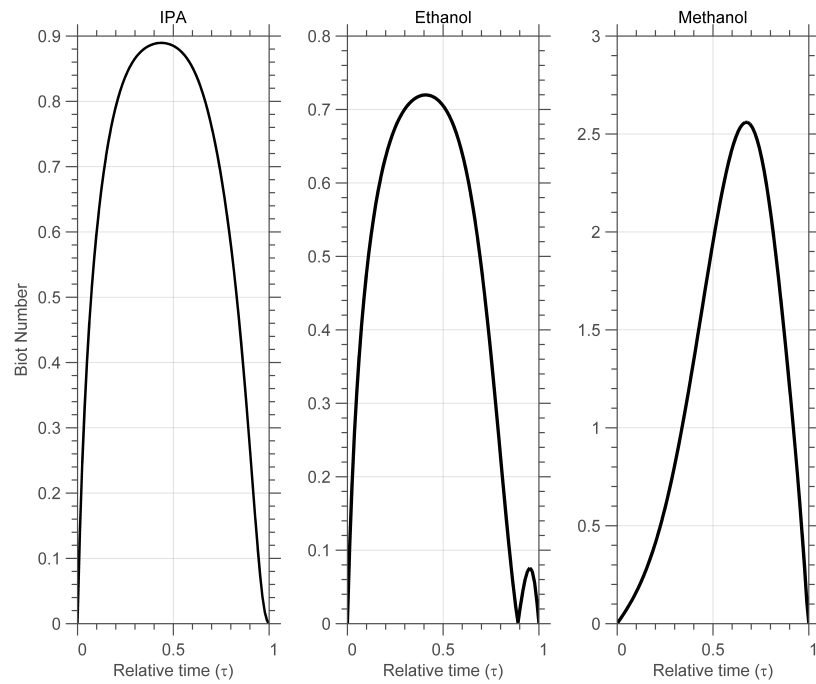


(b) Initial conditions: $x_1 = 0.02, x_2 = 0.1, x_3 = 0.88$; $T^G = 40^\circ\text{C}$, $u^G = 0.5\text{m/s}$

Figure 7.9: Evaporation paths of IPA-ethanol-methanol film into pure air stream; lines of constant τ are composition profiles at relative times; lines of constant η are compositions at the same relative depth in the film ($\eta = 0$ is liquid surface)



(a) Composition profiles for IPA-ethanol-methanol



(b) Biot numbers for IPA-ethanol-methanol

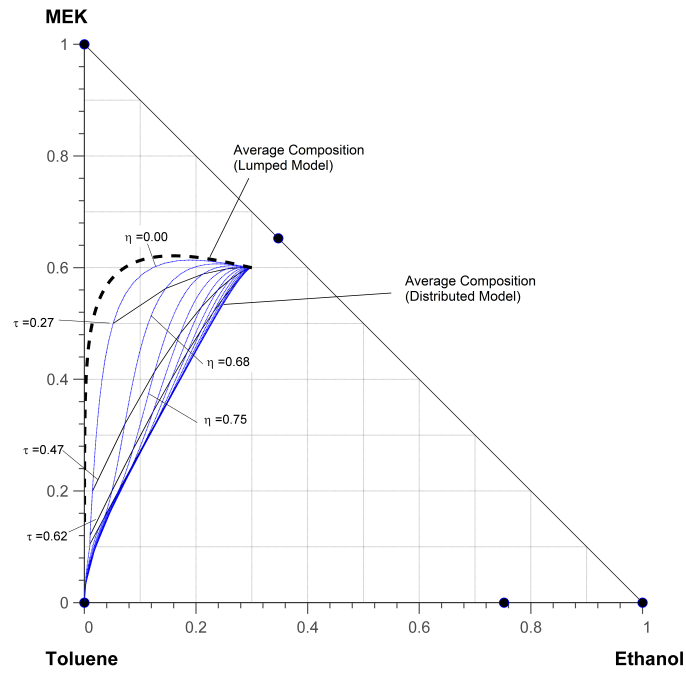
Figure 7.10: Composition profiles and component Biot numbers (Bi_{Mi}) for IPA-ethanol-methanol mixture (see ternary diagram in figure 7.9b)

for the lumped and the distributed models for a variety of initial compositions. From the figure it can be seen how trajectories 1-8 converge (for both lumped and distributed models) on a common terminal composition, namely the acetone-chloroform pseudo-azeotrope. Similarly, trajectories 9-12 converge on the pure methanol node. A separatrix, or separation boundary, running between pseudo-azeotropes on the acetone-methanol and chloroform-methanol edges divides the two areas of the ternary diagram (see chapter 6 for location of boundaries by numerical means).

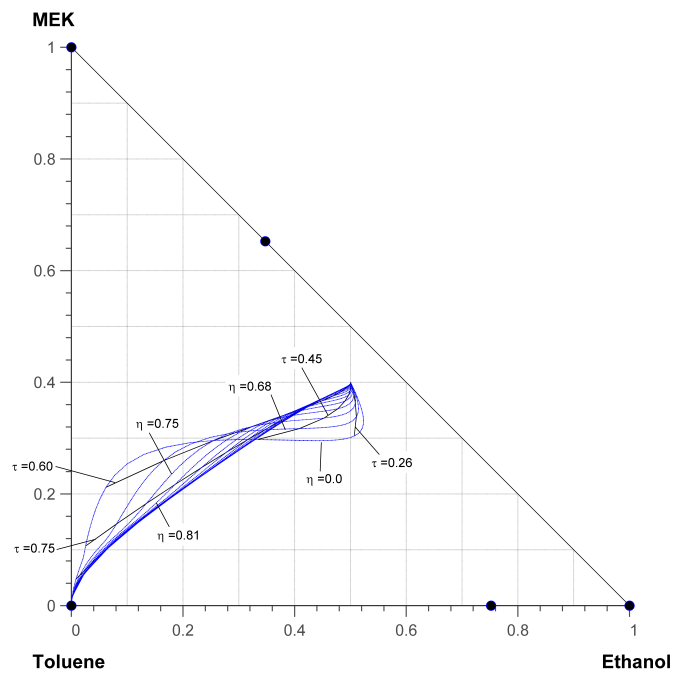
Recall from chapter 3 that a pseudo-azeotrope composition is a function of vapour-liquid equilibria and gas-phase conditions, and does not depend on diffusion within the liquid. This implies that a specific desired terminal composition for an evaporation or drying process can be controlled solely by conditions in the gas phase, and that resistance to mass transfer in the liquid phase does not have a bearing on the end-point composition. The model for computation of pseudo-azeotropic composition (section 3.1.5) is based on fluxes in the gas phase rather than the liquid; liquid composition is computed as an output, based on the requirement of equal selectivity for each component (2 components, in case of binary mixture, 3 for a ternary mixture). Liquid diffusivities affect the evaporation process to the extent that individual components are supplied to the interface at different rates, and so affects the *dynamic* behaviour of the process; the pseudo-azeotropes are *steady-state* values of the evaporation process – consequently, liquid diffusivity is not a parameter of the pseudo-azeotrope model, and the end-points for both cases are the same.

7.4 Chapter Summary and Conclusions

In this chapter the gas-phase limited (lumped) model of chapter 3 was extended to include effects of diffusion in the liquid phase on evaporation trajectories. The conservation equations for individual components in the liquid were cast as partial differential equations, while a lumped model was retained for the energy balance. A generalized Fickian approach was used to calculate diffusive fluxes in the liquid, while an overall material balance was used to determine the movement of the vapour-liquid interface due to evaporation. Due to the multicomponent interaction effects, the PDEs are coupled. The rates of evaporation of the individual components (calculated with the gas-phase model in chapter 3) were used as boundary conditions. A modified finite volume method was developed to perform the spatial discretization, and the overall system was solved using the *method of lines* and a Matlab ODE solver. Composition profiles were computed for a number of example mixtures and profiles resulting from a rigorous multicomponent diffusion model were compared with an effective diffusivity approach. Composition paths for the lumped model and the distributed model were compared for a number of ternary mixtures, and from an analysis of the governing



(a) Initial conditions: $x_1 = 0.3, x_2 = 0.6, x_3 = 0.1$; $T^G = 40^\circ\text{C}$, $u^G = 0.5\text{m/s}$



(b) Initial conditions: $x_1 = 0.5, x_2 = 0.4, x_3 = 0.1$; $T^G = 40^\circ\text{C}$, $u^G = 0.5\text{m/s}$

Figure 7.11: Evaporation paths of ethanol-MEK-toluene film into pure air stream; lines of constant τ are composition profiles at relative times; lines of constant η are compositions at the same relative depth in the film ($\eta = 0$ is liquid surface)

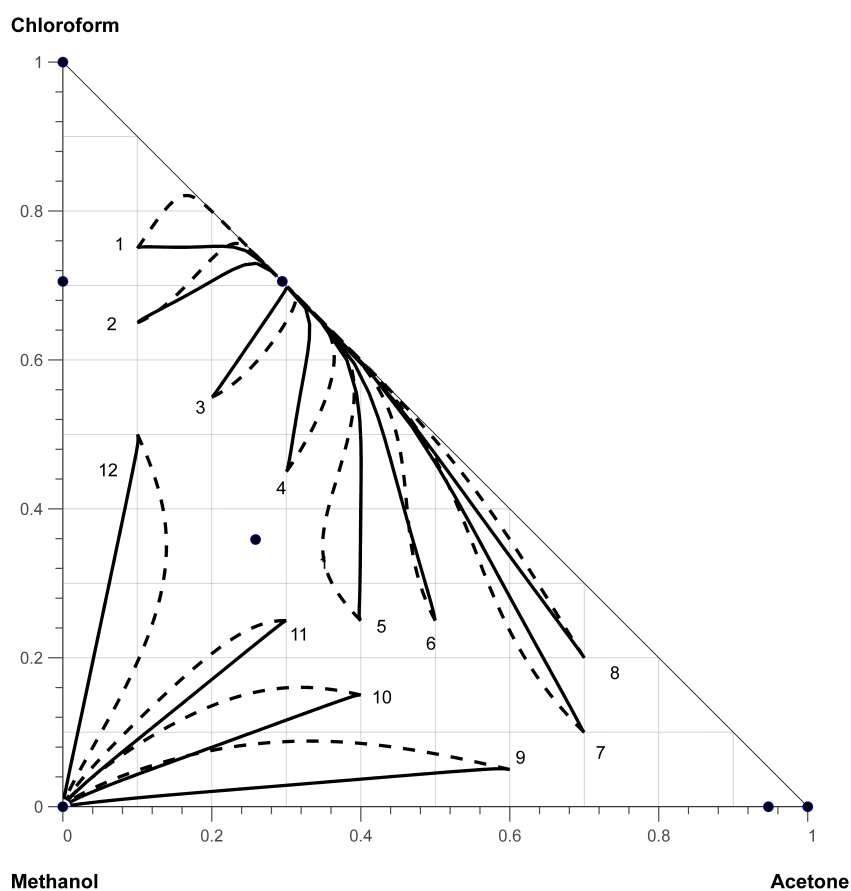


Figure 7.12: Comparison of trajectories for lumped and distributed models for acetone-chloroform-methanol mixture; solid lines are distributed (PDE) model, dashed line is gas-phase-limited model

equations, and simulations of a complex ternary mixture it was concluded that the end-points for the gas-phase limited process were the same as those for which liquid diffusion played a role.

Chapter 8

Conclusions and Further Work

8.1 Summary and Outcomes

The primary aim of this thesis has been the development of the concept of *evaporation maps* for non-ideal, ternary liquid mixtures, using principles of multicomponent mass transfer. The purpose of these maps is to allow composition changes in the liquid phase during a gas-phase limited evaporation or drying process to be simply and clearly depicted on a ternary diagram. The evaporation map concept is motivated by residue curve maps, which are commonly used in the design of distillation separation processes. Chapter 2 presented background material on the governing equations of multicomponent mass transfer, on residue-curve maps, and on evaporation and drying of multicomponent mixtures. In particular, section 2.2.3 reviewed some attempts at accounting for non-equilibrium effects directly into residue curve maps, and highlighted various deficiencies; typically the assumptions used in previous works are not consistent with the fundamental basis upon which residue curve maps are based.

In chapter 3, a comprehensive model for gas-phase limited evaporation maps was developed. This model employed an analytic solution to the Maxwell-Stefan equations for mass transfer in the notional film at the gas-liquid interface, and a lumped, non-isothermal model for the residual liquid phase. The evaporation model was validated against data for evaporation of binary liquid droplets, and a ternary liquid film. For speed of execution, the evaporation model was implemented in the "C" programming language, linked to Matlab via "mex" files. For a given ternary mixture, $T - x$ (temperature-composition) solutions of the model, when projected onto the ternary diagram, form evaporation trajectories; a number of such trajectories combined together shows the overall flow of an evaporation process at specified gas-phase conditions (velocity, temperature, composition), and constitutes an evaporation map. An optimization method was used to ensure an even spread of trajectories over the ternary diagram for each mixture.

A numerical method for computation of binary and ternary pseudo-azeotropes was also developed in chapter 3; together with the pure components, pseudo-azeotropes are fixed points of the system of equations describing the evaporation maps. The pseudo-azeotropes of a mixture must be determined prior to generation of an evaporation map, as they may form a starting or an end-point for the evaporation trajectories. A related model for the multicomponent wet-bulb temperature of a liquid mixture was also developed. It was also shown how the multicomponent wet-bulb model reduces to a simpler version in the case of evaporation of a single component.

Chapter 4 deals with changes in the topology of evaporation maps with changes in the composition in the gas phase. Separate homotopy methods were developed to enable tracking the location of (1) binary and ternary azeotropes and (2) binary and ternary pseudo-azeotropes. In each case, the homotopy parameter was used to gradually introduce non-ideality in the liquid phase as the parameter was varied from $0 \rightarrow 1$. Binary azeotropes and pseudo-azeotropes appeared as branches from pure-component solutions. Ternary azeotropes and pseudo-azeotropes appeared as branches from binary azeotropes and pseudo-azeotropes respectively. Bifurcations in evaporation maps were examined using a numerical continuation procedure. In this approach, the gas phase was gradually pre-loaded with one of the ternary components in turn; the extent of pre-loading acted as the continuation parameter, and the pseudo-azeotropes were tracked as the parameter increases. Bifurcation diagrams for the pseudo-azeotropes show how additional pseudo-azeotropes appear and disappear as the continuation parameter is varied. The existence of limit points in both binary and ternary azeotropes was demonstrated for the acetone-chloroform-methanol mixture. Use of the bifurcation diagrams in principle allows one to determine the required amount of gas-phase pre-loading that leads to a particular terminal composition in the liquid phase.

A measure of the extent of multicomponent effects (due to interaction between species) was also used in chapter 4. The interaction terms computed along the branches of the binary pseudo-azeotropes in an acetone chloroform-methanol mixture were generally non-negligible; typically the off-diagonal terms were $\approx 10\%$ of the diagonal (Fickian) terms in the diffusive fluxes, for a particular gas phase temperature and velocity.

In chapter 5 the mathematical stability of residue curve maps and of evaporation maps was investigated. By linearizing the governing equations, the stability of residue curve maps and evaporation maps can be characterized by the eigenvalues at the fixed points of the system. The eigen-directions at the fixed points show the asymptotic behaviour of trajectories in the neighbourhood of the fixed points. A method for calculation of eigenvalues and eigen-directions for residue curve maps was developed based on existing work by Doherty & Perkins (1978a,b) and Pollmann et al. (1996). The method developed here is novel in that it uses an analytic form of the Jacobian matrix at the fixed points to calculate the eigenvalues.

The method developed for eigenvalues and eigenvectors of evaporation maps was guided by work of Luna & Martinez (1998, 1999) for batch drying of multicomponent mixture, and locates eigenvalues and eigen-directions by firstly calculating derivatives of component fluxes at the fixed points using a numerical finite difference method.

The characteristics of a number of non-ideal ternary mixtures were evaluated in terms of the eigenvalues of the fixed points, and have been shown to qualitatively describe the stability; nodes with two negative eigenvalues are stable, nodes with two positive eigenvalues are unstable, while nodes with eigenvalues of opposing sign are saddles.

Chapter 6 focused on methods for location of separation boundaries in ternary mixtures, both for residue curve maps and evaporation maps. A procedure utilizing the eigen-vectors determined from methods in chapter 5 was firstly described. This method computes separation boundaries by firstly locating the saddle azeotropes (for residue curve maps), or pseudo-azeotropes (for evaporation maps). The separation boundary can be found by moving a small distance from the saddle along the eigen-direction, then integrating forward or backward in time until a stable node is reached.

The second method for location of separation boundaries involved a numerical optimization procedure using (1) a trajectory length approach (based on Lucia & Taylor (2006)) and (2) a novel *integrated area* approach. The trajectory length method is not in general globally optimal, so requires an additional optimization step; the integral area method does not.

Chapter 6 also examined the flexure of the wet-bulb temperature surface. A numerical search procedure, in each of three search directions (for a ternary mixture) was used to locate ridges and valleys in the wet-bulb temperature surface. An alternative approach used a finite difference method applied directly to the wet-bulb surface; both results were generally equivalent. Computations for a number of ternary mixtures show that ridges and valleys do not correspond to separation boundaries in evaporation maps.

Chapter 7 addressed the effects of diffusion in the liquid phase on evaporation trajectories for non-ideal ternary mixtures. Mass conservation equations in the liquid were cast as partial differential equations, while a lumped model was retained for the energy balance. Diffusive fluxes in the liquid were modeled using a generalized Fickian approach, and the rate of interface regression (due to evaporation) was tracked using an overall mass balance. Due to the multicomponent interaction effects, the PDEs are coupled. The rates of evaporation of the individual components (calculated with the gas-phase model in chapter 3) were used as boundary conditions. A modified finite volume method was developed to perform the spatial discretization, and the overall system was solved using the *method of lines* and an ODE solver. Composition profiles were computed for a number of example ternary mixtures and profiles resulting from a rigorous multicomponent diffusion model were compared with an effective diffusivity approach. Some shortcomings in the assumption of one-dimensional diffusion

(quiescent liquid) were identified.

Composition paths for the distributed model were compared with comparable results for the gas-phase limited (lumped) model on ternary diagrams, and the behaviour of the paths was explained in terms of component diffusivities and volatilities.

As several of the features of evaporation maps in this work are motivated by residue curve maps, table 8.1 compares key features of each, and notes where key topics are addressed in the various chapters of this thesis.

Table 8.1: Comparison of some key features of residue curve maps and evaporation maps with references to thesis chapters

Feature	Residue curve map	Evaporation map
Variables (liquid phase)	Composition and bubble point temperature	Composition and wet-bulb temperature
Vapour-liquid relationship	Equilibrium applies between vapour and liquid	Rate-based process, equilibrium applies at interface only; mass transfer described by Maxwell-Stefan theory
Fixed points	Pure components & azeotropes	Pure components & pseudo-azeotropes
Min/max temperature	Binary azeotropes lie at min/max of bubble point temperature	Binary pseudo-azeotropes lie in vicinity, but not at min/max of wet-bulb temperature (see section 3.3.3)
Fixed point location	Newton's method (section 4.2.1); homotopy method (section 4.2.3)	Newton's method (section 3.2.3); homotopy method (section 4.2.4)
Stability characteristics of fixed points	Linearized analysis of analytic Jacobian (section 5.1)	Linearized analysis of numerical Jacobian (section 5.2)
Topology	For a given mixture, function of pressure only	Function of pressure, gas phase conditions (u^G , T^G , y^G); see section 4.3 for analysis of bifurcations in map
Boundaries	Simple distillation boundaries	Evaporation map boundaries (see sections 6.1 and 6.2)
Ridges & valleys	Ridges & valleys can be crossed by residue curves	Ridges & valleys can be crossed by evaporation trajectories (section 6.3)

8.2 Suggestions for Further Work

A number of extensions to the numerical modeling work of this thesis could be undertaken:

1. Although the gas-phase limited evaporation model was validated against some experimental data, the maps generated in this work have all been for a planar geometry, and used heat and mass-transfer coefficients for that purpose. Evaporation maps could also be generated for other geometries e.g. droplets, falling films. A complication arises for droplets however, in that the nature of the heat and mass transfer coefficients means that the pseudo-azeotrope composition is a function of diameter, and would require further investigation.
2. The mixtures covered in this work have all been homogeneous (single phase); adapting the evaporation model to heterogeneous ternary mixtures would require a number of extensions to the theory. An adapted model would have to account for the additional liquid-liquid phase equilibrium that occurs in the two-phase region, and a check on whether the total composition at any point is actually within a two phase region (e.g. using *tangent plane* stability test of Michelsen & Mollerup (2007)). Some work on composition trajectories for two-phase mixtures has been done by Dabral et al. (2002), but this did not include a model that directly accounts for phase splitting. When phase splitting occurs, there may be a layering effect due to differences in density; the less-dense layer is then exposed to the gas stream and may be preferentially removed. Such behaviour has been seen in the evaporation of immiscible droplets (Ray et al. 1992).
3. In this work, the NRTL model has been used to describe non-ideality in the liquid phase. Alternative physical property models such as UNIQUAC, Wilson, UNIFAC (Poling et al. 2001) may also be implemented. These should generally yield equivalent results, subject to their ability to accurately predict azeotropes. The UNIFAC, or other group contribution method, could be used where the binary interaction parameters normally required are unavailable or have not been measured.
4. The models developed in this work use the Maxwell-Stefan equations to address multicomponent effects; the extent of interaction between species in the gas phase was considered during the analysis of bifurcations as the gas phase pre-loading was varied. Additional work can be done to characterise when multicomponent effects are significant, including sensitivity analysis for pre-loading of more than one component, sensitivity to gas temperature and velocity etc.
5. The model developed in this work was based on evaporation from a liquid (or liquid-saturated) surface, and explicitly did not account for presence of solids. An extension of the distributed model (chapter 7) to include mass transfer effects

in porous media could be undertaken. In its simplest form, the liquid diffusion coefficients could be modified in a tortuosity factor. Alternatives would include an effective diffusivity approach. Extending further, diffusion of both liquid and gas phases within the pores (capillaries) of porous media might require solution of separate continuity equations for each species in each phase, and for each phase overall (Pakowski 1992).

6. A practical application of the gas-phase limited evaporation model would be the drying solvent from a mixture in a tray dryer or polymer film coating system. In that case, the heat & mass-transfer area would be discretized over the exposed length using separate lumped parameter models for solvent/polymer mixture and for gas phase in each length increment (Pakowski & Mujumdar 2006).
7. The gas-phase model (chapter 3) used a lumped approach for the liquid phase, while the distributed model (chapter 7) used partial differential equations in one-dimension (normal to the liquid surface) to describe diffusion in the liquid phase. The distributed model could be extended to two dimensions to account for natural circulation effects in the liquid, or heating of film from below. This would include a distributed description of heat transfer in the liquid phase. A further extension could involve the momentum equation (Navier-Stokes equation) by accounting for shear effects at the gas-liquid interface. A suitable approach would be to use a customisable computational-fluid-dynamics (CFD) package using finite volume method to resolve the concentration and velocity profiles in the liquid, while embedding the gas-phase flux as a boundary condition in a user routine. The OpenFOAM software package (Weller et al. 1998) which is open-source and allows the user to customize the governing and boundary equations would be suitable.
8. This work has considered the case of finite gas-phase diffusional resistance with no liquid phase diffusion resistance (chapter 3), and finite diffusion in both gas and liquid phases (chap 7). For the additional case of negligible resistance in both phases, the system would be governed by VLE only, which would likely reduce to the case of a residue curve map. Finite liquid phase resistance, with negligible gas phase resistance would suggest that the composition changes would be unaffected only by VLE and liquid diffusion coefficients. This could be simulated by solving the diffusion equations of chapter 7, assuming gas-phase fluxes are the same (coupled) as those of diffusive fluxes that arise in the liquid phase.
9. In terms of practical application, evaporation maps would be a useful adjunct to a process simulation software package. Currently available industrial software for convective drying such as AspenPlus and Simprosys can handle multiple moisture components (Kemp 2004, 2007, Gong & Mujumdar 2010) but do not provide conceptual design tools similar to the residue curve map tools used in

the synthesis of distillation separation sequences. The addition of a tool to generate evaporation maps could allow rapid determination of the feasible end-points for a convective drying process under given conditions of drying air flow-rate and temperature. Process simulation systems such as AspenPlus, AspenHysys and SimSci PRO-II do generally provide facility for generation of residue curve maps, so the provision of a tool to generate evaporation maps could be done using similar interfaces; the evaporation maps generated in this work were written in the C programming language for speed of execution - a similar programming approach could be adopted for industrial use.

References

- Abramson, B. & Sirignano, W. (1989), 'Droplet vaporisation model for spray combustion calculations', International Journal of Heat and Mass Transfer **32** (9), 1605–1618.
- Aiouache, F. & Goto, S. (2003), 'Reactive distillation-pervaporation hybrid column for tert-amyl alcohol etherification with ethanol', Chemical Engineering Science **58**, 2645–2477.
- Alsam, N. & Sunol, A. (2006), 'Sensitivity of azeotropic states to activity coefficient model parameters and system variables', Fluid Phase Equilib. **240**, 1–14.
- Arya, R. (2013), 'Finite element solution of coupled partial differential and ordinary equations in multicomponent polymeric coatings', Computers and Chemical Engineering **50**, 152–183.
- Arya, R. & Bhargava, C. (2015), 'Simulation analysis of drying of ternary polymeric solution coatings', Progress in Organic Coatings **78**, 155–167.
- AspenTech (2014), AspenPlus Users Guide, AspenTech Inc, Cambridge, MA 02139, USA.
- AspenTech (2015), 'Personal communication'.
- Bader, A., Keller, P. & Haase, C. (2013), 'The influence of non-ideal vapour-liquid equilibrium on the evaporation of ethanol/iso-octane droplets', International Journal of Heat and Mass Transfer **64**, 547–558.
- Barbosa, D. & Doherty, M. (1988), 'The simple distillation of homogeneous reactive mixtures', Chemical Engineering Science **43**, 541–550.
- Baur, R., Krishna, R. & Taylor, R. (2005), 'Influence mass transfer in distillation: Feasibility and design', AIChE Journal **51**(3), 854–866.
- Bausa, J. & Marquardt, W. (2000), 'Quick and reliable phase stability test in VLE flash calculations by homotopy continuation', Computers and Chemical Engineering **24**, 2117–2456.

- Bekiaris, N., Meski, G. & Morari, M. (1995), 'Multiple steady states in heterogeneous azeotropic distillation', Computers & Chemical Engineering **19**, S21–S26.
- Bekiaris, N., Meski, G., Radu, C. & Morari, M. (1993), 'Multiple steady states in homogeneous azeotropic distillation', Industrial & Engineering Chemistry Research **32**, 2023–2038.
- Benitez, J. (2009), Principles and modern application of mass transfer operations, John Wiley and Sons.
- Berggren, J. & Alderborn, G. (2001a), 'Drying behaviour of two sets of microcrystalline cellulose pellets', International Journal of Pharmaceutics **219**, 113–126.
- Berggren, J. & Alderborn, G. (2001b), 'Effect of drying rate on porosity and tableting behaviour of cellulose pellets', International Journal of Pharmaceutics **227**(81-96).
- Bergman, T., Lavine, A., Incropera, F. P. & Dewitt, D. (2011), Fundamentals of Heat and Mass transfer, 7th edn, John Wiley and Sons.
- Beyhaghi, S., Pillai, K., Qadah, D. & Dietz, M. (2011), 'Evaporation and transport of non-dilute, multi-component liquid mixtures in porous wicks: Simulation and experiment validation', International Journal of Heat and Mass Transfer **54**, 5216–5230.
- Bird, R. B. (1998), 'Viewpoints on transport phenomena', Korean Journal of Chemical Engineering **15**(2), 105–123.
- Bird, R., Stewart, W. & Lightfoot, E. (2002), Transport Phenomena, Wiley.
- Blagov, S. & Hasse, H. (2002), 'Topological analysis of vapour-liquid equilibrium diagrams for distillation process design', Phys. Chem. Chem. Phys. **4**, 896–908.
- Botte, G., Ritter, J. & White, R. (2000), 'Comparison of finite difference and control volume methods for solving differential equations', Computers and Chemical Engineering **24**, 2633–2654.
- Bruggemann, S. & Marquardt, W. (2011), 'Conceptual design of distillation processes for mixtures with distillation boundaries: I. Computational assessment of split feasibility', AIChE Journal **57**(6), 1526–1539.
- Burger, M., Schmehl, R., Prommersberger, K., Schafer, O., Koch, R. & Wittig, S. (2003), 'Droplet evaporation modeling by the distillation curve model: accounting for kerosene fuel and elevated pressures', International Journal of Heat and Mass Transfer **46**, 4403–4412.
- Castillo, F. & Towler, G. (1998), 'Influence of multicomponent mass transfer on homogeneous azeotropic distillation', Chemical Engineering Science **53** (5), 963–976.

- Chokshi, S. (2006), 'Strategies for identifying multiplicities in distillation systems using process simulators', Distillation and Absorption .
- Clift, R., Grace, J. & Weber, M. (1978), Bubbles, drops and particles, Academic Press, New York.
- Coumans, W. J., Kerkhof, P. & Bruin, S. (1993), 'Theoretical and practical aspects of aroma retention in spray drying and freeze drying', Drying Technology **12**(1-2), 99–149.
- Curtiss, C. & Bird, R. (1999), 'Multicomponent diffusion', Ind. Eng. Chem. Res. **38**, 2515–2522.
- Cussler, E. (2009), Diffusion, 3rd edn, Cambridge University Press.
- Dabral, M., Francis, L. & Scriven, L. (2002), 'Drying process paths of ternary polymer solution coating', AIChE Journal **48**(1), 25–37.
- Daif, A., Bouaziz, M., Chesneau, X. & Cherif, A. (1998), 'Comparison of multicomponent fuel droplet vaporization experiment in forced convection with the Sirignanao model', Exp. Therm. Fluid Sci. **18**, 282–290.
- Datta, R. & Vilekar, S. (2010), 'The continuum mechanical theory of multicomponent diffusion in fluid mixtures', Chemical Engineering Science .
- DeGroot, S. & Mazur, P. (1984), Non-equilibrium Thermodynamics, Dover Publications, New York.
- DeNevers, N. (2012), Physical and Chemical Equilibrium for Chemical Engineers, 2nd edn, Wiley.
- Dhooge, A., Govaerts, W., Kuznetsov, W. & Yu, A. (2003), 'MatCont: A Matlab package for numerical bifurcation analysis of ODEs', ACM Transactions on Mathematical Software **29**, 141–164.
- Doedel, E., Champneys, A., Fairgrieve, T., Kuznetsov, Y., Sandstede, B. & Wang, X. (1997), Auto97: Continuation and Bifurcation software for ordinary differential equations, Auto97: Continuation.
- Doherty, M. & Cardorola, G. (1985), 'Design and synthesis of homogeneous azeotropic distillations. 3. The sequencing of columns for azeotropic and extractive distillations', Ind. Eng. Chem. Fund. **24**, 47–485.
- Doherty, M. & Malone, M. (2001), Conceptual Design of Distillation Systems, McGraw Hill.
- Doherty, M. & Perkins, J. (1978a), 'On the dynamics of distillation processes - I. The simple distillation of multicomponent non-reacting, homogeneous liquid mixtures', Chemical Engineering Science **33**, 281–301.

- Doherty, M. & Perkins, J. (1978b), 'On the dynamics of distillation processes - II. The simple distillation of model solutions', Chemical Engineering Science **33**, 569–578.
- Doherty, M. & Perkins, J. (1979), 'On the dynamics of distillation processes - III. The topological structure of ternary residue curve maps', Chemical Engineering Science **34**, 1401–1414.
- Duncan, J. & Toor, H. (1962), 'An experimental study of three component gas diffusion', AIChE Journal **8**, 38–41.
- Ferziger, J. & Peric, M. (1999), Computational Methods for Fluid Dynamics, Springer.
- Fick, A. (1855), 'Über diffusion', Poggendorffs Annal. Phys. **94**, 59–86.
- Fidkowski, Z., Malone, M. & Doherty, F. (1993a), 'Computing azeotropes in multicomponent mixtures', Computers & Chemical Engineering **17**(12), 1142–1155.
- Fidkowski, Z., Malone, M. & Doherty, F. (1993b), 'Feasibility of separation for distillation of nonideal ternary mixtures', AIChE Journal **39**(8), 1303–1321.
- Fien, G. & Liu, Y. (1994), 'Heuristic synthesis and shortcut design of separation processes using residue curve maps: A review', Industrial & Engineering Chemistry Research **33**, 2505–2522.
- Foucher, E., Doherty, M. & Malone, M. (1991), 'Automatic screening of entrainers in homogeneous azeotropic distillation', Ind. Eng. Chem. Fund. **29**, 760–772.
- Galeev, A., Salin, A. & Ponikarov, S. (2015), 'Numerical simulation of evaporation of volatile liquids', Journal of Loss Prevention in the Process Industries **38**, 39–49.
- Gamero, R. & Martinez, J. (2005), 'Internal mass transfer during isothermal drying of a porous solid containing multicomponent liquid mixtures', Drying Technology **23**, 1939–1951.
- Gamero, R., Picardo, A., Luna, F. & Martinez, J. (2006), 'An analytical solution of the convective drying of a multicomponent liquid film, in '15th International Drying Symposium (IDS 2006)', pp. 517–523.
- Garhyan, P., Elnashaie, S., Al-Haddad, S., Ibrahim, G. & Elshishini, S. (2003), 'Analysis and exploitation of bifurcation/chaotic behaviour of a continuous fermentor for the production of ethanol', Chemical Engineering Science .
- Gaw, W. & Swinton, F. (1966), 'Occurrence of a double azeotrope in the binary system hexafluorobenzene + benzene', Nature **212**, 283.
- Gmehling, J., Kolbe, B., Kleiber, M. & Rarery, J. (2012), Chemical Thermodynamics for Process Simulation, Wiley-VCH.
- Gong, Z. & Mujumdar, A. (2010), 'Simulation of drying of nonaqueous systems - An application of Simprosys software', Drying Technology **28**, 111–115.

- Govaerts, W. (2000), Numerical methods for bifurcation of dynamical equilibria, SIAM, Philadelphia.
- Govaerts, W. (2011), Matcont and CL-Matcont: Continuation toolboxes in Matlab, Technical report, Utrecht University.
- Graham, T. (1833), 'On the diffusion of gases', Phil. Mag. **2**, 352.
- Graham, T. (1850), 'On the diffusion of liquids', Philosophical Transactions of the Royal Society of London **140**, 1–46.
- Greenberg, M. (1978), Foundations of Applied Mathematics, Prentice-Hall.
- Guckenheimer, J. & Holmes, P. (1985), Nonlinear oscillations, dynamical systems and bifurcations of vector fields.
- Guerrier, B., Bouchard, C., Allain, C. & Benard, C. (1998), 'Drying kinetics of polymer films', A.I.Ch.E.J. **44**, 791–798.
- Guirikov, Y. (1958), 'Structure of the vapour-liquid equilibrium diagrams of ternary homogenous solutions', Russian Journal of Physical Chemistry **32(9)**, 1980–1996.
- Guttinger, T., Dorn, C. & Morari, M. (1997), 'Experimental study of multiple steady states in homogeneous azeotropic distillation', Industrial & Engineering Chemistry Research **36**, 794–802.
- Guyer, J., Wheeler, D. & Warren, J. (2009), 'FiPy: partial differential equations with Python', Computing in Science and Engineering pp. 6–15.
- Hale, J. & Kocak, H. (1991), Dynamics and Bifurcations, number 3 in 'Texts in applied mathematics', Springer-Verlag, New York.
- Harjo, B., Ng., K. & Wibowo, C. (2004), 'Visualization of high-dimensional liquid-liquid diagrams phase diagrams', Ind. Eng. Chem. Res. **43**, 3566–3576.
- Heimann, F., Thurner, F. & Schlunder, E. (1986), 'Intermittent drying of porous materials containing binary mixtures', Chemical Engineering and Processing: Process Intensification **20**, 167–174.
- Hirsch, M., Smale, S. & Devaney, R. (2004), Differential equations, dynamical systems and an introduction to chaos, Vol. 60 of Pure and applied mathematics, 2nd edn, Elsevier, Amsterdam.
- Hirschfelder, A., Curtiss, C. & Bird, R. (1964), Molecular Theory of Gases and Liquids, John Wiley and Sons.
- Huang, Y., Sundmacher, K., Qi, Z. & Schlunder, E. (2004), 'Residue curve maps of reactive membrane separation', Journal of Membrane Science **59**, 2863–2879.

- ICH (2011), ICH Harmonized Tripartite Guide - Impurities: Guideline for Residual Solvents Q3C(R5) International Conference on Harmonisation of Technical Requirements for Registration of Pharmaceuticals for Human Use (ICH).
- Jakobsen, H. (2008), Chemical Reactor Modelling: Multiphase reactive flows, Springer.
- Jaksland, C., Gani, R. & Lien, K. (1995), 'Separation process design and synthesis based on thermodynamic insights', Chemical Engineering Science **50**(3), 511–530.
- Keey, R. B. (1972), Drying Principles and Practice, Pergamon.
- Kelley, C. (1995), Iterative methods for linear and nonlinear equations, SIAM.
- Kemp, I. (2004), 'Development in Aspen technology drying software', Proceedings of 14th International Symposium (IDS) **B**, 767–774.
- Kemp, I. (2007), 'Drying software: Past, present and future', Drying Technology pp. 1249–1263.
- Kermani, M. J. & Stockie, J. (2004), 'Heat and mass transfer modeling of dry gases in the cathode of PEM fuel cells', International Journal of Computational Fluid Dynamics **18**(2), 153–164.
- Khajehnajafi, S. & Pourdarvish, R. (2011), 'Correlations for mass transfer from a liquid spill: Comparisons and recommendations', Process Safety Progress **30**(2), 178–184.
- Kim, J., Lee, A. & Law, C. (1990), 'On the gasification of droplets of azeotropic mixtures: theory and experiment', 23rd symposium on combustion (The Combustion Institute) pp. 1423–1429.
- Kiva, V., Hilmen, E. & Skogestad, S. (2003), 'Azeotropic phase equilibrium diagrams: A survey', Chemical Engineering Science **58**, 1903–1953.
- Knapp, J. & Doherty, M. (1994), 'Minimum entrainer flows for extractive distillation: a bifurcation theoretic approach', AIChE Journal **40**(2), 243–268.
- Kneer, R., Schneider, M., Noll, B. & Wittig, S. (1993), 'Diffusion controlled evaporation of a multicomponent droplet: theoretical studies on the importance of variable liquid properties', International Journal of Heat and Mass Transfer **36**(9), 2403–2415.
- Kohout, M., Schreiber, I. & Kubicek, M. (2002), 'A computational tool for nonlinear dynamical and bifurcation analysis of chemical engineering problems', Computers & Chemical Engineering **26**, 517–527.
- Kreyszig, E. (2010), Advanced Engineering Mathematics, Wiley, New York.
- Krieth, F., Manglik, R. & Bohn, M. (2010), Principles of heat transfer, 7th edn, Cengage Learning.

- Krishna, R. & Standart, L. (1976), 'A multicomponent film model incorporating a general matrix method of solution to the Maxwell-Stefan equations', A.I.Ch.E.J. **22**, 383–389.
- Krishna, R. & Wesselingh, J. (1997), 'The Maxwell-Stefan approach to mass transfer', Chemical Engineering Science **52**, 861–911.
- Kumar, A. & Mazumder, S. (2009), 'Coupled solution of the species conservation equations using unstructured finite-volume method', International Journal for numerical methods in fluids **64**(4), 409–442.
- Kuno, M. & Seader, J. (1988), 'Computing all real solutions to systems of nonlinear equations with a global fixed point homotopy', Ind. Eng. Chem. Res. **27**(1320-1329).
- Kuo, K. (2005), Principles of Combustion, Wiley.
- Kuznetsov, Y. (1998), Elements of Applied Bifurcation Theory, Springer.
- Laroche, L., Bekiaris, N., Andersen, H. & Morari, M. (1992), 'Homogeneous azeotropic distillation: separability and flowsheet synthesis', Ind. Eng. Chem. Res. **31**, 2190–2209.
- Lay, D. (2006), Linear algebra and its applications, 3rd edn, Pearson, New York.
- Lee, K. (2002), 'A method for assessing risk from released hydrocarbon in an enclosed area', Journal of Loss Prevention in the Process Industries **15**(1), 11–17.
- Lightfoot, E. (1974), Transport Phenomena and Living Systems, McGraw Hill, New York.
- Lucia, A. & Feng, Y. (2002), 'Global terrain methods', Computers & Chemical Engineering **26**, 529–546.
- Lucia, A. & Taylor, R. (2006), 'The geometry of separation boundaries: 1 Basic theory and numerical support', A.I.Ch.E.J. **52**, 582–594.
- Luna, F., Birgersson, K. & Martinez, J. (2005), 'Diffusion equation applied to isothermal drying of a multicomponent liquid film', Drying Technology **23**, 1953–1975.
- Luna, F. & Martinez, J. (1998), 'Stability of the dynamical system describing gas-phase controlled drying of ternary mixtures', Drying Technology **16** (9 & 10), 1807–1825.
- Luna, F. & Martinez, J. (1999), 'Stability analysis in multicomponent drying of homogeneous liquid mixtures', Chemical Engineering Science **54**, 5823–5837.
- Mangold, M., Kienle, A., Gilles, E. & Mohl, K. (2000), 'Nonlinear computation in DIVA - methods and applications', Chemical Engineering Science **55**, 441–454.
- Maqua, C., Castanet, G. & Lemoine, F. (2008), 'Bicomponent droplets evaporation: temperature measurement and modelling', Fuel **87**, 2932–3942.

- Marchese, A. & Dryer, F. (1996), 'The effect of liquid mass transport on the combustion and extinction of bicomponent droplets of methanol and water', Combustion and Flame **105**, 104–122.
- Martinez, J. & Setterwall, F. (1991), 'Gas-phase controlled convective drying of solids wetted with multicomponent mixtures', Chemical Engineering Science **9**, 2235–2252.
- Matlab (2010), Matlab, The MathWorks Inc., Natick, Massachusetts.
- Matsuyama, H. (1978), 'Restrictions on patterns of residue curves around heterogeneous azeotropes', J Chem Eng Japan **11**(6), 427–431.
- Maxwell, J. (1860), 'On the dynamical theory of gases', Philosophical Magazine **XIX**, 19–32.
- Maxwell, J. (1866), 'On the dynamical theory of gases', Philosophical Transactions of the Royal Society of London **157**, 49–88.
- Maxwell, J. (1868), 'Illustrations of the dynamical theory of gases', Philosophical Magazine **XX**, 33–36.
- Michelsen, M. & Mollerup, J. (2007), Thermodynamic Models: Fundamentals and computational aspects, 2nd edn, Tie-Line Publications.
- Miller, D. (2012), Spray-drying technology, Vol. 3, Springer, New York, pp. 363–442.
- Muller, D. & Marquardt, W. (1997), 'Experimental verification of multiple steady states in heterogeneous azeotropic distillation', Industrial & Engineering Chemistry Research **36**, 5410–5418.
- Newbald, F. & Amundson, N. (1973), 'A model for evaporation of a multi-component droplet', A.I.Ch.E.J. **1**, 22–30.
- Okamoto, K., Watanabe, N., Hagimoto, Y., Miwa, K. & Ohtani, H. (2010), 'Evaporation characteristics of multi-component liquid', Journal of Loss Prevention in the Process Industries **23**, 89–97.
- Onsager, L. (1931a), 'Reciprocal relations in irreversible processes. I', Phys. Rev. **37**, 405–426.
- Onsager, L. (1931b), 'Reciprocal relations in irreversible processes. II', Phys. Rev. **38**, 2265.
- Padoin, N., Dall'Joe, T., Rangel, L., Ropelato, K. & Soares, C. (2014), 'Heat and mass transfer modelling for multi-component multiphase flow with CFD', International Journal of heat and mass transfer **73**, 239–249.
- Pakowski, Z. (1989), 'Modelling of wet-bulb wetted with binary mixture', Drying Technology **7** (1), 87–100.

- Pakowski, Z. (1990), Stationary states in evaporation of multicomponent liquid droplets to inert gas stream, Technical report, Lodz Technical University.
- Pakowski, Z. (1992), 'The evaporation of ternary liquid azeotropes to air', Proceedings of the 8th International Drying Symposium **1**, 283–292.
- Pakowski, Z. (1994), 'Drying of solids containing multicomponent moisture: recent developments', Proceedings of the 9th International Drying Symposium (IDS '94) **A**, 15–26.
- Pakowski, Z. & Mujumdar, A. (2006), Basic Process Calculations and Simulations in Drying (Handbook of Industrial Drying), 3rd edn, CRC Press.
- Parikh, D. (1997), Handbook of Pharmaceutical granulation technology, CRC Press, Boca Raton.
- Parti, M. (1994), 'Mass transfer Biot numbers', Periodica Polytechnica Ser. Mech. Eng. **38**(2), 109–122.
- Patankar, S. (1980), Numerical Heat Transfer and Fluid Flow, Hemisphere.
- Paudel, A., Worku, Z., Meeus, J., Guns, S. & den Mooter, B. V. (2013), 'Manufacturing of solid dispersions of poorly water soluble drugs by spray drying: Formulation and process considerations', International Journal of Pharmaceutics **453**(1), 253–284.
- Peerenboom, K., van Dijk, J., ten Thije Boonkamp, J., Liu, L., Goedheer, W. & van der Mullen, J. (2011), 'Mass conservative finite volume discretization of the continuity equations in multi-component mixtures', Journal of Computational Physics **230**, 3525–3537.
- Peters, M., Glasser, D., Hildebrandt, D. & Kauchali, S. (2011), Membrane Process design using residue curve maps, Wiley, Hoboken, New Jersey.
- Peters, M., Kauchali, S., Hildebrandt, D. & Glasser, D. (2008), 'Application of membrane residue curve maps to batch and continuous processes', Ind. Eng. Chem. Res. **47**, 2361–2376.
- Peterson, E. & Partin, L. (1997), 'Temperature sequences for categorizing all ternary distillation boundaries', Ind. Eng. Chem. Res. **36**, 1799–1811.
- Pham, H. & Doherty, M. (1990a), 'Design and minimum reflux for heterogeneous azeotropic distillation- II. Residue curve maps', Chemical Engineering Science **45**, 1837–1843.
- Pham, H. & Doherty, M. (1990b), 'Design and synthesis of heterogeneous azeotropic distillations - III. Column sequences', Chemical Engineering Science .
- Poling, B., Prausnitz, J. & O'Connell, J. (2001), The Properties of Gases and Liquids, McGraw Hill.

- Pollmann, P., Bauer, M. & Blass, E. (1996), 'Investigation of vapour-liquid equilibrium of non-ideal multicomponent systems', Gas Separation and Purification **10**, 225–241.
- Popken, T. & Gmehling, J. (2004), 'Simple method for determining the location of distillation region boundaries in quaternary systems', Ind. Eng. Chem. Res. **43**, 777–783.
- Prausnitz, J., Lichtenthaler, R. & de Azevedo, E. (1986), Molecular Thermodynamics of Fluid Phase Equilibria 2nd ed., Prentice-Hall.
- Press, W., Teukolsky, S., Vetterling, W. & Flannery, B. (1992), Numerical recipes in C, 2nd edn, Cambridge University Press.
- Radichkov, R., Muller, T., Kienle, A., Heinrich, S., Peglow, M. & Morl, L. (2006), 'A numerical bifurcation analysis of continuous fluid bed spray granulation with external product classification', Chemical Engineering and Processing **45**, 826–837.
- Ramzan, N., Faheen, M., Gani, R. & Witt, W. (2010), 'Multiple steady states detection in a packed-bed reactive distillation column using bifurcation analysis', Computers & Chemical Engineering **34**(4), 460–466.
- Randolph, A., Makino, A. & Law, C. (1986), 'Liquid phase diffusion resistance in multi-component droplet gasification', 21st Symposium on Combustion / The Combustion Institute pp. 601–608.
- Ray, A., Devakottai, B., Souyri, A. & Huckaby, J. (1992), 'Evaporation characteristics of droplets coated with immiscible layers of nonvolatile liquids', Langmuir **7**, 525–531.
- Reintjes, T., ed. (2011), Solubility enhancement with BASF Pharma Polymers - Solubilizer Compendium, BASF SE.
- Restrepo, J., Olivar, G. & Cardona, C. (2014), 'Bifurcation analysis of dynamic process models using Aspen Dynamics and Aspen Custom Modeler', Computers & Chemical Engineering **54**, 10–20.
- Rev, E. (1992), 'Crossing of valleys, ridges, and simple boundaries by distillation in homogeneous ternary mixtures', Industrial & Engineering Chemistry Research **31**, 893–901.
- Reyes-Labarta, J., Caballero, J. & Marcilla, A. (2010), 'Numerical determination of distillation boundaries for multicomponent homogeneous and heterogeneous azeotropic systems', 20th Symposium on computer aided engineering - ESCAPE20.
- Riede, T. & Schlunder, E. (1988), 'Evaporation and pervaporation of a binary mixture from an inert carrier liquid', Chem. Eng. Technol. **11**, 384–391.
- Riede, T. & Schlunder, E. (1990), 'Selective evaporation of a ternary mixture containing

- one nonvolatile component with regard to drying processes', Chem. Eng. Process. **28**, 151–163.
- Rooks, R., Julka, V., Doherty, M. & Malone, M. (1998), 'Structure of distillation regions for multicomponent azeotropic mixtures', AIChE Journal **44**, 1382–1391.
- Ryan, P. & Doherty, M. (1989), 'Design/optimization of ternary heterogeneous azeotropic distillation sequences', AIChE Journal **35**(10), 1592–1601.
- Salomone, E. & Espinosa, J. (2001), 'Prediction of homogeneous azeotropes with interval analysis techniques exploiting topological considerations', Ind. Eng. Chem. Res. **40**, 1580–1588.
- Sazhin, S. (2006), 'Advanced models of fuel droplet heating and evaporation', Progress in. Energy and Combustion Science **32**, 162–214.
- Schafer, M. (2006), Computational Engineering - Introduction to Numerical Methods, Springer.
- Schlunder, E. (1989a), 'Azeotropes and pseudo-azeotropes', Fluid Phase Equilibria **51**, 71–85.
- Schlunder, E. (1989b), 'Selective drying of mixture-containing products', 6th International Drying Symposium, Versailles **13**, 9–23.
- Schreinemakers, F. (1901a), 'Dampfdruke ternaer gemische, theoretishcer teil: Dritte abhandlung', Zeitschrift fuer Physikalische Chemie (Muenchen, Germany) **36**(6), 710–740. (in German).
- Schreinemakers, F. (1901b), 'Dampfdruke ternaer gemische, theoretishcer teil: Erste abhandlung', Zeitschrift fuer Physikalische Chemie (Muenchen, Germany) **36**(3), 257–289. (in German).
- Schwarzbach, J. (1986), 'Diffusion in porous materials partially wetted with a binary mixture', Chemical Engineering and Processing **26**, 35–44.
- Schwarzbach, J. & Schlunder, E. (1993), 'Fluidized bed drying of materials wetted with a binary mixture', Chem. Eng. Process. **32**, 13–32.
- Selebi, C. & Schiesser, W. (1992), Dynamic Modeling of Transport Process Systems, Academic Press, San Diego.
- Seydel, R. (2010), Practical Bifurcation and Stability Analysis, 3rd. ed., Springer.
- Sidhar, L., Maldonado, C. & Garcia, A. (2002), 'Design and analysis of non-equilibrium separation processes', AIChE Journal **48**, 1179–1191.
- Silva, J., Knoechelmann, A., Meirelles, A., Wolf-Maciel, M. & Lopes, C. (2003), 'On the dynamics of nonequilibrium simple batch distillation processes', Chemical Engineering and Processing **42**, 474–485.

- Sirignano, W. (2010), Fluid dynamics and transport of droplets and sprays, Cambridge University Press.
- Slattery, J. (1999), Advanced Transport Phenomena, Cambridge Series in Chemical Engineering, Cambridge University Press.
- Slaughter, D. & Doherty, M. (1995), 'Calculation of solid-liquid equilibrium and crystallisation paths for melt crystallization processes', Chemical Engineering Science **50**(11), 1679–1694.
- Smith, J. & vanNess, H. (1987), Introduction to chemical engineering thermodynamics, 4th edn, McGraw Hill, New York.
- Smith, L. & Taylor, R. (1983), 'Film models for multicomponent mass transfer: A statistical comparison', Ind. Eng. Chem. Fund. **22**, 97–104.
- Springer, P., Baur, R. & Krishna, R. (2002), 'Influence of interphase mass transfer on the composition trajectories and crossing of boundaries in ternary azeotropic distillation', Separation Science and Technology **20**, 1–13.
- Springer, P., Baur, R. & Krishna, R. (2003), 'Composition trajectories for heterogeneous azeotropic distillation in a bubble-cap tray column', Transactions of the IChemE **81**(A), 413–426.
- Springer, P., Buttinger, B., Baur, R. & Krishna, R. (2002), 'Crossing of the distillation boundary in homogeneous azeotropic distillation: Influence of interphase mass transfer', Ind. Eng. Chem. Res. **41**, 1621–1631.
- Standart, G., Taylor, R. & Krishna, R. (1979), 'The Maxwell-Stefan formulation for irreversible thermodynamics for simultaneous heat and mass transfer', Chem. Eng. Commun. **3**, 277–289.
- Stefan, J. (1871), 'Über das gleichgewicht und die bewegung, insbesondere die diffusion von gasmengen', Sitzungsber. Akad. Wiss. Wien **LXIII**, 63–124.
- Steinbeck, M. (1999), 'Convective drying of porous material containing a partially miscible mixture', Chemical Engineering and Processing **38**, 487–502.
- Steinbeck, M. & Schlunder, E. (1997), 'Convective drying of porous material containing a partially miscible mixture', Chemical Engineering and Processing **37**, 78–88.
- Stewart, W. E. & Prober, R. (1954), 'Matrix calculation of multi-component mass transfer in isothermal systems', Ind. Eng. Chem. Fund. **3**, 224–235.
- Stichlmair, J. & Fair, J. (1998), Distillation, Wiley-VCH, New York.
- Stichlmair, J. & Herguijeula, J. (1992), 'Separation regions and processes of zeotropic and azeotropic ternary distillation', AIChE Journal **38**, 1523–1535.

- Stockie, J., Promislow, K. & Wetton, B. (2003), 'A finite volume method for multicomponent gas transport in a porous fuel cell electrode', International Journal for numerical methods in fluids **41**, 577–599.
- Strogatz, S. (1994), Nonlinear dynamics and chaos, Perseus (Harper Collins), New York.
- Sundmacher, K., Zhiwen, Q., Huang, Y. & Schlunder, E. (2005), Integrated Chemical Processes, Wiley-VCH, Weinheim, Germany, chapter Thermodynamic and kinetic effects on the feasible products of reactive distillation: A-zoe-tropes and A-rheo-tropes, pp. 87–148.
- Taylor, R. & Kooijman, H. (1991), 'Composition derivatives of activity coefficient models (for the estimation of thermodynamic factors in diffusion)', Chem. Eng. Commun. **102**, 87–106.
- Taylor, R. & Krishna, R. (1993), Multicomponent Mass Transfer, Wiley.
- Taylor, R., Krishna, R. & Kooijmanman, H. (2003), 'Real-world modeling of distillation', Chemical Engineering Progress **99**(7), 28–39.
- Taylor, R., Miller, A. & Lucia, A. (2006), 'Geometry of separation boundaries; Systems with reaction', Ind. Eng. Chem. Res. **45**, 2777–2786.
- Taylor, R., R..Baur & Krishna, R. (2004), 'Influence of mass transfer in distillation: Residue curves and total reflux', AIChE Journal **50**(12), 3134–3148.
- Teixeira, J., Sena, F., Silva, A., Strgevitch, L. & Silva, J. (2009), 'Moving boundary in non-equilibrium simple batch distillation in non-ideal systems', Chemical Engineering and Processing: Process Intensification **28**, 1574–1578.
- Thijssen, H. (1971), 'Flavour retention in drying preconcentrated food liquids', J. Appl. Chem. Biotechnol. **21**, 372–377.
- Thijssen, H. & Rulkens, W. (1968), 'Retention of aroma in drying food liquids', De Ingenieur **80**(36), 45–56.
- Turner, F. & Schlunder, E. (1985), 'Wet-bulb temperature of binary mixtures', Chem. Eng. Process. **19**, 337–343.
- Turner, F. & Schlunder, E. (1986), 'Progress towards understanding the drying of porous materials wetted with binary mixtures', Chem. Eng. Process. **20**, 9–25.
- Tolsma, J. & Barton, P. (2000a), 'Computation of heteroazeotropes. Part I: Theory', Chemical Engineering Science **55**, 3817–3834.
- Tolsma, J. & Barton, P. (2000b), 'Computation of heteroazeotropes. Part II: Efficient calculation of changes in phase equilibrium structure', Chemical Engineering Science **55**(18), 3838–3853.

- Toor, H. (1957), 'Diffusion in three component gas mixtures', A.I.Ch.E.J. **3**, 198–207.
- Toor, H. (1964), 'Solution of the linear equations of multi-component mass transfer - II matrix methods', A.I.Ch.E.J. **10**, 460–465.
- Torres, D., O'Rourke, P. & Amsden, A. (2003), 'A discrete multicomponent fuel model', Atomization and Sprays **13**, 131–172.
- Vadapalli, A. & Seader, J. (2001), 'A general framework for computing bifurcation diagrams using process simulation programs', Computers & Chemical Engineering **24**(2-3), 445–464.
- van den Bosch, C. (1997), Methods for the calculation of physical effects due to releases of hazardous materials (Liquids and gases), Yellow Book, Vol. CPR 14E, Committee for the prevention of disasters, chapter Pool Evaporation, pp. 3.1–3.128.
- van Dongen, D. & Doherty, M. (1984), 'On the dynamics of distillation processes: V. The topology of the boiling temperature surface and its relation to azeotropic distillation', Chemical Engineering Science **39**, 883–892.
- van Dongen, D. & Doherty, M. (1985), 'Design and synthesis of homogeneous azeotropic distillation: 1. Problem formulation for a single column', Ind. Eng. Chem. Fund. **24**, 454–463.
- Varma, A. & Morbidelli, M. (1997), Mathematical methods in chemical engineering, Oxford University Press.
- Versteeg, H. & Malalasekera, W. (2007), An Introduction to Computational Fluid Mechanics 2nd ed., Pearson.
- Viduarre, M. & Martinez, J. (1997), 'Continuous drying of a solid wetted with ternary mixtures', AIChE Journal **43** (3), 681–692.
- Villiers, W. D., French, R. & Koplos, G. (2002), 'Navigate phase equilibria via residue curve maps', Chemical Engineering Progress pp. 66–71.
- Vinjamur, M. & Cairncross, R. A. (2002), 'Non-fickian nonisothermal model for drying polymer coatings', A.I.Ch.E.J. **48**(11), 2444–2458.
- Vinjamur, M. & Cairncross, R. A. (2003), 'Guidelines for dryer design based on results from non-fickian model', Journal of Applied Polymer Science **87**, 477–486.
- Vrentas, J. & Vrentas, C. (1994), 'Drying of solvent-coated polymer films', Journal of Polymer Science, Part B: Polymer Physics .
- Wahnschafft, O., Koehler, J. & Westerberg, E. B. (1992), 'The product composition regions of single feed azeotropic distillation columns', Ind. Eng. Chem. Res. **31**, 2345–2362.

- Weller, H., Tabor, G., Jasak, H. & Fureby, C. (1998), 'A tensorial approach to computational continuum mechanics using object-oriented techniques', Computers in Physics **12**(6), 620–631.
- Wesselingh, J. & Krishna, R. (2000), Mass Transfer in Multicomponent Mixtures, Delft University Press, Delft, Holland.
- Wibowo, C. & Ng, K. (2002), 'Visualization of high-dimensional phase diagrams of molecular and ionic mixtures', AIChE Journal **48**, 991–1000.
- Widagdo, S. & Seider, W. (1996), 'Azeotropic distillation', AIChE Journal **42**(1), 96–130.
- Wiggins, S. (1990), Introduction to applied nonlinear dynamical systems and chaos, Texts in applied mathematics, Springer-Verlag, New York.
- Witschi, C. & Doelder, E. (1997), 'Residual solvents in pharmaceutical products: acceptable limits, influence on physicochemical properties, analytical methods and documented values', European Journal of Pharmaceutics and Biopharmaceutics **43**, 215–242.
- Zavala-Tejeda, V., Flores-Tlacuahuac, A. & Vivaldo-Lima, E. (2006), 'The bifurcation behaviour of a polyurethane continuous stirred tank reactor', Chemical Engineering Science **61**, 7368–7385.

Appendix A

Governing Equations

A.1 Multicomponent Fluxes

The treatment of fluxes in multicomponent mixtures is treated in detail in Cussler (2009), Bird et al. (2002) and especially in Taylor & Krishna (1993). For a mixture of i components, where \mathbf{u}_i denotes the velocity of component i defined relative to a stationary reference frame, the mass flux \mathbf{n}_i of species i is given by

$$\mathbf{n}_i = \rho_i \mathbf{u}_i = \omega_i \rho \mathbf{u} \quad (\text{A.1})$$

where ρ_i is the mass concentration (density) of component i , ω_i is the mass fraction of component i and ρ is the total mixture density. The total mass flux of the mixture is then given by

$$\mathbf{n}_t = \sum_{i=1}^n \mathbf{n}_i = \rho \mathbf{v} \quad (\text{A.2})$$

where \mathbf{v} is the *mass-averaged velocity*, and n is the number of components. In equation A.2 we have used the definition of mass flux as a product of mixture density ρ and mass average velocity \mathbf{v} , which is

$$\rho \mathbf{v} = \sum_{i=1}^n \rho_i \mathbf{u}_i \quad (\text{A.3})$$

This can be divided on both sides by ρ , giving the mass-averaged velocity as

$$\mathbf{v} = \sum_{i=1}^n \frac{\rho_i}{\rho} \mathbf{u}_i = \sum_{i=1}^n \omega_i \mathbf{u}_i \quad (\text{A.4})$$

In a similar way, the molar flux \mathbf{N}_i of component i is defined by

$$\mathbf{N}_i = c_i \mathbf{u}_i = x_i c \mathbf{u}_i \quad (\text{A.5})$$

where c is the total molar concentration and c_i is the molar concentration of i . The total molar flux is then the sum of the component fluxes:

$$\mathbf{N}_t = \sum_{i=1}^n \mathbf{N}_i = c\mathbf{u} \quad (\text{A.6})$$

where \mathbf{u} is the *molar-averaged velocity*, defined in a similar way to the mass average velocity:

$$\mathbf{u} = \sum_{i=1}^n \frac{c_i}{c} \mathbf{u}_i = \sum_{i=1}^n x_i \mathbf{u}_i \quad (\text{A.7})$$

where x_i is the mole fraction. The total flux of a component may be partitioned into *convective* and *diffusive* parts. The convective flux is defined in terms of an average velocity, while the diffusive flux is defined as the difference between the total and convective fluxes. Thus, diffusive fluxes cannot be defined independently of both the total and convective fluxes; the movement of the mixture (i.e. the reference velocity) has to be defined before the movement relative to the mixture (i.e. diffusion) can be known. The mass diffusive flux is then simply:

$$\underbrace{\dot{j}_i}_{\substack{\text{mass diffusive flux} \\ \text{of } i \text{ relative to} \\ \text{mass-averaged} \\ \text{velocity } \mathbf{v}}} = \underbrace{\mathbf{n}_i}_{\substack{\text{total mass flux of } i}} - \underbrace{\rho_i \mathbf{v}}_{\substack{\text{convective mass flux of} \\ i \text{ due to mass-averaged} \\ \text{velocity } \mathbf{v}}} \quad (\text{A.8})$$

To see how the diffusive flux depends on the difference in velocities, the above can be re-written as

$$\dot{j}_i = \rho_i (\mathbf{u}_i - \mathbf{v}) = \rho \omega_i (\mathbf{u}_i - \mathbf{v}) \quad (\text{A.9})$$

Similarly, the molar diffusive flux is simply:

$$\underbrace{\mathbf{J}_i}_{\substack{\text{molar diffusive flux} \\ \text{of } i \text{ relative to a} \\ \text{molar-averaged} \\ \text{velocity } \mathbf{u}}} = \underbrace{\mathbf{N}_i}_{\substack{\text{total molar flux of } i}} - \underbrace{c_i \mathbf{u}}_{\substack{\text{convective molar flux} \\ \text{of } i \text{ due to} \\ \text{molar-averaged} \\ \text{velocity } \mathbf{u}}} \quad (\text{A.10})$$

or, in terms of a velocity difference

$$\mathbf{J}_i = c_i (\mathbf{u}_i - \mathbf{u}) \quad (\text{A.11})$$

The relationship between diffusive and convective fluxes can be summarised as follows:

Diffusive Flux	Total Flux	Convective Flux	Description
\dot{j}_i	\dot{n}_i	$\rho_i \mathbf{v}_i$	Mass diffusive flux relative to a mass-averaged velocity
\mathbf{J}_i	\mathbf{N}_i	$c_i \mathbf{u}_i$	Molar diffusive flux relative to a molar-averaged velocity

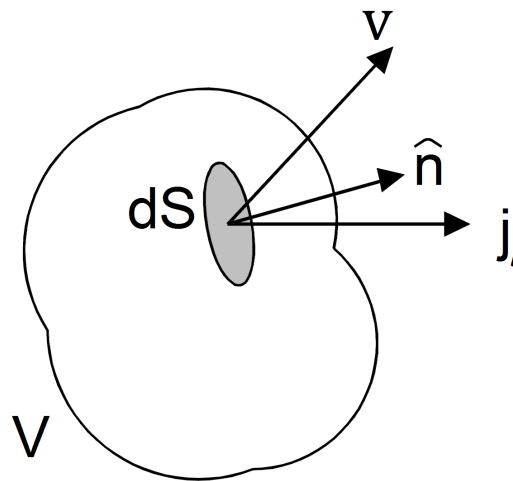


Figure A.1: Arbitrary control volume V fixed in space; mass-averaged velocity \mathbf{v} , unit normal $\hat{\mathbf{n}}$; dS is a differential area on the surface

A.2 Conservation Equations

Conservation equations for species mass and total mass, for momentum and for energy are summarised in this section. These are used in the development of the Maxwell-Stefan equations subsequently. The derivation is based on application of conservation principles to an arbitrary control volume fixed in space. Figure A.1 shows a control volume V , with a differential portion of the surface denoted dS which has a unit normal $\hat{\mathbf{n}}$. The mass-averaged velocity of the fluid volume is \mathbf{v} , while \mathbf{j}_i is the the flux of component i through dS .

Continuity Equation The continuity equation (overall mass conservation) for species i is obtained by applying the principle of conservation of mass to the control volume. This simply states that the accumulation of mass of component i within V is the sum of the mass of i entering V by convection and diffusion, plus that generated due to reaction(s) (Bird et al. 2002, Bird 1998). The mass flow-rate of component i leaving the volume via the differential area dS by convection is $\rho_i(\hat{\mathbf{n}} \cdot \mathbf{v})dS$, while that due to

diffusion is $(\hat{\mathbf{n}} \cdot \mathbf{j}_i) dS$ (Bird 1998). The mathematical form is:

$$\frac{d\rho}{dt} \int_V \rho_i dV = - \int_S (\hat{\mathbf{n}} \cdot \rho_i \mathbf{v}) dS - \int_S (\hat{\mathbf{n}} \cdot \rho_i \mathbf{j}_i) dS + \int_V r_i dV \quad (\text{A.12})$$

where r_i represents rate of production of species i by reaction. Since the volume is fixed, the time derivative may be brought within the integral. The Gauss divergence theorem (Kreyszig 2010) allows surface integrals to be expressed as volume integrals:

$$\frac{d}{dt} \int_{V(t)} (\nabla \cdot \mathbf{F}) = \int_{S(t)} (\mathbf{n} \cdot \mathbf{F}) dS \quad (\text{A.13})$$

where F is any vector function, and in which $V(t)$ and $S(t)$ may depend on time. This allows equation A.12 to be written as:

$$\int_V \frac{\partial}{\partial t} \rho \omega_i dV = - \int_V (\nabla \cdot \rho \omega_i \mathbf{v}) dV - \int_V (\nabla \cdot \rho \omega_i \mathbf{j}_i) dV + \int_V r_i dV \quad (\text{A.14})$$

As the volume V is arbitrary, the integrands can be equated, which yields (using $\mathbf{n}_i = \mathbf{j}_i + \rho \omega_i \mathbf{v}$):

$$\frac{\partial \rho \omega_i}{\partial t} = \underbrace{-\nabla \cdot \rho \omega_i \mathbf{v}}_{\text{convection}} - \underbrace{\nabla \cdot \mathbf{j}_i}_{\text{diffusion}} + \underbrace{r_i}_{\text{reaction}} \quad (\text{A.15})$$

$$= -\nabla \cdot \mathbf{n}_i + r_i \quad (\text{A.16})$$

By adding each of the n component equations, and noting that $\sum_i \rho \omega_i = \rho$, that $\sum \mathbf{j}_i = 0$, and that $\sum_i r_i = 0$ we obtain:

$$\frac{\partial \rho}{\partial t} = -\nabla \cdot \rho \mathbf{v} \quad (\text{Strong Form}) \quad (\text{A.17})$$

which is the *equation of continuity* for the mixture in the so-called *strong* or *conservative* form. The material (or *substantial*) derivative is defined by (Bird et al. 2002):

$$\frac{D()}{Dt} \equiv \frac{\partial ()}{\partial t} + \mathbf{v} \cdot \nabla ()$$

where \mathbf{v} is the mass-averaged velocity. The material derivative describes the change in space and time of a quantity; it represents the time rate of change that would be measured by an observer moving at the mass-averaged velocity (Slattery 1999). Expanding the derivative term in equation A.15 and substituting in the continuity equation allows equation A.15 to be written in so-called *weak* or *non-conservative* form using the material derivative:

$$\frac{D \rho \omega_i}{Dt} = -\nabla \cdot \mathbf{j}_i + r_i \quad (\text{Weak Form}) \quad (\text{A.18})$$

and equation A.17 to be written as:

$$\frac{D\rho}{Dt} = -\rho \nabla \cdot \mathbf{v} \quad (\text{Weak Form}) \quad (\text{A.19})$$

Momentum Equation The conservation equation for momentum can be applied in a similar way to the control volume in figure A.1. This simply implies that linear momentum of the mass in the interior of V changes with time due to momentum crossing the control volume boundary by convection and molecular diffusion, and because of external forces acting on the surface area. The force exerted at dS is $(\hat{\mathbf{n}} \cdot \boldsymbol{\pi})dS$ where $\boldsymbol{\pi}$ is the momentum flux tensor (Bird 1998). The governing equation can be written as

$$\frac{d}{dt} \int_V \rho \mathbf{v} dV = - \int_S (\hat{\mathbf{n}} \cdot \rho \mathbf{v} \mathbf{v}) dS - \int_S (\mathbf{n} \cdot \boldsymbol{\pi}) dS + \int_V \sum_{i=1}^n \rho \omega_i \mathbf{f}_i dV \quad (\text{A.20})$$

where \mathbf{f}_i represents the external forces acting on species i . The momentum flux $\boldsymbol{\pi}$ is defined as

$$\boldsymbol{\pi} = p\boldsymbol{\delta} - \mu \left(\nabla \mathbf{v} + (\nabla \mathbf{v})^T \right) + \left(\frac{2}{3}\mu - \kappa \right) (\nabla \cdot \mathbf{v}) \boldsymbol{\delta} \quad (\text{A.21})$$

$$= p\boldsymbol{\delta} + \boldsymbol{\tau} \quad (\text{A.22})$$

and includes pressure p and the viscous stress tensor $\boldsymbol{\tau}$ (Bird et al. 2002). Applying the Gauss divergence theorem and moving the time derivative outside the integral as before gives

$$\frac{\partial \rho \mathbf{v}}{\partial t} = -\nabla \cdot \rho \mathbf{v} \mathbf{v} - \nabla \cdot \boldsymbol{\pi} - \sum_{i=1}^n \rho \mathbf{f}_i \quad (\text{A.23a})$$

$$= -\nabla \cdot \rho \mathbf{v} \mathbf{v} - \nabla \cdot \boldsymbol{\tau} - \nabla p + \sum_{i=1}^n \rho \mathbf{f}_i \quad (\text{A.23b})$$

also known as the *equation of motion* for the mixture. The last term reduces to $\rho \mathbf{g}$ if the same force per unit mass acts on each species e.g. gravity. Using the material derivative gives the "weak" forms of equation A.23:

$$\rho \frac{D\mathbf{v}}{Dt} = -\nabla \cdot \boldsymbol{\pi} + \sum_{i=1}^n \rho_i \mathbf{f}_i \quad (\text{A.24a})$$

$$= -\nabla \cdot \boldsymbol{\tau} - \nabla p + \sum_{i=1}^n \rho_i \mathbf{f}_i \quad (\text{A.24b})$$

Energy Equation Applying conservation of energy to the volume V is essentially an instance of the first law of thermodynamics. The rate of energy change is the net inflow of kinetic $1/2 \rho v^2$ and internal \hat{U} energy due to conduction through the surface S , work done at the surface by the fluid as it moves across the surface, and because of work

done against external forces. Expressing this in mathematical terms gives

$$\begin{aligned} \frac{d}{dt} \int_V \left(\frac{1}{2} \rho v^2 + \rho \hat{U} \right) dV = & - \int_S \hat{\mathbf{n}} \cdot \left(\frac{1}{2} \rho v^2 + \rho \hat{U} \right) \mathbf{v} dS - \\ & \int_S (\hat{\mathbf{n}} \cdot \mathbf{q}) dS + \int_S (\hat{\mathbf{n}} \cdot (\boldsymbol{\pi} \cdot \mathbf{v})) dS + \int_V \sum_{i=1}^n (\mathbf{j}_i + \rho \omega_i \mathbf{v}) \cdot \mathbf{f}_i dV \end{aligned} \quad (\text{A.25})$$

where \mathbf{q} is a heat flux which may consist of a number of contributing factors:

$$\mathbf{q} = k \nabla T + \sum_{i=1}^n h_i \mathbf{j}_i + \text{radiation, Dufour effect, etc.} \quad (\text{A.26})$$

where k is a thermal conductivity, and h_i is enthalpy of species i . The flux is therefore a sum of a conventional Fourier term, the transport of energy by diffusion via \mathbf{j}_i , and additional terms which are often ignored. The Dufour effect will be addressed in section A.3. By bringing the time-derivative in equation A.25 inside the integral, converting the surface integrals to volume integrals and equating the integrands which result, we obtain

$$\begin{aligned} \frac{\partial}{\partial t} \left(\frac{1}{2} \rho v^2 + \rho \hat{U} \right) = & - \nabla \cdot \left(\frac{1}{2} \rho v^2 + \rho \hat{U} \right) \mathbf{v} - \nabla \cdot \mathbf{q} - \nabla \cdot (\boldsymbol{\pi} \cdot \mathbf{v}) + \\ & \sum_{i=1}^n (\mathbf{j}_i + \rho \omega_i \mathbf{v}) \cdot \mathbf{f}_i \end{aligned} \quad (\text{A.27})$$

which is the *(total) energy equation*. The last term reduces to $\mathbf{v} \cdot \rho \mathbf{g}$ if the external forces acting on the chemical species are the same. Using the material derivative gives the "weak" form

$$\rho \frac{D}{Dt} \left(\frac{1}{2} \rho v^2 + \rho \hat{U} \right) = - \nabla \cdot \mathbf{q} - \nabla \cdot (\boldsymbol{\pi} \cdot \mathbf{v}) + \sum_{i=1}^n (\mathbf{j}_i + \rho \omega_i \mathbf{v}) \cdot \mathbf{f}_i \quad (\text{A.28})$$

$$= \nabla \cdot \mathbf{q} - \nabla \cdot (\boldsymbol{\pi} \cdot \mathbf{v}) + \sum_{i=1}^n \mathbf{n}_i \cdot \mathbf{f}_i \quad (\text{A.29})$$

Neglecting kinetic energy terms, and noting that the momentum flux $\boldsymbol{\pi} = p\boldsymbol{\delta} + \boldsymbol{\tau}$, we can write the energy equation in terms of internal energy only as

$$\rho \frac{D\hat{U}}{Dt} = - \nabla \cdot \mathbf{q} - \boldsymbol{\tau} : \nabla \mathbf{v} - p \nabla \cdot \mathbf{v} + \sum_{i=1}^n \mathbf{f}_i \cdot \mathbf{j}_i \quad (\text{A.30})$$

which is the form of the energy equation used in the formulation of the Maxwell Stefan equations in section A.3. To put the energy equation in terms of temperature, note that the energy conservation equation can be written in terms of enthalpy h , so that

$$\rho \frac{Dh}{Dt} = \frac{Dp}{Dt} - \nabla \cdot \mathbf{q} - \boldsymbol{\tau} : \nabla \mathbf{v} + \sum_{i=1}^n \mathbf{f}_i \cdot \mathbf{j}_i \quad (\text{A.31})$$

since $h = U + p/\rho$. Choosing T , p and ω_i as independent variables, the enthalpy differential for a multicomponent mixture can be written as

$$dh = \sum_{i=1}^n \left(\frac{\partial h}{\partial \omega_i} \right)_{T,p} d\omega_i + \left(\frac{\partial h}{\partial T} \right)_{p,\omega_i} dT + \left(\frac{\partial h}{\partial p} \right)_{T,\omega_i} dp$$

From thermodynamics (Smith & vanNess 1987) we can write:

$$h_i \equiv \left(\frac{\partial h}{\partial \omega_i} \right)_{T,p} \quad C_P = \left(\frac{\partial h}{\partial T} \right)_{\omega_i,p} \quad \left(\frac{\partial h}{\partial p} \right)_{\omega_i,p} = \hat{V} - T \left(\frac{\partial \hat{V}}{\partial T} \right)_{\omega_i,p}$$

and substituting into equation A.31 eventually yields an energy equation in terms of temperature:

$$\rho C_P \frac{DT}{Dt} = \underbrace{-\nabla \cdot \mathbf{q}}_{\textcircled{1}} - \underbrace{\boldsymbol{\tau} : \nabla \mathbf{v}}_{\textcircled{2}} - \underbrace{\left(\frac{\partial \ln \hat{V}}{\partial \ln T} \right)_{p,\omega} \frac{Dp}{Dt}}_{\textcircled{3}} + \underbrace{\sum_{i=1}^n h_i \nabla \cdot \mathbf{j}_i}_{\textcircled{4}} + \underbrace{\sum_{i=1}^n \mathbf{f}_i \cdot \mathbf{j}_i}_{\textcircled{5}} \quad (\text{A.32})$$

The use of the material derivative of temperature $\frac{DT}{Dt}$ essentially gives the change in temperature of a fluid element that is moving at the mass-averaged velocity. Term $\textcircled{1}$ is the conventional heat flux due to thermal conduction, species diffusion and radiation from equation A.26. Term $\textcircled{2}$ is due to viscous heating in the fluid. Terms $\textcircled{3}$ represents the change in pressure associated with the change in temperature; for ideal gases, $\frac{\partial \ln \hat{V}}{\partial \ln T} = 1$. Term $\textcircled{4}$ represents energy changes due to gradients in diffusive fluxes, and term $\textcircled{5}$ accounts for enthalpy changes caused by body forces.

Using equation A.32, the simplified form of the energy equation that is used in the development of the multicomponent evaporation models in chapter 3 and 7 neglects all but the first term on the right-hand side; using the form of the heat flux from equation A.26 yields

$$\rho C_P \frac{dT}{dt} = -\nabla \cdot \mathbf{q} = k \nabla T + \sum_{i=1}^n h_i \mathbf{j}_i \quad (\text{A.33})$$

where the material derivative reduces to the derivative with respect to time only when the mass-averaged velocity is zero. Conservation equations for other quantities such as mechanical energy, or angular momentum may be derived but are not relevant for this work.

A.3 Maxwell-Stefan Equations

The development of modern approaches to modeling multicomponent mass transport is based on the work of Fick (1855) who developed a mathematical framework for diffusion using experimental work by Graham (1833, 1850). Maxwell (1860, 1866,

1868) developed a theory for diffusion in binary gas mixtures, which was then extended by Stefan (1871) to the multicomponent case. The conventional derivation of multicomponent diffusion is based on irreversible thermodynamics (IRT) (Bird et al. 2002, Curtiss & Bird 1999) or on the kinetic theory of gases (Hirschfelder et al. 1964). The theory of IRT (Onsager 1931a,b) allows the developments of Maxwell and Stefan to be generalized to include thermal, pressure and forced diffusion effects, and to allow a general description of macroscopic mass transport for a multicomponent system (Curtiss & Bird 1999, Standart et al. 1979, DeGroot & Mazur 1984, Hirschfelder et al. 1964). Datta & Vilekar (2010) presented an alternative derivation based on principles of linear momentum conservation involving balance of diffusion "drag" and diffusion driving forces. In the next section, an intuitive description of the multicomponent effects and the Maxwell-Stefan equations accounting for pressure forces only is briefly discussed; the section thereafter provides a more rigorous derivation of the Maxwell-Stefan equations suitable for generalized driving forces (in addition to pressure forces).

A.3.1 Maxwell-Stefan Equations from Momentum Balance

Figure A.2a shows schematically the interactions between molecules in binary and ternary mixtures. For the binary case, species 1 has mass m_1 and velocity u_1 , while species 2 has mass m_2 and velocity u_2 . A simple statement of conservation of momentum in an elastic collision between a molecule of 1 and 2 is simply:

$$m_1(\mathbf{u}_1 - \mathbf{u}_{f1}) + m_2(\mathbf{u}_2 - \mathbf{u}_{f2}) = 0 \quad (\text{A.34})$$

where \mathbf{u}_{f1} and \mathbf{u}_{f2} are the post-collision velocities. Similarly, conservation of kinetic energy gives:

$$m_1(\mathbf{u}_1^2 - \mathbf{u}_{f1}^2) + m_2(\mathbf{u}_2^2 - \mathbf{u}_{f2}^2) = 0 \quad (\text{A.35})$$

Solving for the final velocities gives:

$$\mathbf{u}_{f1} = \frac{\mathbf{u}_1(m_1 - m_2) + 2m_2\mathbf{u}_2}{m_1 + m_2} \quad (\text{A.36a})$$

$$\mathbf{u}_{f2} = \frac{\mathbf{u}_2(m_2 - m_1) + 2m_1\mathbf{u}_1}{m_1 + m_2} \quad (\text{A.36b})$$

Knowing \mathbf{u}_{f1} and \mathbf{u}_{f2} , we can write the momentum exchanged in a collision between 1 and 2 as:

$$m_1(\mathbf{u}_1 - \mathbf{u}_{f1}) = m_1\mathbf{u}_1 - \frac{m_1}{m_1 + m_2} (\mathbf{u}_1(m_1 - m_2) + 2m_2\mathbf{u}_2) \quad (\text{A.37})$$

$$= \frac{2m_1m_2(\mathbf{u}_1 - \mathbf{u}_2)}{m_1 + m_2} \quad (\text{A.38})$$

so that the momentum exchange is directly proportional to the difference in velocities. The rate at which collisions occur between molecules of the two species depends on the concentrations of each:

$$\begin{array}{l} \text{Number of 1-2 collisions per} \\ \text{unit volume per unit time} \end{array} \propto x_1 x_2 \quad (\text{A.39})$$

A concise statement of the forces acting on the species can be written as (Taylor & Krishna 1993):

$$\begin{array}{ccccccc} \text{Sum of forces} & & \text{Rate of change of} & & \text{Momentum} & & \text{Rate of 1-2} \\ \text{acting on} & & \text{momentum of} & & \text{exchanged per} & & \text{collisions per unit} \\ \text{particles of type} & \propto & \text{particles of type} & \propto & \text{collision between} & \times & \text{volume} \\ \text{"1" per unit} & & \text{"1" per unit} & & \text{"1" and "2"} & & \\ \text{volume} & & \text{volume} & & & & \end{array} \quad (\text{A.40})$$

Considering the control volume in figure A.2b, the motion of molecules across the boundary walls (shaded) causes momentum to exit and enter the volume. If the control volume moves with the molar average velocity of the mixture \mathbf{u} , then the flow of molecules in is balanced by the flow out, so there is no net momentum change due to movement through the walls. The force acting on species 1 at the left plane of the control volume is $Ap_1|_z$ where p is the (isobaric) pressure and $p_1 = px_1$ is the partial pressure for component 1. Similarly, the force on the right plane is $Ap_1|_{z+dz}$. Dividing by the volume Adz and taking limit as $dz \rightarrow 0$ gives:

$$\begin{array}{l} \text{Net force acting on type 1 per} \\ \text{unit volume in z direction} \end{array} = \lim_{dz \rightarrow 0} \frac{Ap_1|_z - Ap_1|_{z+dz}}{dz} \quad (\text{A.41})$$

$$= -\frac{dp_1}{dz} \quad (\text{A.42})$$

Combining these ideas, and including the other two dimensions, the force (momentum) balance becomes:

$$-\nabla p_1 = -p\nabla x_1 \propto x_1 x_2 (\mathbf{u}_1 - \mathbf{u}_2) \quad (\text{A.43})$$

$$= f_{12} x_1 x_2 (\mathbf{u}_1 - \mathbf{u}_2) \quad (\text{A.44})$$

where f_{12} is a constant of proportionality, similar to a type of "drag" coefficient between species 1 and 2 (Wesselingh & Krishna 2000). A binary diffusion coefficient can be defined as:

$$\mathbb{D}_{12} = \frac{p}{f_{12}} \quad (\text{A.45})$$

so that the momentum balance can be written as:

$$\underbrace{\nabla x_1}_{\substack{\text{diffusion driving force} \\ \text{for species 1}}} = \underbrace{-\frac{x_1 x_2 (\mathbf{u}_1 - \mathbf{u}_2)}{\mathbb{D}_{12}}}_{\text{drag force on species 1}} \quad (\text{A.46})$$

which is the Maxwell-Stefan equation for a binary, ideal mixture. A similar analysis for component 2 gives:

$$\underbrace{\nabla x_2}_{\substack{\text{diffusion driving force} \\ \text{for species 2}}} = \underbrace{-\frac{x_1 x_2 (\mathbf{u}_2 - \mathbf{u}_1)}{\mathbb{D}_{21}}}_{\text{drag force on species 2}} \quad (\text{A.47})$$

Since $\nabla x_1 + \nabla x_2 = 0$, it follows that the Maxwell-Stefan binary diffusion coefficients are symmetric (Taylor & Krishna 1993): $\mathbb{D}_{12} = \mathbb{D}_{21}$. For the ternary case (figure A.2a) interactions between each of the species must be considered. The Maxwell-Stefan equations for components 1 and 2 in a ternary system can be written by extension of equations A.46 and A.47:

$$\underbrace{\nabla x_1}_{\substack{\text{diffusion driving force} \\ \text{for species 1}}} = - \underbrace{\frac{x_1 x_2 (\mathbf{u}_1 - \mathbf{u}_2)}{\mathbb{D}_{12}}}_{\substack{\text{drag force on species 1} \\ \text{due to species 2}}} - \underbrace{\frac{x_1 x_3 (\mathbf{u}_1 - \mathbf{u}_3)}{\mathbb{D}_{13}}}_{\substack{\text{drag force on species 1} \\ \text{due to species 3}}} \quad (\text{A.48})$$

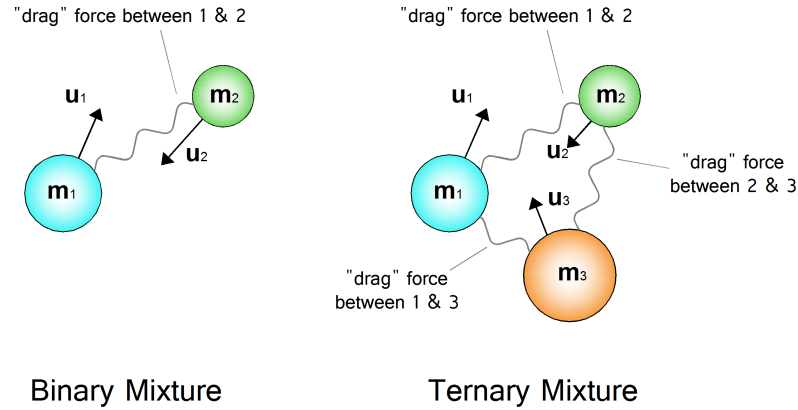
$$\underbrace{\nabla x_2}_{\substack{\text{diffusion driving force} \\ \text{for species 2}}} = - \underbrace{\frac{x_1 x_2 (\mathbf{u}_2 - \mathbf{u}_1)}{\mathbb{D}_{21}}}_{\substack{\text{drag force on species 2} \\ \text{due to species 1}}} - \underbrace{\frac{x_2 x_3 (\mathbf{u}_2 - \mathbf{u}_3)}{\mathbb{D}_{23}}}_{\substack{\text{drag force on species 2} \\ \text{due to species 3}}} \quad (\text{A.49})$$

Generalizing to an n-component system, where all ij interactions must be considered gives the Maxwell-Stefan equations in general form for ideal system at constant pressure:

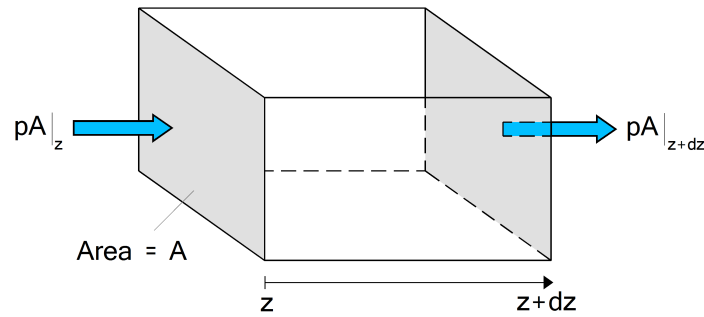
$$\nabla x_i = \sum_{\substack{j=1 \\ i \neq j}}^n \frac{x_i x_j (\mathbf{u}_i - \mathbf{u}_j)}{\mathbb{D}_{ij}} \quad (\text{A.50})$$

Only n-1 of equations A.50 are independent because the ∇x_i sum to zero, so that the n-th composition gradient is simply:

$$\nabla x_n = - \sum_{i=1}^n \nabla x_i \quad (\text{A.51})$$



(a) "Drag" forces in binary and ternary mixtures



(b) Control volume for forces balance

Figure A.2: Species Interaction for binary and ternary mixtures

A.3.2 Generalized Maxwell-Stefan Equations from IRT

In this section, a derivation of the generalized driving force for diffusion is presented based on principles of IRT. This includes forces such as pressure and temperature gradients, electromagnetic fields, gravity etc. Most literature references present the generalized driving force without derivation, however given its central importance to this work, and for sake of completeness, it is presented here in full. This is largely based on material in Lightfoot (1974) and Taylor & Krishna (1993). In chapter 3 an analytic solution to the Maxwell-Stefan equations in the gas film at the gas-liquid interface is used as a basis for the generation of evaporation maps for ternary mixtures. The starting point is a conservation equation for entropy (Lightfoot 1974):

$$\rho \frac{D\hat{S}}{Dt} = -(\nabla \cdot \mathbf{j}_s) + \sigma_s \quad (\text{A.52})$$

where ρ is total density, \hat{S} is specific entropy (per unit mass), \mathbf{j}_s is the entropy flux relative to a mass average velocity, and σ_s is entropy generation rate per unit volume.

For a multicomponent system we can write an entropy differential (Smith & vanNess 1987):

$$d\hat{U} = T ds - p dv + \sum_{i=1}^n \frac{\mu_i}{M_i} d\omega_i \quad (\text{A.53})$$

where μ_i/M_i is the chemical potential per unit mass, M_i is the molecular weight, and v is the specific volume. Applying the material derivative operator to equation A.53, multiplying by ρ and noting that $\rho = 1/v$ gives

$$T\rho \frac{Ds}{Dt} = \underbrace{\rho \frac{D\hat{U}}{Dt}}_{\textcircled{1}} + \underbrace{\frac{p}{\rho} \frac{D\rho}{Dt}}_{\textcircled{2}} - \underbrace{\sum_{i=1}^n \frac{\mu_i}{M_i} \rho \frac{D\omega_i}{Dt}}_{\textcircled{3}} \quad (\text{A.54})$$

The underlined terms above can be replaced by terms derived in section 2.1; substitute equation A.30 for term $\textcircled{1}$, equation A.17 for the derivative in term $\textcircled{2}$, and equation A.18 for the derivative in term $\textcircled{3}$. Substituting in this way for the right-hand side of equation A.54 gives an entropy balance equation:

$$T\rho \frac{Ds}{Dt} = \left(\nabla \cdot \mathbf{q} - \tau : \nabla \mathbf{v} - p \nabla \cdot \mathbf{v} + \sum_{i=1}^n \mathbf{f}_i \cdot \mathbf{j}_i \right) + \left(\frac{p}{\rho} \rho \nabla \cdot \mathbf{v} \right) + \left(\sum_{i=1}^n \frac{\mu_i}{M_i} (-\nabla \mathbf{j}_i + \sigma_i) \right) \quad (\text{A.55})$$

Collecting terms and re-arranging equation A.55 gives

$$T\rho \frac{Ds}{Dt} = \underbrace{\nabla \cdot \mathbf{q}}_{\textcircled{1}} - \tau : \nabla \mathbf{v} + \sum_{i=1}^n \mathbf{f}_i \cdot \mathbf{j}_i + \underbrace{\sum_{i=1}^n \frac{\mu_i}{M_i} \nabla \mathbf{j}_i}_{\textcircled{2}} - \sum_{i=1}^n \frac{\mu_i}{M_i} \sigma_i \quad (\text{A.56})$$

The temperature T can be brought to the right-hand side, and the chain rule applied to terms $\textcircled{1}$ and $\textcircled{2}$ so that

$$\nabla \left(\frac{1}{T} \mathbf{q} \right) = \frac{1}{T} \underbrace{\nabla \mathbf{q}}_{\textcircled{1}} + \mathbf{q} \nabla \left(\frac{1}{T} \right) \quad (\text{A.57a})$$

$$\nabla \left(\sum_{i=1}^n \frac{1}{T} \frac{\mu_i}{M_i} \mathbf{j}_i \right) = \frac{1}{T} \underbrace{\sum_{i=1}^n \frac{\mu_i}{M_i} \nabla \mathbf{j}_i}_{\textcircled{2}} + \sum_{i=1}^n \mathbf{j}_i \nabla \left(\frac{1}{T} \frac{\mu_i}{M_i} \right) \quad (\text{A.57b})$$

where the terms from equation A.56 are again numbered. Substituting these forms into equation A.56 gives

$$\begin{aligned}
\rho \frac{Ds}{Dt} = & \underbrace{-\nabla \cdot \left[\frac{1}{T} \left(\mathbf{q} - \sum_{i=1}^n \frac{\mu_i}{M_i} \mathbf{j}_i \right) \right]}_{\text{Entropy transport by diffusion}} + \\
& \underbrace{\mathbf{q} \cdot \nabla \left(\frac{1}{T} \right) - \sum_{i=1}^n \mathbf{j}_i \cdot \left(\frac{1}{T} \frac{\mu_i}{M_i} \right) - \frac{1}{T} \boldsymbol{\tau} : \nabla \mathbf{v} + \frac{1}{T} \sum_{i=1}^n \mathbf{f}_i \cdot \mathbf{j}_i - \frac{1}{T} \sum_{i=1}^n \frac{\mu_i}{M_i} \sigma_i}_{\text{Entropy production}} \quad (\text{A.58})
\end{aligned}$$

The convective flux of entropy lies in the material derivative of entropy on the left hand side, with transport and production terms on the right-hand side. The diffusive transport term includes a contribution from mass diffusion \mathbf{j}_i for each component, as well as a contribution from diffusion of energy \mathbf{q} .

The entropy production term includes a number of terms; apart from the last, which is a source term, the other contributions can be cast as products of a flux and a driving force:

$$\begin{aligned}
\mathbf{q} \cdot \nabla \left(\frac{1}{T} \right) &= (\text{heat flux}) \cdot (\text{temperature driving force}) \\
\sum_{i=1}^n \mathbf{j}_i \cdot \left(\frac{1}{T} \frac{\mu_i}{M_i} \right) &= (\text{mass flux}) \cdot (\text{chemical potential driving force}) \\
\frac{1}{T} \boldsymbol{\tau} : \nabla \mathbf{v} &= (\text{momentum diffusive flux}) : \left(\begin{array}{c} \text{driving force for} \\ \text{momentum flux} \end{array} \right) \\
\frac{1}{T} \sum_{i=1}^n \mathbf{f}_i \cdot \mathbf{j}_i &= (\text{body force}) \cdot (\text{species diffusive flux}) \\
\sum_{i=1}^n \frac{\mu_i}{M_i} \sigma_i &= \text{entropy generation due to source terms e.g. reaction}
\end{aligned}$$

The implication is that entropy is produced whenever each individual term in A.58 is non-zero, for example in the case where there is a heat flux *and* a temperature driving force, or where a mass flux *and* a chemical potential gradient exists. Comparing equation A.58 with equation A.52, we can express the diffusive and transport contributions as:

$$\mathbf{j}_s = \nabla \cdot \left[\frac{1}{T} \left(\mathbf{q} - \sum_{i=1}^n \frac{\mu_i}{M_i} \mathbf{j}_i \right) \right] \quad (\text{A.59})$$

and

$$\sigma_s = \mathbf{q} \cdot \nabla \left(\frac{1}{T} \right) - \sum_{i=1}^n \mathbf{j}_i \cdot \left(\frac{1}{T} \frac{\mu_i}{M_i} \right) - \frac{1}{T} \boldsymbol{\tau} : \nabla \mathbf{v} + \frac{1}{T} \sum_{i=1}^n \mathbf{f}_i \cdot \mathbf{j}_i - \frac{1}{T} \sum_{i=1}^n \frac{\mu_i}{M_i} \sigma_i \quad (\text{A.60})$$

$$= -\frac{\mathbf{q}}{T} \cdot \nabla \ln T - \sum_{i=1}^n \mathbf{j}_i \cdot \left[\underbrace{\nabla \left(\frac{1}{T} \frac{\mu_i}{M_i} \right)}_{\textcircled{1}} - \frac{1}{T} \mathbf{f}_i \right] - \frac{1}{T} \boldsymbol{\tau} : \nabla \mathbf{v} - \frac{1}{T} \sum_{i=1}^n \frac{\mu_i}{M_i} \sigma_i \quad (\text{A.61})$$

For a general quantity $\phi(T, P, x_i)$, the chain rule can be used to break out the dependencies of variables explicitly:

$$\nabla\phi(T, P, x_i) = \frac{\partial\phi}{\partial T}\nabla T + \frac{\partial\phi}{\partial p}\nabla p + \sum_{i=1}^n \frac{\partial\phi}{\partial x_i}\nabla x_i$$

Applying the chain rule in this way to term ① of equation A.61 gives:

$$\nabla\left(\frac{1}{T}\frac{\mu_i}{M_i}\right) = \frac{\partial(\mu_i/M_i)}{\partial T}\nabla\frac{T}{T} + \frac{1}{T}\frac{(\mu_i/M_i)}{p}\nabla p + \frac{1}{T}\nabla_{T,p}\frac{\mu_i}{M_i} \quad (\text{A.62})$$

$$= \frac{1}{T}\left(\frac{1}{M_i}\frac{\partial\mu_i}{\partial p}\nabla p + \nabla_{T,p}\frac{\mu_i}{M_i}\right) \quad (\text{A.63})$$

$$= \frac{1}{T}\left(\frac{\bar{V}_i}{M_i}\nabla p + \nabla_{T,p}\frac{\mu_i}{M_i}\right) \quad (\text{A.64})$$

where $\bar{V}_i = \partial\mu_i/\partial p$ is the partial molar volume of component i . In equation A.64, the temperature and pressure dependencies have been explicitly dealt with, but the final term has not yet been expanded. Inserting A.64 into equation A.61 gives:

$$T\sigma_s = -q\nabla\ln T - \sum_{i=1}^n \mathbf{j}_i \cdot \underbrace{\left[\nabla_{T,p}\frac{\mu_i}{M_i} + \frac{\bar{V}_i}{M_i}\nabla p - \mathbf{f}_i\right]}_{\Lambda_i} - \boldsymbol{\tau} : \nabla \mathbf{v} - \sum_{i=1}^n \frac{\mu_i}{M_i}\sigma_i \quad (\text{A.65})$$

The term denoted Λ_i in equation A.65 can be expanded by adding a vanishing term as follows (Lightfoot 1974):

$$\sum_{i=1}^n \mathbf{j}_i \cdot \left[\nabla_{T,p}\frac{\mu_i}{M_i} + \frac{\bar{V}_i}{M_i}\nabla p - \mathbf{f}_i\right] = \sum_{i=1}^n \mathbf{j}_i \cdot \Lambda_i = \sum_{i=1}^n \mathbf{j}_i \cdot \left(\Lambda_i - \frac{1}{\rho}\nabla p + \sum_{k=1}^n \omega_k \mathbf{f}_k\right) \quad (\text{A.66})$$

To see that the underlined vanishes and does not affect the result, note firstly that it does not depend on i . Then, denoting the underlined term by c in the following:

$$\sum_{i=1}^n \mathbf{j}_i \cdot (\Lambda_i - c) = \sum_{i=1}^n \mathbf{j}_i \cdot \Lambda_i + c \sum_{i=1}^n \mathbf{j}_i \quad (\text{A.67})$$

the last term is zero because the sum of the diffusive fluxes is zero:

$$\sum_{i=1}^n \mathbf{j}_i = 0$$

In the same way, the underlined term has no effect on the summation in equation A.66. The physical significance of the underlined portion is that it consists of the last two terms in the momentum equation A.23 (divided by ρ) and represents how pressure gradients and body forces affect changes in momentum. Now, from equation A.66,

replacing \mathbf{j}_i with $\rho\omega_i(\mathbf{u}_i - \mathbf{v})$ from equation A.9:

$$\sum_{i=1}^n \mathbf{j}_i \cdot \Lambda_i = \sum_{i=1}^n \left(\rho\omega_i(\mathbf{u}_i - \mathbf{v}) \cdot \left[\nabla_{T,p} \frac{\mu_i}{M_i} + \left(\frac{\bar{V}_i}{M_i} - \frac{1}{\rho} \right) \nabla p - \mathbf{f}_i + \sum_{k=1}^n \omega_k \mathbf{f}_k \right] \right) \quad (\text{A.68})$$

$$= \sum_{i=1}^n \left((\mathbf{u}_i - \mathbf{v}) \cdot \left[c_i \nabla_{T,p} \mu_i + (\phi_i - \omega_i) \nabla p - \rho\omega_i \left(\mathbf{f}_i - \sum_{k=1}^n \omega_k \mathbf{f}_k \right) \right] \right) \quad (\text{A.69})$$

$$= cRT \sum_{i=1}^n \mathbf{d}_i \cdot (\mathbf{u}_i - \mathbf{v}) \quad (\text{A.70})$$

$$= cRT \sum_{i=1}^n \frac{1}{\rho\omega_i} \mathbf{d}_i \cdot \mathbf{j}_i \quad (\text{A.71})$$

where $\phi = c_i/\bar{V}_i$ is a volume fraction, and c is the total molar concentration. The generalised driving force for diffusion \mathbf{d}_i is here defined by:

$$cRT\mathbf{d}_i \equiv \underbrace{c_i \nabla_{T,p} \mu_i}_{\textcircled{1}} + \underbrace{(\phi_i - \omega_i) \nabla p}_{\textcircled{2}} - \underbrace{\rho\omega_i \left(\mathbf{f}_i - \sum_{k=1}^n \omega_k \mathbf{f}_k \right)}_{\textcircled{3}} \quad (\text{A.72})$$

The physical interpretation of $cRT\mathbf{d}_i$ is that it represents the force acting on species i per unit volume of mixture tending to move component i relative to the solution (Taylor & Krishna 1993). Term ① accounts for *concentration diffusion* due to gradients in chemical potential (or concentration, in a practical application). Term ② accounts for *pressure diffusion*, which shows how a pressure gradient can affect separation in a mixture where there is a difference between volume and mass fractions ($\phi_i - \omega_i$), such as in the separation of uranium isotopes for fuel enrichment in gaseous centrifuges. Term ③ is a *forced* diffusion term (Bird et al. 2002), and is relevant to processes where external forces act differently on individual species. For ideal gas mixtures, equation A.72 reduces to (Taylor & Krishna 1993):

$$\mathbf{d}_i \equiv \nabla x_i + (x_i - \omega_i) \frac{\nabla p}{p} - \frac{\rho\omega_i}{p} \left(\mathbf{f}_i - \sum_{k=1}^n \omega_k \mathbf{f}_k \right) \quad (\text{A.73})$$

or simply:

$$\mathbf{d}_i \equiv \frac{dx_i}{dz} \quad (\text{A.74})$$

when terms involving pressure difference ∇p and body forces \mathbf{f} can be neglected. It can also be shown from the Gibbs-Duhem equation that (Lightfoot 1974):

$$\sum_{i=1}^n \mathbf{d}_i = 0$$

Table A.1: Contributions to entropy production rate (terms in equation A.75)

Term	Significance
1	Entropy production due to heat flux in presence of temperature gradient
2	Entropy production due to species diffusion in presence of a generalised diffusive gradient \mathbf{d}_i
3	Entropy production due to momentum diffusive fluxes in presence of velocity gradients
4	Entropy production due to source terms (e.g. chemical reaction)

Table A.2: Forces and fluxes in entropy production (terms in equation A.75)

Flux	Force
\mathbf{j}_i	$\frac{-cRT}{\rho\omega_i} \mathbf{d}_i$
\mathbf{q}	$-\nabla \ln T$
$\boldsymbol{\tau}$	$-\nabla \mathbf{v}$

Now, inserting the form for \mathbf{d}_i from equation A.72 into equation A.65 gives:

$$T\sigma_s = \underbrace{-\mathbf{q}\nabla \ln T}_{\textcircled{1}} - \underbrace{cRT \sum_{i=1}^n \frac{1}{\rho\omega_i} \mathbf{d}_i \cdot \mathbf{j}_i}_{\textcircled{2}} - \underbrace{\boldsymbol{\tau} : \nabla \mathbf{v}}_{\textcircled{3}} - \underbrace{\sum_{i=1}^n \frac{\mu_i}{M_i} \sigma_i}_{\textcircled{4}} \quad (\text{A.75})$$

representing four contributors to the production of entropy for a multicomponent mixture. The significance of each of the terms in equation A.75 is summarised in table A.1. The second postulate of irreversible thermodynamics (linearity postulate) states that the fluxes are directly proportional to the driving forces (Bird et al. 2002):

$$\mathbf{j}_\alpha = \sum_{j=1}^n L_{ij} x_j \quad (\text{A.76})$$

where \mathbf{j} is any flux (mass, momentum, or energy), and x_j is an corresponding driving force; these are listed in table A.2. The L_{ij} are known as the Onsager phenomenological coefficients (constants of proportionality). The fourth postulate of irreversible thermodynamics states that the L_{ij} are symmetric, so that $L_{ij} = L_{ji}$ (Onsager 1931a,b). The third postulate (Curie's postulate) stipulates that fluxes are functions of forces only if the fluxes and forces are of the same tensorial order. The possible dependencies for \mathbf{j}_i and \mathbf{q} are shown in table A.3 and considered in detail below.

Species Diffusive Flux \mathbf{j}_i : As a result of Curie's postulate the species diffusive flux for component i may be written as a linear combination of two driving forces, denoting

Table A.3: Possible dependencies from third postulate of irreversible thermodynamics

Flux	Tensorial Order	Dependencies
\mathbf{j}_i	1	$-\nabla \ln T, \frac{-cRT}{\rho\omega_i} \mathbf{d}_i$
\mathbf{q}	1	$-\nabla \ln T, \frac{-cRT}{\rho\omega_i} \mathbf{d}_i$
$\boldsymbol{\tau}$	2	$-\nabla \mathbf{v}$

the Onsager coefficients as L_{ij} and L_{iq} for the diffusive and temperature driving forces respectively (Curtiss & Bird 1999):

$$\mathbf{j}_i = - \sum_{j=1}^{n-1} L_{ij} \frac{cRT}{\rho\omega_i} \mathbf{d}_j - L_{iq} \nabla \ln T \quad (\text{A.77})$$

$$= - \sum_{j=1}^{n-1} D_{ij}^o \mathbf{d}_j - \underbrace{D_{ij}^T \nabla \ln T}_{\text{Soret effect}} \quad (\text{A.78})$$

where D_{ij}^o is the Fickian diffusivity, and D_{ij}^T are the multicomponent thermal diffusion coefficients. Equation A.78 is a generalised Fick's law, where the additional term involving $\nabla \ln T$ is the contribution of a temperature gradient to diffusion of component i , called the *Soret effect* (Bird et al. 2002). The Soret effect is generally not significant except in cases for large temperature gradients.

Inverting equation A.78 in order to express the driving force in terms of the fluxes (Curtiss & Bird 1999) gives the generalised Maxwell-Stefan equations

$$\mathbf{d}_i = - \sum_{\substack{j=1 \\ j \neq i}}^n \frac{x_i x_j}{\rho \mathfrak{D}_{ij}} \left(\frac{\mathbf{j}_i}{\omega_i} - \frac{\mathbf{j}_j}{\omega_j} \right) - \nabla \ln T \sum_{\substack{j=1 \\ j \neq i}}^n \frac{x_i x_j}{\mathfrak{D}_{ij}} \left(\frac{D_i^T}{\rho\omega_i} - \frac{D_j^T}{\rho\omega_j} \right) \quad (\text{A.79})$$

\mathfrak{D}_{ij} is the Maxwell-Stefan diffusivity for the ij pair and has the physical significance of an inverse drag coefficient. For ideal gas mixtures in the absence of pressure gradients and external forces, the underlined term A.79 can be ignored, and the Maxwell-Stefan equation expressed in terms of molar fluxes \mathbf{N}_i and \mathbf{J}_i is

$$\mathbf{d}_i = - \sum_{\substack{j=1 \\ j \neq i}}^n \frac{x_i \mathbf{N}_i - x_j \mathbf{N}_j}{c \mathfrak{D}_{ij}} = - \sum_{\substack{j=1 \\ j \neq i}}^n \frac{x_i \mathbf{J}_i - x_j \mathbf{J}_j}{c \mathfrak{D}_{ij}} \quad (\text{A.80})$$

Heat Flux \mathbf{q} : In a similar way, Curie's postulate allows the heat flux to be written as the sum of two contributions from table A.3:

$$\mathbf{q} = -L_{qq} \nabla \ln T - \underbrace{\sum_{i=1}^n L_{qi} \frac{cRT}{\rho\omega_i} \mathbf{d}_i}_{\text{Dufour effect}} \quad (\text{A.81})$$

so that the heat flux \mathbf{q} is a function of a temperature gradient but also of the mass driving forces inherent in the definition of \mathbf{d}_i . The Dufour effect describes the flow of heat caused by concentration gradients. By choosing $L_{qq} = kT$, where k is the thermal conductivity, Fourier's law (or constitutive relationship) is recovered.

Substituting the expression for \mathbf{d}_i from equation A.79 into the the right-hand side of equation A.81 gives

$$\mathbf{q} = \underbrace{-k\nabla T}_{\text{Fourier's law}} - \underbrace{\sum_{i=1}^n h_i \mathbf{j}_i}_{\text{Species diffusion}} + \underbrace{\sum_{i=1}^n \sum_{\substack{j=1 \\ i \neq j}}^n \frac{cRT x_i x_j}{\rho \omega_i \mathfrak{D}_{ij}} \left(\frac{\mathbf{j}_i}{\rho \omega_i} - \frac{\mathbf{j}_j}{\rho \omega_j} \right)}_{\text{Dufour effect}} \quad (\text{A.82})$$

which shows how the heat flux consists of a conventional Fourier contribution, and contributions written in terms of species diffusive fluxes \mathbf{j}_i . The second term does not arise due to irreversible thermodynamics, but arises due to the addition of enthalpy due to species fluxes. Similarly, a radiative heat flux term can be included if required. Most often, the Dufour contribution is neglected. In this work, the heat flux \mathbf{q} uses the first two terms from equation A.82, incorporated into the energy equation given by A.33, and is used to derive the heat balance for evaporating mixtures in chapters 3 and 7, as well as expression for multicomponent wet-bulb temperature in chapter 3.

Appendix B

Physical Property Modelling

B.1 Vapour-Liquid Equilibria

The NRTL (Non-Random Two Liquid) model (Prausnitz et al. 1986) is used to represent the activity coefficients for the non-ideal liquid phase. The molar excess Gibbs energy is represented by

$$\frac{g^E}{RT} = - \sum_{i=1}^n x_i \frac{\sum_{j=1}^n \tau_{ji} G_{ji} x_j}{\sum_{k=1}^n G_{ki} x_k} \quad (\text{B.1})$$

The binary interaction parameters were obtained from *Aspen Properties Plus* (Aspen-Tech 2014), wherein the activity coefficient for component i in a n -component mixture is given by:

$$\ln \gamma_i = \frac{\sum_{j=1}^n \tau_{ij} G_{ji} x_j}{\sum_{k=1}^n G_{ki} x_k} + \sum_{j=1}^n \frac{x_j G_{ij}}{\sum_{k=1}^n G_{kj} x_k} \left(\tau_{ij} - \frac{\sum_{j=1}^n \tau_{ij} G_{ji} x_j}{\sum_{k=1}^n G_{ki} x_k} \right) \quad (\text{B.2})$$

$$G_{ij} = \exp(-\alpha_{ij} \tau_{ij}) \quad (\text{B.3})$$

$$\tau_{ij} = A_{ij} + \frac{B_{ij}}{T} + E_{ij} \ln T + F_{ij} \quad (\text{B.4})$$

$$\alpha_{ij} = C_{ij} + D_{ij} (T - 273.15) \quad (\text{B.5})$$

$$\tau_{ii} = 0 \quad (\text{B.6})$$

$$G_{ij} = 1 \quad (\text{B.7})$$

where T is in Kelvin. The A_{ij} - F_{ij} are the binary interaction parameters of the NRTL model. For the mixtures used in this work, the D_{ij} , E_{ij} and F_{ij} are all zero. To verify

the accuracy of the input parameters, dew-point and bubble-point temperatures were calculated for a selection of the binary pairs of the various ternary mixtures used in this work. Calculated values for dew-point and bubble point are shown in figures B.1-B.3 for the various mixtures used in this work. As the figures indicate, agreement between the computed temperatures and values extracted from AspenPlus data-based is generally good.

Table B.1: NRTL parameters for IPA-ethanol-methanol

Constants		IPA	Ethanol	Methanol
A	IPA	-	0.0	0.0
	Ethanol	0.0	-	0.0
	Methanol	0.0	0.0	-
B	IPA	-	-266.377	-407.2343
	Ethanol	347.2905	-	6.408
	Methanol	603.0983	-13.0821	-
C	IPA	-	0.3125	0.3012
	Ethanol	0.3125	-	0.3356
	Methanol	0.3012	0.3356	-

Table B.2: NRTL parameters for water-ethanol-methanol

Constants		Water	Ethanol	Methanol
A	Water	-	0.0	0.0
	Ethanol	0.0	-	0.0
	Methanol	0.0	0.0	-
B	Water	-	670.4442	423.323
	Ethanol	-55.1698	-	6.408
	Methanol	-127.7571	-13.0821	-
C	Water	-	0.3031	0.2994
	Ethanol	0.3031	-	0.3356
	Methanol	0.2994	0.3556	-

Table B.3: NRTL parameters for IPA-water-ethanol

Constants		IPA	Water	Ethanol
A	IPA	-	1.3115	0.0
	Water	6.8284	-	0.0
	Methanol	0.0	0.0	-
B	IPA	-	426.398	-266.377
	Water	-1483.46	-	670.4442
	Ethanol	347.2905	-55.7571	-
C	IPA	-	0.3	0.3125
	Water	0.3	-	0.3031
	Ethanol	0.3125	0.3031	-

Table B.4: NRTL parameters for ethanol-MEK-toluene

Constants		Ethanol	MEK	Toluene
A	Ethanol	-	0.0	0.0
	MEK	0.0	-	0.0
	Toluene	0.0	0.0	-
B	Ethanol	-	32.4554	414.7047
	MEK	233.0871	-	253.1558
	Toluene	289.1683	-91.3609	-
C	Ethanol	-	0.301	0.3
	MEK	0.301	-	0.2996
	Toluene	0.3	0.2996	-

Table B.5: NRTL parameters for DCM-methanol-ethyl acetate

Constants		DCM	Methanol	Ethyl Acetate
A	DCM	-	0.0	0.0
	Methanol	0.0	-	0.0
	Ethyl Acetate	0.0	0.0	-
B	DCM	-	763.5569	41.1924
	Methanol	37.3076	-	173.8828
	Ethyl Acetate	-282.9557	211.7217	-
C	DCM	-	0.483	0.3
	Methanol	0.483	-	0.2962
	Ethyl Acetate	0.3	0.2962	-

Table B.6: NRTL parameters for benzene-acetone-chloroform

Constants		Acetone	Chloroform	Methanol
A	Acetone	-	0.0	0.0
	Chloroform	0.0	-	0.0
	Methanol	0.0	0.0	-
B	Acetone	-	-323.708	101.8559
	Chloroform	114.9639	-	690.066
	Methanol	114.1347	-71.9029	-
C	Acetone	-	0.3043	0.3084
	Chloroform	0.3043	-	0.3
	Methanol	0.3084	0.3	-

Table B.7: NRTL parameters for acetone-chloroform-methanol

Constants		Benzene	Acetone	Chloroform
A	Benzene	-	0.0	0.0
	Acetone	0.0	-	0.0
	Chloroform	0.0	0.0	-
B	Benzene	-	286.7998	-145.0343
	Acetone	-97.2924	-	-323.708
	Chloroform	89.088	114.9639	-
C	Benzene	-	0.3007	0.3061
	Acetone	0.3007	-	0.3043
	Chloroform	0.3061	0.3043	-

B.2 Composition Derivatives of NRTL model

In the calculation of pseudo-azeotropes (section 3.2.3, 4.2.1 and 4.2.4), numerical values of the composition derivatives of the activity coefficients are required. These are given by the following formula (Taylor & Krishna 1993), where the A_{ij} and B_{ij} refer to values in tables B.1-B.7:

$$\frac{\partial \ln \gamma_i}{\partial x_j} = \epsilon_{ij} + \epsilon_{ji} - \sum_{k=1}^n \frac{x_k}{S_j} (G_{ik}\epsilon_{jk} + G_{jk}\epsilon_{ik})$$

where

$$\epsilon_{ij} = \frac{G_{ij}}{S_j} \left(\tau_{ij} - \frac{C_j}{S_j} \right)$$

$$G_{ij} = \exp(-\alpha_{ij}\tau_{ij})$$

$$\tau_{ij} = A_{ij} + \frac{B_{ij}}{T}$$

$$S_i = \sum_{j=1}^n x_j G_{ji}$$

$$C_i = \sum_{j=1}^n x_j G_{ji} \tau_{ji}$$

$$\tau_{ii} = 0 \quad G_{ii} = 1$$

B.3 Vapour Pressure

To determine the partial derivatives, a vapour pressure expression of the following form is used (Prausnitz et al. (1986)):

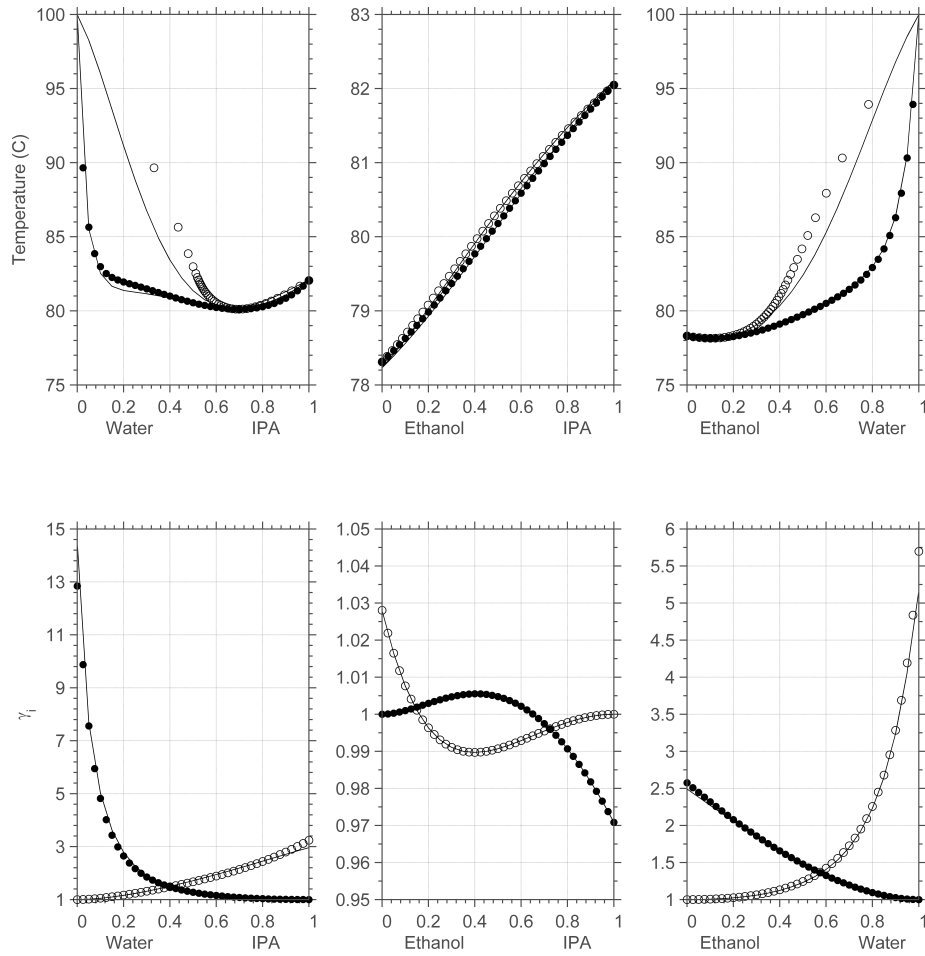


Figure B.1: Txy and activity coefficient predictions for binary pairs in IPA-water-ethanol mixture; \bullet = bubble-point (AspenPlus), \circ = dew-point (AspenPlus). Solid lines are predictions using NRTL parameters from table B.3.

$$p_i = P_i^c \exp \left\{ \frac{1}{1 - \left(1 - \frac{T}{T_i^c}\right)} \left(A_i \left(1 - \frac{T}{T_i^c}\right) + B_i \left(1 - \frac{T}{T_i^c}\right)^{1.5} - D_i \left(1 - \frac{T}{T_i^c}\right)^6 \right) \right\} \quad (\text{B.8})$$

Parameters for each of the pure components used in this work are given in table B.8.

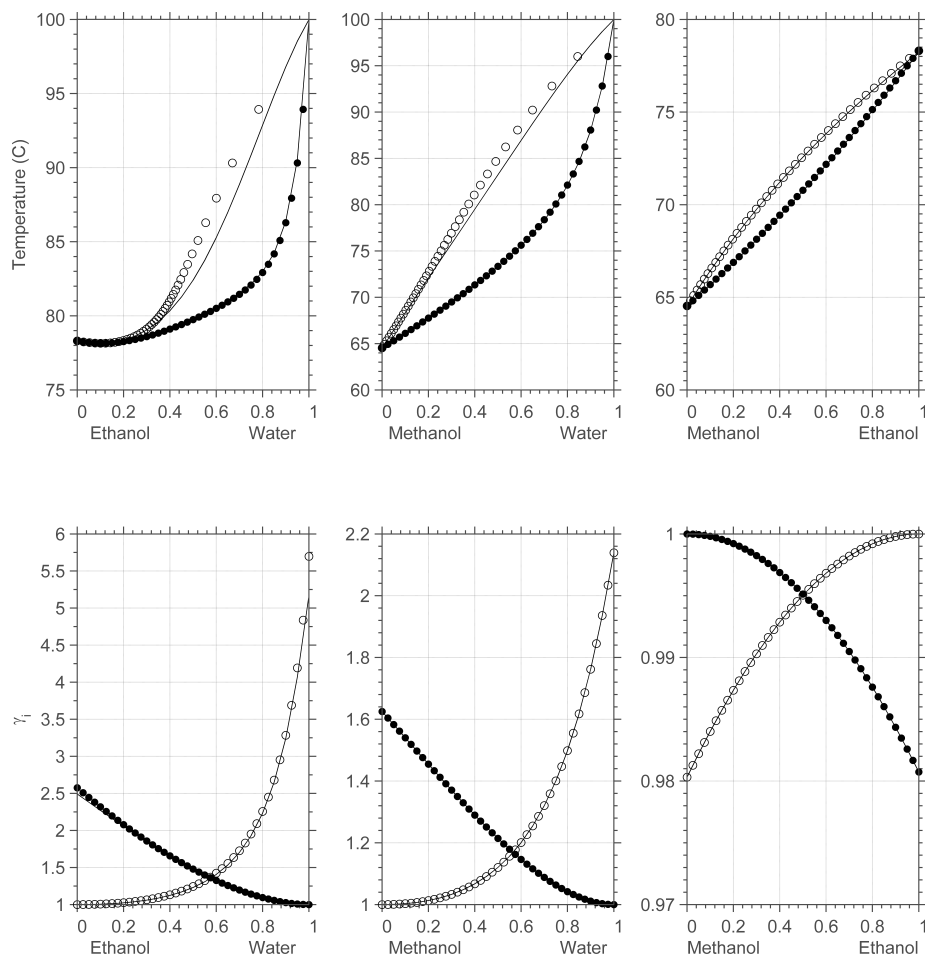


Figure B.2: Txy and activity coefficient predictions for binary pairs in water-ethanol-methanol mixture; ● = bubble-point (AspenPlus), ○ = dew-point (AspenPlus). Solid lines are predictions using NRTL parameters from table B.2.

B.4 Diffusivity

B.4.1 Gas/Vapour Diffusivity

Binary gas phase diffusion coefficients were estimated using an expression developed by Chapman and Enskog potentials (Cussler 2009):

$$D_{AB} = \frac{0.0018583 \left(T^{3/2} \left(\frac{1}{M_A} - \frac{1}{M_B} \right)^{1/2} \right)}{p \sigma_{AB}^2 \Omega} \quad (\text{B.9})$$

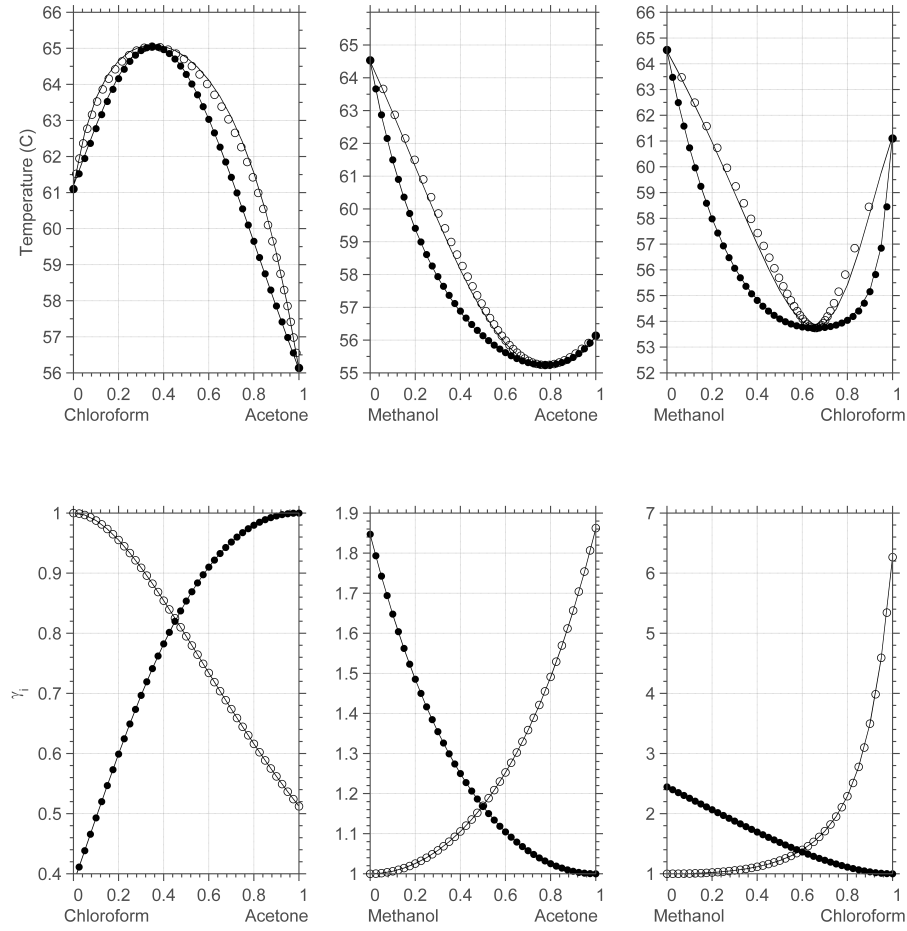


Figure B.3: Txy and activity coefficient predictions for binary pairs in acetone-chloroform-methanol mixture; • = bubble-point (AspenPlus), ○ = dew-point (AspenPlus). Solid lines are predictions using NRTL parameters from table B.6.

where σ_{AB} and Ω_{AB} are characteristic molecular properties given by:

$$\Omega_{AB} = \frac{1.0636}{(T^*)^{0.1561}} + \frac{0.19399}{\exp(0.47635T^*)} + \frac{1.03587}{\exp(1.52996T^*)} + \frac{1.7646}{\exp(3.89411T^*)} \quad (\text{B.10})$$

$$\sigma_{AB} = \frac{\sigma_A + \sigma_B}{2} \quad (\text{B.11})$$

$$(\text{B.12})$$

where

$$T^* = \frac{kT}{\epsilon_{AB}} \quad (\text{B.13})$$

$$\epsilon_{AB} = (\epsilon_A + \epsilon_B)^{1/2} \quad (\text{B.14})$$

Table B.8: Parameters for Antoine vapour pressure correlation

Constants	IPA	Ethanol	Methanol	Water	MEK
A	-8.16927	-8.51838	-8.54796	-8.58138	-7.71476
B	-0.094312	0.34163	0.76982	0.34163	1.71061
C	-8.10	-5.73683	-3.1085	-5.73683	-3.6877
D	7.85	8.32581	1.54481	8.32581	-0.75169

Constants	Toluene	DCM	Ethyl Acetate	Acetone	Chloroform
A	-7.28607	-7.35739	-7.68521	-7.45514	-6.95546
B	1.38091	2.17546	1.36511	1.202	1.16625
C	-2.83433	-4.07038	-4.0898	-2.43926	-2.1397
D	-2.79168	3.50707	-1.75342	-3.559	3.44421

(B.15)

and T is in Kelvin. The Lennard-Jones potentials σ and ϵ/k , as determined from viscosity data, are given in table B.9 for the various pure components .

Table B.9: Lennard Jones potentials (Prausnitz et al. 1986)

Constants	IPA	Ethanol	Methanol	Water	MEK
σ	4.53	4.53	3.626	2.641	5.92
ϵ/k	362.6	362.6	481.8	809.1	410.0

Constants	Toluene	DCM	Ethyl Acetate	Acetone	Chloroform
σ	5.92	4.89	5.205	4.6	5.389
ϵ/k	410.0	356.3	521.3	560.2	340.2

B.4.2 Liquid Diffusivity

The method of Wilke-Chang (Prausnitz et al. 1986) was used to calculate diffusion coefficients in the liquid phase. The diffusivity coefficient of species A (solute) in infinitely low concentration in species B (solvent) is given by [cm^2/s]:

$$D_{AB}^o = 7.4 \times 10^{-8} \frac{(\phi M_B)^{1/2} T}{\mu_2 V_1^{0.6}} \quad (B.16)$$

where M_B is the molecular weight of the solvent [g/mol], μ is the liquid viscosity [cP], V_1 is the molar volume of solute, and T is the liquid temperature [Kelvin]. ϕ is an association factor (2.26 for water, 1.9 for methanol, 1.5 for ethanol and 1.0 for unassociated solvents).